TESIS DE LA UNIVERSIDAD DE ZARAGOZA

2017

43

María Virumbrales Muñoz

Development of microfluidic tools to reproduce and characterize the tumor microenvironment

Departamento

Instituto de Investigación en Ingeniería [I3A]

Director/es

Doblaré Castellano, Manuel
Ochoa Garrido, Ignacio
Fernández Ledesma, Luis José

ISSN 2254-7606

Prensas de la Universidad Universidad Zaragoza

ISSN 2254-7606

Universidad Zaragoza
1542

Tesis Doctoral

DEVELOPMENT OF MICROFLUIDIC TOOLS TO REPRODUCE AND CHARACTERIZE THE TUMOR MICROENVIRONMENT

Autor

María Virumbrales Muñoz

Director/es

Doblaré Castellano, Manuel
Ochoa Garrido, Ignacio
Fernández Ledesma, Luis José

UNIVERSIDAD DE ZARAGOZA

Instituto de Investigación en Ingeniería [I3A]

2017

Development of microfluidic tools to reproduce and characterize the tumor microenvironment.

PhD Dissertation presented by

María Virumbrales Muñoz

Faculty supervisors

Manuel Doblaré Castellano

Luis José Fernández Ledesma

Ignacio Ochoa Garrido

Applied Mechanics and Bioengineering group (AMB)

Instituto de Investigación en Ingeniería de Aragón (I3A)

Universidad de Zaragoza

Index.

List of abreviations. i
List of figures. iii
List of tables. vii
Abstract. viii
Resumen. ix
Acknowledgements. x
Agradecimientos. xiii
Outline. xvi
Chapter 1: Background. 1
1.1 Dissecting anti-cancer drug development decay. 1
1.2 Cancer prevalence and mortality. 3
1.3 Cancer development (tumorigenesis). 4
1.4 Features of the tumor microenvironment (TME). 6
1.4.1 Cellular components of the TME. 6
1.4.2 Non-cellular components of the TME: Extracellular matrix. 10
1.4.3 Non-cellular components of the TME: soluble molecules and biological gradients. 11
1.5 Three-dimensional cell culture as a crucial improve-ment to current in vitro models. 14
1.5.1 The importance of 3D in vitro cell culture. 14
1.5.2 Most common 3D in vitro tumor models. 17
1.6 Classical 3D cell culture strategies for reproducing and characterizing different aspects of the TME. 20
1.6.1 ECM: Natural scaffolds and hydrogels. 20
1.6.2 Substrate topography. 24
1.6.3 Hypoxia. 25

1.6.4 Other soluble factors. 28

1.6.5 Co-culture. 31

1.7 Microfluidics and microtechnologies as an alternative to reproduce and characterize the TME. 34

1.8 Aims and objectives. 40

Chapter 2: Development of microfluidic systems for 2D-3D cell co-cultures. 41

2.1 Introduction. 41

2.2 Materials and Methods. 44

2.2.1 Microdevice fabrication and setup. 44

2.2.2 Air-hydrogel interface generation and optimization in the microdevice. 46

2.2.3 Microdevice biocompatibility and 3D cell culture microenvironment characterization. 47

2.2.4 Preparation of soluble recombinant TRAIL and anchoring to lipid vesicles. 51

2.2.5 Drug diffusion assays. 52

2.2.6 Imaging. 52

2.2.7 Image analysis and processing. 52

2.2.8 Statistical analysis. 52

2.3 Results and discussion. 53

2.3.1 Hydrophilic features and liquid handling within the microdevice. 53

2.3.2 Air-hydrogel interface analysis and optimization in the microdevice. 55

2.3.3 Microdevice biocompatibility and characterization of the 3D cell culture microenvironment. 57

2.3.4 Characterization of the endothelial barrier model. 60

2.3.5 Co-culture model with a 2D endothelium and MDA-MB-231 breast tumor cells cultured in 3D in a collagen matrix. 63

2.3.6 Drug screening in the tumor-endothelium model. 66

2.3.7 Adaptation of the design for mass-production of the microdevice. 71

2.4 Chapter summary. 73

Chapter 3: Oxygen-sensitive three-dimensional matrix for in situ hypoxia detection in cell culture. 75

3.1 Introduction. 75

3.2 Materials and methods. 77

3.2.1 Chemical synthesis of the oxygen sensitive compound. 77

3.2.2 Oxygen-sensitive probe covalent coupling to ungelated collagen. 78

3.2.3 Preparation of the conjugated hydrogel and characterization of covalent binding. 79

3.2.4 Probe-collagen Conjugation efficiency. 80

3.2.5 Analysis of the hydrogel architecture and anisotropy by confocal reflection microscopy. 80

3.2.6 Detailed hydrogel architecture characterization by SEM imaging. 81

3.2.7 Mechanical characterization. 81

3.2.8 Coupled oxygen-sensitive probe photostability. 82

3.2.9 Cell culture. 83

3.2.10 Cell viability within the 3D oxygen sensitive hydrogel. 83

3.2.11 Oxygen probe calibration and in situ oxygen measurements. 84

3.3 Results and discussion. 84

3.3.1 Preparation of the 3D oxygen-sensitive hydrogel-based matrix. 84

3.3.2 Properties of the 3D oxygen-sensitive matrix. 89

3.3.3 Photostability of the 3D oxygen-sensitive matrix. 92

3.3.4 Biocompatibility of the 3D oxygen-sensitive matrix. 95

3.3.5 Calibration of the 3D oxygen-sensitive matrix. 99

3.3.6 Application of the 3D oxygen-sensitive matrix for oxygen mapping of 3D cell culture. 100

3.4 Chapter summary. 102

Chapter 4: Enabling cell recovery from 3D cell culture microfluidic devices for tumor microenvironment genetic signature evaluation. 104
4.1 Introduction. 104
4.2 Materials and methods. 106
4.2.1 Microdevice fabrication. 106
4.2.2 Hydrogel preparation and setup handling. 107
4.2.3 Cell culture. 108
4.2.4 Cell staining. 108
4.2.5 Validation of the model for drug testing. 109
4.2.6 Hydrogel degradation procedure. 110
4.2.7 Hydrogel degradation tracking. 110
4.2.8 Gene expression assays. 111
4.2.9 Patterning method. 113
4.2.10 Image analysis. 114
4.2.11 Statistical analysis. 114
4.3 Results and discussion. 114
4.3.1 Microdevice fabrication and setup. 114
4.3.2 Necrotic core generation in the microdevice. 116
4.3.3 Cell proliferation in the model. 117
4.3.4 Oxygen gradient in the microdevice. 119
4.3.5 Apoptosis quantification. 120
4.3.6 Validation of the tumor slice model for drug testing. 121
4.3.7 Cell recovery from the microdevices. 124
4.3.8 Cell viability of the recovery procedure. 127
4.3.9 Characterization of RNA extracted from recovered cells. 128
4.3.10 RT-PCR demonstration of RNA from recovered cells. 129

4.3.11 Cell patterning in the microdevice. 130
4.4 Chapter summary. 132
Chapter 5: Conclusions. 133
Capítulo 5: Conclusiones. 134
Chapter 6: Future work. 135
Output. 137
Appendix 1: Graphene oxide increases the viability of C2C12 myoblasts microencapsulated in alginate. 142
A1 Introduction to Atomic force microscopy. 142
A2 Application of AFM to microcapsule characterization. 145
A2.1 Introduction. 145
A2.2 Material and methods. 147
A2.2.1 Biomaterials. 147
A2.2.2 Atomic force microscopy (AFM). 148
A2.2.3 Statistical analysis. 148
A2.3 Results. 149
A2.4 Conclusions. 152
References. 153

List of abreviations.

2D	Two-dimensional.
3D	Three-dimensional.
CAM	Calcein Acetoxymethyl ester.
DAPI	4',6-diamidino-2-phenylindole.
DMEM	Dulbecco´s modified Eagle medium.
DNA	Deoxyribonucleic acid.
DOX	Doxorubicin.
ECM	Extracellular matrix.
EDC	N-(3-Dimethylaminopropyl)-N'-ethylcarbodiimide hydrochloride.
EDTA	Ethylenediaminetetraacetic acid.
FBS	Fetal bovine serum.
HIF	Hypoxia-Inducible Factor.
HUVEC	Human Umbilical Vascular Endothelial Cell.
LUV	Large Unilamellar Vesicle.
MCTS	Multicellular tumor spheroids.
MES	2-(N-Morpholino) ethanesulfonic acid, 4-Morpholineethanesulfonic acid.
MT-MMP	Membrane Type Matrix MetalloProteinase.
NBDG	2-(N-(7-Nitrobenz-2-oxa-1,3-diazol-4-yl) Amino)-2 Deoxyglucose.
PBS	Phosphate buffered saline.
PDMS	Polydimethylsiloxane.

PEG	Poly-ethylene glycol.
PI	Propidium iodide.
PFA	Paraformaldehyde.
RNA	Ribonucleic acid
RT-PCR	Real Time Polymerase Chain Reaction.
Sulfo-NHS	N-Hydroxysulfosuccinimide.
TNF-α	Tumor Necrosis Factor – α.
TRAIL	TNF-α Related Apoptosis-Inducing Ligand.
TME	Tumor microenvironment.

List of figures.

Figure 1.1: Large pharma productivity from 2005–2010.

Figure 1.2: Ten Leading Cancer Types for the Estimated New Cancer Cases and Deaths by Sex, United States, 2016.

Figure 1.3: The hallmarks of cancer.

Figure 1.4: Tumor microenvironment.

Figure 1.5: Multifactorial Contributions of Activated Stromal Calls to the Hallmarks of Cancer.

Figure 1.6: Distinct elastic modulus of human tissues suggesting tissue-specific stiffness.

Figure 1.7: Diffusion mechanism for molecules in static liquids.

Figure 1.8: Adhesive, topographical, mechanical, and soluble cues in 2D and 3D.

Figure 1.9: Schematic representing the various 3D models of cancer.

Figure 1.10. Spheroid characteristics.

Figure 1.11: Summary of features a biomaterial should comply with, organized in terms of importance according to the author's opinion.

Figure 1.12: Effect of cell adhesion patterns on cell shape, architecture and contractility.

Figure 1.13: Main types of hypoxic chambers. Left- Binder® hypoxia-hyperoxia incubator.

Figure 1.14: Scheme showing how hydrogels can be used to expose cells to biomolecule gradients.

Figure 1.15: Transwell assay scheme.

Figure 1.16: Zigmond Chamber.

Figure 1.17: Schematics of different co-culture methods.

Figure 1.18: Endothelial cell-lined lumens and possible morphologies.

Figure 1.19: Generation of microvascular networks in the presence of BM-hMSC and different biomolecules.

Figure 1.20: Microfluidic tumor-vascular interface model.

Figure 1.21: Establishment of Vascularized Micro-Tumors (VMTs).

Figure 2.1: Experimental configuration and microdevice fabrication.

Figure 2.2: Schematic representation of the device, showing capillary forces exerted by the geometry, and capillary valves integrated into the design.

Figure 2.3: Microdevice fabrication process flow.

Figure 2.4: Phenotypical characterization of the extracted HUVEC cells by means of flow cytometry to confirm their endothelial lineage.

Figure 2.5: Phenotypical characterization of the extracted HUVEC cells through tube formation assay to confirm their endothelial lineage.

Figure 2.6: Fabricated SU-8 microdevice.

Figure 2.7: Contact angle measurements for the SU-8 material.

Figure 2.8: Effect of the plasma treatment on the microdevice spontaneous filling.

Figure 2.9: Characterization of the hydrogel-air interface in the microdevice using confocal microscopy.

Figure 2.10: Viability of the MDA-MB231 cells grown in the microdevice in a 3D hydrogel matrix.

Figure 2.11: Whole microwell images of cell proliferation through Premo FUCCI® transfection for different cell densities.

Figure 2.12: Characterization of the hypoxia level in the device for different cell densities.

Figure 2.13: Characterization of the endothelium generated on the top of the hydrogel matric in the microdevice.

Figure 2.14: Whole microwell immunofluorescence images to verify the endothelium integrity.

Figure 2.15: Co-culture of MDA-MB231 tumor cells with HUVECs cells.

Figure 2.16: Whole microwell immunofluorescence images to assess endothelium integrity.

Figure 2.17: Quantification of the effect of co-culture of MDA-MB231 tumor cells with HUVECs cells.

Figure 2.18: Drug testing assay using TRAIL in the co-culture established models.

Figure 2.19: Quantification of the endothelium integrity in samples treated with both sTRAIL and LUV-TRAIL.

Figure 2.20: Whole microwell immunofluorescence images to verify the endothelium integrity after exposure to the TRAIL drug.

Figure 2.21: Diffusion/penetration across an endothelium seeded on a collagen gel.

Figure 2.22: Quantification of MDA-MB-231 tumor cell death in 3D along the device microwell depth in control conditions, and with sTRAIL and LUV-TRAIL treatment in the established microfluidic co-culture model.

Figure 3.1: Synthesis of the carboxylic acid terminated [Ru(BPhen)2]2+ (BPhen=batophenanthroline) probe.

Figure 3.2: Coupling of the dye to rat tail collagen via EDC/NHS activation.

Figure 3.3: Oxygen-sensitive molecule synthesis.

Figure 3.4: Images of a probe-conjugated hydrogel and a native hydrogel.

Figure 3.5: Full spectra of the oxygen-sensitive probe, both conjugated and in solution

Figure 3.6: Absorbance intensity of the Ru-based oxygen-sensitive probe as a function of the concentration.

Figure 3.7: Determination of the Ru-based compound conjugation efficiency to the hydrogel.

Figure 3.8: Physical characterization of the 3D oxygen-sensitive matrix by SEM.

Figure 3.9: Physical characterization of the 3D oxygen-sensitive matrix

Figure 3.10: Young's Moduli determined for 3D hydrogel matrices

Figure 3.11: Photostability of the 3D oxygen-sensitive matrix.

Figure 3.12: Quantification of bleaching and recovery dynamics for the analyzed ROIs.

Figure 3.13: Variations in the fluorescence intensity as a function of continuous radiation

Figure 3.14: Short term biocompatibility of the oxygen-sensitive matrix.

Figure 3.15: Cell viability assessed over a period of culture of 7 days for the 3D oxygen sensitive matrix and control hydrogels.

Figure 3.16: Cell proliferation assay in both control collagen and collagen conjugated with 3.8 µM oxygen-probe

Figure 3.17: Quantification of the ROS levels in control and oxygen-probe-coupled collagen

Figure 3.18: Cell viability (HCT-116) determined at 3 h and 72 h for control collagen and collagen conjugated with 3.8 µM oxygen-sensitive probe, after light exposure or without any exposure to light.

Figure 3.19: Calibration of the fluorescent response of the oxygen-sensitive matrix to hypoxia.

Figure 3.20: Response of the oxygen-sensitive matrix to oxygen consumption by different cell densities in a 3D cell culture.

Figure 3.21: Response of the oxygen-sensitive matrix to oxygen consumption by a 3D cell culture at 1, 4 and 24 hours after seeding.

Figure 3.22: Oxygen map performed for a $5 \cdot 10^6$ HCT-116 cell/ml cell culture

Figure 4.1: Schematic representation of the tumor microenvironment model reproduced in this chapter and microdevices utilized to that end.

Figure 4.2: Necrotic core generation. U-251 MG cells embedded within the collagen hydrogel were cultured at different cell densities.

Figure 4.3: Necrotic core generation within the microdevice.

Figure 4.4: HCT-116 cell proliferation.

Figure 4.5: Cell proliferation for U-251 MG and HCT-116 cells

Figure 4.6: Oxygen profile analysis.

Figure 4.7: Apoptosis characterization for HCT-116 and U-251 MG cells.

Figure 4.8: Doxorubicin effect on HCT-116 cells.

Figure 4.9: Scheme of the procedure for genomic analysis of the tumor microenvironment development.

Figure 4.10: Optimization of the enzymatic degradation of collagen hydrogels.

Figure 4.11: Recovery efficiency from the microdevices.

Figure 4.12: Biocompatibility of the cell extraction method.

Figure 4.13: Assessment of the quantity and quality of RNA extracted from recovered cells.

Figure 4.14: Proof of concept for the genetic profiling procedure.

Figure 4.15: Patterning method in the microfluidic device.

Figure A1: The AFM has inspired a variety of other scanning probe techniques.

Figure A2: Scheme of the operation of an AFM.

Figure A3: Scheme of the forces present in tip-sample interactions during approach and retraction cycles.

Figure A4: Fabrication and final aspect of the fabricated alginate microcapsules.

Figure A5. Atomic force microscopy (AFM) images from microcapsules.

Figure A6: Apparent Young's Moduli for the alginate microcapsules.

List of tables.

Table 1.1: Key differences in cellular characteristics and processes in two-dimensional and three-dimensional culture system.

Table 1.2: Common extra-cellular matrices for use in 3D *in vitro* cultures in the literature.

Table 1.3: Analysis of the advantages and disadvantages of the main incubation chambers available in the market in terms of operation and result.

Table 4.1: RT-PCR primers for the chosen targets in gene profiling of the tumor microenvironment evolution.

Abstract.

Despite the rising cancer prevalence worldwide, and particularly in developed countries, the development of new anti-cancer drugs is plummeting in efficiency. To revert this worrying tendency, new tools to reproduce and characterize the tumor microenvironment are required. One of them is the development of new and more precise *in vitro* models.

In this context, microfluidics appears as a powerful alternative which can help to establish more reliable pre-clinical drug testing and therefore, to enable a more comprehensive and rational drug research and development. In the present Thesis, two microfluidic models of the microenvironment of solid tumors are developed together with the tools required for their characterization.

In chapter 1, state-of-the-art *in vitro* tools and technologies related to tumor microenvironment mimicry are revisited. In chapter 2, a new microfluidic co-culture model to study tumor-endothelium crosstalk is presented and discussed, as well as the penetration and anti-tumor capacity of two formulations of an apoptosis-inducing drug. In chapter 3, a new tool to measure oxygen tension at any point of a 3D culture system is developed. Chapter 4 details a new tumor model centered in the generation and characterization of biological gradients. Furthermore, we demonstrate that coupling microfluidic technology in 3D cell cultures with traditional molecular biology benchtop techniques enables to genetically profile tumor evolution overtime. Finally, chapter 5 states the conclusions of the present Thesis and yields possible future work lines.

Resumen.

A pesar de que la incidencia del cáncer está en aumento, sobre todo en los países desarrollados, el desarrollo de nuevos fármacos contra esta enfermedad es cada vez menos efectivo. Para revertir esta tendencia, aparece la necesidad de desarrollar mejores herramientas para reproducir y caracterizar el microentorno tumoral. Una de ellas son modelos *in vitro* más precisos.

En este contexto, la microfluídica se presenta como una potente alternativa para el desarrollo de estos nuevos modelos *in vitro* más precisos, que puedan emplearse para un desarrollo y selección de fármacos más racional y efectivo. Así, en la presente tesis se desarrollan dos modelos microfluídicos del microentorno tumoral para tumores sólidos, junto a las herramientas necesarias para su caracterización.

En el capítulo 1 se realiza una revisión del estado de la cuestión en lo referente a modelos de cáncer *in vitro* y su caracterización. En el capítulo 2 se desarrolla un modelo microfluídico de co-cultivo que permite estudiar las interacciones endotelio-tumor, así como la capacidad de penetración y erradicación de células tumorales de nuevos fármacos. En el capítulo 3 se presenta una herramienta para caracterizar los niveles de oxígeno molecular en cualquier punto de un cultivo *in vitro* 3D. En el capítulo 4 se presenta un modelo de tumor centrado en la generación y caracterización de gradientes biológicos, así como su adaptación a las técnicas tradicionales de biología molecular para el análisis del perfil genético del microentorno tumoral a lo largo del tiempo. Finalmente, en el capítulo 5 se detallan las conclusiones de la presente tesis y se esbozan futuras líneas de trabajo.

Acknowledgements.

After four years, this period of my life is finally coming to an end. It has been a period of intense learning, not only scientifically, but also on a personal level.

It is said that no duty is more urgent than that of saying thanks. Therefore, I would like to thank everyone who took part in one way or another, in this equally exciting and intense journey.

First, I would like to thank my supervisors for the opportunity they gave me. Iñaki, I want to thank you for granting me the opportunity to work here and for believing in me in the first place. It was a huge turning point for me, and it gave me the chance I had been looking for a long while. Thank you for all the courage you transmitted us every day. Next, I would like to express my gratitude to Luis for his everlasting trust, for pointing me in the right direction many times, and for all the fruitful discussions over these four years. Finally, I would like to thank Manolo, for taking such an interest in my research, for making just the right comments at the right time.

I would like to express my gratitude to all members of my former group, Genoxphos, for preparing me for this experience, for your support and the opportunity to assist in teaching.

I would also like to express my gratitude to the Ministry of Education of the Spanish Government. I would also like to thank my visit funding agencies: CIBER and Ibercaja-CAI. Thank you for the invaluable experience.

Besides, I would like to thank all the other members of our group for their help in many various aspects of my PhD: Clara, Rebeca, José Luis, Rosa, Guillermo, Alan, Sara, Roxana, Lara, Irene, Isabel, Carlos M., and Aitor, among many others. Thanks, Alodia, Teodora, Sandra and Jacobo for close collaboration and great fun.

I would also like to thank the students whom I had the opportunity to help with their projects: Juan, Javier, Pablo, and Marta. Thank you for your trust during your projects, and thank you for all the good moments we shared together. My special thanks go to Laura P., for fruitful discussions and lots of fun in the lab.

Since alone we can do so little and together we can do so much, I would like to express my deepest thanks to our collaborators. Without all of them, this Thesis would have not been possible: Diego and Luis; Carlos, Inés, Elena and Maria José; Pilar and Julián. It was a pleasure working with you all.

I am especially thankful to NanoBioCel group, from the University of the Basque Country (Jesús, Laura S., José Luis…). Thanks for opening a new and exciting research line for my Thesis. Thank you also for all your help and insights in the early stages of the Thesis. My special thanks go to Edorta. Thank you for your trust, your patience, your insights and most of all, your friendship. I enjoyed working with you immensely.

Finally, I am very grateful to the girls from next door, for all the great moments together: Nieves, Cristina, and Mar. Thank you all so much.

I want to seize this opportunity to say thanks to the great people I met in my visits: On the one hand, my very sincere thanks go to Séverine, for all her insights and comments which have nurtured my work very much. I also want to thank those who contributed to making my everyday nicer in Twente: Floris, Jean-Baptiste, Ashish, Adithya, Miguel, Alba, Miquel, Lara, Alex, Bjorn, Renée, Marinke, Lissette, Anne, Rogier, Allison and many others. Thank you for everything. On the other hand, I'm grateful to Anna, for granting me this opportunity. Thank you to everyone who made my stay easier and more enjoyable in Nottingham: Delyan, Amar, Pam, Phil, Bev, Helen, Aleks, Teresa, Santi, Henry, Yin Mar, James, (big) Aziz, (small) Aziz, Abdullah, Giovanna. Special thanks to Aishah, for her friendship, huge support and long fun talks over tea.

Furthermore, I want to say thanks to all my friends, who were a great support during this particularly convoluted period of my life. My present and former roommates: Sofía, Núria, María, among others. You know my daily struggles and successes better than anyone. Thank you for letting me to share them with you. The same "thank you" goes to Oihana, who was a great support the whole time. I also want to thank my invincible friends, who are always there, no matter what happens or where I go: Edu, Cova, David, Iris, Nerea, Jorge and Victor. Thanks for everything.

Moreover, I want to express my profound thanks to my parents and grandparents. Thank you for your spiritual and material support. I most certainly wouldn't be here without you. I want to extend this gratitude to the rest of my family, who have supported me throughout the years.

Finally, I want to save the most special thanks for Chema, for supporting me in every possible way, and being there for me every step of this way.

THANK YOU.

Agradecimientos.

Tras cuatro años, este periodo de mi vida finalmente se está acabando. Ha sido un periodo de aprendizaje muy intenso para mí, no sólo en el ámbito científico sino también a nivel personal. Desde siempre me han enseñado que es de bien nacido ser agradecido. Por ello, me gustaría agradecer a todos aquéllos que, de una forma u otra han participado en este viaje, que ha resultado ser tan emocionante como intenso.

Primero, me gustaría agradecer su oportunidad y confianza a mis supervisores. Iñaki, gracias por darme la oportunidad de trabajar con vosotros y por creer en mí desde el principio. Gracias por el ánimo que nos transmites cada día. Tu apoyo ha resultado ser un punto de inflexión para mí, y me dio la oportunidad que llevaba buscando tanto tiempo. Seguidamente, quiero expresar mi gratitud a Luis por su confianza intemporal, por reencaminarme hacia la dirección correcta en los momentos de duda y por tantas discusiones interesantes durante estos cuatro años. Finalmente, querría agradecer a Manolo, por tomarse tanto interés en mis trabajos, por hacer los comentarios precisos en el momento correcto.

Además, me gustaría agradecer a todos los miembros de mi grupo anterior, Genoxphos, por prepararme para esta experiencia, por vuestro apoyo y la oportunidad de ayudar en tareas docentes.

Igualmente, me gustaría expresar mi gratitud a las entidades que me han financiado para poder hacer este viaje: el Ministerio de Educación del Gobierno de España, así como CIBER e Ibercaja-CAI. Gracias por una experiencia de un valor incalculable.

Por otro lado, también me gustaría agradecer al resto del grupo GEMM (y ahora AMB) por su ayuda en diferentes aspectos de mi tesis: Clara, Rebeca, José Luis, Rosa, Guillermo, Alan, Sara, Roxana, Lara, Irene, Isabel, Teodora, Carlos M. y Aitor, entre otros. Gracias Alodia, Sandra y Jacobo por trabajar conmigo codo con codo y siempre con una sonrisa.

Querría, del mismo modo, dar las gracias a los estudiantes a los que tuve el privilegio de tutelar en sus proyectos: Juan, Javier, Pablo, Marta y especialmente a Laura P., por aportarme tanto como yo a ella, sin olvidar los momentos divertidos.

Dado que la unión hace la fuerza, no puedo sino agradecer profundamente a nuestros colaboradores sus respectivos granitos de arena para hacer posible esta tesis. Diego y Luis; Carlos, Inés, Elena y Maria José; Pilar y Julián.

Quiero expresar mi reconocimiento al grupo NanoBioCel de la Universidad del País Vasco (Jesús, Laura S., José Luis). Gracias por abrir una línea adicional de trabajo en mi tesis, de la que he disfrutado enormemente, aunque por motivos de tiempo no haya podido incluirla este volumen. Quiero hacer una mención especial a Edorta: Gracias por tu confianza, tu paciencia, tu saber hacer y, sobre todo, por tu amistad.

Gracias también a las chicas del grupo de al lado, por todos los buenos momentos juntas: Nieves, Cristina y Mar. Gracias.

I want to seize this opportunity to say thanks to the great people I met in my visits: On the one hand, my very sincere thanks go to Séverine, for all her insights and comments which have nurtured my work very much. I also want to thank those who contributed to making my everyday nicer in Twente: Floris, Jean-Baptiste, Ashish, Adithya, Miguel, Alba, Miquel, Lara, Alex, Bjorn, Renée, Marinke, Lissette, Anne, Rogier, Allison and many others. Thank you for everything. On the other hand, I'm grateful to Anna, for granting me this opportunity. Thank you to everyone who made my stay easier and more enjoyable in Nottingham: Delyan, Amar, Pam, Phil, Bev, Helen, Aleks, Teresa, Santi, Henry, Yin Mar, James, (big) Aziz, (small) Aziz, Abdullah, Giovanna. Special thanks to Aishah, for her friendship, huge support and the long fun talks over tea.

De la misma forma, quiero dar las gracias a mis amigos, que me apoyaron sin condiciones en este convulso periodo de mi vida. Todas mis compañeras de piso: Sofía, Nùria, María… Conocéis mis luchas y victorias diarias mejor que nadie. Gracias por dejarme compartirlas con vosotras. Lo mismo se aplica para Oihana, *eskerrik asko* por tu apoyo, amiga. También quiero agradecer a mis invencibles amigos, que siempre

están ahí pase lo que pase y vaya donde vaya: Edu, Cova, David, Iris, Nerea, Jorge y Víctor. Gracias por todo.

También quiero dedicar un apartado especial a mis padres y abuelos. Gracias por vuestro apoyo, tanto espiritual como material. Puedo decir con la mayor de las certezas que no estaría aquí sin vosotros. Quiero extender mi gratitud al resto de mi familia, que me ha apoyado durante todos estos años.

Finalmente, quiero dedicar mi agradecimiento más especial a Chema, por apoyarme de todas las formas posibles y por estar conmigo a cada paso de este camino que ahora llega a su fin.

GRACIAS.

Outline.

The following thesis is devided into 5 chapters and an appendix. Although each part can be independently read, all of them should be considered within the overall picture. The content of each chapter is summarized in this section.

- Chapter 1: It provides a general framework for the following chapters of the Thesis. It describes state of the art techniques and motivation of the Thesis, leading to the objectives and chapter structure.

- Chapter 2: This chapter describes the development and characterization of a simple, high-throughput compatible microfluidic model. This model comprises breast cancer tumor cells and an endothelium, and is focused on endothelium visualization. Framework, methods, results and partial conclusions are detailed for a set of experiments.

- Chapter 3: It describes the development and characterization of an oxygen-sensitive hydrogel for cell culture applications. The hydrogel was thoroughly characterized and used for oxygen mapping of colon cancer cells in cell culture.

- Chapter 4: This chapter summarizes the development of a model of the tumor microenvironment centered on tumor cell metabolism and self-generated gradients within the sample. This model was developed in our group and has already been published. Furthermore, the model was coupled with long established molecular biology methods of analysis: Real Time Polymerase Chain reaction (RT-PCR) and flow cytometry.

- Chapter 5: In this chapter, the main conclusions of the previous chapters are outlined, both in English and Spanish. Also, some suggestions regarding future work are described. Yielded publications and other output items of the Thesis are also listed here.

- Appendix A: This section comprises a side project which was carried out within the general framework of the Thesis: the importance of the microenvironment. However, the techniques implied are microencapsulation and Atomic Force Microscopy (AFM). Although related to the previous topics, the methodology was somewhat different. Therefore, the appendix has a brief section on the fundamentals of AFM, followed by a structure analogous to that presented in chapters 2-4.

Chapter 1: Background.

1.1 Dissecting anti-cancer drug development decay.

Since 1950, the number of new US Food and Drug Administration (FDA)-approved drugs per billion of US dollars spent in research and development in the drug industry has halved approximately every 9 years.

This tendency has been persistent for the past decade despite all efforts. Particularly, if we look at drug productivity for the period 2005-2010 for the large pharmaceutical companies it can be appreciated that FDA-approved new molecular entities (NMEs) plummeted to an alarming number of 7 in 2010, whereas the annual expenditure in research and development has not but increased to a staggering $60 billion (Figure 1.1) [1].

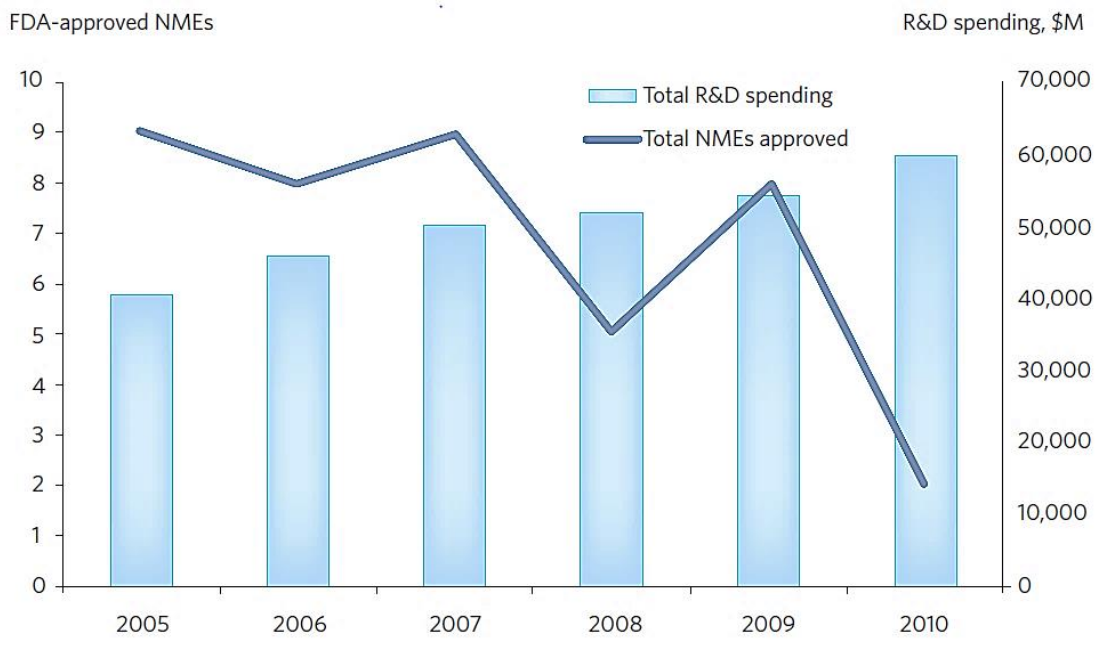

Figure 1.1: Large pharma productivity from 2005–2010. Combined FDA-approved NMEs versus research and development spending for nine large pharmaceutical companies (AstraZeneca, Bristol-Myers Squibb, Eli Lilly, GlaxoSmithKline, Merck, Novartis, Pfizer, Roche and Sanofi-Aventis). Figures shown are in millions of US dollars. Source: FDA CDER; Bernstein [1]. NME includes biologicals and vaccines.

One of the suggested reasons for this downward tendency in drug research is a poor selection of targets. This selection is often performed by means of brute force, taking advantage of high-throughput screening methods, which consists of trying many

compounds to assess their possible anti-tumor activity [2]. Thereby, these methods do not seem to be accurate enough in selecting new potentially effective drugs. Furthermore, the approval of new therapies is dependent on their exceedance of the current treatment's efficiency. In other words, new therapies need to be significantly better or have less secondary effects than the current standard of care [3].

Moreover, there is accumulated evidence that preclinical studies with conventional cell lines in 2D Petri Dishes and animal models have usually proven unable to predict drug efficacy in human trials [4,5]. The over-reliance on these imprecise models, results in the current poor levels of success for promising drugs in latest stages of the drug approval [6].

Overall, there is an urging need to replace existing models with a new generation of validated models whose response is more reliable with respect to that observed *in vivo* [7-9].

Many solutions have been proposed to overcome this tendency. On the one side, it has been proposed to increase our understanding of the molecular bases of cancer (among other illnesses) and to identify more effective targets susceptible of pharmacological modulation ameliorating key disease phenotypes [6]. On the other side, it has been proposed to improve the preclinical phase of drug approval through the development of new *in vitro* models, which would also help improving our understanding of the molecular bases of cancer [10-12].

This latter proposition should include the development, characterization and validation of new comprehensive *in vitro* models to replace existing ones. It has been proposed that newly-developed models should include more physical and biological features of the TME [2].These optimized models would ideally reproduce *in vivo* results accurately *in vitro*, thus definitely changing the current drug research and development tendency. However, to create these models, we first need a deeper understanding of cancer etiology and its underlying mechanisms.

1.2 Cancer prevalence and mortality.

Cancer is a leading cause of death worldwide in countries of any income level. To add to the existing burden, the number of cancer diagnoses and deaths is expected to grow rapidly as populations and life expectancy grow, and maintain lifestyles that increase cancer risk [13]. The following figure reflects an estimation for new cancer cases and estimated cancer deaths in 2016 (Figure 1.2).

Estimated New Cases

Males			Females		
Prostate	180,890	21%	Breast	246,660	29%
Lung & bronchus	117,920	14%	Lung & bronchus	106,470	13%
Colon & rectum	70,820	8%	Colon & rectum	63,670	8%
Urinary bladder	58,950	7%	Uterine corpus	60,050	7%
Melanoma of the skin	46,870	6%	Thyroid	49,350	6%
Non-Hodgkin lymphoma	40,170	5%	Non-Hodgkin lymphoma	32,410	4%
Kidney & renal pelvis	39,650	5%	Melanoma of the skin	29,510	3%
Oral cavity & pharynx	34,780	4%	Leukemia	26,050	3%
Leukemia	34,090	4%	Pancreas	25,400	3%
Liver & intrahepatic bile duct	28,410	3%	Kidney & renal pelvis	23,050	3%
All Sites	**841,390**	**100%**	**All Sites**	**843,820**	**100%**

Estimated Deaths

Males			Females		
Lung & bronchus	85,920	27%	Lung & bronchus	72,160	26%
Prostate	26,120	8%	Breast	40,450	14%
Colon & rectum	26,020	8%	Colon & rectum	23,170	8%
Pancreas	21,450	7%	Pancreas	20,330	7%
Liver & intrahepatic bile duct	18,280	6%	Ovary	14,240	5%
Leukemia	14,130	4%	Uterine corpus	10,470	4%
Esophagus	12,720	4%	Leukemia	10,270	4%
Urinary bladder	11,820	4%	Liver & intrahepatic bile duct	8,890	3%
Non-Hodgkin lymphoma	11,520	4%	Non-Hodgkin lymphoma	8,630	3%
Brain & other nervous system	9,440	3%	Brain & other nervous system	6,610	2%
All Sites	**314,290**	**100%**	**All Sites**	**281,400**	**100%**

Figure 1.2: Ten Leading Cancer Types for the Estimated New Cancer Cases and Deaths by Sex, United States, 2016. Estimates are rounded to the nearest 10 and cases exclude basal cell and squamous cell skin cancers and in situ carcinoma except urinary bladder. Reproduced with permission from Siegel et al [13].

Particularly, in 2012, worldwide, there were 14.1 million new cancer diagnoses. Out of these, there were 8.2 million cancer deaths, and 32.6 million people living with cancer within 5 years of diagnosis [14]. The incidence rate was almost 25% higher in men than

in women, with rates of 205 and 165 cases per 100 000 people per year, respectively [15]. Furthermore, the GLOBOCAN 2012 database (International Agency for Research on Cancer of the World Health Organization) estimates a 27% overall increase in cancer incidence by 2035, whereas the death count will rise a 78% by that year. This means that 15-20 million people will approximately die of cancer every year in the upcoming two decades [16].

1.3 Cancer development (tumorigenesis).

Cancer is long known to originate from accumulation of damage into the information encoded in cellular DNA. In other words, cancer is a genetic disease which onsets when DNA information in cells becomes corrupted through errors called DNA mutations. Once enough damage has occurred, it can lead to abnormal patterns of gene expression that may derive in an anomalous functioning of normal cell functions, such as uncontrolled cell growth and survival [17,18].

Aside from this classical conception of cancer initiation, which remains valid, we nowadays have a more in-depth view of cancer initiation (also called tumorigenesis), development and final evolution. Nowadays, we know that tumorigenesis is a multi-step process, where tumor cells (also known as neoplastic cells) progressively acquire alterations which eventually affect different processes (Figure 1.3).

Their main trait is their uncontrolled growth. Whereas normal cells require specific growth signal to proliferate, tumor cells can divide independently of those growth signals and ignore anti-growth signals. Besides, they acquire a limitless replicative potential, which is a feature that normal cells do not possess. Furthermore, tumor cells are capable of evading apoptosis signals and of modifying their metabolism for a higher proliferation efficiency [19]. In this situation, exacerbated consumption of oxygen and nutrients lead to hypoxia and nutrient depletion, thus subjecting them to an extreme evolutionary pressure. This pressure favors the survival of those cells which can resist harsher environmental conditions within the TME. Hence, the genomic instability present in those cells, in turn, facilitates their adaptability to this new environment, helping them to survive in harsher conditions [20]. In this context,

cells can induce a supporting vasculature to enhance their supply of oxygen and nutrients. Thereafter, they obtain a new source of nourishment to continue their growth, as well as colonizing new tissues to continue expanding, and, possibly colonize other tissues through a process called metastasis (Figure 1.3) [19,21].

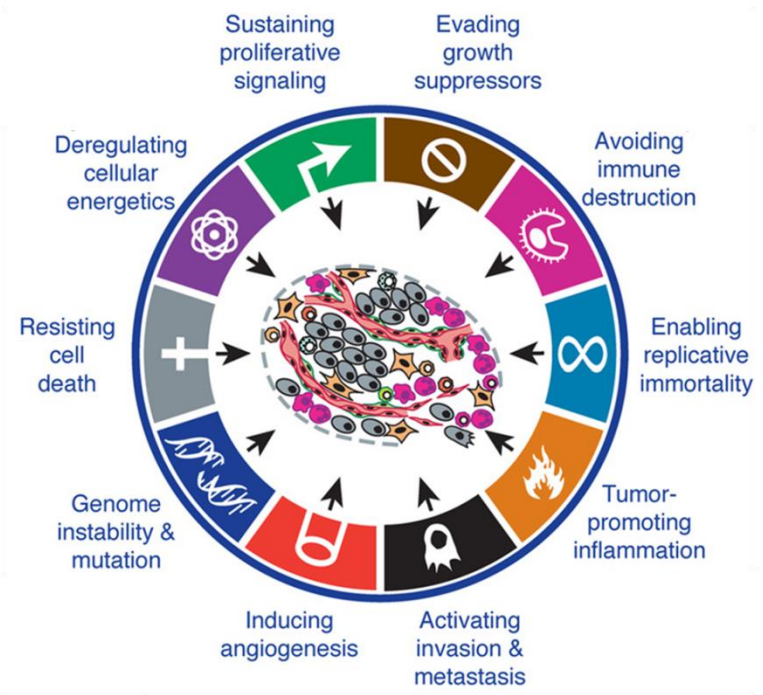

Figure 1.3: The hallmarks of cancer. During the neoplastic process, cells progressively suffer different cumulative alterations that lead to the acquisition of the shown characteristics. To generate cancer, all different alterations are proposed to may occur. Reproduced with permission from Hanahan et al [21].

To sum up, tumor development is a highly dynamic process originating from a genomic instability. These aberrant tumor cells proliferate in and help to generate a very harsh tumor microenvironment (TME), that promotes death or recruitment of surrounding cell types. Furthermore, tumor cells may evolve differently within the same tumor, while different steps and different evolution paths can occur in different tissues, thus explaining the high heterogeneity of tumor types, subtypes and cell types within the same tumor.

All in all, the interplay between cancer cells and their TME is critical for the development of the tumor; e.g. recruited blood vessels provide extra nutrients and oxygen for the tumor, and macrophages may facilitate tumor development. Finally, it is known that the TME enhances the tumor survival and promotes its functions, thus

having a significant impact on tumor evolution, resistance to therapy and on the patient survival. Thereby, this Thesis is subsequently focused on the tumor microenvironment.

1.4 Features of the tumor microenvironment (TME).

As it has been already established, cancers are more complex than just one rogue clonally expanded cell. Cancers are not a *solo* performance, but rather an ensemble production: the tumor microenvironment (TME) is constituted by surrounding blood vessels, the extracellular matrix (ECM), other non-malignant cells and signaling molecules [22]. Overall, the TME is the context in which a tumor develops, interacting with the tumor cells, and thus influencing deeply its evolution through a bidirectional and dynamic communication between tumor cells and microenvironment [23,24]. In this section, the main aspects of the TME are described, distinguishing between cellular and non-cellular components of the TME.

1.4.1 Cellular components of the TME.

As anticipated, in previous section, cells from the normal tissue (stromal cells) and cells from the immune system are subverted and recruited by the tumor cells to generate tumorigenic microenvironments. Most of the hallmarks of cancer are enabled and sustained to varying degrees through contributions of these subverted cells that, therefore, play a key role in the processes of stromal cell recruitment, activation, programming, and persistence which are increasingly better understood (Figure 1.4) [25].

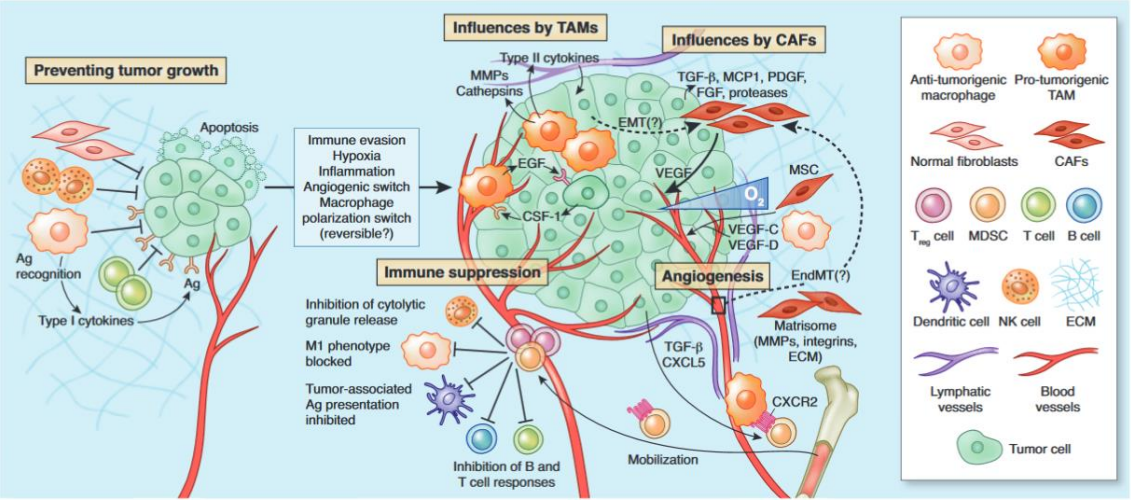

Figure 1.4: Tumor microenvironment. Multiple stromal cell types converge to support a tumorigenic primary niche. After circumventing cell-intrinsic mechanisms of apoptosis, tumor cells are subject to elimination pressures by the immune system. Tumor cell–specific antigens have a role during this process. They are recognized by cytotoxic immune cells, leading to their destruction. Fibroblasts and macrophages within the tumor microenvironment also contribute to a growth-suppressive state; however, these cells may later become "educated" by the tumor to acquire pro-tumorigenic functions. For instance, tumor-associated macrophages (TAMs) support diverse phenotypes within the primary tumor, including growth, angiogenesis and invasion, by secreting a plethora of pro-tumorigenic proteases, cytokines and growth factors (for example, EGF, which participates in a paracrine signaling loop through tumor-secreted CSF-1). As tumor grows, immune-suppressor cells, including myeloid-derived suppressor cells (MDSCs) and T regulatory cells (T reg) are mobilized into the circulation in response to activated cytokine axes that are induced by tumorigenesis (for example, TGF-β and CXCL5-CXCR2). MDSCs and T reg cells infiltrate the growing tumor to disrupt immune surveillance through multiple mechanisms, including, but not limited to, disruption of antigen presentation by dendritic cells (DCs), inhibition of T and B cell proliferation and activation or inhibition of natural killer (NK) cell cytotoxicity. Cancer-associated fibroblasts (CAFs), which become activated by tumor-derived factors (for example, TGF-β, FGF or PDGF, among others), secrete ECM proteins and basement membrane components, regulate differentiation, modulate immune responses and contribute to deregulated homeostasis. CAFs are also a key source of VEGF, which supports angiogenesis during tumor growth. In addition to cellular contributions, several extracellular properties contribute to tumor progression, including low oxygen tension, high interstitial fluid pressure and changes in specific components of the ECM like EndMT, endothelial-to-mesenchymal transition or Ag, antigen. Reproduced with permission from Quail et al [24].

Some of the main cell types interacting with tumor cells are endothelial cells, fibroblasts, pericytes and immune infiltrating cells.

Endothelial cells are prominent among stromal cells. Over the years, the biology of blood vessels has increasingly been studied. Of particular relevance is the "angiogenic switch", which is the process through which an endothelial cell stops being quiescent and starts forming a new vessel. Those located in the proximity of a developing tumor are subverted and generate an angiogenic process to nourish the forming tumor. It has

been found that recruited endothelial cells present a distinctive marker profile from naïve or quiescent endothelial cells. Endothelial cells facilitate four out of eight of the described tumor hallmarks: 1) sustaining proliferative signaling; 2) resisting cell death; 3) avoiding immune destruction, and 4) activating invasion and metastasis (see figure 1.5). Since metastasis is considered the turning point for most tumors, and is responsible for 90% of cancer deaths, [26] endothelial cell recruitment is of the outmost importance in tumor development.

Fibroblasts are also key players in TME. Fibroblasts are a predominant, multifunctional cell type in connective tissue. They are responsible for depositing extracellular matrix (ECM) and basement membrane components, regulating differentiation events in associated epithelial cells, modulating immune response and mediating homeostasis [27]. They are the cell type implied in most tumor hallmarks (all but enabling replicative immortality, see figure 1.5), which is why they are drawing increasing attention in the cancer research community. Notably, they are implied in wound healing, a behavior that is disrupted when they become associated to a tumor, promoting the growth and invasion of the tumor rather than “curing the wound”.

Pericytes have long been known to play a role in TME. Normal pericytes provide paracrine support signals to developing blood vessels. Once recruited, they destabilize the vascular integrity and function through a mechanism regulated by hypoxia [28,29]. This destabilization, along with the aberrant structure presented by the supporting blood vessels created for tumors, is the basis for an effect known as “enhanced permeability and retention effect”, which is discussed in chapter 2 due to its potential use as a therapeutic target [30,31].

Finally, immune cells are also in the spotlight, due to the dual role as immune agents and factor producers. It is a common belief that immune responses prevent and inhibit tumor development; however, recent evidence has also suggested that immune cells in the TME interact intimately with the transformed cells to promote oncogenesis [32]. Immune inflammatory cells have been described to participate in 6 out of 8 hallmarks of cancer, being only absent of the deregulation of cell energetics and of enabling replicative immortality (Figure 1.5) [25].

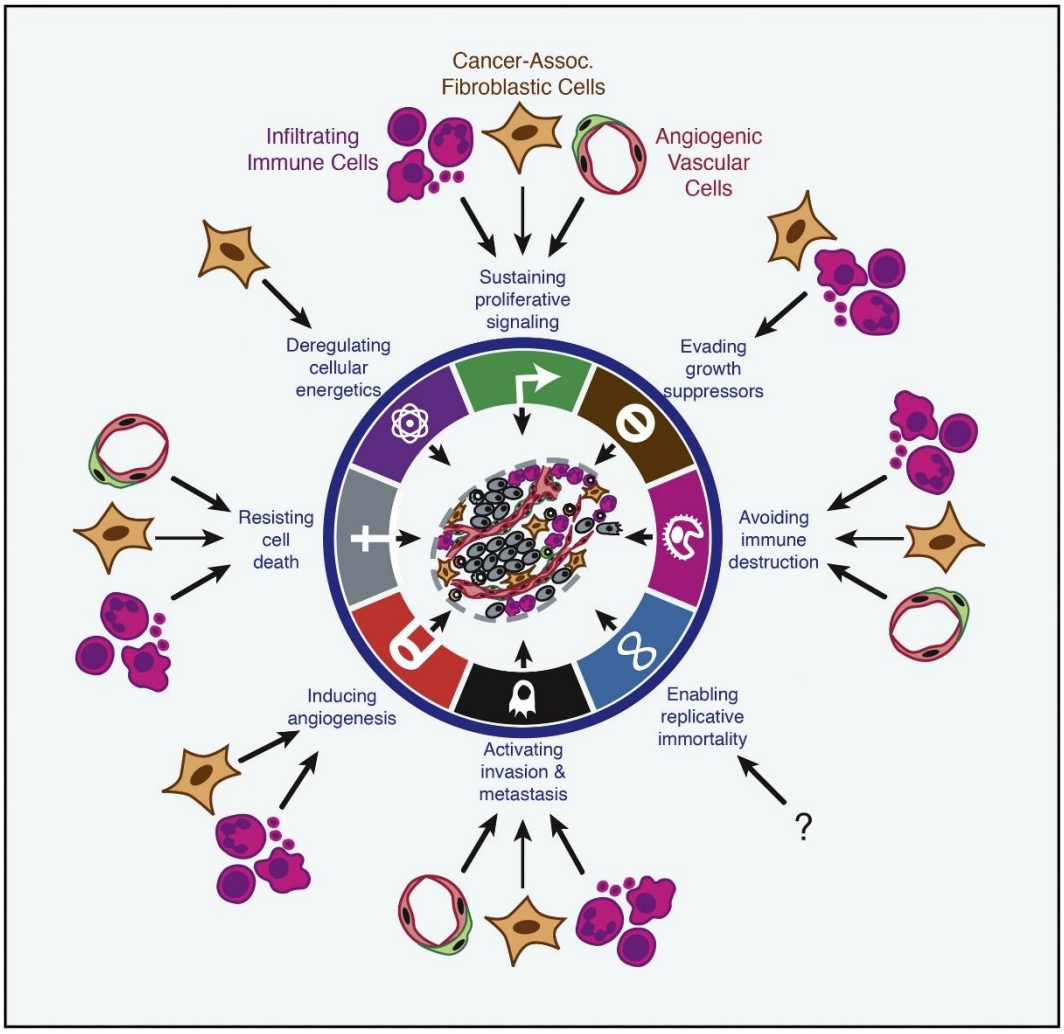

Figure 1.5: Multifactorial contributions of activated/recruited stromal calls to the hallmarks of cancer of the eight acquired hallmark capabilities—six core and two emerging [21], seven demonstrably involved contributions by stromal cells of the tumor microenvironment. The stromal cells can be divided into three general classes, depicted here by their involvement hallmarks, illustrating the diversity of their functional contributions. Notably, the importance of each of these stromal cell classes varies with tumor type and organ, governed by parameters of the distinctive tumor microenvironments and underlying oncogenetic alterations in cancer cells and cancer stem cells that arise in primary tumors, and their invasive and metastatic colonization. Moreover, distinctive cell types and sub cell types within these classes can exert variable roles in enabling these capabilities, and in some cases by opposing them. Reproduced with permission from Hanahan et al. [25].

After examining the important influence of stromal cells in the TME and hence, on tumor development, it is not surprising that many recent therapies aim to use stromal cells as a therapeutic target.

Altogether, we have provided enough evidence of the necessity to incorporate stromal cells in newly-developed tumor models, both to understand the TME better and to perform drug-testing in a more relevant environment. Nonetheless, many other non-

cellular components constitute the TME, and therefore in the following chapters they are described and discussed in depth.

1.4.2 Non-cellular components of the TME: Extracellular matrix.

The extracellular matrix (ECM) constitutes the non-cellular component present within all tissues and organs. It is mainly composed of proteins, polysaccharides and water and is crucial for cell function. The ECM not only provides essential physical scaffolding for cells to constitute tissues but also offers crucial biochemical and biomechanical stimuli required for tissue morphogenesis, differentiation and homeostasis [33].

Each tissue has an ECM with a unique composition and architecture, generated during tissue development through a dynamic and reciprocal dialogue between the various cellular components (e.g. epithelial, fibroblast, adipocyte, endothelial cells). This dialogue is both of biochemical and biophysical nature, and results in a continuously evolving cellular and protein microenvironment. Moreover, the ECM is a highly dynamic structure that is constantly being remodeled by cells within [33,34].

Recent evidence indicates that the ECM has a capacity to limit cancer initiation at early stages and drives disease progression toward malignancy at later stages. Actually, ECM composition can be used as a diagnostic tool, to indicate cancer prognosis in the clinic [35].

On the other hand, mounting evidence suggests that in cancer, and altered function of MMPs results in ECM-anchored factor release, thereby leading to unregulated tumor growth, tissue remodeling, inflammation, tissue invasion, and metastasis [36].

A number of well-known studies also provide compelling evidence that different tissues present different stiffness (Figure 1.6) [37]. In fact, mechanical properties have been described to drive cell shape, cell proliferation and homeostasis, among other cellular processes, through several transduction mechanisms [38,39].

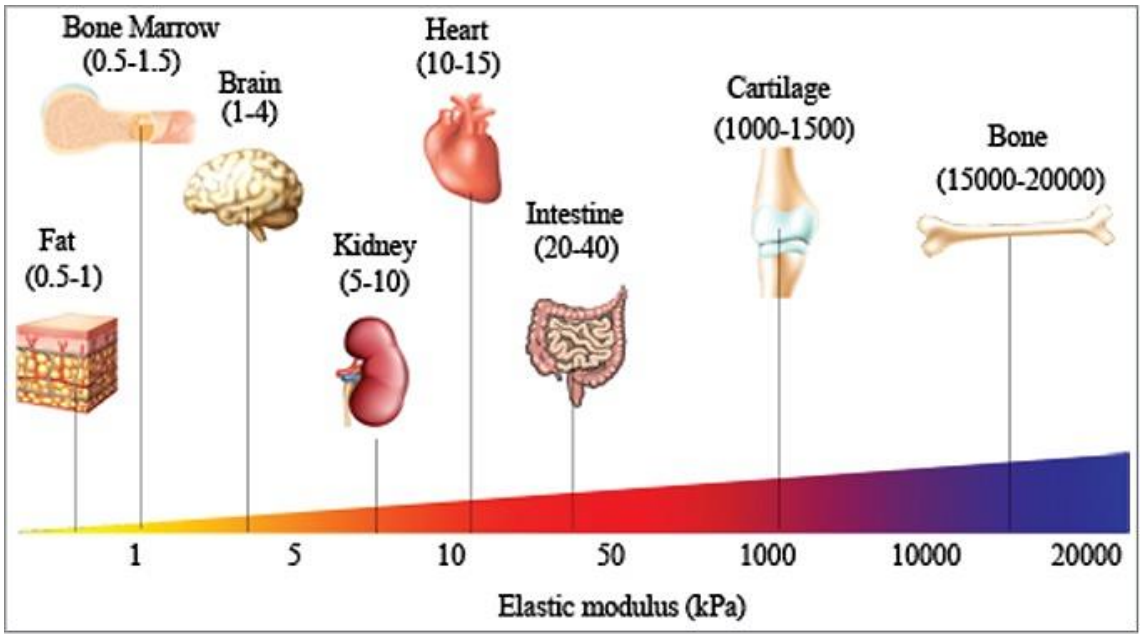

Figure 1.6: Distinct elastic modulus of human tissues suggesting tissue-specific stiffness. Different tissues with their specific elastic modulus in the body are correlated with their functions. Reproduced with permission of Handorf et al. [38].

Aside from stiffness, ECM composition, topography and architecture are also important to cell function [40,41]. Given the importance of the ECM and its influence on cells, newly developed *in vitro* models should carefully consider the integration of the ECM for relevant results.

After discussing the integration of the ECM in *in vitro* systems, biological gradients and their importance in biological systems is examined.

1.4.3 Non-cellular components of the TME: soluble molecules and biological gradients.

1.4.3.1 Physics involved in biological gradients.

To successfully understand the importance of the gradients in a biological context, a brief introduction on the basics of gradients and diffusion is necessary. Thus, diffusion is explained in a basic manner, and subsequently the focus is set on the importance of diffusion in live tissues.

Physics work differently for fluids at the micro-scale. Particularly, diffusion becomes a key process at this scale.

Diffusion can be explained as follows: molecules in a static solution characterized by a low Reynolds number (extra documentation on this matter can be found in the literature [42]) where no convection occurs, tend to spread throughout the whole volume of liquid until the concentration has been equilibrated.

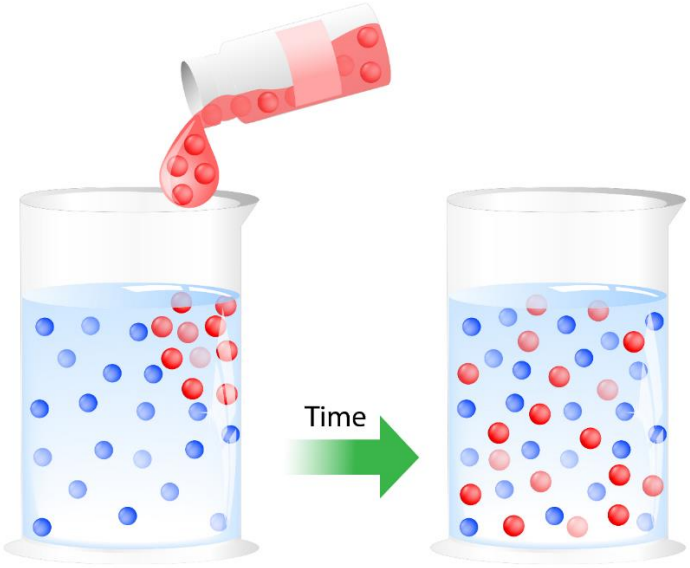

Figure 1.7: Diffusion mechanism for molecules in static liquids. Molecules tend to spread out from the source until the concentration has been balanced throughout the liquid volume. Image purchased from online image repository Dreamstime.com [43].

If the system does not have an active consumption of the molecule of interest, the process finishes after the concentration has been equilibrated. Conversely, if an active consumption of the molecule occurs, a gradient of this molecule is established.

Once exploring the basics of diffusion, we can discuss the importance of gradients and biological systems, and consider the necessity of integrating biological gradients in *in vitro* models.

1.4.3.2 The importance of gradients in biological systems.

As anticipated in the previous section, in biological systems, oxygen and nutrients are continuously consumed by tissues and supplied by blood vessels. Thus, biomolecular gradients (i.e. a lower concentration the further from the molecule source) are key players in tissues as a supply-demand mechanism for nutrients and oxygen.

Furthermore, biomolecular gradients are an important, evolutionarily conserved signaling mechanism for guiding growth, migration, and differentiation of cells within the dynamic, three-dimensional environment of living tissue. Gradients play essential roles in many phenomena including development, inflammation, wound healing, and cancer [44,45]. Among biomolecular gradients, the roles of oxygen and nutrients are of relevance for this Thesis, and as such, are consequently explored in-depth.

Particularly for cancer, diffusion is the main mode of molecule transport. In the case of oxygen, low oxygen tension in tumors promotes many different biological responses. The main response is the expression of HIF-1α, which, in turn, leads to other effects.

Hypoxia-inducible factor (HIF) is a sequence-specific DNA-binding protein that can promote or repress the transcription of a broad range of genes that are involved in maintaining biological homeostasis. HIF is mostly non-functional in oxygenated cells but becomes active under specific conditions, including low oxygen (hypoxic) stress [46].

A well-known consequence of hypoxia is angiogenesis. Angiogenesis is driven by the activity of HIF-1α (hypoxia-inducible factor 1α), a hypoxia-regulated transcription factor, whose overexpression is associated with poor patient prognosis [47,48]. Hypoxia also enhances tumor cell invasion by various mechanisms [49,50]. Finally, hypoxia has been described to enhance drug resistance [48,51-53].

As for nutrient gradients, they have been less explored in the literature since they comprise many different molecules, such as glucose, aminoacids, fatty acids, biochemical cues and factors. Therefore, the characterization of the diffusion dynamics of each of these numerous components becomes a daunting task. This is due to the difficulty of visualization of a sole component and the necessity to find or generate fluorescent surrogates for every cited molecule. Moreover, diffusion dynamics from the blood vessels is modified by the presence of a tumor nearby.

Tumor blood vessels are often farther apart than in normal tissues, and have variable blood flow, leading to poor delivery of nutrients and impaired clearance of metabolic breakdown products from the tumor [51,54].

All in all, gradients play a key role in many cell functions, including drug delivery. Thereafter, gradients should be integrated in newly-developed *in vitro* models for a response closer to that observed *in vivo*.

In vitro models should recreate spatial and structural complexity (different cell types, ECM, gradients…) of tissues. Thus, 3D culture systems have proven to be very useful in reproducing tissue features *in vitro*. In the next section, 3D *in vitro* cell culture is described.

1.5 Three-dimensional cell culture as a crucial improvement to current in vitro models.

1.5.1 The importance of 3D in vitro cell culture.

Among the suggested improvements for the development of new *in vitro* models, there is compelling evidence that three-dimensionality plays a central role in modulating cell behavior and drives some physiological key processes, as it has already been discussed in previous sections. For example, 3D cellular phenomena in development, tissue homeostasis and disease are conducted by adhesive, mechanical and chemical cues originating from other cells and the extracellular environment [55,56].

Three-dimensional microenvironment affects cell behavior in many ways. Differences between a two-dimensional and a three-dimensional microenvironment for cell culture are summarized below (Figure 1.8).

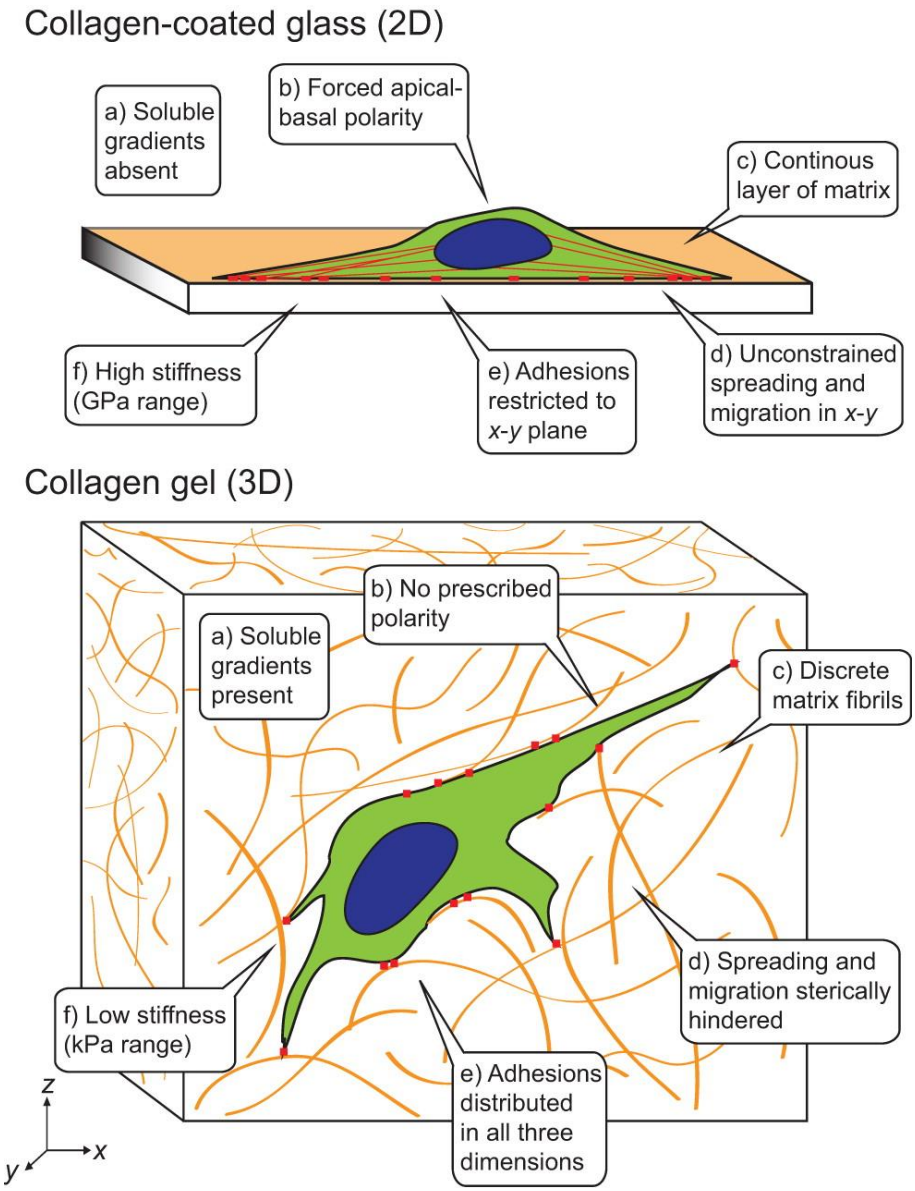

Figure 1.8: Adhesive, topographical, mechanical, and soluble cues in 2D and 3D. The cues encountered by a cell are strikingly different between an ECM-coated glass or plastic surface (2D) and a typical 3D ECM, such as collagen. Reproduced with permission from Baker et al. [55].

Nowadays there is a vast amount of literature reporting differences in cell behavior between cells cultured in 2D compared to cells in 3D. The following table (Table 1.1) presents some of the aspects of cell behavior which have been described to be modified between 2D and 3D.

Cellular characteristics and observed change	References
Cell morphology	
Cells are more stretched in flat substrates than in 3D.	[55,57-59]
Cell-cell and cell-matrix interactions	
Less frequent and constricted in a 2D environment than in 3D.	[60,61]
Gene expression	
In 3D, overall gene expression becomes more similar to that observed in tumors.	[62-64]
Cell cycle	
Most common cell cycle phase is modified between 2D and 3D.	[59,65]
Cell proliferation	
Duration of the cell cycle phases is modified.	[66,67]
Media/drug reach	
Drugs and nutrients may not be able to penetrate and reach cells tightly connected to each other.	[59,63]
Cell migration	
Cell migration mechanisms vary dramatically from 2D to 3D.	[68,69]
Cell differentiation	
Cells are more undifferentiated in 2D than in 3D.	[57,70]
General cell function	
Many authors report strong changes in general function when cells are cultured in 3D compared with those in 2D (drug resistance, number and specificity of focal adhesions…).	[71-77]

Table 1.1: Key differences in cellular characteristics and processes in two-dimensional and three-dimensional culture system. Adapted from Edmondson et al. [66].

Once established that a 3D microenvironment dramatically affects cell behavior in many aspects, the following section focuses on the most common 3D models *in vitro*.

1.5.2 Most common 3D in vitro tumor models.

Nath and Devi [78] presented in 2016 the following figure (Figure 1.9), which summarized the most common 3D *in vitro* models.

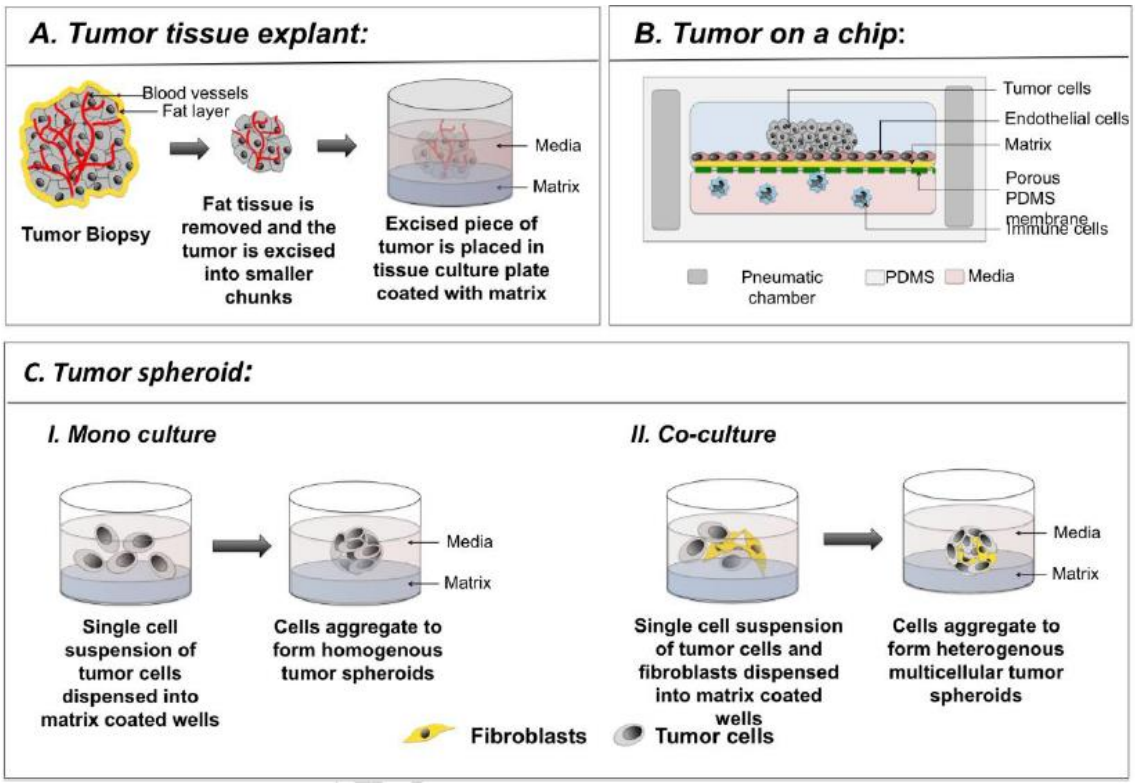

Figure 1.9: Schematic representing the various 3D models of cancer. A. Excised tumor biopsy is processed to remove the excess fat and necrotic cells, and cut into small pieces. After washing the tumor in PBS, it is placed on a tissue culture plate that has been coated with a matrix, such as Matrigel of methylcellulose, to which the tumor sits atop firmly or is embedded. Media is added and the tumor is cultured for the duration of the experiment. B. "Tumor on a chip" represents a vasculature mimicking microfluidic device consisting of PDMS chambers with highly organized microchannels and pneumatic chamber (dark grey) on either side. The microchannels (pink) contain media, in which immune cells and circulating tumor cells navigate. The top chamber contains matrix coated (yellow) porous membrane (green), with a monolayer of endothelial cells on top. The tumor cells are loaded through an inlet into the top chamber. Cells that have been genetically modified to express fluorescent protein can be observed in real time to monitor their functional changes, such as invasion, and migration. C. Schematic depicting tumor spheroid formation where tumor spheroids have been generated by culturing tumor cells alone or in combination with fibroblasts.

In this section, the features of multicellular tumor spheroids (MCTS) and tumor tissue explants are discussed.

MCTS are tightly bounded cellular spheres with size range from 20 µm to several mm. They have been used as models for solid tumors for the past few decades, both of a

single cell type and featuring different cell types in a sole spheroid [79]. Their advantages for cell culture have been thoroughly described in the literature [79-82].

Firstly, MCTS generation is cost-effective and can be coupled to high-throughput assays. Secondly, they are representative of human tissues regarding cell structure, intercellular adhesion, drug response, diffusion rates and biological gradients for oxygen, nutrients and catabolites. Thirdly, when MCTS diameter is 400-500 µm, these gradients generate a necrotic core similar to that found in tumors *in vivo*, as well as a quiescent region and a proliferating outer region. These features are illustrated in Figure 1.10.

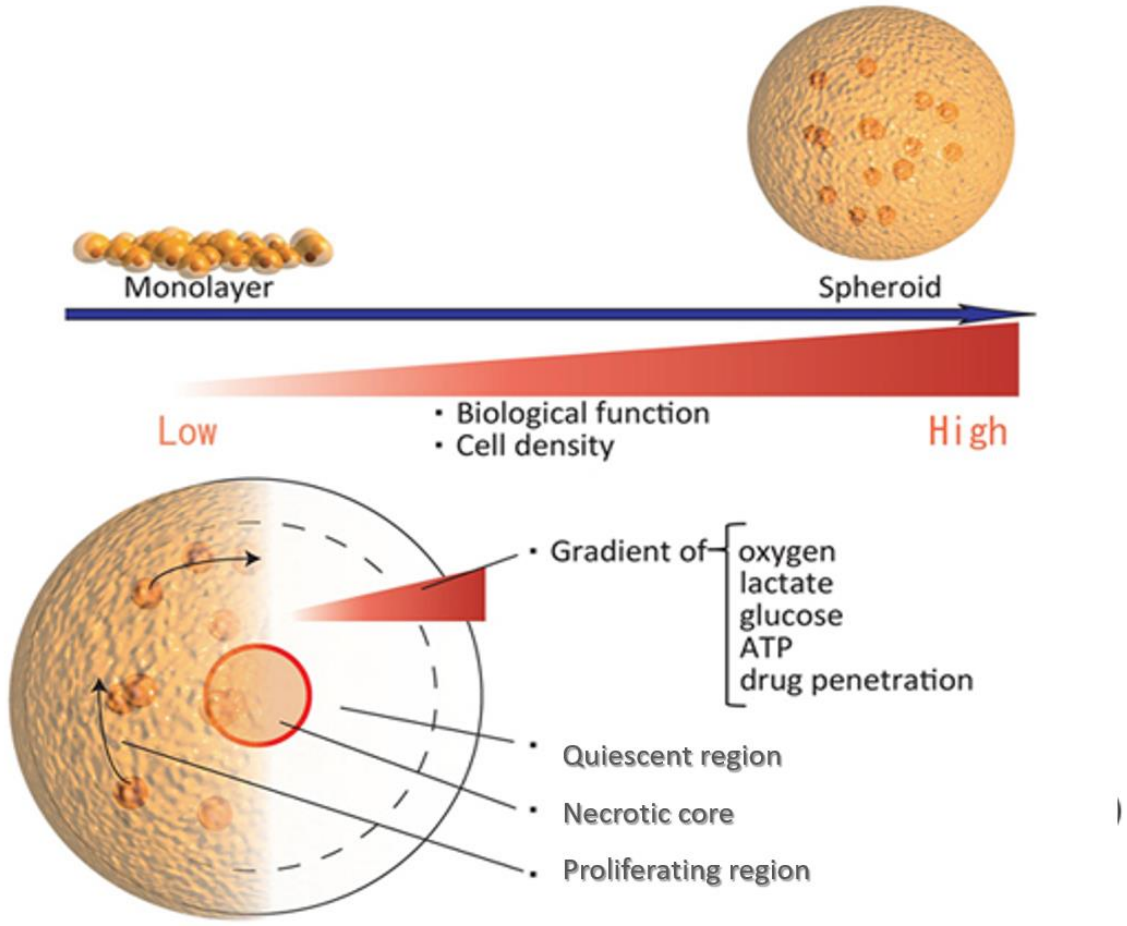

Figure 1.10. Spheroid characteristics. Spheroids show increased biological function and increased cell density. Hepatic spheroids form from cell aggregates, and accumulate and express E-cadherin. Pathophysiological gradients of oxygen, lactate, glucose, ATP and drug penetration are subsequently established in spheroids. However, this leads to a lack of oxygen and nutrition in the core, resulting in necrosis. In co-culture of hepatocytes and endothelial cells, endothelial cells move into spheroids and form endothelial networks. Adapted from Ota and Miki [83].

MCTS also present some limitations which are relevant to the purpose of this Thesis. Firstly, while MCTS generation in large numbers is not problematic, size and shape reproducibility within generated spheroids is often challenging due to the small numbers of cells implied. Secondly, vascularized and controlled cell patterning within spheroids cannot be achieved, which does not account for natural tissue structure. Finally, monitorization and result interpretation can be a difficult task. Particularly, for those spheroids over 400-500 µm in diameter, light cannot penetrate through the structure, thus making monitorization of the spheroid through microscopy very difficult. Furthermore, spheroid manipulation is somewhat strenuous for embedding purposes or sectioning. Even though histology assessments have indeed been performed on MCTS [84], this approach is not viable for large sample numbers. All in all, MCTS represent a valid model for solid tumors, but incur in technical difficulties of use.

The second model explained on in this section is tumor explants, and involves culturing excised human tumors in tissue culture plates. Since they are pieces of native tumors, they naturally present the architecture, cell types and spatial complexity of actual tumors [85]. Likewise, diffusion processes and nutrient gradients are present and accounted for, which eventually makes drug response most relevant for drug development assays. Nonetheless, sampling of tumors results in inhomogeneous samples, hence inter and intra-tumor variability is very high and results in an elevated dispersion of results [78]. Moreover, blood vessels are isolated from a circulatory system and so, the viability of the explants varies with the type of tumor [86]. Finally, monitorization issues present in MCTS are also encountered in tumor explants [78].

All in all, these two models present important cons, which cannot easily be overcome. In this context, microfluidic presents itself as a comprehensive alternative, and is discussed in detail in forthcoming sections.

1.6 Classical 3D cell culture strategies for reproducing and characterizing different aspects of the TME.

1.6.1 ECM: Natural scaffolds and hydrogels.

1.6.1.1 Reproduction of biological scaffolding *in vitro.*

A vast number of biocompatible materials, both synthetic and of natural origin have been developed over the years. For the purposes of this Thesis, solely scaffolding materials for *in vitro* cell culture has been considered, thus omitting those intended for structural medical implants or Tissue Enginerering.

Regardless of their origin, biomaterials intended for cell culture should ideally have some key features to be used for cell culture (Figure 1.11).

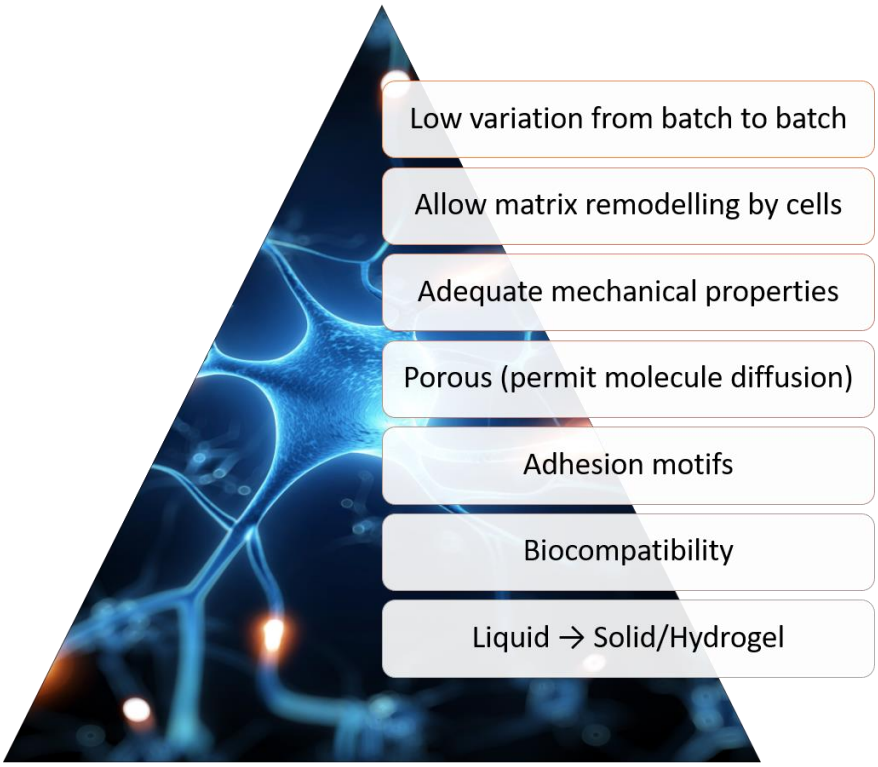

Figure 1.11: Summary of features a biomaterial should comply with, organized in terms of importance, according to the author's opinion. Background image purchased from online image repository Dreamstime.com [43].

At the bottom of the pyramid stands the logistical feasibility of the 3D culture. In other words, to embed cells within the biomaterial for 3D culture, the biomaterial should

allow phase transition from liquid to gel or solid, while maintaining a degree of humidity and cytocompatibility [55]. This is a common feature for hydrogels, therefore hydrogels are the most usual choice for 3D cell culture [87]. An additional feature is the presence of cell-adhesive domains, which is crucial to provide basic anchorage and hence, maintain cell viability. In case of synthetic polymers, cell-adhesive ligands must be incorporated in the polymer, whereas they are naturally available in natural polymers. This issue has often been solved by integrating RGD (Arginine-Glycine-Aspartic Acid tripeptides) in the synthetic polymer [88,89]. A porous structure is also required, since nutrient diffusion and cell migration need to occur in *in vitro* 3D systems.

Mechanical properties are an issue which has been extensively explored in the literature for biomaterials intended for cell culture. Up to date, there is no ideal biomaterial in terms of mechanical properties. While low Young's Moduli can easily be mimicked through the use ECMs of natural origin (0.1-2 kPa), higher stiffness have mostly been limited to synthetic polymers, which need modifications to reach biocompatibility and adhesion. A noteworthy example of the latter is PEG (poly-ethylene glycol)-based hydrogels [90,91].

Moreover, it has already been established that the ECM is modified by cells through proteolytic degradation with membrane-type metalloproteinase enzymes (MT-MMP). MT-MMPs are a family of nine or more highly homologous $Zn^{(++)}$-endopeptidases that collectively cleave most if not all of the constituents of the extracellular matrix [92]. Commonly, tumor cells degrade the matrix during migration processes, therefore, matrix remodeling should be accessible to embedded cells [65]. In the case of ECMs of natural origin, as already mentioned, these materials inherently possess adhesive ligands and other biological activity, and can readily be remodeled by cells [55].

Among natural ECMs, Matrigel® has been described as a plentiful ECM option given that it comprises different collagens, laminin and entactin; thereby accounting for the complexity of *in vivo* matrices. A list of common cell culture matrices is detailed below (Table 1.2).

ECM type (Source)	Reference
Natural	
Gelatin	[93,94]
Collagen	[95,96]
Fibrin	[97,98]
Hyaluronic acid	[99,100]
Alginate	[101,102]
Matrigel	[103,104]
Synthetic	
PEG derivatives	[105,106]

Table 1.2: Common extra-cellular matrices for use in 3D in vitro cultures in the literature. Mixed matrices composed by two or more ECM components are not detailed.

For several decades, ECM from natural sources has served as an important tool for biologists. These materials include purified collagen type I, fibrin gels formed by thrombin cleavage of fibrinogen, reconstituted basement membrane (e.g. Matrigel) and hyaluronic acid. Because of their cellular origin, these materials inherently present adhesive ligands and other biological activity, and can rapidly be remodeled by cells. For this same reason, these systems present limitations in isolating certain cell responses. For example, Matrigel comprises collagens, laminin and entactin, but also possesses an uncharacterized population of growth factors that varies substantially between batches [64,103], hence decreasing reproducibility among different assays.

Collagen is the major insoluble fibrous protein in the extracellular matrix and in connective tissue. In fact, it is the single most abundant protein in the animal kingdom. There are at least 16 types of collagen, but 80 – 90% of the collagen in the body consists of types I, II, and III. These collagen molecules pack together to form long thin *fibrils* of similar structure, whose fundamental structural unit is a long (300-nm), thin (1.5-nm-diameter) protein that consists of three coiled subunits: two α1(I) chains and one α2(I). Each chain contains precisely 1050 amino acids wound around one another in a characteristic right-handed triple helix. All collagens were eventually shown to contain three-stranded helical segments of similar structure. The unique properties of

each type of collagen are due mainly to segments that interrupt the triple helix and that fold into other kinds of three-dimensional structures [107]. Since collagen is so abundant and collagen subtypes are similar to each other, the use of collagen type I as culture matrix accounts for many features of live tissues, while keeping sample preparation simple [108-110].

With respect to synthetic materials, the most commonly used are PEG (poly-ethileneglycol) -based hydrogels. These materials typically present a structural backbone, cell-binding ligands, and a 'cell-friendly' crosslinking mechanism. These gels are highly tunable and often modular in their inclusion of additional functionalities, such as MMP cleavable domains. The advantages of synthetic materials are best evidenced by the ever-expanding flexibility and diversity that is achievable in these systems. For example, gels in which dynamic changes in stiffness can be induced in response to light have been developed [111-113].

From all hydrogels described above present certain pros and cons. In this Thesis, type I collagen was chosen as ECM. As it has previously been commented, type I collagen is the most abundant component of the ECM [33], is highly reproducible and produces porous structured hydrogels quickly, as has been thoroughly established in the literature [114-117]. Hence, it is one of the matrices which covers most of the features described in this section and it was found adequate as a simple ECM for recreating tumor microenvironment. This matrix is used and discussed in depth in Chapters 2, 3.

1.6.1.2 Characterization of scaffolds.

Characterization of scaffolds in terms of composition is not a standard procedure in most laboratories. This is a common practice only for studies regarding matrix remodeling carried out by cells and is be explored in the context of this Thesis. A few examples of protein analysis studies in this context are provided for further reference [118,119].

Scaffold architecture is typically inspected by means of Scanning Electron Microscopy (SEM). This technique has large field depth and uses electrons instead of light to form images. Hence, it provides topographical high-resolution rich information of the

samples. This technique requires drying the hydrogels, and thus modifying them significantly. Nonetheless, several procedures have been developed for removing the water from the hydrogel while preserving the structure [98].

The possibilities of using fluorescently labelled collagen or detecting the collagen fibers through immunofluorescence detection have also been described [120]. Other options to elucidate the inner structure of the hydrogels are confocal reflection microscopy [98] or Second Harmonic Generation microscopy [121], which do not require hydrogel modification. Even though they do not provide the detailed view of SEM, they can provide great insight into hydrogel architecture, particularly in the case of collagen hydrogels. Both techniques are further explained and explored in Chapter 3.

1.6.2 Substrate topography.

1.6.2.1 Reproduction of scaffold topography *in vitro*.

Topography has also been described to influence cell behavior, although it is rarely mentioned as an important feature for 3D cell cultures, because inner architecture is difficult to control for hydrogels, particularly for those of natural origin.

On this regard, micropatterned substrates have been established for cell culture, which provide control over geometry and cell adhesive cues without altering the physical or chemical attributes of the microenvironment (Figure 1.12) [55,122,123].

These substrates are typically stiff due to the fact that photolithography materials are usually stiff, which currently makes controlling topography mutually exclusive with controlling substrate rigidity [55].

Characterization of scaffold topography is not a standard practice in most laboratories, and remains limited to those laboratories studying the effects of certain topographies on cell behavior. Nonetheless, this factor becomes very important for gels intended for implantation and is discussed in Appendix 1.

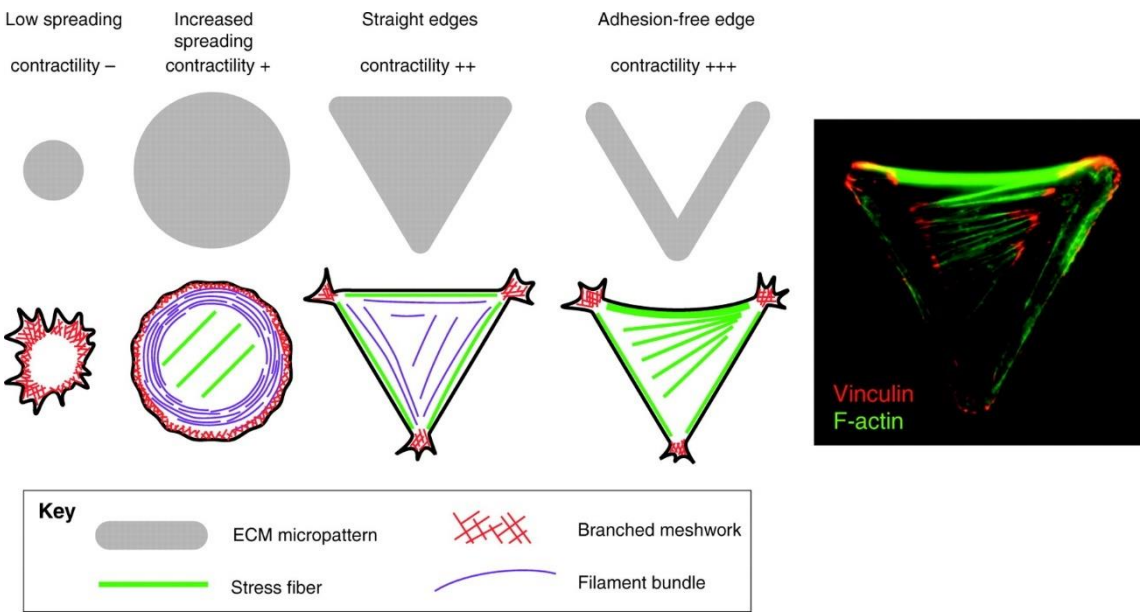

Figure 1.12: Effect of cell adhesion patterns on cell shape, architecture and contractility. A cell preferentially assembles branched actin networks when confined to a small micropattern (first shape, far left). As the cell spreads, it forms circumferential actin bundles that move inwards, as well as stress fibers within the cell center (second shape). Straight edges promote the assembly of stress fibers (third shape), which become more pronounced above non-adhesive (or concave) edges (fourth shape, far right), e.g. along the edge that connects the two extremities of the V shape where the cell is highly contracted (micrograph). Reproduced with permission from Théry, M [123].

After highlighting the importance of the cell culture substrate and its intrinsic properties, hypoxia, which is an important cue for biomimetic cell culture, will be discussed.

1.6.3 Hypoxia.

1.6.3.1 Hypoxia reproduction *in vitro.*

In vitro hypoxic conditions have been classically achieved through three different methods: spheroid cell culture, chemical preconditioning and incubation in hypoxic chambers. The first option for achieving hypoxia in cell culture is high-density cell culture, which is most commonly carried out through MCTS, as was described in previous sections.

On the other hand, chemical induction of hypoxia has been reported in the literature as an inexpensive and effective method. Preconditioning with cobalt chloride ($CoCl_2$) blocks the HIF degradation pathway in normoxia, resulting in HIF accumulation which resembles hypoxic conditions. Conversely, Deferoxamine mesylate (DFA) has been

found to induce HIF-1α/3α expression via hypoxia responsive element (HRE) gene transcription modulation when supplemented in the µM range [124,125]. The precise mechanism through which hypoxia is induced is not well-known, but it is known that they both induce apoptosis [125].

DFA is an iron chelator, a fact that has made this compound less popular as preconditioning agent for hypoxia. Particularly, it is known that it has side-effects due to its chelating properties. There is evidence pointing to a different effect of conventional hypoxia and DFA preconditioning. DFA requires a significantly longer time course than hypoxia and its mechanism is not dependent on the early generation of ROS [126].

On the other hand, the influence of $CoCl_2$ has recently been revisited, and found it has an influence on the metabolism of reactive oxygen species and second lipid mobilization and its metabolism [127].

Finally, in case of incubation of cells in hypoxic chambers, in which the percentage of oxygen is controlled, several different options are nowadays available (Figure 1.13).

Figure 1.13: Main types of hypoxic chambers. Left- Binder® hypoxia-hyperoxia incubator. Center- Mini-hypoxia chamber from Hypoxia Chamber®. Right- In vivo® Baker-Ruskinn workstation.

As mentioned above, all cited approaches have the constraint of having only one fixed oxygen concentration to work with. In Table 1.3, other pros and cons of each of these approaches are analyzed. Once the methods for generating hypoxia have been described, the characterization of hypoxia in cell culture systems is explained.

Hypoxia- incubator	
Provides incubation temp.	Yes
Price	High
Difficulty of operation vs precision	Low / High
Manipulation interrupts hypoxia	Yes
Hypoxia chamber	
Provides incubation temp.	No
Price	Low
Difficulty of operation vs precision	Medium /Medium
Manipulation interrupts hypoxia	Yes
Hypoxia workstation	
Provides incubation temp.	Yes
Price	Very high
Difficulty of operation vs precision	High / High
Manipulation interrupts hypoxia	Yes

Table 1.3: Analysis of the advantages and disadvantages of the main incubation chambers available in the market in terms of operation and result.

1.6.3.2 Hypoxia characterization.

There is extensive literature about hypoxia characterization *in vitro*. Two main methods are described in the literature for hypoxia characterization: HIF-1α quantification and quantification of oxygen levels.

In molecular biology laboratories, HIF-1α detection is mostly performed through three methodologies based in proteomics: Western Blotting, Immunofluorescence and Luciferase assays. They all quantify the amount of protein HIF-1α, which usually requires terminating the cell assay and presents great experimental difficulty due to the low stability of HIF1-α [128].

The characterization of oxygen levels is presented as an interesting, real-time non-terminal alternative. Since characterization of oxygen levels *in vitro* is a central topic in this Thesis, this topic is covered in depth in Chapter 3.

After discussing the reproduction and characterization of hypoxia *in vitro*, other soluble factors commonly found *in vivo* are discussed.

1.6.4 Other soluble factors.

1.6.4.1 Biomolecule gradient generation.

As established in previous sections, biological gradients have a key role in many biological processes and behaviors. Cancer is a particularly important example, which justifies a recurring interest in the biomedical community. Therefore, several different setups have been developed in the past for recreating biomolecule gradients *in vitro*.

The first and simplest example of gradient is described in this section. This method consists of a droplet of a hydrogel of natural origin, which acts as source for the molecule of interest. This droplet is placed on a Petri dish where cells are seeded later. Diffusion of the biomolecule of interest occurs over time through the culture medium, creating a gradient around cells seeded in a Petri Dish (Figure 1.14). While this method is very simple, it presents certain limitations concerning gradient persistence over time, control over the gradient and reproducibility [129-131].

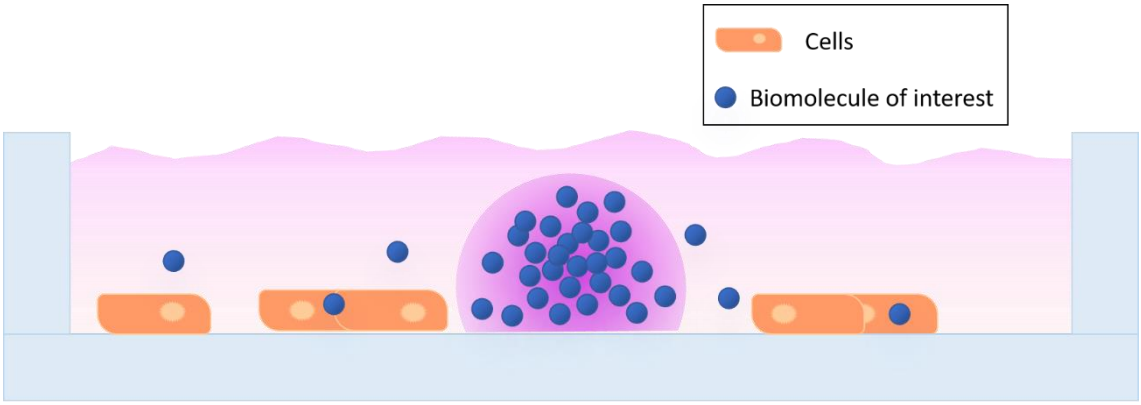

Figure 1.14: Scheme showing how hydrogels can be used to expose cells to biomolecule gradients. The hydrogel is used as a source for the biomolecule of interest, which diffuses through culture media and creates a gradient which is sensed by cells cultured in the dish.

The second method is the Boyden chamber, more commonly known as Transwell assay. It consists of a culture well in which an insert is placed. This insert has a porous membrane at the bottom, thus connecting both chambers through added media. To operate this device, cells are seeded on the membrane of the insert. The biomolecule

of interest is then placed in a solution below. Cells are therefore subjected to a gradient established by diffusion of the molecule of interest (Figure 1.15). Among other applications, this method has been extensively used for chemotaxis, where it has provided tremendous insight in the past decades [132].

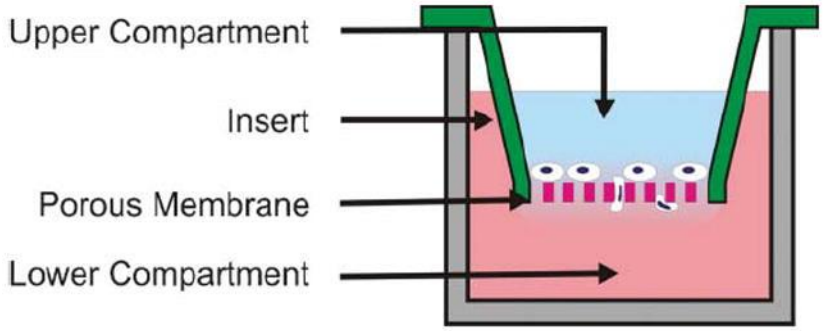

Figure 1.16: Transwell assay scheme. This assay is based on the Boyden Chamber method. Cells seeded on a porous membrane are placed in a well containing a chemoattractant solution. The chemoattractant in the lower compartment diffuses into the upper compartment forming a gradient across the membrane. Cells respond by migrating through the membrane to the bottom surface where they can be subsequently fixed, stained, and counted. Reproduced with permission from Keenan and Folch [44].

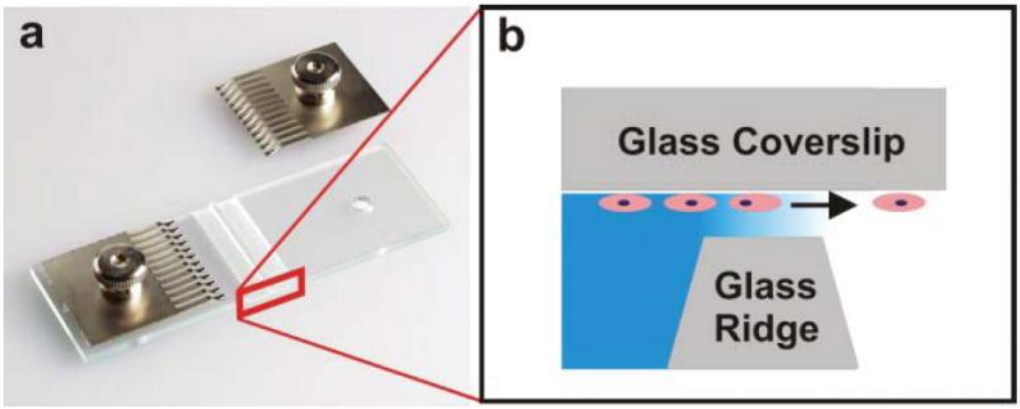

Figure 1.17: Zigmond Chamber. (a) The device consists of two etched channels separated by a glass ridge. The metal tines are used to clamp an inverted glass coverslip seeded with cells to the device. (b) A cross section schematic of the device shows cells on the inverted coverslip migrating in response to the gradient established between the coverslip and the glass ridge. Reproduced with permission from Keenan and Folch [44].

The geometry and precise dimensions of the Zigmond Chamber (Figure 1.16b) produces a gradient that is reproducible, mathematically predictable, and can be

indirectly estimated using fluorimetric dyes. Nevertheless, the life-span of the produced gradient is 1-2h and they cannot be modified after equilibration [133,134].

As established before, MCTS are also a method to create biomolecule gradients within the 3D culture, although it is not achieved through a particular setup. This method presents the advantage over the previous methods since the gradient is self-induced, so it can be sustained for as long as the cell assay lasts.

Overall, classical methods present interesting alternatives for creating biomolecular gradients *in vitro*, but do not often provide a high degree of control over the gradient and, except for MCTS, do not provide a gradient that persists for over a few hours. Thus, characterization of soluble gradients becomes an important tool to assess the dynamics and biological importance of newly established gradients *in vitro*.

1.6.4.2 Characterization of the diffusion/consumption dynamics of soluble factors.

As established in previous sections, biological gradients are of great importance. Thus, much work has previously focused on characterizing diffusion dynamics in biological systems.

An approach to gradient characterization is computational modelling. The physics of diffusion has been thoroughly explored in the literature. Fick's Law is a well-known and established approach to estimate the diffusion rate [135]. However, it requires a diffusion coefficient for the substance of interest, which should be empirically determined first. There are also methods to estimate such coefficient, such as the Stokes-Einstein Equation and the Ogstron approximation [136,137]. While these methods provide much insight on the diffusion dynamics, they do not always account for all factors implied in diffusion, making it necessary to ultimately determine diffusion rates experimentally. Furthermore, active consumption by cells embedded in the system is a parameter which must be calculated empirically. Although complex computational models exist to estimate these parameters, only *in vitro* methods to study diffusion of molecules of interest are described.

In biological sciences, diffusion has usually been quantified by means of fluorescent compounds. In case the molecule of interest does not present intrinsic fluorescence, labelled substitutes or analogues of similar molecular weight are available on the market. A couple of examples are detailed here, although many more are present in the literature.

2-(N-(7-Nitrobenz-2-oxa-1,3-diazol-4-yl)Amino)-2 Deoxyglucose (NBDG) is a fluorescent nonhydrolyzable glucose analog that has been used to monitor glucose uptake and transport in live cells. Although sensitive to its environment NBD fluorescence typically displays excitation/emission maxima of ca. 465/540 nm [138,139].

Dextrans are hydrophilic polysaccharides characterized by their moderate to high molecular weight (usually in the range of kDa-MDa), good water solubility and low toxicity. They are widely used as both anterograde and retrograde tracers in neurons among many other applications [140]. Dextrans are biologically inert due to their uncommon poly-(α-D-1,6-glucose) linkages, which render them resistant to cleavage by most endogenous cellular glycosidases. They have also low immunogenicity. Several different molecular weight dextrans are commercially available as diffusion models [141,142].

Finally, diffusion of newly developed drugs, particularly in the case of nanoparticles or liposomes, must be characterized *in vitro* in a suitable system as part of the pre-clinic validation. This aspect is discussed in depth in Chapter 2.

1.6.5 Co-culture.

1.6.5.1 Co-culture establishment *in vitro.*

As has been established in previous sections, the TME is composed of many different cell types, interacting with each other to create a highly dynamic system. The most common classical co-culture 2D assays are illustrated in the following figure (Figure 1.17), although similar concepts can be extrapolated to 3D hydrogels. Traditional co-culture assays usually consist of the combination of the different cell types in an unpatterned manner or the indirect co-culture of two cell types (adding media in

which Cell Type 1 was cultured to Cell Type 2). Transwell assays and co-culture spheroids have also been thoroughly explored in the literature [143-146].

While these methods have provided much insight to unravel the nature of the interaction of many different cell types, cell structure in these assays is not similar to that present in a tumor or healthy tissue *in vivo*. Furthermore, paracrine interactions are highly dependent on cell proximity, which makes structure and physiological distances highly relevant. Moreover, the inclusion of the endothelium has proven to be very difficult for most *in vitro* methods [147,148].

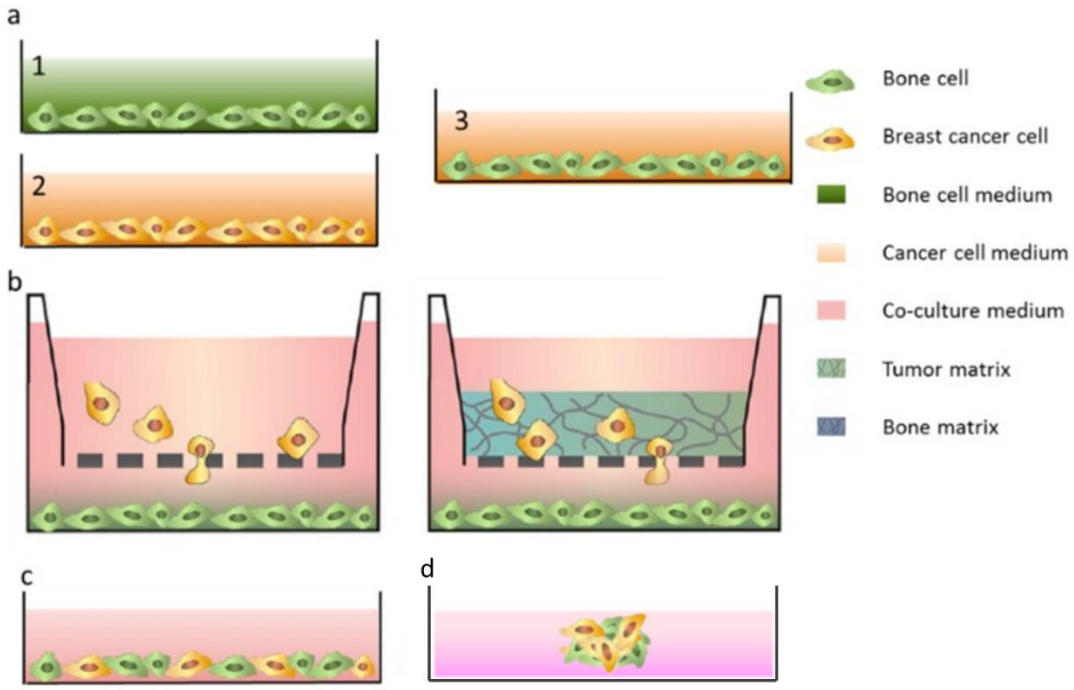

Figure 1.18: Schematics of different co-culture methods. (a) Conditioned medium culture. Culture medium from population (2) is used to culture population (1), originating an indirect, monodirectional co-culture system (3); (b) left: Transwell co-culture: population 1 is seeded on the bottom of a culture dish and population 2 is cultured on a porous insert, allowing the exchange of soluble factors, migration of cells through the membrane but without contact between the two populations; right: Transwell can also be used to measure invasion, by coating the porous membrane with a layer of a protein matrix; (c) 2D direct co-culture system, in which the two populations are mixed and seeded on the bottom of a culture plate, with a shared medium; (d) Co-culture spheroid. Adapted from [149,150].

1.6.5.2 Co-culture characterization.

Once the co-cultures are established, the interaction between cell types should be assessed. The most common way to do this is to label different cell types with distinctive fluorophores, or perform immunofluorescence assays by choosing distinctive markers. The latter proves a challenging task in 3D system, since antibody diffusion and detection of specific markers is hindered by the presence of the ECM. Hence, transfection with fluorescent proteins or using live cell stainings are usually more convenient. This allows distinction of different cell types and their organization.

Furthermore, cell shape and movement are often of interest, particularly in the case of metastasis. Thus, cell tracking and image processing should be performed, either for a few sample cells within the cell population or by using cell distribution as a movement parameter.

The characterization of soluble factors can be performed by means of proteomic analysis. This includes immune detection of proteins (via Western Blot or Enzyme-linked ImmunoSorbent Assays) or newer approaches such as MagPix®, a multiplex bead-based detection method similar to flow cytometry or immune detection of specific proteins [151-153].

Finally, the exosome technology is currently gathering attention in the scientific community. Exosomes are extracellular vesicles ranging from 30 to 100 nm in size. They are generated through the endolysosomal pathway and released by exocytosis. Their contents include miRNAs, mRNAs, lipids, DNA membrane proteins and lipids and cytokine receptors. Therefore, they have emerged as important “nanoshuttles” of information between cells [154]. Exosomes can be isolated by means of ultracentrifugation and analyzed by light microscopy, electronic microscopy, flow cytometry or specific commercial solutions. Furthermore, the content of the exosomes can be analyzed to characterize the nature of inter-cellular communication [155]. Although complicated, this technology is cutting edge and of extreme interest. Coupling molecular biology techniques with 3D cell culture, although unexplored so far, could prove to be extremely useful to further develop *in vitro* models and

thoroughly characterize them for *in vitro* drug testing. This issue is explored further in Chapter 4.

1.7 Microfluidics and microtechnologies as an alternative to reproduce and characterize the TME.

Microfluidics principally studies fluid behavior and liquid manipulation at the microscale. As it was already mentioned in previous sections, liquids behave very differently at the microscale, in comparison to their conduct in macro systems. The absence of mixing motions within and the prevalence of capillarity over gravity are some of the hallmarks defining microscale physics. More detailed information on this subject can be found in the reviews from Bhatia et al, Portillo-Lara et al and Young et al, among others [156-161]. These features have been exploited for a fine control of the physical properties of the microenvironment, to mimic and monitor tumor microenvironment. Combined with the reduction in reagent volumes and costs, microfluidics is ideally suited to develop new platforms for cell culture and *in vitro* models.

There have been some excellent proposals in the literature to reproduce and characterize the tumor microenvironment for drug testing applications. Some of the most well-known examples of microfluidic systems applied to the study of TME are described below.

The Beebe group presented in 2012 a method for patterning lumen structures through ECM hydrogels confined within a passive pumping microfluidic platform [162]. In a posterior piece of work, they presented a simpler and more reproducible method to fabricate lumens in natural and synthetic gels in absence of specialized equipment [163]. These lumens could be subjected to biological gradients and exhibited the expected response (Figure 1.19).

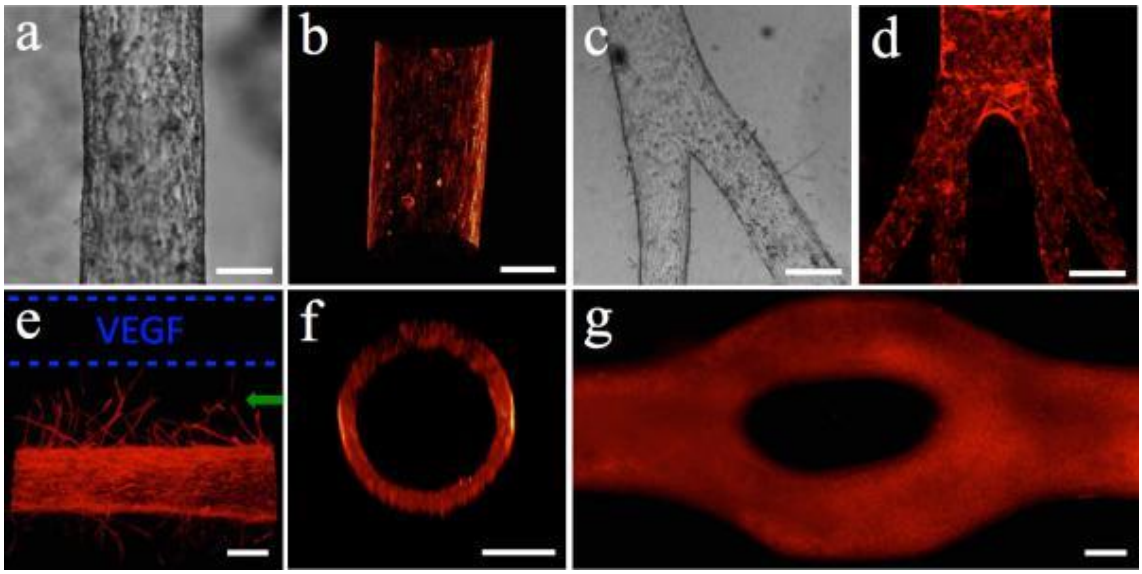

Figure 1.19: Endothelial cell-lined lumens and possible morphologies. (a) Image of endothelial cell-lined lumen and (b) 3D volume reconstruction of the biomimetic blood vessel using F-actin staining (phalloidin). (c) Bright field image of bi-branched lumen and (d) multi-branched (tertiary branches) with phalloidin staining. (e) Angiogenesis via vascular endothelial growth factor (VEGF) gradient from source (dashed blue lines). (f) Cross-section of circular lumen lined with endothelial cells (phalloidin staining). (g) Bifurcated lumen lined with endothelial cells. Bar=150µm. Reproduced with permission from Jiménez-Torres et al [163].

The Kamm group developed 3D functional, perfusable microvascular networks composed of human ECs and BM-hMSCs phenotypically transitioning toward mural cells by vasculogenesis-like approach. Furthermore, they investigated the role of biochemical factors in the transition toward a mural cell lineage. This approach can be used to develop advanced *in vitro* models where the interactions between a functional vasculature tissue parenchyma is critical to mimic pathophysiological processes (intra- and extravasation processes involving leukocytes and cancer cells) and test diffusion and drug effects in complex microenvironments (Figure 1.20) [97,164,165].

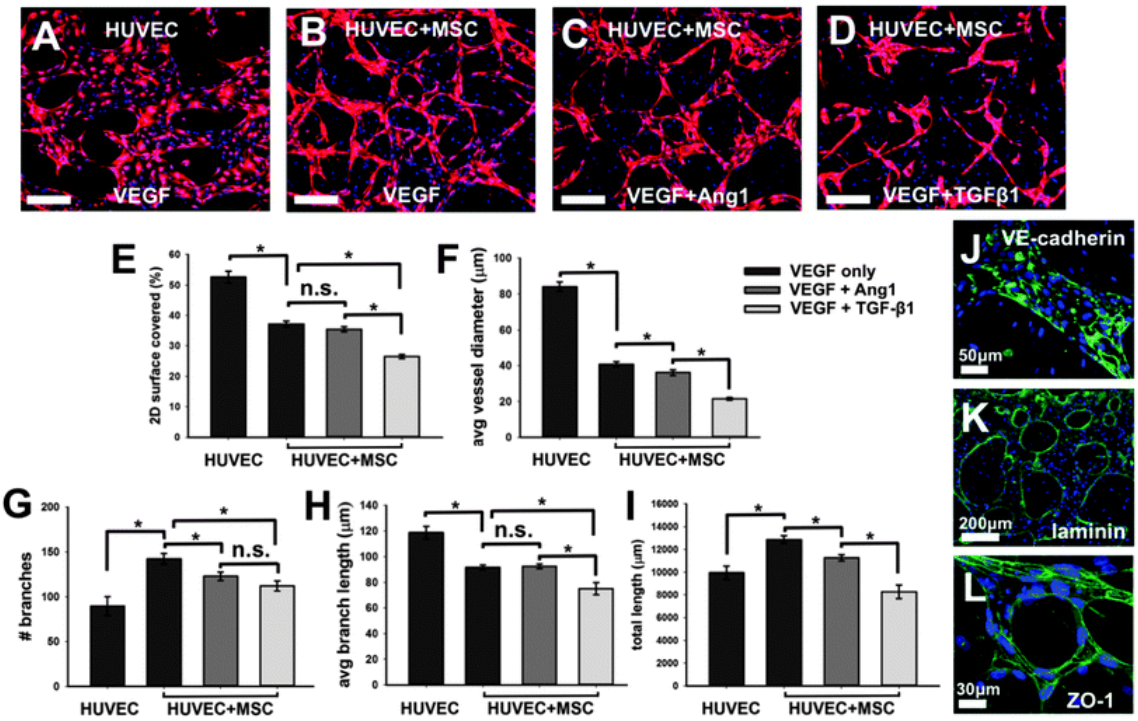

Figure 1.20: Generation of microvascular networks in the presence of BM-hMSC and different biomolecules. Initially uniformly dispersed HUVECs form perfusable networks by vasculogenesis-like process in VEGF supplemented standard endothelial growth medium with and without BM-hMSCs or with VEGF + Ang-1 and BM-hMSCs (A–D). Microvascular networks under various conditions are quantified (E–I). Functionality of microvessels are confirmed by staining with VE-cadherin (J, green) for adherens junctions, laminin (K, green) for matrix secretion, and ZO-1 (L, green) for tight junctions. Cell nuclei were stained with DAPI (blue). Scale bars = 200 μm, unless noted. Reproduced with permission from Jeon et al [97].

Another approach from the Kamm group is the development of microfluidic-based approach to investigate tumor cell intravasation by means of high-resolution live imaging with endothelial barrier function measurement in the presence of macrophages. They also characterized the timescales of tumor-endothelial cell interactions during intravasation and demonstrate the interplay of endothelial permeability and tumor-endothelial signaling (Figure 1.21). While this model presents a low-throughput, it certainly shows potential for drug testing and personalized medicine [166,167].

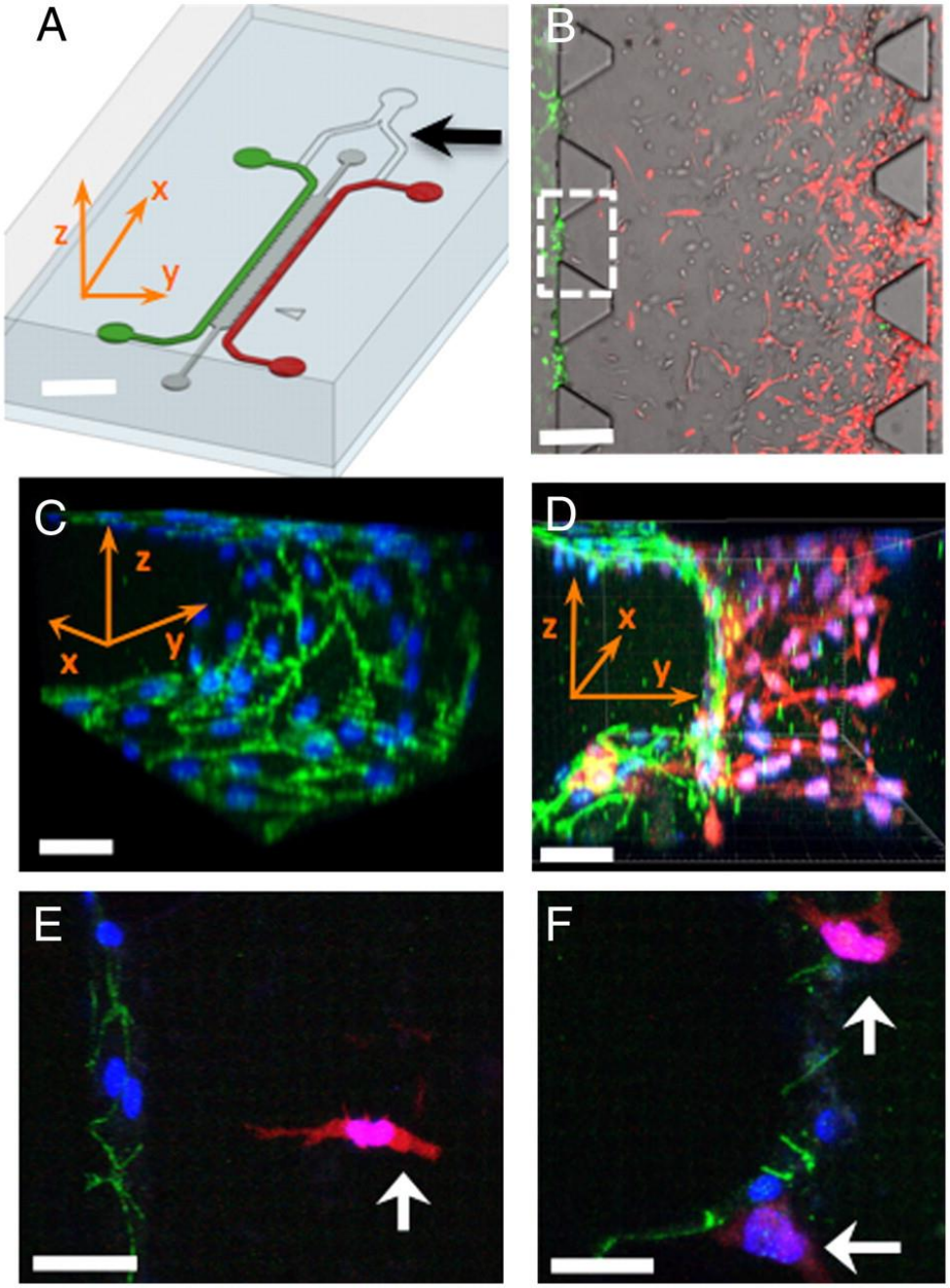

Figure 1.21: Microfluidic tumor-vascular interface model. (A) Endothelial channel (green), tumor channel (red), and 3D ECM (dark gray) between the two channels. Channels are 500 µm wide, 20 mm in length, and 120 µm in height. Black arrow shows the y-junction. (Scale bar: 2 mm.) (B) Phase contrast image showing the fibrosarcoma cells (HT1080, red) invading through the ECM (gray) toward the endothelium (MVEC, green). A single 3D ECM hydrogel matrix region is outlined with the white dashed square. (Scale bar: 300 µm.) (C) VE-cadherin and DAPI staining to show the confluency of the endothelial monolayer on the 3D ECM (outlined with white square in B). (D) Three-dimensional rendering of a confocal z-stack of a single region showing the tumor cells invading in 3D and adhering to the endothelium. (Scale bar: 30 µm.) (E) HT1080 cell (white arrow) invading in 3D toward the endothelium. (Scale bar: 30 µm.) (F) HT1080 cells in contact with the endothelial monolayer. In C–F all scale bars are 30 µm. Green, VE-cadherin; blue, DAPI; red, HT1080-mCherry. x-, y-, z- coordinate indication is appropriately adjusted in A, C, and D. Reproduced with permission from Zervantonakis et al [167].

Later, they extended this approach to study metastasis and epithelial-mesenchymal transition [143,164,165].

The group of S. George developed a 3D vascularized micro-organ platform for *in vitro* studies [168]. Vascularization was developed spontaneously within the 3D tumor in the microdevice. They validated their platform for drug testing and coupled fluorescence lifetime imaging microscopy for metabolism investigation (Figure 1.22) [168,169].

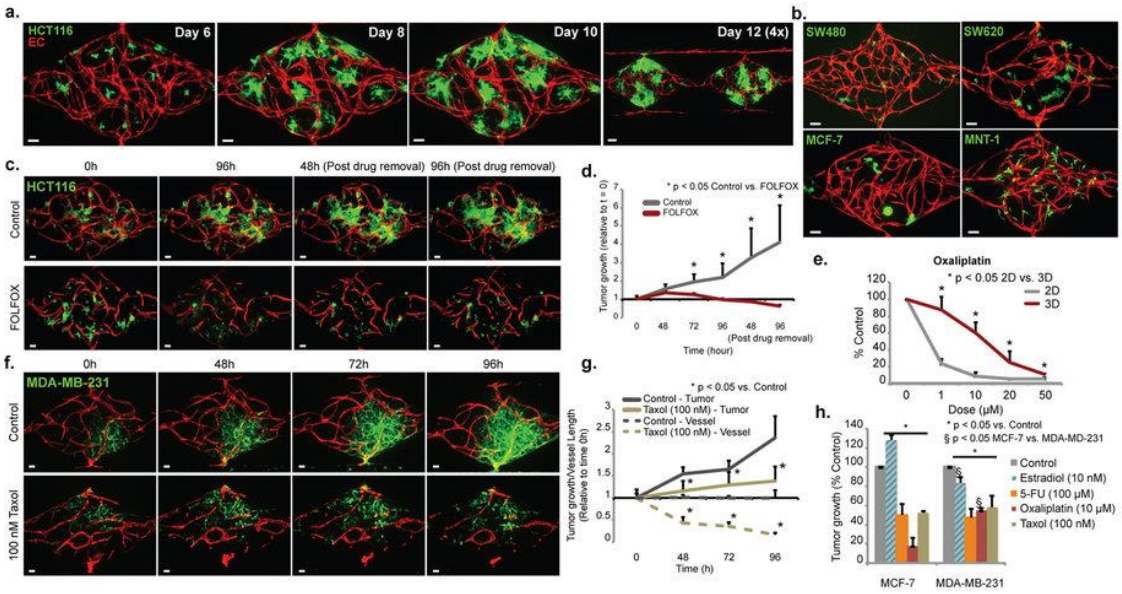

Figure 1.22: Establishment of Vascularized Micro-Tumors (VMTs). (a) Time course of HCT116 growth in the VMT. Lentivirally-transduced HCT116 (green) and EC (red) were visualized by confocal microscopy. Stromal/perivascular cells were unlabeled. (Scale bar 100 µm). (b) The VMT platform supports growth of multiple tumor cell types, including additional CRC (SW620, SW480), breast cancer (MCF-7) and melanoma (MNT-1). Images were taken between days 10 and 12. (c, d) Time course of HCT116 (green) response to FOLFOX (10 µM Folinic acid (leucovorin), 100 µM 5-FU, and 5 µM Oxaliplatin) in the VMT. Data are shown relative to t = 0, which is time of first exposure to drug (usually 6–8 days after initiation of culture). Cells were also monitored for 96 h after drug removal. Error bars show mean ± S.D. of 3 replicates (n = 2) ($p < 0.05$ control vs treated FOLFOX). (Scale bar 50 µm). (e) Dose-response of Oxaliplatin on HCT116 cells. VMTs or cells growing in 2D were exposed to drug for 48 h, and tumor cell number and viability were assessed by fluorescence intensity measurement or XTT assay. Data are normalized to time zero of drug exposure and shown as percentage of control. Error bars show mean ± S.D. (n = 3) ($p < 0.05$, 2D vs VMT). (f, g) Time course of MDA-MB-231 cells exposed to Taxol (100 nM). Data are normalized to first day of drug exposure. Error bars show mean ± S.D. of 3 replicates ($p < 0.05$ control vs treated Taxol). (h) Differential effects of anti-tumor drugs on the breast cancer cell lines MCF-7 (ERα+) and MDA-MB-231 (triple-negative). VMTs were first exposed to E2/drugs between days 6 and 8 and cultured for an additional 96 h. Drugs were removed from the media at 48 h. Data are normalized to first day of drug exposure and are shown as percentage of control. Error bars show mean ± S.D. (n = 2–4) (*$p < 0.05$ vs control; §$p < 0.05$ MCF-7 vs MDA-MB-231). Reproduced with permission of Sobrino et al.[168].

Later, they adapted their approach for high-throughput drug testing, in an effort to develop approaches which can be adopted by the pharmaceutical industry for drug research and development [169].

Although these models present many of the features discussed in previous sections, they all have in common the material of fabrication: PDMS. This material is not industrially scalable and requires especial equipment [3]. Moreover, PDMS is oxygen-permeable, thus making it difficult to generate a hypoxia gradient within [170]. Finally, it has been previously reported that PDMS sequesters certain hydrophobic drugs, thereafter it is not a good choice for drug screening [171]. Thus, a simple, industrially scalable, high-throughput, user-friendly model integrating all these features remains to be developed.

As for TME characterization, real-time imaging remains the main technique and provides great insight on the series of biological events taking place in the TME, as well as their time scales. However, the methods to characterize the different aspects of the TME must be applied individually. Furthermore, molecular biology techniques should integrate better with microfluidic tools to attract the biological community for a more relevant and efficient drug research and development process.

Therefore, the main focus of this Thesis is to develop new platforms to recreate and study the TME which can be scalable for mass production.

In the following chapter, a simple platform is developed to re-create the TME by combining two cell types in patterned co-culture: endothelial cells in 2D and tumor cells in 3D. Furthermore, the effect of biological gradients within the model was assessed, as well as interactions between both cell types. Finally, this model was validated for drug testing.

1.8 Aims and objectives.

This Thesis focuses on finding new strategies based on microfluidics to reproduce and characterize the tumor microenvironment. Thus, as anticipated in the previous section, we intended to develop microfluidic platforms for cell co-culture which would focus on reproducing the TME for more relevant new drug assessment.

Keeping this goal in mind, we developed the following partial objectives:

1. **Development of an open microfluidic platform compatible with high-throughput which allows for the confinement of liquids.** Thereafter, the microfluidic model of the TME could be established in this microdevice.

2. **Assessment of the biocompatibility of such platform for *in vitro* studies.** Since the microdevice is intended for cell culture, the microdevice should not significantly diminish the viability of cells cultures.

3. **Establishment, characterization and validation of a microfluidic co-culture model of the TME for drug testing purposes.**

4. **Development of a technology which enables cell recovery from the microdevice for subsequent analysis through traditional molecular biology techniques.**

Chapter 2: Development of microfluidic systems for 2D-3D cell co-cultures.

2.1 Introduction.

Our understanding of cancer has undergone significant changes in the last years. We used to think of cancer as a clonally expanded cell population originated from a single cell [172], whereas it is now evident that tumors consist of highly complex systems, where the tumor microenvironment plays a fundamental role [21]. Spatial and temporal complexities (such as biochemical signals and gradients thereof), together with a variety of cell types and phenotype differences within the same cell type add up to concoct this orchestrated environment in tumor tissues, which is known as the tumor microenvironment (TME) [21,24,173,174]. It has been previously reported that this high complexity and heterogeneity plays a significant role in drug resistance [175]. Moreover, tumor cells also interact with the stroma, conditioning their initiation, development and resistance to therapy [176].

Furthermore, the endothelium plays an important role in cancer development and drug delivery. The endothelium regulates nutrient diffusion and responds to hypoxic signals produced by tumor cells, to promote new blood vessel formation via angiogenesis. Additionally, blood vessel permeability is essential for the delivery of drugs to cancer cells, which, in turn, conditions the overall effect of the drug on the patient [30,177]. Of particular interest is the Enhanced Permeability and Retention (EPR) effect, which is caused by the generation of a porous architecture in the blood vessels surrounding the solid tumors, leading to an increased vascular permeability. The EPR effect results in more efficient oxygen and nutrient supply to the tumor sites than that from regular vessels [30]. Likewise, nanomedicine-based treatments take advantage of this EPR effect for the local accumulation of nano-vehicled agents which are meant for diagnostic or therapeutic purposes [30]. Currently, the delivery and efficiency of treatments against cancer disease are still mostly tested in classical *in vitro* 2D models [161,178,179], which usually lack an extracellular matrix, do not

include different cell types arranged in a structured manner and lack biological gradients (e.g., of oxygen and nutrients). Consequently, 2D models are unable to faithfully reproduce the tumor-endothelium interactions, where crosstalk depends on the 3D environment, as well as on 3D direct cell-cell interactions. Of particular interest for the generation of sophisticated models are the so-called organ-on-a-chip platforms, which combine different cell types and microfabricated structures and allow mimicking the architecture of a complete organ and/or tissues [156]. As such, microfluidic technology shows great potential in the field of cancer research to mimic faithfully the TME [180]. Up to date, significant efforts in the field of microfluidics have focused in reproducing the tumor microenvironment, and, in particular, studying the interactions of cancer cells and the endothelium [164,165,181,182]. For instance, Kamm's group has established co-culture of breast cancer cells and endothelial cells to study cellular extravasation and vascular permeability [183], as well as tissue-specific metastasis [184-186]. Additionally, they successfully characterized molecular mechanisms of metastasis in breast cancer and macrophage extravasation [187-189]. Also worth mentioning are the efforts in establishing distinctively patterned co-cultures made by the Beebe's group for drug screening and biosensing applications [162,190]. Interested readers in microfluidic cell culture approaches in cancer are referred to excellent reviews by Sung et al, Portillo-Lara et al and Regier et al. [148,160,191].

From these examples, we can infer that despite all these efforts, microfluidic technology remains restricted to engineering laboratories and has mainly focused on proof-of-concept applications. The fact that microfluidics is rarely used in traditional cell biology laboratories can be explained by the high difficulty of operation and low- or medium-throughput of most microdevices [158,192]. Therefore, to bridge the gap between microfluidics and basic and translational research laboratories, a new generation of microdevices is needed, which balances simplicity of operation, reproducibility, biological relevance and usefulness in the described contexts. Additionally, integration of endothelial layers in microfluidic models has also been proven difficult. This integration requires a continuous interface to provide support and allow endothelial cells to attach correctly. Furthermore, a common method to

assess endothelium integrity *in vitro* relies on TEER (TransEpithelial Electrical Resistance) measurements [193,194]. Nonetheless, this approach presents a few drawbacks, which limits its applicability: it requires the integration of an electrical setup within the biological setup; it requires specific electrodes to be built-in or added externally to the microfluidic system; and, more importantly, the lack of stability for these measurements is a well-known problem, which yet, remains to be overcome [195]. Optimized optical inspection and easy access to the endothelium would provide not only an advantageous alternative but also additional information on cell morphology and tight junctions in the endothelium by means of immunofluorescent staining.

In this context, we present here a simple and self-filling SU-8-based microdevice, which exploits capillary forces, to study endothelium-tumor interactions. The proposed microdevice consists of several linear arrays of microwells (Figure 2.1), in which 3D tumor models are created by embedding tumor cells in a 3D collagen matrix and, on top of which confluent HUVEC monolayers are prepared as 2D mimics of the endothelial barrier. Although similar approaches have already been reported [196], our device allows filling an array of microwells in only one single pipetting step and a few seconds, fulfilling thereby the key-requirements of simplicity of operation and user-friendliness.

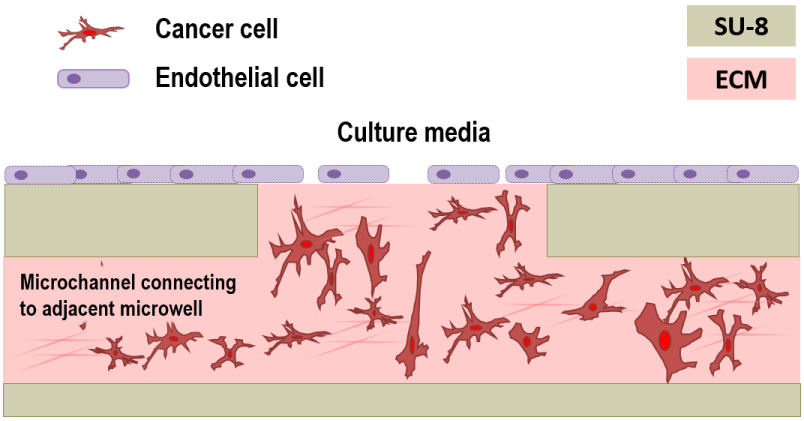

Figure 2.1: Experimental configuration and microdevice fabrication. The image shows a scheme of the co-culture cancer model recreated in the present study within the device.

Additionally, the design of the microdevice has been optimized for optical examination of the endothelium to evaluate its integrity. This approach can replace TEER measurements for an easier and more comprehensive approach on endothelium

integrity. Here, we first demonstrate co-culture of breast tumor cells (MDA-MB-231) seeded in 3D with an endothelium (HUVEC) and thoroughly characterized these models (Figure 2.1).

Next, we applied our model to study the cytotoxic effects of drugs and their penetration in the 3D tumor environment. To that end, the anti-tumor agent TNF-related apoptosis inducing ligand (TRAIL) was evaluated. TRAIL is a protein secreted by immune cells which is able to induce apoptosis in malfunctioning cells [197]. *In vivo,* TRAIL is secreted as anchored to liposomes, and this clustered form has been found to have a higher potential for inducing apoptosis [198]. Here, two different drug formulations were tested; a soluble version (sTRAIL) and an "improved" formulation based on liposomes decorated with TRAIL (LUV-TRAIL). Altogether, we have developed a simple and highly versatile microfluidic device with a physiologically relevant tumor-endothelium co-culture model, which allows testing the penetration and efficiency of drugs on tumor tissues.

2.2 Materials and Methods.

2.2.1 Microdevice fabrication and setup.

The device consists of three independent arrays composed of five different wells each, which are connected within an array by a microchannel (Figure 2.2). As the device was conceived to use capillarity as a driving force to spontaneously fill the whole microdevice, special care was taken to avoid sudden transition in the microchannel dimensions. Additionally, capillary valves were integrated to constrain the liquid within the microdevice and prevent it from flowing outward the microwells.

The fabrication was carried out as follows: A thin Kapton film (125 µm thickness) was temporarily bonded on top of a Pyrex substrate (Figure 2.3.a). Kapton was used because of its low adhesion to SU-8, allowing easy release of the devices from the substrate after their fabrication. Once the Kapton film was fixed to the substrate, a first SU-8-50 layer was deposited on it, followed by a soft-bake treatment, which consists of heating the wafer up to 65 ^{0}C for 30 min and cooling it down to room

temperature. Next, another SU-8 layer was spin-coated followed by a second soft-bake step. Next, a 140 mJ/cm^2 exposure dose was applied to cure the first layer of the device using a 365-nm wavelength UV lamp, followed by a post-bake step (Figure 2.3.b). The post-bake step consisted of heating the wafer up to 65^{0}C for 15 min and cooling it down to room temperature. Following this, the same procedure was repeated to prepare another 80-µm thick layer of SU-8 on top of the first one (spin-coating of 60 µm and 20 µm layers, followed by corresponding soft-bakes). A second step exposure of 140 mJ/cm^2 through a mask allowed defining the microchannels and microwells (Figure 2.3.c). Then, a post-bake was performed followed by a development step to remove the unexposed SU-8 material. Specifically, the wafer was immersed into a SU-8 developer for 5 min, followed by a rinse step in isopropanol, distilled water and a drying step using nitrogen (Figure 2.3.d). Thus, an open microchannel with microwell structures was fabricated.

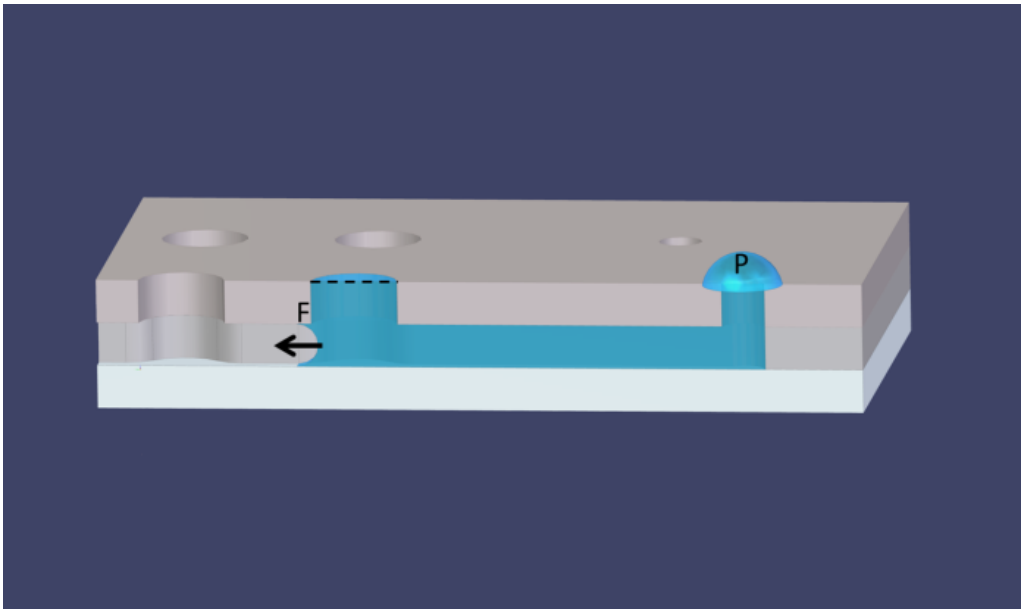

Figure 2.2: Schematic representation of the device, showing capillary forces exerted by the geometry, and capillary valves integrated into the design (dotted line). The scheme includes the hydrogel droplet that was placed on the top of the main inlet, to avoid evaporation of the solution in the hydrogel and to ensure the formation of a flat hydrogel-air interface.

To close the microchannel and define the microwells, another wafer was processed as before: a 90-µm thick SU-8 layer was processed (spun and soft-baked) on top of another Kapton film temporary bonded to a Pyrex wafer (Figures 2.3.e and 2.3.f). Inlets, outlets and microwells were defined by photolithography using the same

exposure and baking parameters as before. The second wafer was finally developed (Figure 2.3.g). Next, both wafers (bottom and cover) were aligned and bonded to each other by applying a pressure of 1 bar and heating up to 90^0C for 15 min (Figure 2.3.h). Finally, the bonded SU-8 devices were manually released from the Kapton (Figure 2.3.i). The final thickness of the device was sufficient to ensure mechanical rigidity and easy handling in absence of a supporting substrate.

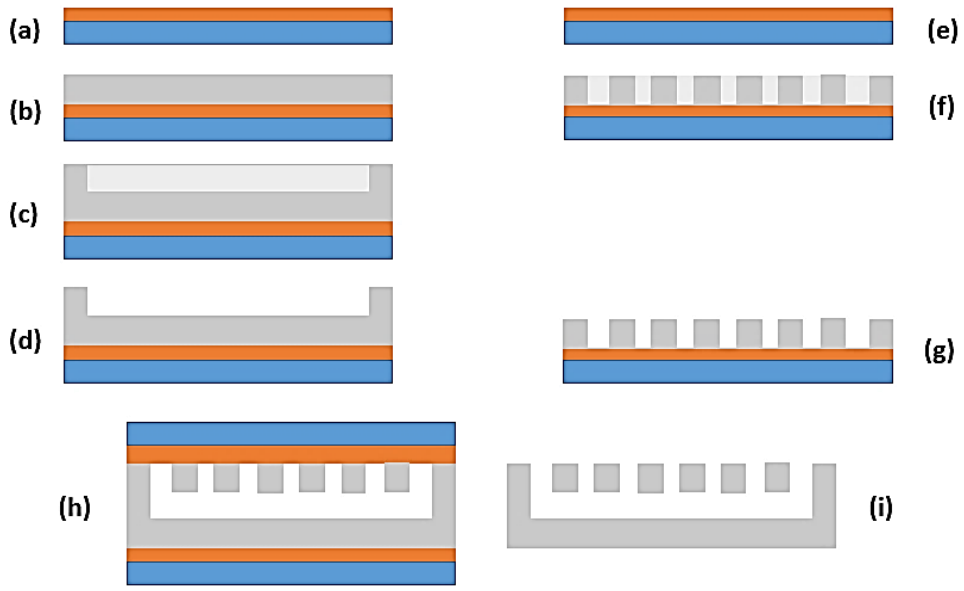

Figure 2.3: Microdevice fabrication process flow: (a) Kapton film bonding to a pyrex wafer, (b) deposition of a 90-µm thick SU-8 layer, UV-exposure and polymerization of the microchannel and microwell structures, (c) spinning of a NN- µm thick SU-8 layer and patterning of the microchannel and microwell structures, (d) development of the two SU-8 layers, (e) Kapton film bonding to a pyrex wafer (f) spinning of a 90-µm thick SU-8 layer and patterning by photolithography, (g) cover development, (h) SU-8 to SU-8 thermal bonding, (i) SU-8 device release.

For easy introduction of the hydrogel and hydrogel confinement, the SU-8 was rendered hydrophilic through an oxygen plasma treatment analogous to that described in Jokinen et al [199], consisting in an 80 s treatment at 300 W, using a pressure of 0.4 mBar and 50% O_2 to flood the chamber.

2.2.2 Air-hydrogel interface generation and optimization in the microdevice.

100 µl of hydrogel mixture was prepared as follows to yield a final collagen concentration of 1.2 mg/ml: 36.60 µl of a 3.37 mg/ml stock solution of Type I rat tail

Collagen (Corning, 354236) was neutralized by adding 0.9 µl NaOH at 1 M (Sigma 221465). Ionic strength was adjusted by adding 20 µl of DMEM 5x (Sigma, D5030). Finally, the volume was adjusted to 100 µl by adding sterile distilled water. Using a chilled tip, 5 µl droplets of the resulting collagen preparation were placed on top of each inlet to allow spontaneous loading. Afterward, the microfluidic device was placed in an incubator (37^0C and 5% CO_2) upside down for 12 min to allow collagen polymerization.

To assess the effect of evaporation at the hydrogel interface we supplemented a 1.2 mg/ml collagen gel with 0.2 µm FluoSpheres® (Thermo-Fisher, ref. F-8811) diluted to a final concentration of 1:100 from the stock solution. The resulting collagen mixture was sonicated for 5 min at 4^{o}C before use to ensure proper dispersion of the Fluospheres®.

2.2.3 Microdevice biocompatibility and 3D cell culture microenvironment characterization.

2.2.3.1 Cell isolation and culture.

MDA-MB-231 cells, derived from breast adenocarcinoma, were kindly provided by Dr. Joan Massagué (Memorial Sloan-Kettering Cancer Centre). MDA-MB-231 cells were routinely grown in high glucose-DMEM culture medium (Lonza BE12-614F) supplemented with 10% FBS (Sigma F7524) and 2 mM L-glutamine (Lonza17-605C) and 1% penicillin (1000 U/mL), 1% streptomycin (1000 µg/mL) (Penicillin/Streptomycin, Lonza DE 17-602E) within a humidified TEB-1000 incubator set at 5% CO_2, 20% O_2 and 37 ^{o}C (EBERS Medical Technology). Media was refreshed every other day and cells were passaged every 4 days using a Trypsin/EDTA solution (Lonza, CC-5012).

Human Umbilical Vein Endothelial Cells (HUVECs) were extracted at the Miguel Servet Hospital (Zaragoza, Spain) from healthy donors after informed consent according to current ethical regulations. Isolation was performed according to Crampton et al. [200] from umbilical cords 1-3 hours after delivery. A fraction of the isolated cells was tested using a FACSAria (BD) flow cytometer to confirm cell positiveness for the endothelial markers CD31, CD105, CD146 and negative for CD45.

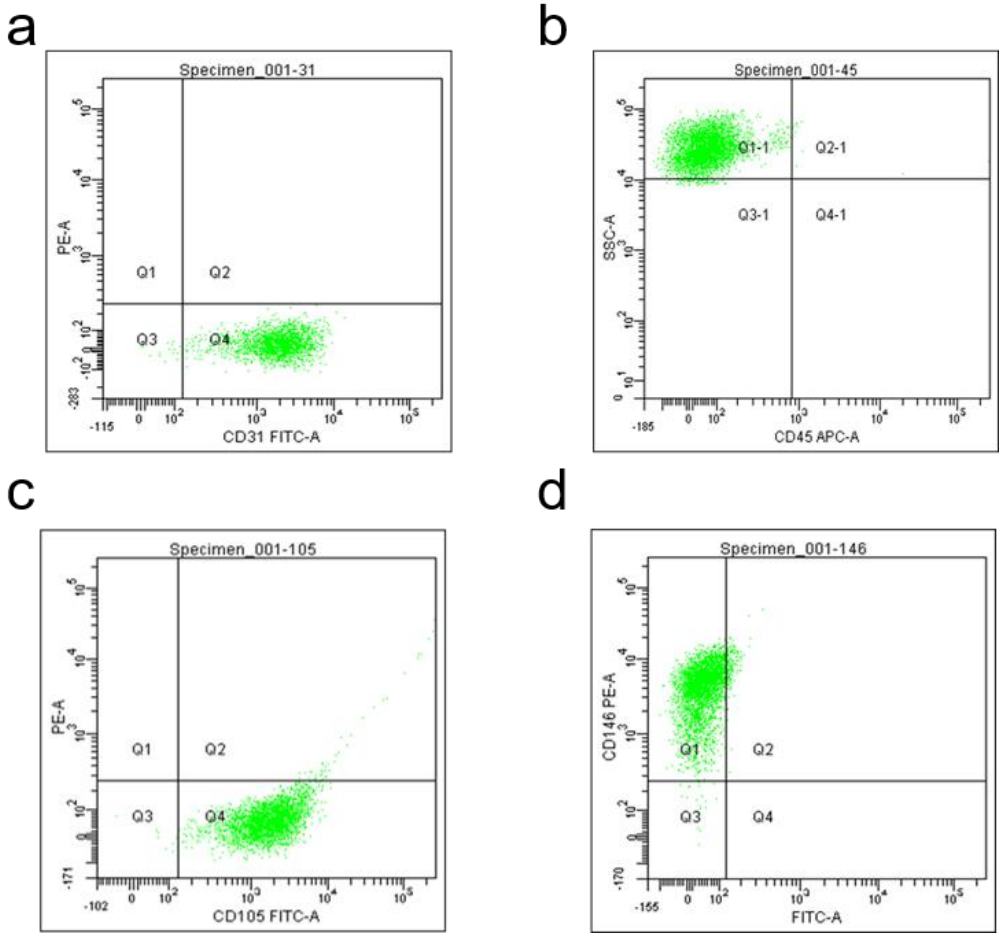

Figure 2.4: Phenotypical characterization of the extracted HUVEC cells to confirm their endothelial lineage. Flow cytometry was performed for the markers CD31 (a), CD45 (b), CD105 (c) and CD156 (d).

After testing, HUVEC cells were cultured in EGM-2 culture medium (Lonza CC-3176) prepared according to the manufacturer's instructions. Only passages 2-4 cells were used for experiments. The angiogenic potential of HUVEC cells was confirmed as previously reported by DeCicco-Skinner [201] by seeding the extracted HUVECs on top of a Matrigel® (Corning, 354248) -filled microdevice at a final density of 20,000 cells/cm^2 (Figure 2.5).

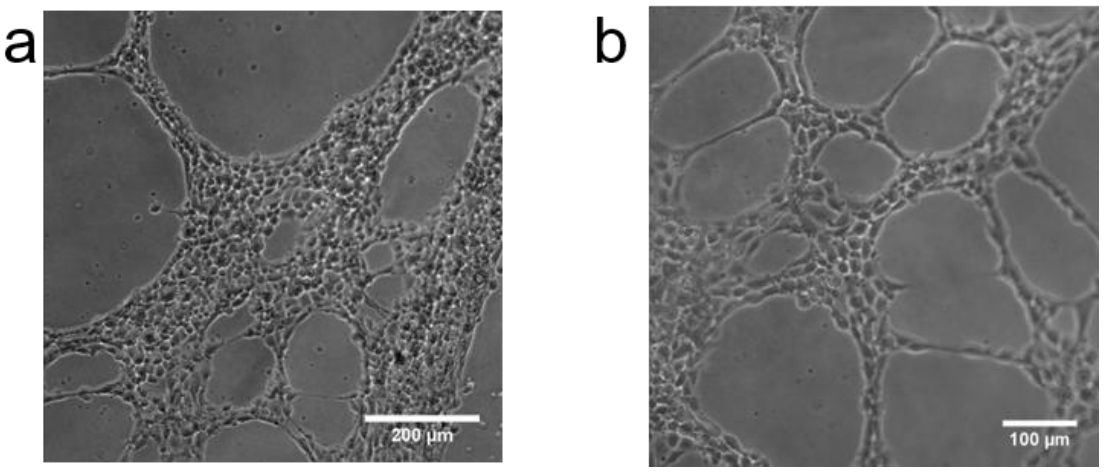

Figure 2.5: Phenotypical characterization of the extracted HUVEC cells to confirm their endothelial lineage. Cells were cultured in Matrigel to check their angiogenic potential through the tube formation assay. Results confirm cells are HUVECs.

2.2.3.2 Cell culture in microdevices.

For 3D cell culture, a 100 µl of hydrogel mixture with a final collagen concentration of 1.2 mg/ml was prepared as before; however, in the last step, the volume was first adjusted to 50 µl by adding sterile distilled water before adding 50 µl of a MDA-MB-231 cell suspension. The resulting cell suspension in hydrogel was carefully homogenized by pipetting up and down several times. Next, the device was filled with the mixture and the hydrogel was polymerized as described above.

To prepare a HUVEC monolayer on top of the collagen in the microwells, HUVEC cells were trypsinized, counted and resuspended in EGM-2. Cells were seeded on top of the microdevice at a final density of 250,000 cells/cm^2 (saturating concentration). Media was refreshed every other day in the microdevice.

2.2.3.3 Cell viability staining.

Microdevices were incubated for 15 min in Calcein AM (Invitrogen ref. C3100MP) and propidium iodide (PI) (Sigma-Aldrich, P4170) in Phosphate Buffered Saline (PBS) (Lonza 17-516F) at final concentrations of 1 µg/ml and 4 µg/ml, respectively, to assess cell viability. Confocal Z-stacks were acquired for each microwell and throughout the entire height of the microwell at 100x magnification.

2.2.3.4 Immunofluorescence staining.

HUVEC cells in the microdevices were washed with PBS and fixed with 3.7% paraformaldehyde overnight at 4ºC. The following steps were performed at room temperature, unless specified otherwise. Cells were permeabilized using 0.1% Triton X-100 (Sigma, T8787) for 5 min and blocked with 1% BSA (Sigma, A1933) for 30 min. Samples were washed twice with 0.05% Tween-20 (Sigma P2287) in PBS between every step.

To quantify endothelium integrity (i.e. the percentage of the microwell surface area covered by HUVEC cells seeded on top of the microdevices), HUVEC cells were stained for VE-cadherin, Actin, and Nuclei. Microdevices were incubated with VE-Cadherin D87F2 XP Rabbit mAb (Cell Signaling 2500S) in 1% BSA, 0.1% Triton X-100 PBS overnight at 4ºC and washed thrice with 0.05% Tween-20 PBS (Sigma-Aldrich ref. P2287). Next, microdevices were incubated with Alexa Fluor 488 Donkey anti-rabbit IgGs (ThermoFischer A-21206), Phalloidin-TRITC for actin staining and Nucblue® Fixed Cell Stain ReadyProbes® for nuclei staining (Life Technologies R37606) for an hour. Finally, microdevices were washed thrice with 0.05% Tween-20 PBS.

2.2.3.5 Hypoxia staining.

The existence of a hypoxic microenvironment within the microdevice was assessed using the hypoxia-sensing dye Image-iT® Hypoxia Reagent (Life Technologies, H10498) and confocal microscopy. This reagent exhibits increased fluorescence upon decrease of the oxygen tension inside the cell. Image-iT® was dissolved in DMSO at a concentration of 1 mM and used according to manufacturer's instructions. Cells were embedded in 1.2 mg/ml collagen hydrogel at three different densities ($0.4x10^6$, $2x10^6$ and 10^7 cells/ml) taking advantage of the independent microwell arrays included in the design. 24 hours after seeding, the hypoxia-sensing dye was added and cell-induced hypoxia gradients within the microwells were imaged for concentrations of $0.4x10^6$ and 10^7 cells/ml.

2.2.3.6 Proliferation staining.

Cell proliferation was characterized in live cells using the Premo Fucci® Cell Cycle Sensor (ThermoFischer P36237), similarly as in our previous work [202]. Briefly, cells were seeded in 3D as previously described, at three different cell densities ($0.4x10^6$, $2x10^6$ and 10^7 cell/ml) in the three independent microwell arrays included in the design. Cells were transfected *in situ* 4 h after seeding, using *ca*. 50 virus particles per cell during 24 h. This cell cycle sensor was transduced into the cells by using two different reporters coupled to TagRFP (red) or emGFP (green), which are expressed alternatively during the G1 phase or the S/G2/M phases, respectively.

2.2.3.7 Live cell membrane staining.

With the aim of distinguishing HUVEC cells from MDA-MB-231 cells when combined in the same microdevice, Vybrant® DiI and DiO were, respectively, used according to the manufacturer's instructions. Briefly, cells were trypsinized from the culture dish and resuspended in relevant media to inactivate Trypsin. Cells were then pelleted and resuspended in serum-free medium to a concentration of 1 million cells/ml. A solution containing 5 µl of Vybrant® stock per ml of media was added to each cell suspension and cells were left to stain for 15 min at 37^0C in the dark. Finally, cells were thoroughly washed with PBS and resuspended in EGM-2 medium for further use.

2.2.4 Preparation of soluble recombinant TRAIL and anchoring to lipid vesicles.

Once the co-culture model was established, we used it to test the two TRAIL-based formulations: human soluble recombinant TRAIL (sTRAIL) and Large Unilamellar Vesicles (LUV) with sTRAIL anchored to their surface (LUV-TRAIL). LUV-type liposomes coated with sTRAIL were prepared as previously described [198,203,204]. The lipid composition consisted in a mixture of phosphatidylcholine, sphingomyelin, cholesterol, and 1,2-dioleoyl-sn-glycero-3-[[N-(5-amino-1-carboxypentyl)-iminodiacetic acid] succinyl](nickel salt) (Avanti Polar Lipids) in a 55:30:10:5 weight ratio to mimic the human exosome lipid composition. sTRAIL corresponding to amino acids 95–281 cloned into the pET-28c plasmid (Novagen - kindly provided by Dr. M.

MacFarlane)[183] with a 6 histidine tag was attached to the liposome surface as previously described [205]. Generated LUV-TRAIL was characterized as described elsewhere [203] and stored at 4^0C until use.

2.2.5 Drug diffusion assays.

To assess the penetration rate across the endothelium and through the hydrogel for the different compounds, the microdevices were prepared as described in previous sections and filled with collagen as described in sections 2.1 and 2.2. Microdevices were covered with a 4 mg/ml TRITC-LUVs or 30 µM TRITC 70 kDa Dextran solution, and Z-stack confocal images were taken for at least 2 h throughout the entire microwell height.

2.2.6 Imaging.

Phase contrast and fluorescence microscopy images were taken using a Nikon Eclipse Ti® inverted fluorescence microscope equipped with a C1 modular confocal microscope system. To acquire whole microwell images, 250-µm thick confocal stacks were performed, by taking images every 10 µm. Finally, a thermostated chamber within the microscope was equilibrated to 37 ^{0}C and 5% CO_2 whenever live cell imaging was performed.

2.2.7 Image analysis and processing.

Image analysis was performed using Fiji® (http://fiji.sc/Fiji). To analyze cell viability, viable and dead cells were counted manually, whereas cell distribution and marker expression were quantified as the percentage of the microwell area where the marker is being expressed. Finally, cell circularity was assessed manually for at least 20 cells in each sample.

2.2.8 Statistical analysis.

Results are presented as the mean ± standard error. The normal distribution was tested by the Kolmogorov-Smirnov test. ANOVA tests were performed for multiple comparisons, followed by post-hoc Bonferroni tests. Data were analyzed using statistical significance set at $p < 0.05$.

2.3 Results and discussion.

2.3.1 Hydrophilic features and liquid handling within the microdevice.

SU-8 was selected as building material due to its previously reported biocompatibility in cell culture applications [175,206], as well as some additional intrinsic advantages over native PDMS (Polydimethylsiloxane) for the fabrication of cell culture systems, including broader chamber design possibilities [207], convenient mechanical properties [208], monolithic integration with a variety of sensors and, importantly in our case, low gas permeability [209], which facilitates the creation of an oxygen gradient without any need for external systems. SU-8 therefore provides a high degree of control over the fabricated structures and capillary valves as included here. Once the microdevices were fabricated (Figure 2.6), they were treated with O_2 plasma to promote spontaneous filling of the devices.

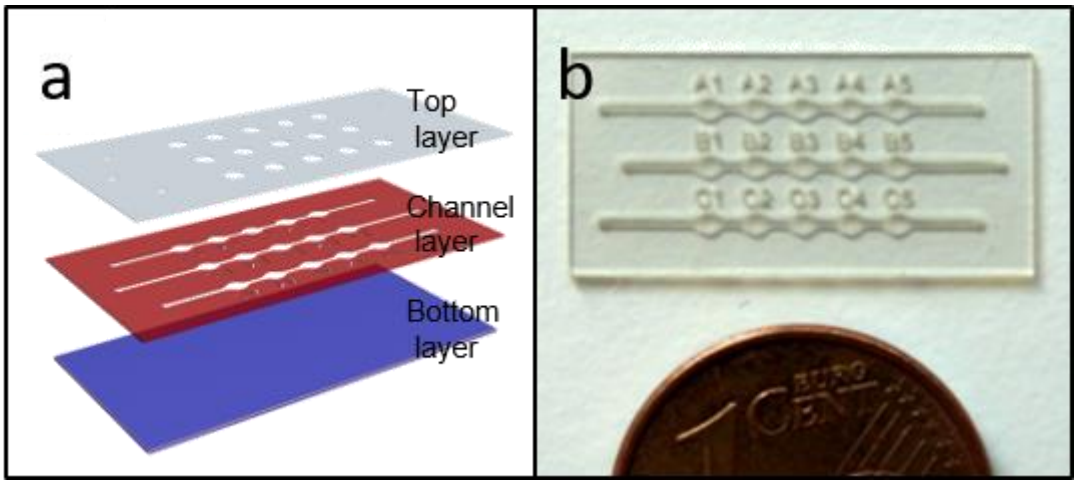

Figure 2.6: Fabricated SU-8 microdevice. a- Schematic representation of an open device, showing the different SU-8 layers: the bottom layer (blue) the channel layer (red), including the channels and microwells and a top layer (grey) with microwell structures to yield open microwells and closed microchannels; b – Photography of a final microdevice.

Because of this treatment, the contact angle was reduced from 82.6 ± 1.6º to 21.1 ± 2.3º (N=10, Figure 2.7), and spontaneous hydrogel introduction was observed in the microwell arrays (Figure 2.8, left panels).

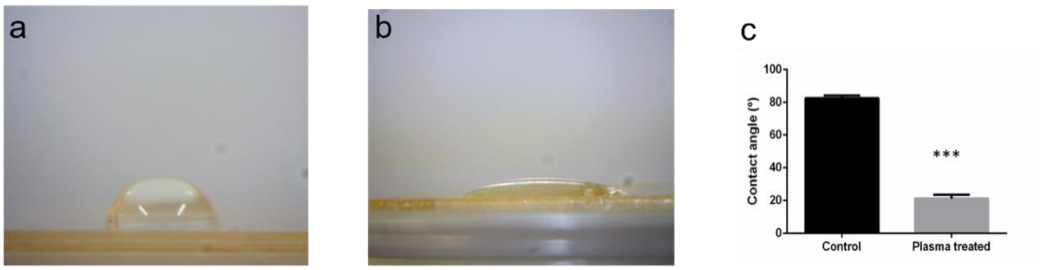

Figure 2.7: Contact angle measurements for the SU-8 material without (a) and after (b) O2 plasma treatment. Measurements were performed at least 6 independent times for each condition. P-value was 0.0007. Graph shows average ± SEM.

This behavior was also expected according to the microdevice design. Besides, spontaneous microdevice filling occurred in a few seconds (Figure 2.8, right panels), ensuring thereby the hydrogel filled completely the microdevice before collagen polymerization would occur. Interestingly, in absence of plasma treatment, capillary forces were not strong enough to fill the microdevice completely, and hydrogel injection was extremely slow. Consequently, the hydrogel remained pinned in the microchannels connecting the microwells without filling the entire microdevice (Figure 2.8, right panels).

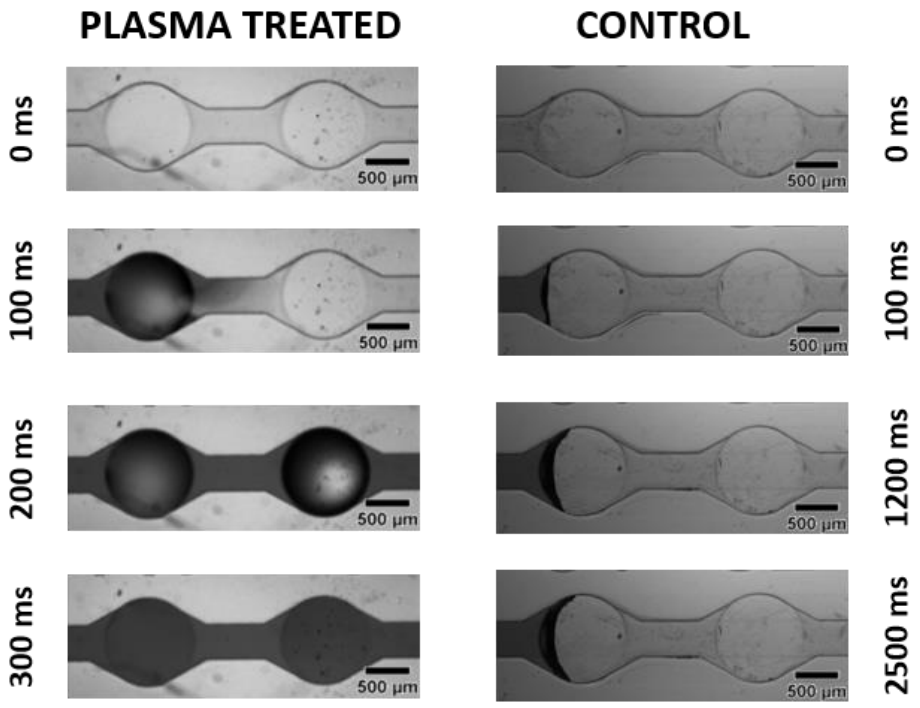

Figure 2.8: Effect of the plasma treatment on the microdevice spontaneous filling. Left- Bright field 20x images showing the filling dynamics of a microdevice after plasma treatment at 0, 100, 200 and 300 ms, respectively; Right- Bright field 20x images showing the filling dynamics of a microdevice without any plasma treatment at 0, 100, 1200 and 2500 ms, respectively.

2.3.2 Air-hydrogel interface analysis and optimization in the microdevice.

Next, we characterized the air-hydrogel interface in the microdevice after collagen polymerization to ensure a flat interface was created, which is essential for cell imaging. To that end, the microdevice was filled with collagen supplemented with FluoSpheres® and the interface was characterized both immediately after filling the microdevice and after collagen polymerization.

The interface was flat immediately after collagen perfusion (Figure 2.9.a), showing homogeneous distribution of the FluoSpheres® in the hydrogel. However, after polymerization a 200 µm-deep meniscus appeared, causing the Fluosphere® microbeads to cluster in the center at the interface (Figure 2.9.b). We assumed this meniscus was created due to water evaporation during the polymerization process at 37^{o}C within the incubator. Therefore, to avoid the formation of such meniscus, we placed a hydrogel droplet at the device inlet (Figure 2.9.c) to counteract evaporation. As presented in Figure 2.2, the pressure exerted by the droplet was enough to maintain a flat air-liquid interface during the whole hydrogel polymerization process, by preventing any evaporation of the solution.

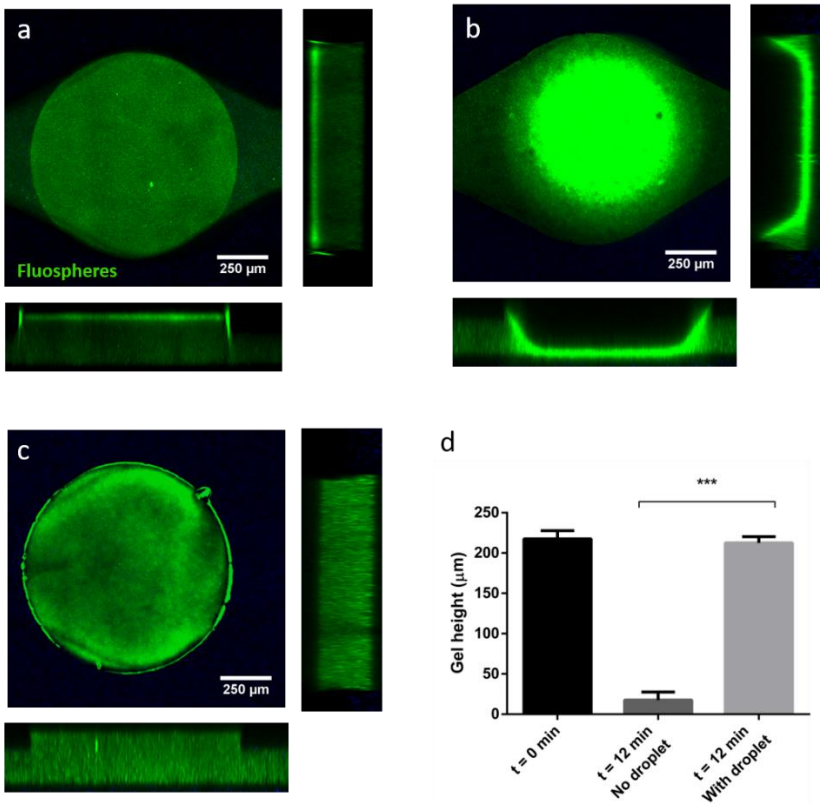

Figure 2.9: Characterization of the hydrogel-air interface in the microdevice using confocal microscopy. 100x images flanked by z-stack orthogonal views of the gel interface at 0 minutes after hydrogel introduction (a) and 12 minutes after the introduction of the hydrogel, with (b) or without addition of a droplet of water added (c). Water evaporation caused a dramatic contraction of the hydrogel (c) and FluoSpheres® accumulation at the interface, which forms a deep meniscus in the well. c- Hydrogel polymerized with an additional hydrogel droplet placed on the main inlet during 12 min. No meniscus was observed and the hydrogel-air interface was flat as desired. d – Quantification of the hydrogel height in the microwells just after introduction of the hydrogel (t = 0 min) and 12 minutes later, after gel polymerization, when no droplet was added on the inlet (t=12 min. No droplet) and when a droplet was added on the inlet (t=12 min with droplet). Graph shows Average ± SEM. (p-value < 0.001).

2.3.3 Microdevice biocompatibility and characterization of the 3D cell culture microenvironment.

As a next step, cell viability was examined in 3D culture in the collagen to confirm the device biocompatibility. Therefore, we seeded MDA-MB-231 breast tumor cells at a final density of $5x10^6$ cells/ml in a 1.2 mg/ml collagen hydrogel. After three days in culture, cell viability was assessed with calcein AM (green) and propidium iodide (red). Through this method, live cells were stained in green, whereas dead cells were stained in red. Cell viability inside the microdevice was similar to that observed for control hydrogels also loaded with the same number of cells but cultured on a Petri dish (Figures 2.10 a-c), and in both cases a cell viability higher than 98% was observed. Additionally, we evaluated the three-dimensional cell distribution along the microwell height. Typically, cells would occupy between 15 and 30% of the surface area of the microwell in each 10 µm-thick layer imaged by confocal microscopy, and no significant difference was observed throughout the whole well height (Figure 2.10.d). Altogether, there was no significant accumulation of cells at a specific height in the collagen in the microwells, and no sedimentation of the cells at the bottom of the microwells.

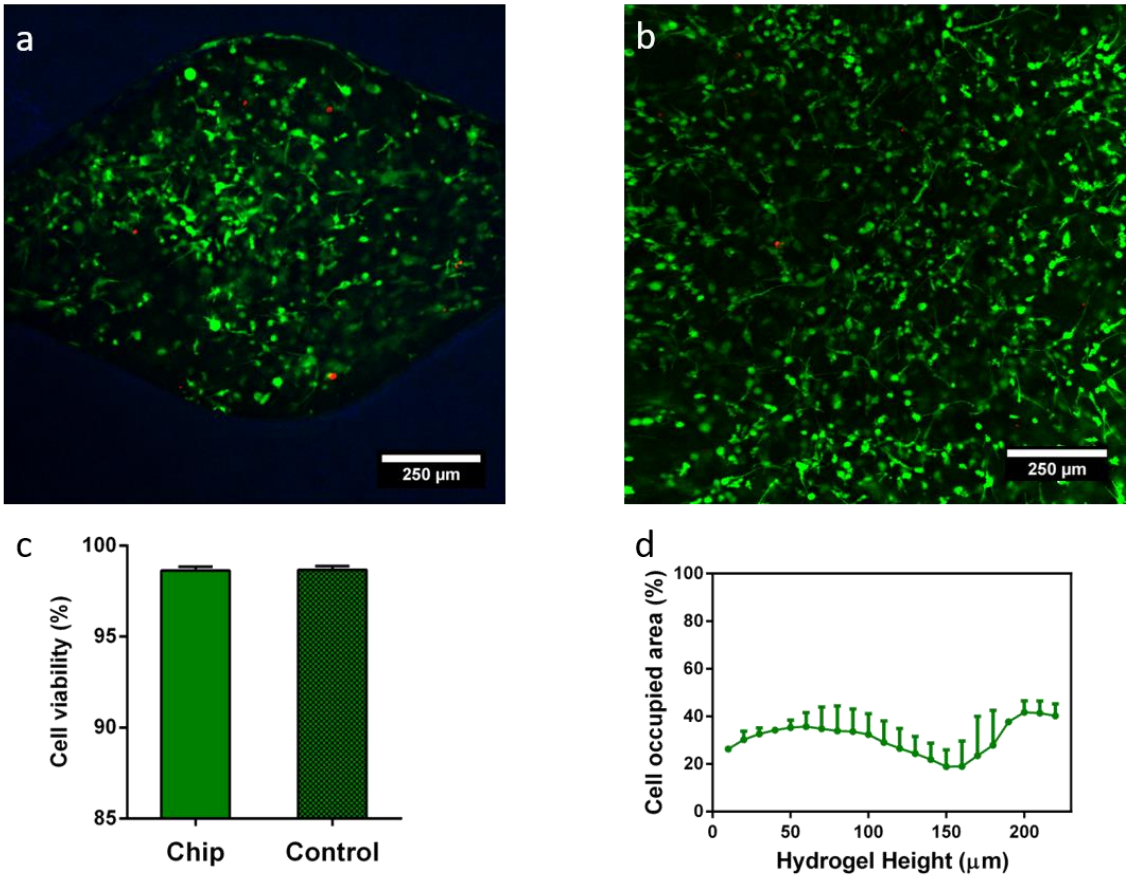

Figure 2.10: Viability of the MDA-MB231 cells grown in the microdevice in a 3D hydrogel matrix. Viable cells were stained with Calcein AM (green), whereas dead ones were labelled with propidium iodide (red). a- 100x confocal image showing the cell viability in one microwell in the device. b- 100x confocal image of the same cells grown in 2D on a Petri dish (control). c- Quantification of the MDA-MB-231 cell viability within the microdevice and in Petri dishes. d- Quantification of the cell occupied area as a function of the hydrogel depth. 0 µm refers to the top of the microwell.

Furthermore, we characterized the tumor cell behavior and function within the microwells. Firstly, we investigated cell proliferation for different cell seeding densities ($0.4x10^6$, $2x10^6$ and 10^7 cells/ml) using Premo® FUCCI Cell Cycle Indicator, which stains G0/G1 phase cells in red and S, G2 and M phase cells in green. MDA-MB-231 tumor cells embedded in the collagen gel were transfected with this proliferation marker within each independent array of microwells in a sole microdevice (Figure 2.11 a-c), and the proliferation index of cells was determined as the number of cells in G2/M/S divided by the total number of seeded cells. Results revealed that the proliferation index significantly diminished for higher cell concentrations (Figure 2.11 c). Specifically, a 5-fold cell concentration increase (from $0.4x10^6$ to $2x10^6$ cells/ml) was accompanied by a reduction in proliferation to 53.3%, and a 4-fold increase in concentration by a 28.7% decrease in proliferation.

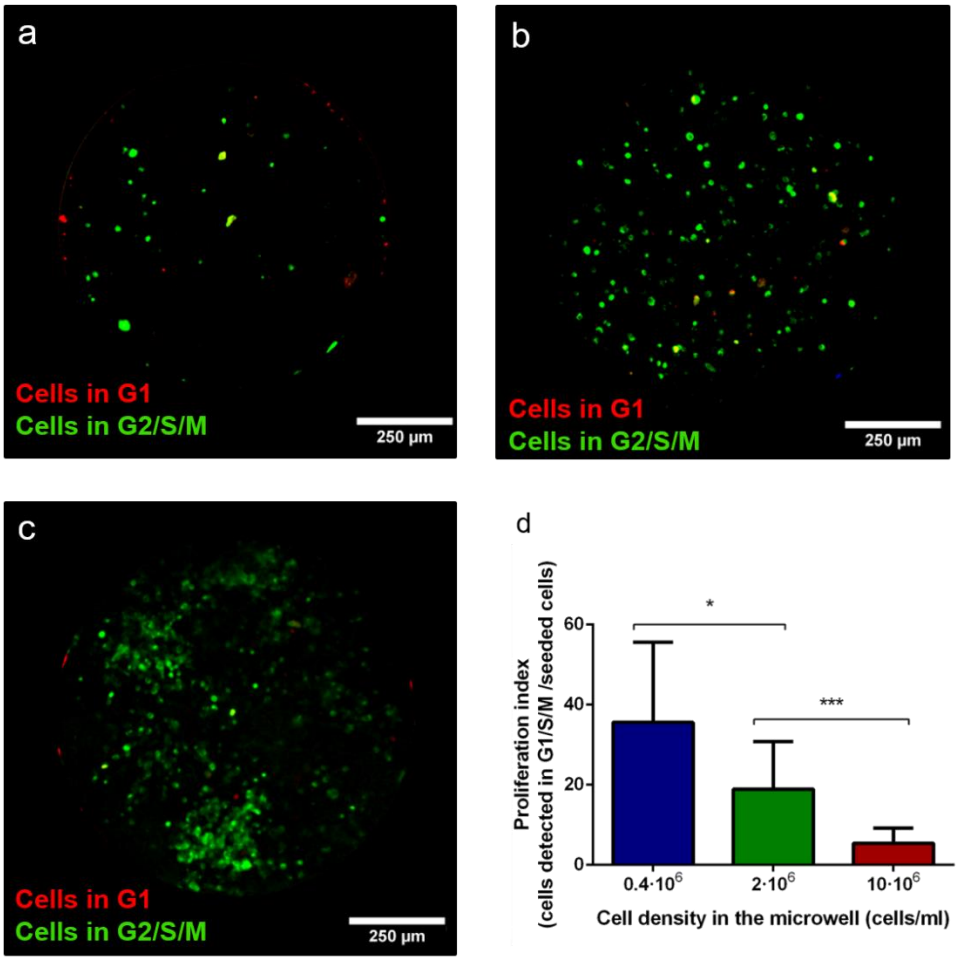

Figure 2.11: Whole microwell images of cell proliferation through Premo FUCCI® transfection for different cell densities $0.4 \cdot 10^6$ (a), $2 \cdot 10^6$ (b) and 10^7 cells/ml (c). Green cells are in the G2/S/M phases, whereas red cells are arrested in the G1 phase (non-proliferating cells). (d) Proliferation index of cells cultured in the hydrogel in the microdevice, calculated by normalizing the number of cells in G2/S/M (as characterized by Premo FUCCI transfection in situ) with the total number of seeded cells. Graph shows average ± SEM (p-value < 0.0001).

Proliferation differences can be accounted for variations in nutrient and oxygen availability. To test this hypothesis –*i.e.*, if there was a significant change in oxygen concentration depending on the cell concentration, we checked for the presence of hypoxia within the microwells. For this experiment, we compared microwells prepared with either high or low cell concentrations in collagen hydrogels. The graph presenting these results in Figure 2.12 indicates significantly different hypoxia profiles for the two cell densities tested here (0.4×10^6 and 2×10^7 cells/ml).

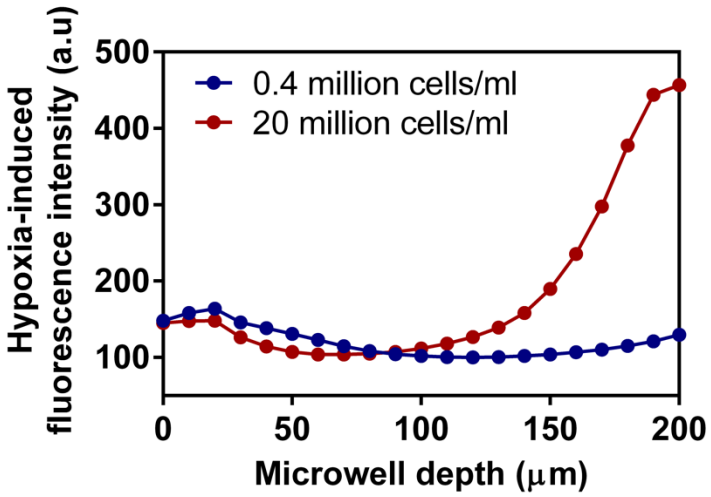

Figure 2.12: Characterization of the hypoxia level in the device for different cell densities (0.4·106, and 2x107 cells/ml) using Hypoxia-IT®. Graph shows average ± SEM.

For a low cell concentration ($0.4x10^6$ cells/ml), a low and constant fluorescence level was found throughout the entire height of the microwell after 24 h, indicating a low hypoxia level. In contrast, a gradient in oxygen concentration was observed for the high cell concentration (10^7 cells/ml) with marked hypoxia at the bottom of the well after 24 h of culture under the same conditions (Figure 2.12). Altogether, culture of cells in the hydrogel in the microwells beyond a certain cell concentration threshold resulted in the appearance of deprived oxygen conditions, which could explain the marked decrease we recorded in terms of cell proliferation, as initially hypothesized. Furthermore, with our model we are able to mimic the typical architecture found in tumor tissues *in vivo*, which typically contain a hypoxic non-proliferating core and a proliferative periphery with direct access to oxygen [80]. This structure is particularly relevant to assess the efficiency of drugs, since some drugs are more effective on proliferating cells and not active under hypoxic conditions, while others are specifically activated in an oxygen-poor environment [82].

2.3.4 Characterization of the endothelial barrier model.

The second main component of the co-culture is the endothelium layer on top of the 3D culture in each microwell. The endothelium was created by seeding HUVEC cells at a density of 250,000 cells/cm^2 on microwells in a microdevice previously filled with 1.2 mg/ml type I collagen, and letting them attach for 24 h, to create a confluent monolayer to mimic an endothelium. The endothelium integrity was characterized by

immunostaining for F-Actin, VE-cadherin and Nuclei. These markers allowed us not only to assess the percentage of the microwell surface area that was covered with cells (F-actin), but also to demonstrate the existence of cell-cell adhesions (VE-cadherin), confirming the endothelium is not leaky.

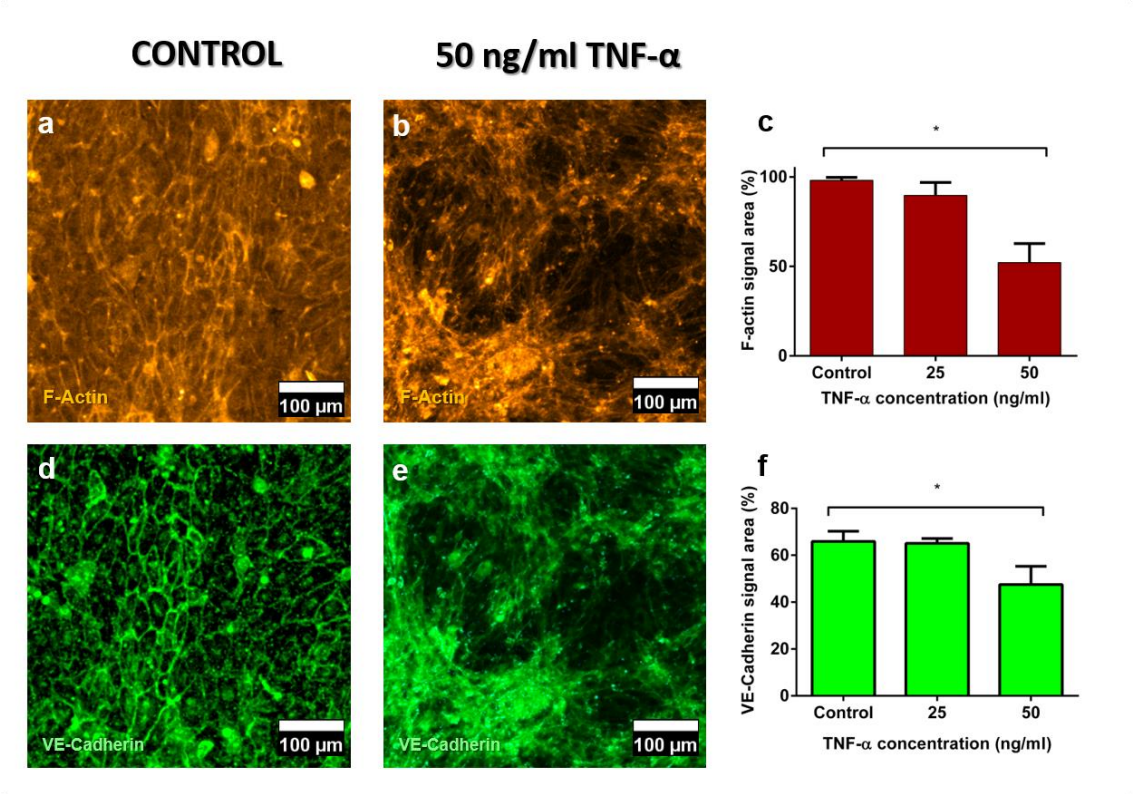

Figure 2.13: Characterization of the endothelium generated on the top of the hydrogel matric in the microdevice. Endothelial cells (HUVECs) were labelled with Phalloidin-TRITC (yellow) for actin staining and VE-Cadherin (green) for endothelial cell junction staining. a and d- Control endothelium; b and e – Endothelium treated with 50 ng/ml TNF-α for 24 hours c- Quantification of the endothelium integrity in terms of Phalloidin signal area for all samples (not treated, and treated with 25 and 50 ng/ml TNF-α). Samples were compared with the control. P-value: 0.02. f- Quantification of endothelium integrity in terms of VE-cadherin signal area for all samples (not treated, and treated with 25 and 50 ng/ml TNF-α). Samples were compared with the control. P-value for 50ng/ml TNF-α = 0.005. Graphs show average ± SEM and magnification is 200x for all images.

As presented in Figure 2.13, the hydrogel surface in the microwells was totally covered by the HUVEC cells, which had established cell-cell contacts across the complete area of the microwell (Figure 2.14). Besides, no apparent gap was visible between the cells, indicating the formation of a tight endothelium after 24 h of culture.

The endothelium integrity was further quantified by comparing the surface area occupied by cells (derived from the F-actin or VE-cadherin fluorescence signal) with the

total surface area of a microwell (Figures 2.13.c and 2.13.f, respectively). These measurements indicate that a tight endothelium was successfully created with this procedure.

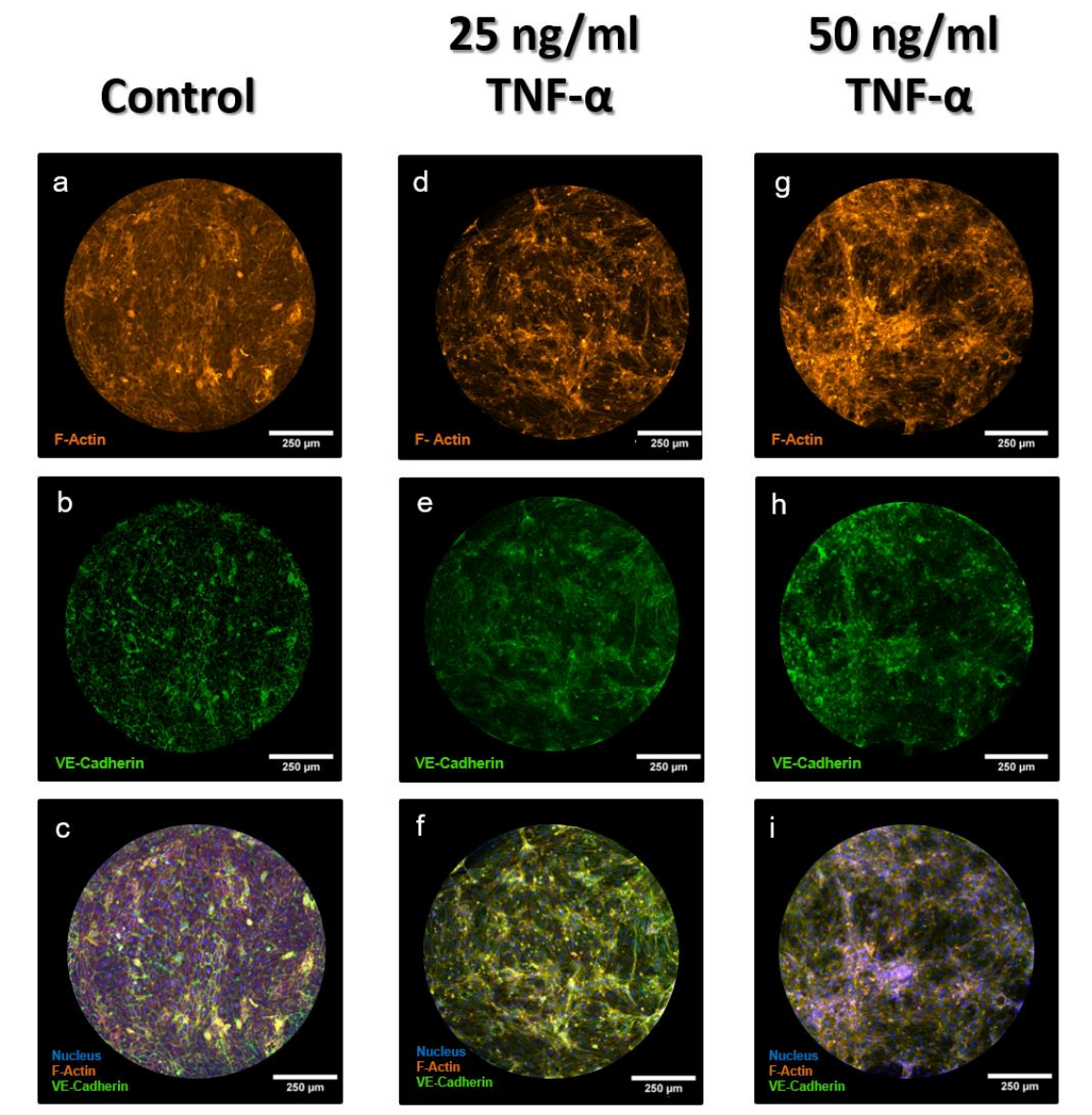

Figure 2.14: Whole microwell immunofluorescence images to verify the endothelium integrity. Images show F-actin, VE-cadherin and Merge (F-actin, VE-cadherin and DAPI) for Control conditions (a, b and c, respectively); cells supplemented with 25 ng/ml of TNF-α (d, e and f, respectively) and cells supplemented with 50 ng/ml of TNF-α (g, h and i, respectively).

We next evaluated the functionality of the endothelium model by treating it with pro-inflammatory factors such as TNF-α. TNF-α has been reported to increase endothelium permeability at concentrations of 25 and 50 ng/ml [210]. As expected, after 24 h

exposure to TNF-α, we observed the creation of gaps in the HUVEC monolayer (Figures 2.14.b & 2.14.e), and a quantitative decrease in the area occupied by cells (Figures 2.14.c & 2.14.f), as assessed for both VE-cadherin and F-actin staining, and this decrease was found statistically significant for a TNF-α concentration of 50 ng/ml. This assay confirms that the 2D endothelium model is entirely functional and responsive to inflammation, as previously described in the literature.

2.3.5 Co-culture model with a 2D endothelium and MDA-MB-231 breast tumor cells cultured in 3D in a collagen matrix.

After establishment and characterization of both the 3D tumor cell culture and 2D endothelium, both elements were combined in the same microdevice.

First, the respective HUVEC and MDA-MB-231 cell distributions were investigated by imaging after cell membrane staining with two different Vybrant® cell trackers: MDA-MB-231 cells were labelled in green, and HUVEC cells in red (Figure 2.15.a).

As observed in separate mono-culture conditions, a flat endothelium was created on the top of each microwell, with a homogeneous three-dimensional distribution of the tumor cancer cells in the collagen matrix under the endothelium layer. Up to 24 h after cell seeding, the endothelium was found to be integer and tight (Figure 2.15 b-c), but as time passed, changes in the endothelium appearance and integrity were detected.
Specifically, after 48 h of co-culture, the shape of the endothelial cells evolved compared to control conditions in the absence of tumor cells in the collagen, moving from a polyhedral shape towards a spindled one (Figures 2.15 e & 2.17 a). The HUVEC cell circularity was further quantified in control conditions (mono-culture, 48 h) and after 24 h and 48 h of co-culture with the 3D tumor model (Figure 2.17 a), revealing a 4% decrease in cell circularity between the control and co-culture after 24 hours (from 0.78 to 0.76). Moreover, the cell circularity decreased by 15% at 48 hours of co-culture compared to the control (from 0.78 to 0.68). Next to this, the cell-cell connections in the endothelium disappeared, as indicated by a loss in the characteristic VE-cadherin distribution for blood vessels. The integrity of the endothelium was quantified as before, revealing a significant decrease by 52% compared to control conditions. (Figure 2.17 b).

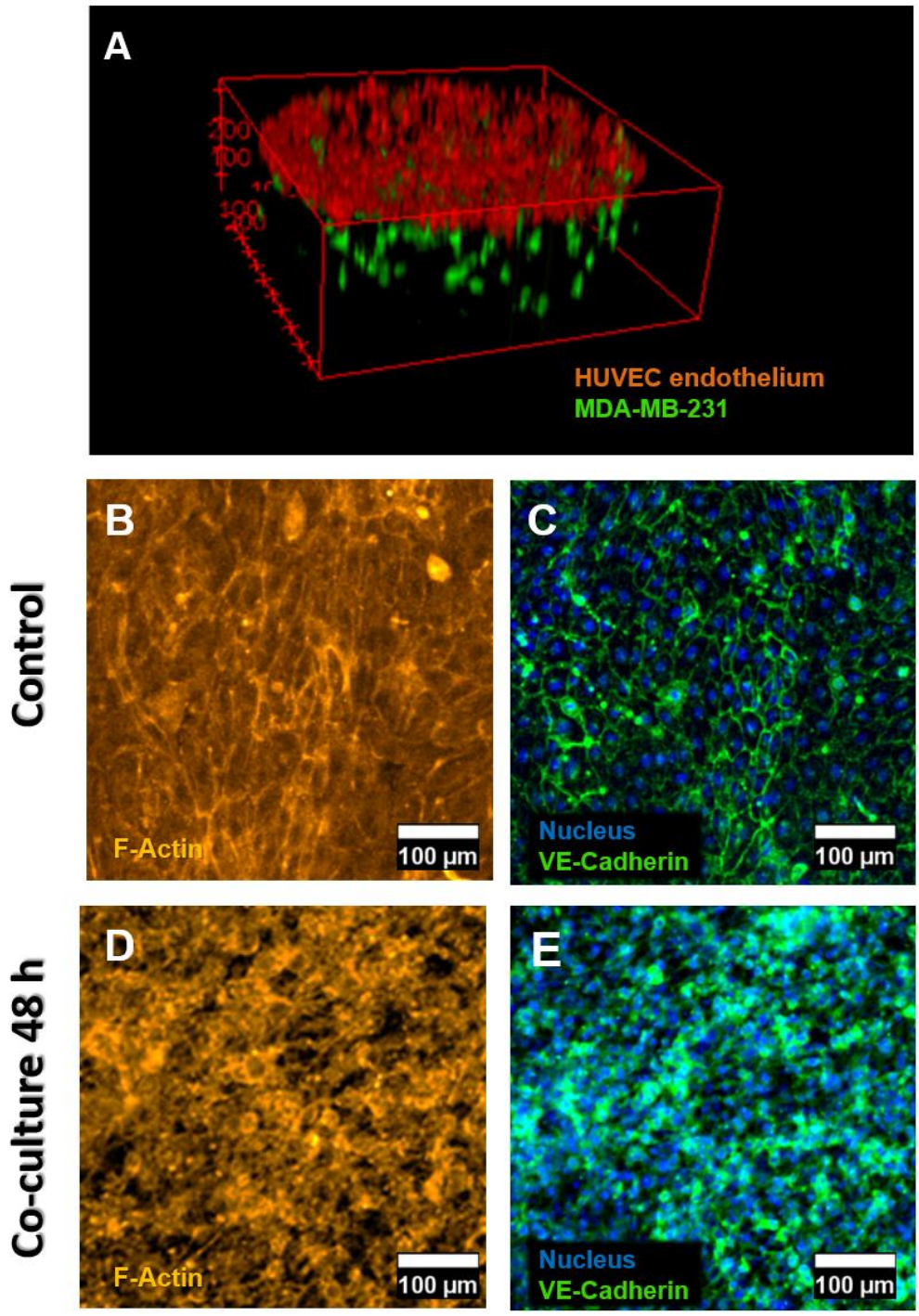

Figure 2.15: Co-culture of MDA-MB231 tumor cells with HUVECs cells. a- 3D reconstruction of the 2D-3D co-culture model within the microdevice after 24 hours of seeding, tumor cells being grown in the 3D hydrogel matrix and HUVECs as a monolayer on top of the hydrogel in the microwells. b-g- Assessment of the integrity of the endothelium monolayer in the co-culture system, compared to control conditions (endothelium mono-culture). b- Actin staining of a control HUVEC endothelium (mono-culture). c- Detail of a control HUVEC endothelium (mono-culture) stained with VE-Cadherin and NucBlue®. d-Actin staining of a HUVEC endothelium in co-culture with MDA-MB-231 tumor cells, 48 hours after cell seeding. e-Detail of a HUVEC endothelium in co-culture with MDA-MB-231 tumor cells, 48 hours after seeding, stained with VE-Cadherin and NucBlue®. Magnification is 200x for all images.

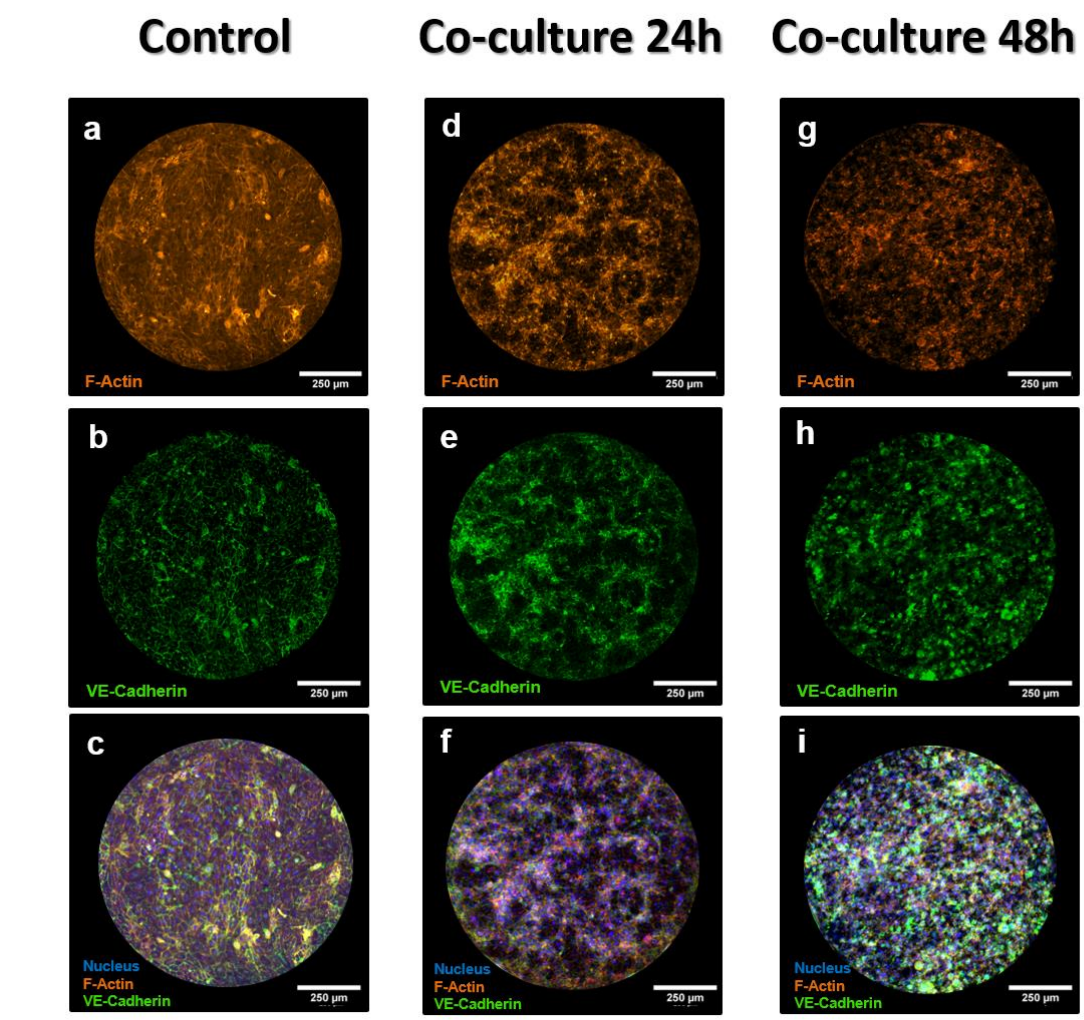

Figure 2.16: Whole microwell immunofluorescence images to assess endothelium integrity. Images show F-actin, VE-cadherin and Merge (F-actin, VE-cadherin and DAPI) for Control conditions (a, b and c, respectively); cells in co-culture with MDA-MB-231 cells for 24 hours (d, e and f, respectively) and cells in co-culture for 48 hours (g, h and i, respectively).

Importantly, this decrease in F-actin signal is very similar to that observed for a monoculture endothelium treated with 50 ng/ml of TNF-α for 24 h (Figure 2.13 c). These results altogether demonstrate that co-culture of an endothelium with MDA-MB-231 breast tumor cells resulted in the creation of a leaky vasculature, as observed *in vivo* in tumor-associated vessels, which should also present an EPR effect [30,177,211].

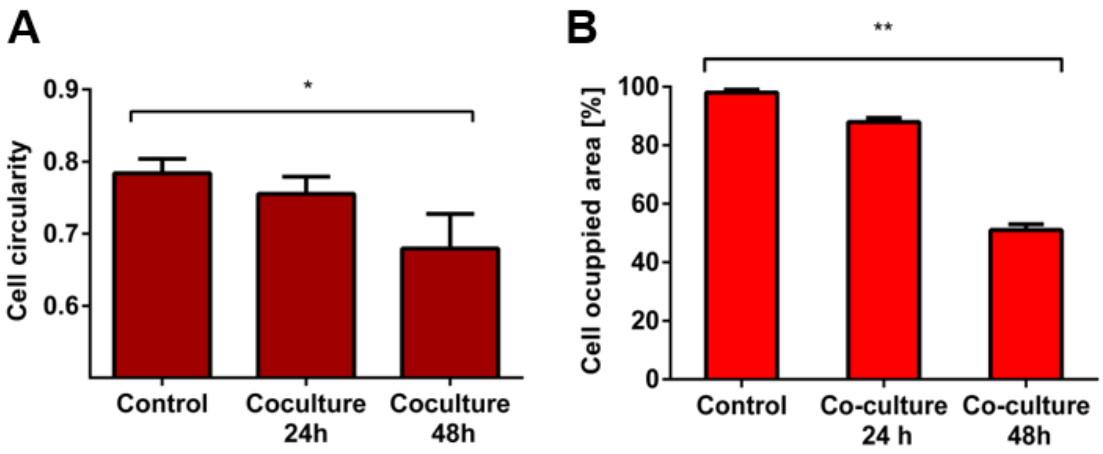

Figure 2.17: Quantification of the effect of co-culture of MDA-MB231 tumor cells with HUVECs cells. a-Assessment of the HUVEC cell circularity for control (mono-culture) and co-culture conditions after 24 and 48 hours (p-value < 0.0001). b-Assessment of the integrity of the HUVEC endothelium for the co-culture after 24 and 48 hours compared to control conditions (mono-culture of a HUVEC monolayer) quantified as F-actin signal area (p-value = 0.0016). Graphs show average ± SEM.

2.3.6 Drug screening in the tumor-endothelium model.

Since the proposed co-culture tumor cells-endothelium model exhibited this key-characteristic of leaky endothelium, we decided to apply it for drug penetration assays and evaluating the EPR effect, which is particularly interesting for nanoparticle-based medicines. For this drug assay, we chose the death ligand TRAIL (TNF-related apoptosis inducing ligand), which was tested in its soluble form (60 kDa) and as a conjugate with a large unilamellar vesicle (LUV) [212]. Both forms were tested at a concentration of 0.33 ng/ml for 24 h in our co-culture model to evaluate their efficiency.

As a first step, the toxicity of both drug formulations was assessed on the endothelium alone. The drug effect on the endothelium was quantified as previously described in terms of changes in the endothelium integrity.

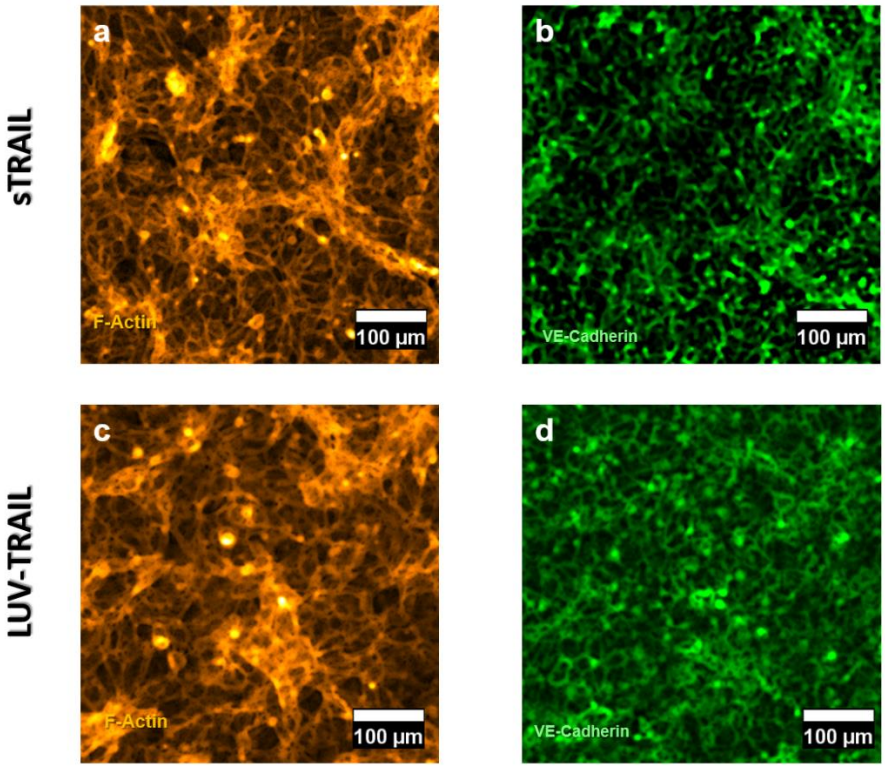

Figure 2.18: Drug testing assay using TRAIL in both its soluble form (sTRAIL, 0.33 ng/ml) and anchored to a LUV (LUV-TRAIL, 0.33 ng/ml) in the co-culture established models. Endothelium immunofluorescence after exposure to sTRAIL (a, b) and LUV-TRAIL (c, d) for Phalloidin-TRITC (yellow) and VE-Cadherin (green), respectively.

No significant decrease in the cell occupied area was observed after treatment with both sTRAIL and LUV-TRAIL (Figures 2.18 a-d) using F-actin and VE-cadherin staining, compared to control monolayers (Figure 2.19). Nonetheless, a noticeable change in the fluorescence signal pattern was found, particularly in the case of F-actin expression (Figures 2.18 a & c).

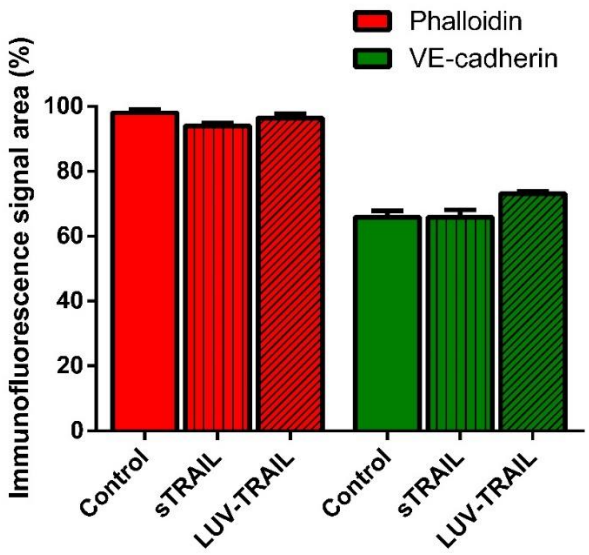

Figure 2.19: Quantification of the endothelium integrity using the Phalloidin (red) and the VE-cadherin (green) signal area for control conditions (no TRAIL exposure) and samples treated with both sTRAIL and LUV-TRAIL. No significant differentes were found. Graph shows average ± SEM.

Particularly, F-Actin and VE-cadherin local accumulation and alignment in certain areas of the microwell was observed, which is significantly different from the patterns obtained in control microwells. This is consistent with angiogenic and mitogenic events, as previously described in endothelial cells after TRAIL treatment [213].

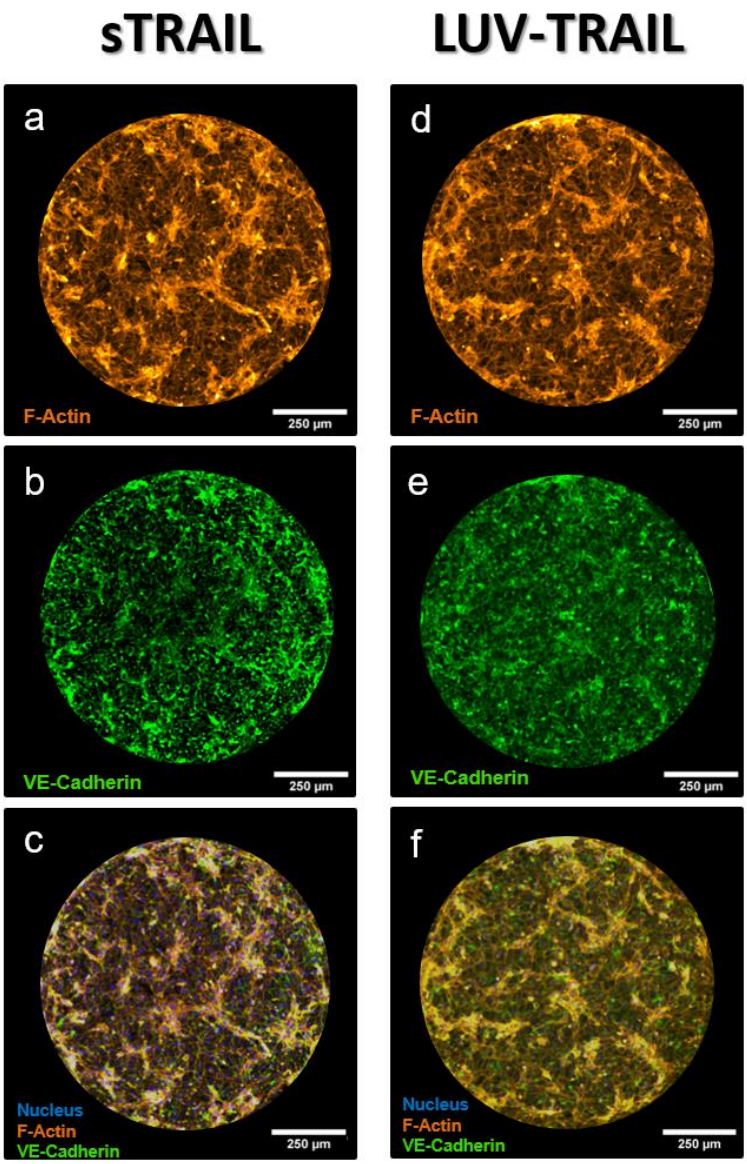

Figure 2.20: Whole microwell immunofluorescence images to verify the endothelium integrity after exposure to the TRAIL drug. Images show F-actin, VE-cadherin and Merge (F-actin, VE-cadherin and DAPI) for sTRAIL (a, b and c, respectively) and LUV-TRAIL (d, e and f, respectively). Images were taken after 24 hours of treatment. Concentration for both drugs was 0.33 ng/ml.

Before testing both drug formulations on the co-culture models, we assessed their penetration in the microwells using fluorescent surrogates such as a dextran with a comparable size to sTRAIL (70 kDa) and a rhodamine-conjugated LUV as a model for LUV-TRAIL. As expected, the penetration rate was much lower in the case of the LUV, after both 15 min and 2 h, which is to be accounted for by the larger size of this LUV-based formulation. Nonetheless, both formulations can entirely penetrate across a healthy endothelium after 2 hours (Figure 2.21), despite their size difference.

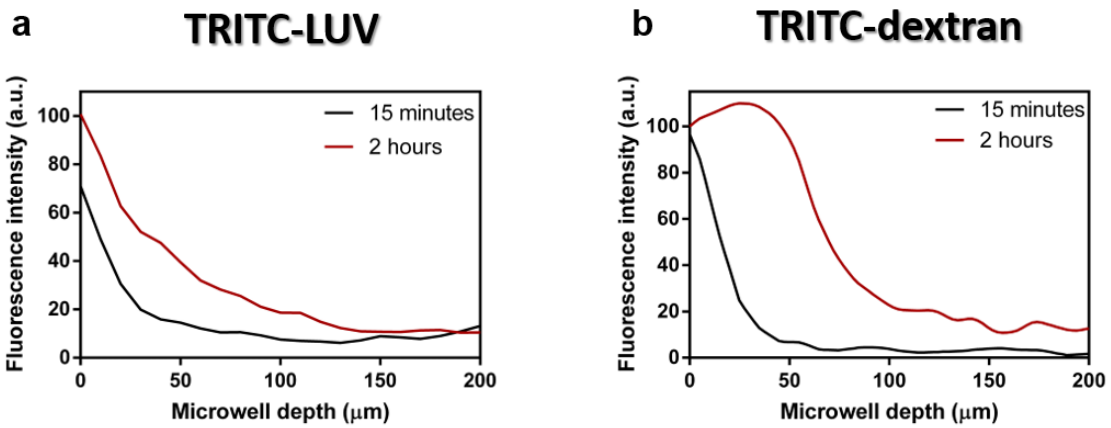

Figure 2.21: Diffusion/penetration assays using TRITC-labelled LUV (0.33 ng/ml) and TRITC-Dextran (70 kDa, 30 μM) used as models for the LUV-TRAIL and s-TRAIL, respectively, across an endothelium seeded on a collagen gel.

No accumulation of the model drugs at a specific height in the microwell height was observed after two hours, which suggests the formulations should be able to penetrate up to the bottom of the microwell with sufficient duration of the assay.

Finally, the two drugs were tested on the established co-culture model combining a HUVEC endothelium and a 3D tumor cell culture. Cell viability was evaluated as before in the collagen matrix using Calcein AM and PI. After treatment of the co-culture with TRAIL for 24 hours at 0.33 ng/ml, viability staining revealed that both drugs induced cell death throughout the entire microwell, with an expected decay in cytotoxicity when going deeper in the microwell (Figure 2.22).

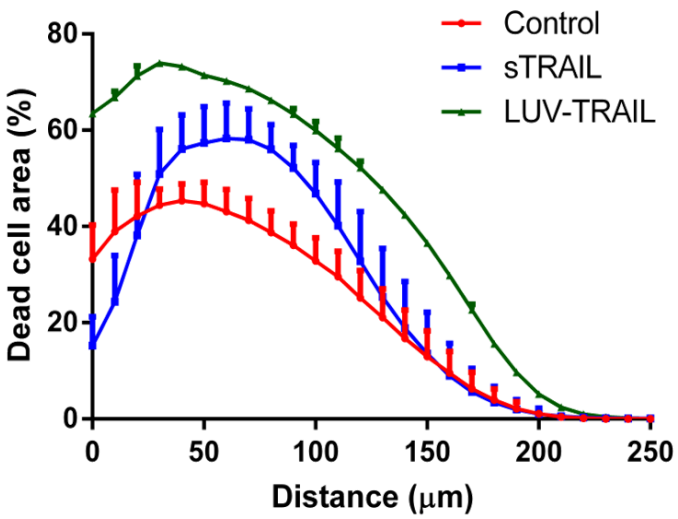

Figure 2.22: Quantification of MDA-MB-231 tumor cell death in 3D along the device microwell depth in control conditions, and with sTRAIL and LUV-TRAIL treatment in the established microfluidic co-culture model. Here, 5 million MDA-MB-231 cells/ml were seeded in the hydrogel matrix. Graphs show average ± SEM.

Specifically, despite having a lower penetration rate, LUV-TRAIL induced death in a higher number of cells relative to the total cell number (65% higher for the whole microwell), which confirms LUV-TRAIL is more active than TRAIL.

Interestingly, the lower part of the 3D tumor cell culture, where hypoxia was found to be more pronounced, also correlated well with lower drug efficiency. This could be due to either a lower penetration rate of LUV-TRAIL in this area or to a lower efficiency of the drug in hypoxic areas. Higher resistance to TRAIL in hypoxic microenvironments has indeed been previously described [52].

Overall, we have demonstrated that the simple and user-friendly configuration of this microdevice allows reproducing key features of tumors, which should be accounted for in drug tests.

2.3.7 Adaptation of the design for mass-production of the microdevice.

Despite SU-8 being an ideally suited option for the development of prototypes, the implementation of the described design requires mass-production above the possibilities of this material. Therefore, SU-8 was replaced as building material by cyclic olefin polymers (COP), a sort of polymers that is highly used for cell culture platforms.

COP has been described in the literature as highly biocompatible [214], has excellent optical properties and maintains a low oxygen permeability necessary to develop the model described in this chapter. Therefore, the adapted microdevice was fabricated by means of mold-injection with COP.

Next, the presented microdevice has been adapted to include fluid flow by means of an additional piece, while maintaining the basic features and proportions of the design. Hence, the adapted microdevice is now composed of two different pieces. The first one is a direct adaptation of the SU-8 prototype (Figure 2.23 left) including micropipette adapted ports for an easy liquid handling. These ports also act as reservoirs to ensure correct microdevice filling and meniscus reduction. This piece can be used independently or in combination with a second piece.

The second piece (Figure 2.23 middle) is mounted on top of the first one, and acts as an upper channel for the described structure. This channel is intended for fluid flow integration, but also allows reagent reduction in a substantial manner.

The top piece can be inserted in the bottom one to obtain a new version of the microdevice integrating fluid flow (Figure 2.23 right). The resulting microdevice has been patented and is now commercialized.

Figure 2.23: Image prototypes for the COP microdevice developed from the SU-8 prototype. Left- The bottom piece entails three arrays of microwells connected by a microchannel. Fluidic ports are placed in both ends of the microdevice for an easier liquid handling. Middle- The top piece comprises three microchannels intended for coupling fluid flow on top of the bottom piece microwells, but it can also be used to diminish reagent volumes substantially. Right- The microdevice resulting from integrating both pieces is shown.

2.4 Chapter summary.

In chis chapter, we reported an SU-8 multi-well microfluidic platform to study the interactions between tumor cells grown in 3D in a collagen matrix in microwells and a tumor-associated endothelium grown on top of the collagen matrix, and for drug testing assays. A key-advantage of our device is that it provides easy and precise fluidic control and instantaneous self-filling of the arrays of microwells with viscous hydrogel solutions in one single pipetting step, thanks to the specific geometry of the device with presence of capillary valves and proper surface hydrophilicity. Therefore, our device fulfills the requirements of being easy to operate and accessible to the biomedical community, while still allowing recreating complex microenvironments. So far, our device comprises 3 independent arrays of microwells, but its design and mode of operation lend themselves well to parallelization for medium to high-throughput assays, which makes our platform particularly interesting for drug testing. Furthermore, the platform is fabricated from SU-8, which presents a low permeability to oxygen, which is advantageous for creating hypoxic environments, as found for instance in tumor tissues. Finally, the device is prepared using 90-µm thick substrates, so that it is fully compatible with *in situ* confocal microscopy examination of the cells in the 3D environment, as well as on the top of the microwells.

In this chapter, we developed and thoroughly characterized 3D tumor as well as 2D endothelium models, before their combination within one single device. The 3D tumor model faithfully reproduced key-features found in tumor tissues *in vivo* such as preferential proliferation for cells with access to more oxygen and nutrients, and creation of an oxygen gradient and a hypoxic core with no cellular proliferation, providing a dense tissue initially formed. Both healthy and functional endothelium as well as a leaky endothelium were successfully prepared in our device, and their integrity evaluated using immunofluorescence and confocal microscopy. As such, our device can easily mimic vascular integrity in different physiopathological conditions. Interestingly, our study particularly revealed that co-culture of a 3D tumor model with HUVEC cells grown in 2D resulted in the creation of a leaky endothelium, as found in tumor tissues. Next, the established co-culture was used for drug penetration assay

across the endothelium and in the tumor tissue and testing of an apoptosis-inducing drug, TRAIL, evaluated here as a soluble formulation (sTRAIL) and a liposome-conjugated formulation (LUV-TRAIL). In this chapter, we confirmed that LUV-TRAIL is more efficient in killing cancer cells than its soluble counterpart, despite its lower diffusion rate. In the future, it would be interesting to test other drugs, such as compounds activated in a hypoxic environment, and to combine tumor cells with other cell types such as stromal and immune cells, which are known to influence the behavior of tumor cells and to modulate their response to drug treatment.

Altogether, the 3D tumor-2D endothelium co-culture model proposed in this chapter entails a great potential not only for drug screening and testing of precision medicine, given that only 5-µl samples are required for each assay, but also for more fundamental *in vitro* studies on cellular interactions in complex tumor models. As such, this chapter is entirely in line with the development and use of enhanced and clinically relevant *in vitro* models, which would allow diminishing the number of experiments conducted on animals and accelerate drug development and approval, hence improving patients' prognosis and life quality at a faster pace.

Chapter 3: Oxygen-sensitive three-dimensional matrix for in situ hypoxia detection in cell culture.

3.1 Introduction.

Oxygen is a key molecule in cell biology. Its relevance in many cellular pr-ocesses like cell death (e.g. apoptosis and necrosis), cell migration, cell metabolism or even cell differentiation has thoroughly been described [215-219]. Oxygen has a cascade delivery process which results in a decrease of oxygen tension, from the 21% in the atmosphere to 1-14% in tissues [220]. Hence, low oxygen tensions are physiological and should be recapitulated and monitored *in vitro* to properly mimic *in vivo* behavior and unravel the biological impact of oxygenation in tissues.

The oxygen tension *in vitro* is typically characterized in vitro using two main approaches: (1) using an electrochemical sensor and (2) using optical means. Electrochemical detection of oxygen proceeds via oxygen reduction, and the measured signal directly relates to the dissolved oxygen concentration in solution. The most common electrochemical oxygen sensor consists of a Clark electrode [221]. Such Clark electrodes have been miniaturized [222,223], and applied for industrial purposes such as water quality management, [222] or for clinical monitoring [224] and biological research [225]. Despite their good sensitivity and short response time [226], electrochemical sensors suffer from certain limitations such as the fact that they consume oxygen during the measurements and may be bio-incompatible with some sensitive cells [227]. Particularly, oxygen consumption in the electrode can be a disadvantage for precise measurements, since it is not innocuous for the system [228]. Furthermore, biocompatibility is to be carefully considered when integrating new materials and compounds within a cell culture system [229]. Alternatively, optical oxygen sensors have been reported; they take advantage of transition metal salts, *e.g*. Ruthenium, Platinum or Iridium which are complexed to a phenanthroline-derived moiety, whose luminescence is quenched in presence of oxygen, proportionally to the oxygen tension [230,231]. These probes can be directly incorporated in culture media,

provided they are soluble in aqueous solutions [232-235], or encapsulated in a substrate. Some examples for this last approach are conjugation of the probe molecule to films, to the microdevice material where the experiments are performed [236-243], or to microparticles added in a liquid suspension [244-249]. The optical oxygen sensing method is simple, reversible and does not consume any oxygen in the measuring process. Furthermore, an additional system or support material is needed to include the fluorescent probe in the sample (e.g. nanoparticles or sensing films), to avoid probe diffusion in the system [228] and cells, which could result in cytotoxicity in the long term.

Some other interesting alternatives have been described in the literature, where an oxygen probe was conjugated to a scaffold and cells were subsequently seeded [250]. Excellent reviews on this regard have been published by Quaranta *et al* [251], Papkovsky and Dmitriev [231] and Grist et al [252]. However, the need for a support material hinders experimental setups and makes measurements only possible near the support material where the probe is conjugated. Specifically, in case of oxygen sensing films, biocompatibility is to be carefully considered, and sensing is limited to film extension within the cell culture setup. In case of nanoparticle-conjugated probes, measurements can be difficult to obtain at every location of the system.

Finally, scaffold-conjugated probes overcome previously mentioned limitations. Nonetheless, confinement of the scaffolds experimental setups could be challenging, as well as achieving homogeneous cell distribution within the scaffold. Therefore, despite the multiple existing approaches, monitoring of oxygen in three-dimensional cell cultures within a biomimetic extracellular matrix remains a challenging task.

In this work, we report a novel 3D oxygen sensitive matrix based con collagen for oxygen mapping in 3D cell culture systems. We achieved this matrix by conjugating a bis-phenanthroline, COOH-terminated ruthenium oxygen-sensitive molecule to the NH_2 groups of ungelated collagen type I via NHS/EDC chemistry. Afterwords, we verified the conjugation reaction was successful and determined the final concentration of the probe immobilized in the collagen matrix. Next, the properties of the conjugated matrix were assessed and compared to those of the native matrix to

study the possible influence of the Ru-based complex on the hydrogel architecture. Particularly mechanical properties (e.g. Young's Modulus) and microfiber orientation were investigated for various concentrations in the Ruthenium-based oxygen-sensitive probe. Moreover, biocompatibility was assessed, and cytotoxicity effects of the modified matrix on the proliferation rate of a colon cancer cell line, which has been reported to generate a high hypoxia rate [253,254], were dismissed.

Overall, we have developed an innovative and versatile tool to quantitatively map oxygen variations in three-dimensional biomimetic systems. This tool inflicts no apparent long-term harm on cultured cells and can be applied to any system, regardless of the setup. We anticipate this tool will facilitate the generation of accurate *in vitro* models under well-defined oxygen tensions and will contribute to elucidating the influence of oxygen variations thereof in various biological processes.

3.2 Materials and methods.

3.2.1 Chemical synthesis of the oxygen sensitive compound.

$Ru(PhPhen)_2Cl_2$ (Sigma-Aldrich GmbH, Buchs, Switzerland) (Molecule 1, 100 mg, 0.084 mmol) and Phe-CO_2H (Molecule 2, 26 mg, 0.084 mmol) were dissolved in a mixture of EtOH: H_2O (1:2, 15 mL) and heated overnight at 110°C. The EtOH was removed under reduced pressure and the resulting suspension was added to a saturated NaCl solution (20 mL) and extracted three times with $CHCl_3$ (20 mL). The organic phases were collected, washed with a saturated NaCl solution (20 mL) and dried over Na_2SO_4. The solvent was removed and the resulting solid dissolved in $CHCl_3$ (10 mL) and precipitated with diethyl ether (50 mL). After filtration, the solid was washed with toluene and dried under vacuum giving a (50 mg, 0.044 mmol, 52%) product (bis(4,7-diphenyl-1,10-phenantroline) (5-((1,10-phenantrolin-5-yl) amino)-5-oxopentanoic acid) ruthenium (2+)) (Molecule 3) which was further purified by HPLC (data not shown). Reactions are detailed below (Figure 3.1):

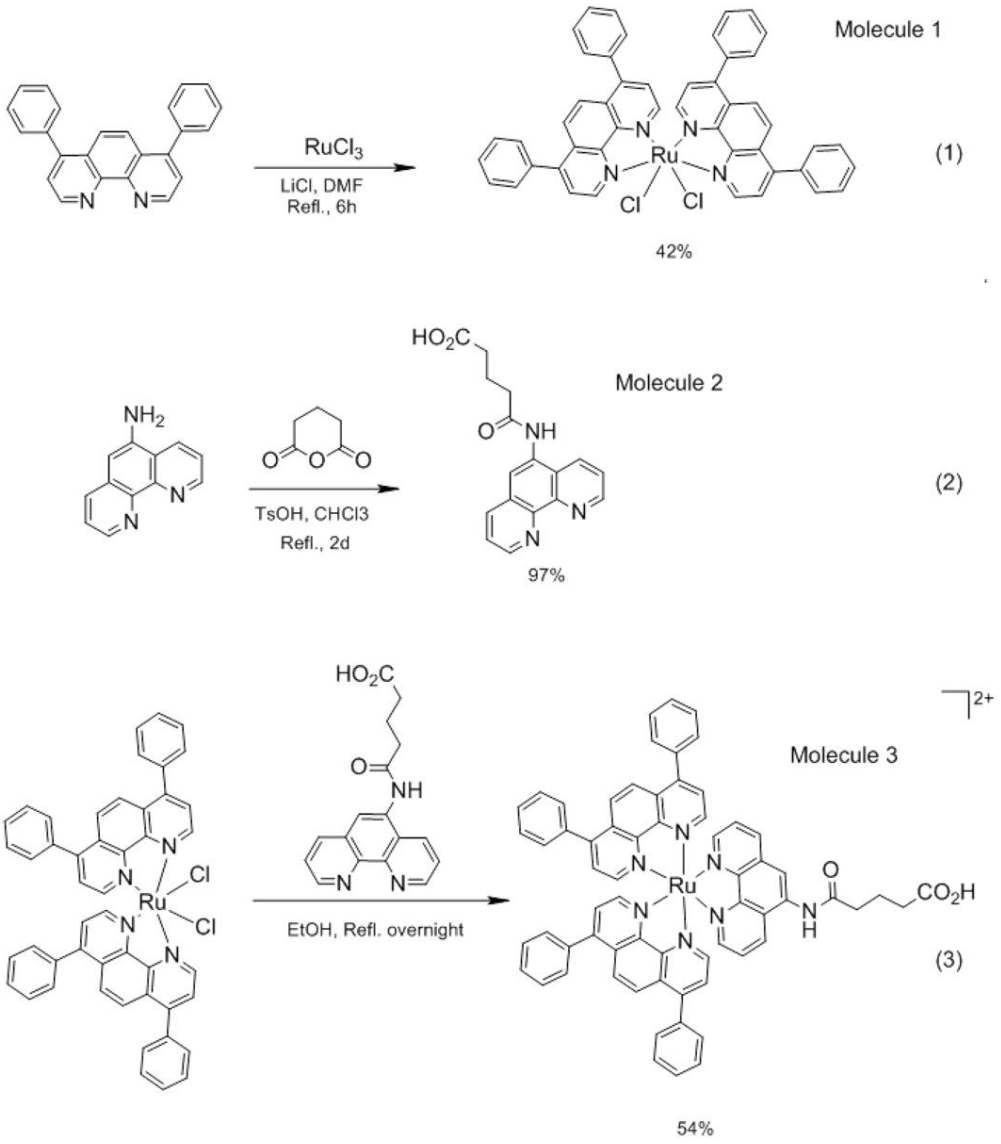

Figure 3.1: Synthesis of the carboxylic acid terminated [Ru(BPhen)2]2+ (BPhen=batophenanthroline) probe.

3.2.2 Oxygen-sensitive probe covalent coupling to ungelated collagen.

N-Hydroxysulfosuccinimide sodium salt (Sulfo-NHS) (Sigma-Aldrich 56485, Madrid, Spain) and N-(3-Dimethylaminopropyl)-N'-ethylcarbodiimide hydrochloride (EDC) (Sigma-Aldrich E7750) were both individually dissolved at 10 mg/ml in a 10 mM 2-(N-Morpholino) ethanesulfonic acid (MES) (Sigma-Aldrich M8250) aqueous solution, adjusted to pH = 4.5 for optimal reaction conditions. 1 mg of the COOH-terminated oxygen-sensitive probe (Molecule 3) was dissolved in DMSO (50 µl), and this solution was mixed with the NHS/EDC mixture (200 µL) to yield a final concentration of

1 mg/mL in MES buffer, pH 4.5, to activate the -COOH moieties of the oxygen sensitive probe (Molecule 4) with NHS/EDC. The resulting solution was let to react at room temperature for two hours while avoiding direct exposure to light. Thereafter, a 3 mg/ml stock solution of rat tail collagen type I (GIBCO, A1048301) was thoroughly mixed with the solution of activated oxygen-sensitive probe in ice (approx. 4 ^{0}C) the latter being introduced for coupling with concentrations of 5, 15, 50, 100 and 200 µM. Reagents were kept in ice during the whole process and reaction mixtures were let to react at 4°C for at least 12 hours before use. The reaction carried out is detailed below (Figure 3.2).

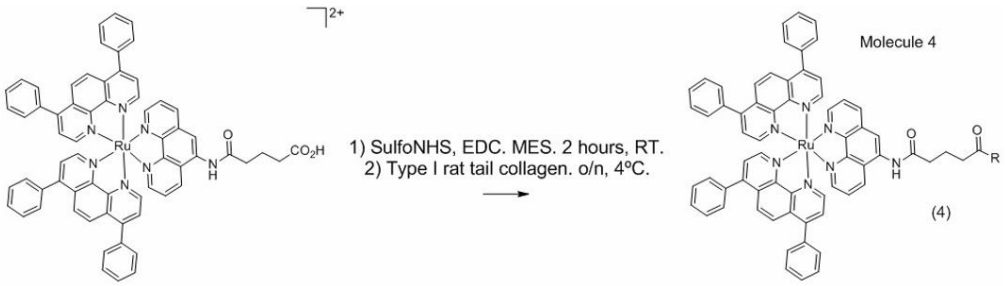

Figure 3.2: Coupling of the dye to rat tail collagen via EDC/NHS activation.

3.2.3 Preparation of the conjugated hydrogel and characterization of covalent binding.

100 µl of the collagen hydrogel mixture to yield a final collagen concentration of 1.2 mg/ml was prepared as follows: First, the collagen was neutralized by adding a solution of 1 M NaOH (Sigma 221465) at a 6% (v/v) proportion of the stock collagen solution. Next, the ionic strength was adjusted by adding Phosphate buffered saline (10 µL) 10x (PBS, Lonza17-517Q), and the volume was completed adjusted (to 100 µl) with sterile distilled water. Collagen hydrogel droplets (3 µL) were formed on the bottom of glass Petri dishes and allowed to polymerize at 37^{o}C for 15 min. Excess PBS was added to wash uncoupled probe for 24 h at 37^{0}C and PBS was refreshed once before the measurements.

3.2.4 Probe-collagen Conjugation efficiency.

Absorbance measurements at 430 nm were conducted at room temperature using a Biotek® Synergy™ HT multi reader (BioTek Instruments, Inc. VT, USA). First, the absorbance spectra: Ru-based complex before conjugation and after conjugation (to a collagen hydrogel) were recorded to check that the absorbance properties were not affected by the covalent anchoring to collagen matrix. To do so, blocks of 1.2 mg/ml collagen hydrogel (50 µL) were prepared for all initial concentrations in the Ruthenium-based probe (i.e. 0, 5, 15, 50 and 100 µM). Furthermore, native collagen hydrogels were placed in solutions of activated Ruthenium-based probe at a concentration of 5, 50 and 100 µM where they rested for one week, so that their reactivity was lost overtime. Full absorbance spectra were also recorded for these collagen samples to check for spectral changes derived from conjugation.

Next, a calibration curve was drawn for the activated Ruthenium-based probe in PBS in a 96-well plate by measuring the absorbance of solutions prepared with known quantities of the probe. Next, 50 µl pieces of hydrogel at 1.2 mg/ml were prepared for every initial Ru-based probe concentration (0, 5, 15, 50, 100 and 200 µM). As before, absorbance measurements were conducted in the hydrogel samples. The effective probe concentration in the hydrogels was extracted from the calibration curve obtained with the soluble probe and the measured absorbance values for the hydrogel samples. From that, the conjugation efficiency was determined. In all cases, recorded values were corrected by subtracting the absorbance values for the 0 µM samples.

3.2.5 Analysis of the hydrogel architecture and anisotropy by confocal reflection microscopy.

Confocal reflection images were acquired using a Nikon Eclipse Ti® microscope equipped with a C1 modular confocal microscope system (Nikon) after collagen polymerization using droplets of hydrogels prepared in glass-bottom Petri dishes. To enable reflection mode, the barrier filter of a 450/35 nm filter cube was removed, and the sample was visualized using a 488-nm laser. In this configuration, the laser light reflected by the hydrogel was captured by the photomultiplier tube, allowing the visualization of the collagen fibers. Fibriltool® software [255] was used for data

analysis and to calculate the average orientation and anisotropy of the fiber arrays in a region of interest in the confocal reflection microscopy images.[16] A constantly sized region of interest was analyzed from each image and an anisotropy index ranging from 0 (purely isotropic, i.e. random organization) to 1 (perfect fiber orientation) was extracted.

3.2.6 Detailed hydrogel architecture characterization by SEM imaging.

Scanning electron microscopy (SEM) imaging was performed as previously described [256,257]. To facilitate hydrogel handling and contrast, hydrogels were prepared in a non-adhesive PDMS setup, fabricated as follows: PDMS (Sylgard 184, Dow Corning, GMBH) was prepared with a 10:1 pre-polymer: curing agent ratio according to the manufacturer's instructions. A 4 mm-high PDMS block was prepared in a mold, cured for 2 h at 60^0C and subsequently punched to create 3 mm diameter cylinder microwells. The PDMS block was autoclaved and, in sterile conditions, placed on top of a 35-mm diameter Petri Dish (734-2317 VWR, Spain). This setup was incubated with a sterile 7.5% BSA solution in PBS (Gibco 05260-037) at 37^0 C for 2 h. Thereafter, the setup was washed twice with PBS and allowed to dry. Control collagen samples and collagen samples prepared with an 8 µM oxygen-sensitive compound concentration were prepared as described in previous sections. Due to BSA passivation, hydrogels could be extracted from the PDMS setup and transferred to Eppendorf tubes.

SEM images were acquired using an SEM Inspect™ F50 (FEI Company, Eindhoven, The Netherlands) in a fixed energy range (0–30 keV). Samples were first frozen separately in liquid nitrogen. Subsequently, the Eppendorf tubes containing the samples were subjected to lyophilizing (Telstar cryodos Freeze Dryer) for at least 24 h. Finally, the hydrogel samples were coated with a carbon film before being examined with SEM.

3.2.7 Mechanical characterization.

The mechanical characterization of hydrogels was performed using AFM and a JPK CellHesion® system (JPK Instruments, Berlin, Germany) coupled with an inverted microscope (NIKON Ti®, Nikon Instruments). The procedure was analogous to that described in previous work [258]. Briefly, droplet samples (20 µL) were prepared for each initial oxygen-sensitive probe concentration (0, 2.3, 3.2, 3.8, 8 µM) as described

before in a Petri Dish (TPP Techno Plastic Products AG, 93040) and measured in Dulbecco's Modified Eagle's Medium (Lonza, BE12-707F) and 20 mM in HEPES buffer (Sigma–Aldrich). The samples were maintained at a constant temperature of 37˚C during the measurements. PNP- TR cantilevers (NanoAndMore, GMBH) tip B were selected for force spectroscopy measurements. The spring constant was precisely characterized by the thermal noise method before each measurement. An 8x8 grid of force spectroscopy measurement was programmed for each sample. Three samples were characterized for each condition. Measurements were performed using a fixed Z-length distance for indentation and retraction (50 µm) to prevent the tip from sticking to the hydrogel. Data were processed with JPK DP® Software (JPK, AG) by applying the Hertz model (variant for square pyramidal tips) to each curve in the Force Map. Mode values were extracted from data histograms for every hydrogel condition.

3.2.8 Coupled oxygen-sensitive probe photostability.

Photobleaching assays were performed as described in previous work [259] using a Nikon Eclipse Ti® microscope equipped with a C1 modular confocal microscope system. Briefly, we compared the photobleaching rate for collagen hydrogels prepared as described previously using an initial concentration in oxygen-sensitive probe of 3.8 µM probe- and other samples supplemented with 0.1 µM fluorescein (free acid) (Sigma-Aldrich, F2456) as a reference. Samples were continuously exposed to an ultrahigh pressure 130 Mercury lamp (Intensilight C-HGFIE, Nikon, Tokyo, Japan) at full intensity through a GFP filter (excitation peak at 485 nm, bandwidth 20 nm; emission peak at 530 nm, bandwidth 30 nm) using a 20x objective. After 15, 30, 60, 180 and 420 s, 100x magnified confocal images were acquired using a 488-nm laser and a 650-nm long pass filter. Thereby, a graph could be plotted showing the variations in the fluorescence intensity as a function of the laser irradiation time. To assess photobleaching dynamics and fluorescence intensity variations in the conjugated gels, intensity histograms were extracted for the different images via ImageJ® software. Intensity values were plotted for every condition and compared.

To assess fluorescence recovery after photobleaching (FRAP), we allowed recovery times of 10 minutes in the probe-conjugated hydrogel samples and fluorescein

supplemented hydrogel samples used for the photostability assay. Thus, regions of interest covering both bleached and unbleached areas were analyzed with ImageJ®.

3.2.9 Cell culture.

HCT-116 cells, human epithelial colon cancer cell line (kindly donated by Dr. Martinez Lostao, University of Zaragoza), were grown in high-glucose Dulbecco´s modified Eagle medium (DMEM) (LonzaBE12-614F, Basel, Switzerland) supplemented with 10% v/v fetal calf serum (Sigma F7524, St. Louis, US), L-glutamine (Lonza17-605F) and penicillin/streptomycin (DE 17-602E) within a humidified TEB-1000 incubator set at 5% CO_2 and 37ºC (EBERS Medical Technology, Zaragoza, Spain). Medium was refreshed every other day and cells were passaged every 4 days using Trypsin/EDTA solution (Lonza, CC-5012). To do so, culture medium was aspirated by means of a plastic pipette and cell culture flask was rinsed with 0.1 ml of PBS/cm^2. Next, Trypsin/EDTA solution (0.02 mL/cm^2) was added to the flask and left to incubate for 5 min at 37°C. Furthermore, cells were harvested with Supplemented High Glucose DMEM (0.1 mL/cm^2) and pelleted (300 g for 5 min). Cells were subsequently resuspended in the desired volume of supplemented High Glucose DMEM for reseeding.

3.2.10 Cell viability within the 3D oxygen sensitive hydrogel.

Cells were trypsinized and resuspended at a concentration of 10^6 cell/mL in supplemented high-glucose DMEM as described in the previous section. Using a chilled tip, cells were pipetted in a 1.2 mg/mL collagen solution, using both native collagen and conjugated collagen. Following this, droplet gels (3 µl) were pipetted in a 96 multi-well plate (Sarstedt, 82.1581.001, Nümbrecht, Germany), which was placed into an incubator (37°C and 5% CO_2) for 15 min to allow collagen polymerization. After polymerization, supplemented high-glucose DMEM was added to the wells. To assess the viability of the cells embedded in the gel, NucBlue® Live and NucGreen® Dead reagents (Molecular Probes™, Eugene, US) were added for 30 min incubation according to the manufacturers' instructions. Microscopy z-stack images were taken every 50 µm using a Nikon Eclipse Ti® microscope equipped with a C1 modular confocal microscope system. Next, images were opened with Fiji® software (http://fiji.sc/Fiji) and z-projected to obtain a single picture combining all seeded cells

in the gel. Both blue-stained cells (stained with NucBlue®) and green-positive cells (stained with NucGreen®) were counted manually. Due to the high cell concentration, long-term cell discrimination was not always possible. Therefore, the cell-occupied area was quantified and compared for native collagen and collagen conjugated to the oxygen-sensitive probe. Specifically, the different plane images composing the z-stack were z-projected using ImageJ® to compose a sole image to avoid double counting of cells present in various images. Once projected, NucBlue® images were binarized and blue pixels were automatically counted and normalized to the total number of pixels in the image.

3.2.11 Oxygen probe calibration and in situ oxygen measurements.

Conjugated-collagen (3.8 µM in oxygen-sensitive probe) blocks were prepared as described in previous sections. Hydrogels were washed twice during 48 h with PBS and incubated for 24 h under 1, 2.5, 5, 10, 12.5, 17.5 and 20% of oxygen in an incubator, which allowed precise oxygen tension setting (TEB-1000, Ebers Medical). Next, stacked confocal images were acquired (every 50 µm) within a few minutes and the fluorescence intensity was quantified for each oxygen concentration, at the same height of the hydrogel. *In situ* oxygen measurements were performed by means of confocal microscopy as described in previous sections, keeping the imaging parameters consistent. Fluorescence intensity measurements were extracted using ImageJ® from the confocal images and converted to oxygen concentrations using the calculated calibration curve. Finally, oxygen concentrations were rendered as an oxygen map by using ImageJ®.

3.3 Results and discussion.

3.3.1 Preparation of the 3D oxygen-sensitive hydrogel-based matrix.

In this work, we chose to create a novel oxygen-sensitive matrix for cell culture, which would provide 3D information on local oxygen concentrations in a biomimetic *in vitro* system.

To achieve this goal, we firstly selected a hydrogel to support 3D cell culture as supporting material for our approach. Hence, we chose to use collagen because it is

one of the main components of the extra-cellular matrix, and it is widely used for cell culture [104,109,157]. The use of distributed matrix, rather than a localized supporting material, provides the opportunity to map oxygen concentrations at any location, with the only aid of a fluorescence microscope.

Next, we synthetized a Ruthenium oxygen-sensitive compound with three phenanthroline-derived moieties, as described above (2 bisphenylphenantroline and a phenantroline group terminated by an acid moiety), although not combined in the same molecule [230,252]. Particularly, we chose Ru over other transition metals because it yields compounds with a more straightforward synthesis, longer lifetimes and remarkable photophysical properties, therefore providing more opportunities as biological sensors [225]. This molecule offers the possibility of modification of one of its ends to a carbonyl group, so that it can be subsequently conjugated to a substrate containing terminal amine moieties via NHS-EDC reaction (Figure 3.3).

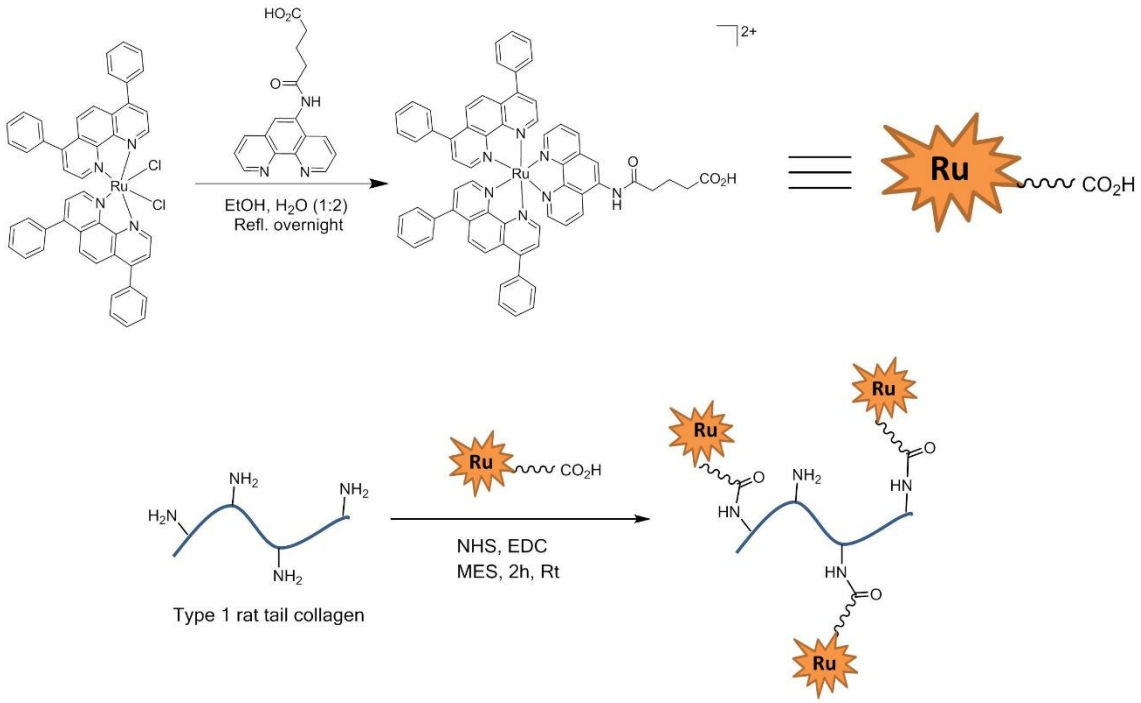

Figure 3.3: Oxygen-sensitive molecule synthesis. To monitor the oxygen concentration, an oxygen-sensitive Ru(II)-based dye is synthesized, from a [Ru(bpp)2]2+ (bpp = bisphenylphenanthroline) moiety functionalized with a 1,10-phenanthroline unit equipped with a 0.5 nm spacer and a terminal carboxylic acid. This image was kindly provided by Dr. Albert Ruggi.

The conjugation of the probe to the hydrogel avoids diffusion of the probe and probe loss due to culture media refreshing, as well as prevents probe internalization by the cells in culture, thus compromising the biocompatibility of the system. Moreover, the oxygen-sensitive probe is ubiquitously distributed through the matrix, therefore providing 3D data at any location of the system. After the coupling reaction, we verified conjugation by characterizing the amount of probe which was chemically conjugated to the matrix. Firstly, we observed a change of color in the conjugated hydrogels compared to native ones (Figure 3.4).

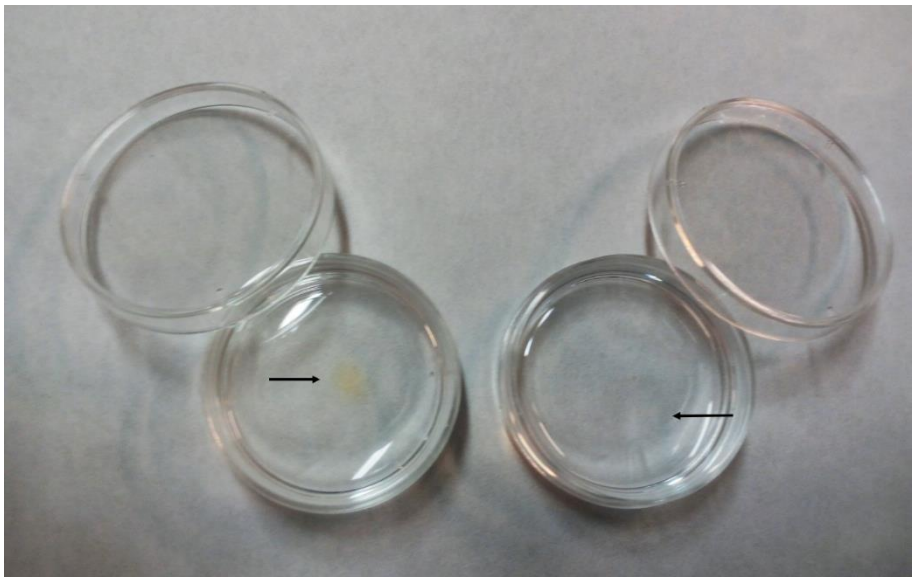

Figure 3.4: Images of a probe-conjugated hydrogel (left, yellow) and a native hydrogel (right, transparent) after polymerization in Petri Dishes and addition of phosphate-buffered saline. The probe-conjugated hydrogel stays yellow after washing.

To this end, we compared recorded spectra (350-700 nm) of a collagen hydrogel supplemented with unconjugated probe and a collagen hydrogel subjected to conjugation with the oxygen-sensitive probe. The spectrum of a plain hydrogel was subtracted as baseline to discard collagen intrinsic absorbance. Results can be seen in Fig. 3.5a. Thus, a distinctive absorbance peak could be observed in the spectrum of the conjugated gel compared to the plain hydrogel. Results are shown in Fig. 3.5b.

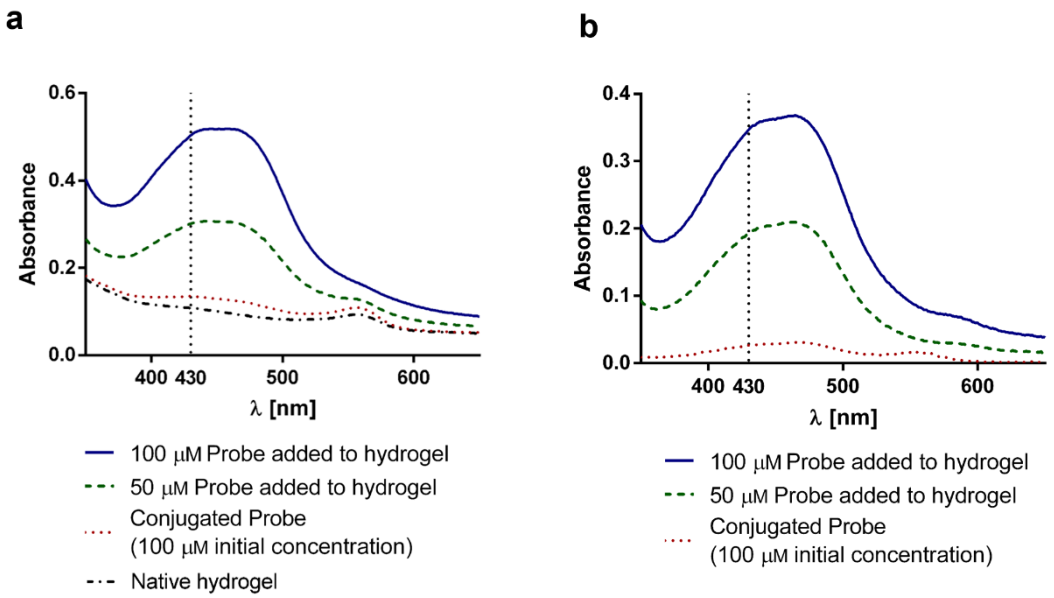

Figure 3.5: Full spectra of the oxygen-sensitive probe, both conjugated and in solution. a) Spectra of the oxygen-sensitive probe both in suspension in a hydrogel (100 μM in blue and 50 μM in green), conjugated to a hydrogel (100 μM of initial concentration, thoroughly washed to eliminate unconjugated traces) and the native hydrogel (in black). B) Corrected spectra by subtracting the native hydrogel absorbance from the spectra shown in (a). No significant peak displacement was observed between both species.

Spectra showed no significant displacement of the absorbance peak for the conjugated and unconjugated probe, therefore, and considering that a hydrogel is mostly composed of water, we assumed that a calibration curve in liquid would be a valid method to interpolate absorbance data and retrieve the effective concentration of probe conjugated to the hydrogel.

Since no influence of 3D hydrogel environment was observed in the probe absorbance properties, we decided to use absorbance values in a liquid environment as a reference to determine the coupling efficiency of Ru-based stuff to collagen matrix.

Hence, we obtained a calibration curve by preparing solutions with the probe in suspension dissolved in MES buffer and added to phosphate buffered saline (PBS), pH=7.4 and quantified the absorbance for each of them at 430 nm (Figure 3.6). Absorbance for the control sample was subtracted to correct for unspecific

absorbance. Then, the Lambert-Beer coefficient was extracted from these data getting $\varepsilon = 33186\ M^{-1}cm^{-1}$.

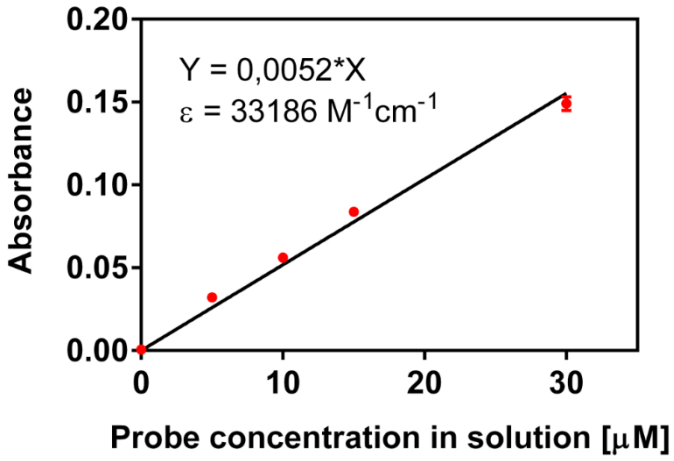

Figure 3.6: Absorbance intensity of the Ru-based oxygen-sensitive probe in PBS solution (phosphate buffered saline) as a function of the probe concentration. Plot shows average ± SEM, fitted through a regression model.

Thereafter, we prepared hydrogels for initial concentrations of 0, 5, 15, 50 and 100 µM in probe. Gels were washed with PBS to eliminate the excess of unconjugated probe and absorbance was evaluated again for 430 nm and interpolated in the previous calibration curve. Data showed effective concentrations of probe ranging from 2-8 µM, as initial concentrations of probe increased (Figure 3.7). This is consistent with saturating sites of union within the hydrogel. Subsequently, the final concentration of the probe specified is covalently attached to the collagen structure.

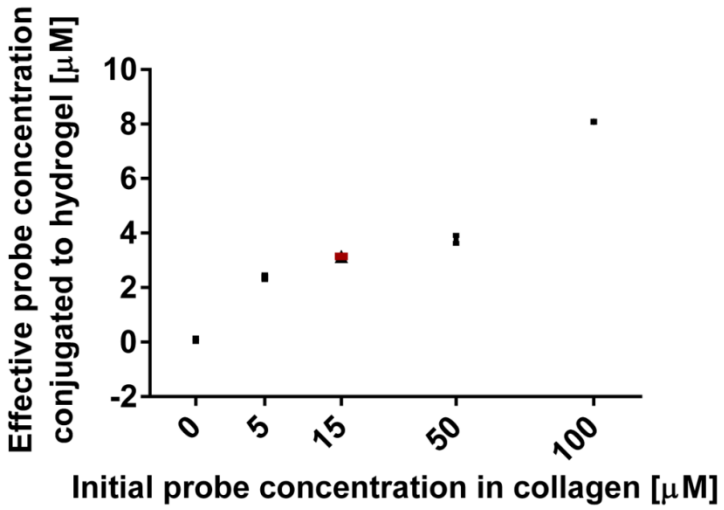

Figure 3.7: Determination of the Ru-based compound conjugation efficiency to the collagen hydrogel. Effective Ru-based compound concentration in the collagen hydrogel derived from the absorbance curve in 3.4 as a function of the initial concentration in Ru-based probe used for the conjugation. Plot shows average ± SEM.

3.3.2 Properties of the 3D oxygen-sensitive matrix.

After the conjugation procedure was assessed, we investigated whether the addition of the probe structure could disturb the natural collagen structure. Possible disturbances could alter matrix architecture and subsequently introduce changes in mechanical properties, eventually altering 3D cell culture in the modified matrix. Therefore, we subsequently examined these aspects to validate the modified matrix for *in vitro* cell assays.

As a first step, we imaged the structure of conjugated and unconjugated collagen hydrogel using SEM. For this characterization, we firstly tested the conjugated collagen hydrogel with the highest amount of immobilized oxygen-sensitive probe (final concentration of 8 μM). The resulting SEM pictures are presented in figures 3.6a and b: the fiber size was found to be similar, and the ramifications in the mesh to be analogous, which would entail a comparable pore size for the 3D collagen matrix. Altogether, no obvious structural changes were detected for the conjugated collagen with the highest (8 μM) concentration in oxygen-sensitive probe, from which we assume that the collagen architecture was unaffected for the different Ru-based compound concentrations tested here (Figure 3.8).

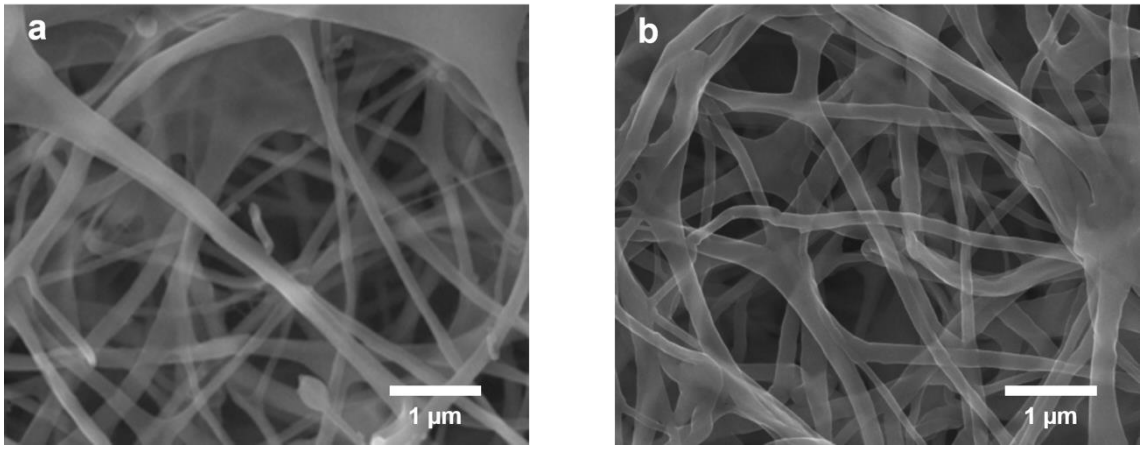

Figure 3.8: Physical characterization of the 3D oxygen-sensitive matrix by SEM. SEM images for a control hydrogel (0 µM oxygen-sensitive probe) a) and a hydrogel with 8 µM oxygen-sensitive probe b).

Next, the mesh structure of the collagen hydrogel was studied in more detail to assess differences in organization of the hydrogel at molecular level (Figure 3.7a&b). Therefore, filament anisotropy was characterized via Fibriltool® analysis on confocal reflection microscopy images (Figure 3.9c). The filament density in both images, obtained with native collagen and collagen with 8 µM immobilized O_2-sensitive probe, appears to be comparable (Figure 3.9a & b). The anisotropy was quantified by determining the anisotropy index for collagen hydrogels. This is a parameter which quantifies the orientation of fibrils (or lack thereof) constituting a compound of fibrils. The analysis of this parameter was performed with various final probe concentrations as well as native collagen (control): for all samples an anisotropy index of 0.012 ± 0.0008 was found, and no significant variation between conjugated and native collagen for any concentration in oxygen-sensitive probe was found (Figure 3.9c).

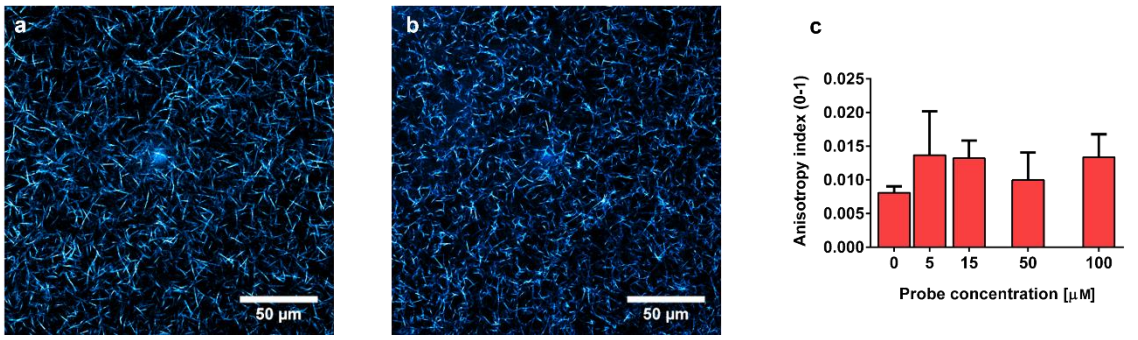

Figure 3.9: Physical characterization of the 3D oxygen-sensitive matrix. Confocal reflection microscopy images for the control hydrogel c) and a hydrogel with a final concentration of 8 µM in oxygen-sensitive probe d). e) Anisotropy index. Plot shows average ± SEM. No statistically significant differences were found.

Last, we also examined the mechanical properties of the collagen material, before and after conjugation of the oxygen-sensitive probe; the hydrogel mechanical properties are particularly important for cell migration and cell differentiation. The hydrogel Young's Modulus was determined using AFM and derived from cantilever indentation curves. Non-significant variations are observed for hydrogels up to 3.8 µM of probe concentration, whereas a significant Young Modulus decrease of 12.5 Pa was observed for the highest probe concentration (8 µM, p-value < 0.0001) (Figure 3.10). This indicates a slight disruption of the mesh by the presence of the compound at this concentration.

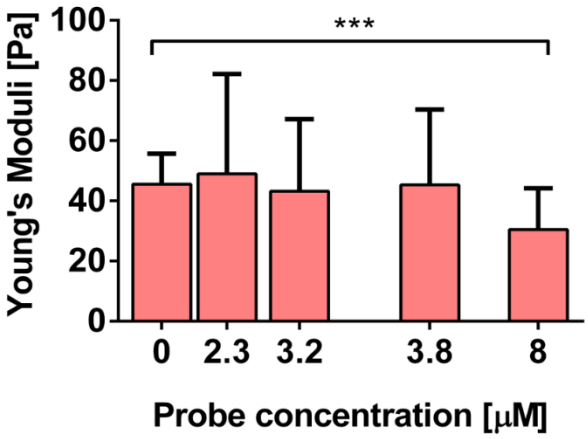

Figure 3.10: Young's Moduli determined for 3D hydrogel matrices prepared with different concentrations in oxygen-sensitive probes (p-value < 0.0001). Plot shows average ± SEM.

Overall, these data collectively suggest that the presence of the oxygen-sensitive Ru-based complex in the collagen matrix for concentrations of 3.8 µM and below had no significant influence on the collagen fiber organization, at a molecular level or on its mechanical properties. This suggests that the modified matrix could be safely used for 3D cell culture with very similar results to native collagen matrices.

3.3.3 Photostability of the 3D oxygen-sensitive matrix.

Given the potential use of this matrix as a fluorescent oxygen probe, we investigated the photostability for the conjugated hydrogel to validate its use as a fluorescent probe for time-lapse oxygen measurements. Consequently, we assessed the photostability properties of the probe molecule in a 5 µl-hydrogel droplet format.

A circular ROI was bleached on the droplets with a fluorescent lamp at full power (Figure 3.11 a-b). After bleaching the conjugated hydrogel droplet, we observed no fluorescence recovery in the following 10 minutes (Figure 3.11 c). In contrast, when soluble fluorescein was added to the solution, fluorescence was recovered after 10 minutes (Fig. 3.11 e-f).

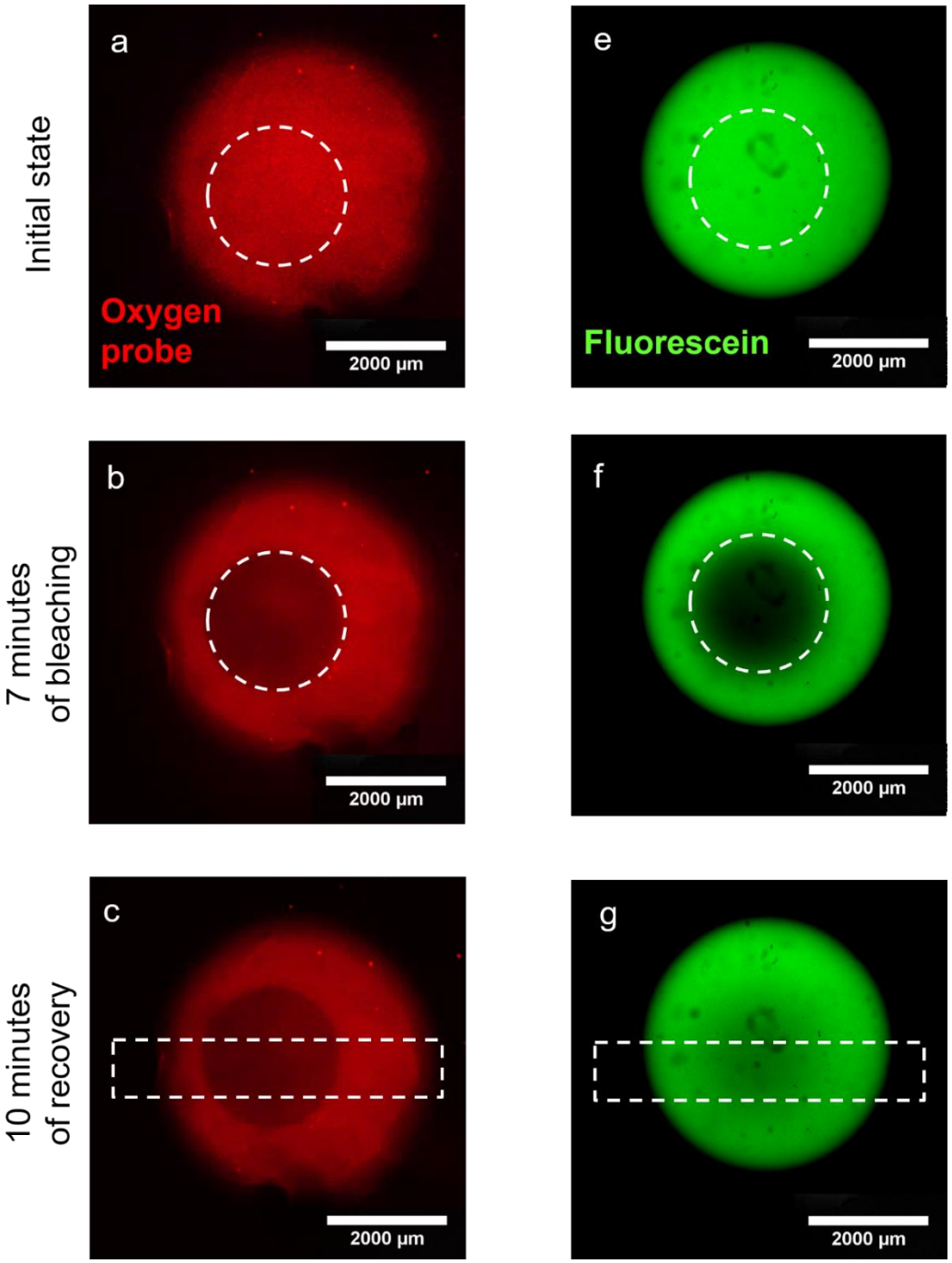

Figure 3.11: Photostability of the 3D oxygen-sensitive matrix. Photobleaching performed on collagen hydrogel droplets with either 3.8 µM covalently attached Ru-based compound or 0.1 µM soluble Fluorescein. a) and e) Fluorescence microscopy images of the collagen droplets before exposure to the laser light, with the conjugated probe a) and soluble fluorescein e). In both cases the bleached region of interest is indicated as a dashed circle. (b) and (f) Fluorescence microscopy images of the collagen droplets after photobleaching both fluorophores for 420 s using a 488-nm fluorescent light, full intensity. c) and g) Fluorescence microscopy images of the collagen droplets after recovery (420 s of bleaching + 600 s of recovery) for the Ru-based compound and fluorescein, respectively. The analyzed region of interest is indicated as a dashed rectangle; and the intensity was evaluated for this entire surface. Bleaching was carried out with a 488-fluorescent light (Intensilight C-HGFIE, Nikon, Tokyo, Japan) for the Ru-based oxygen-sensitive probe (a) and soluble fluorescein (e).

ROIs were quantified to extract quantitative data for posterior analysis, hence confirming the visual observations. In case of the oxygen-sensitive probe, we confirmed no fluorescence intensity recovery after 10 minutes, whereas in case of fluorescein, recovery is clearly detected due to fluorophore diffusion through the hydrogel (Figure 3.12).

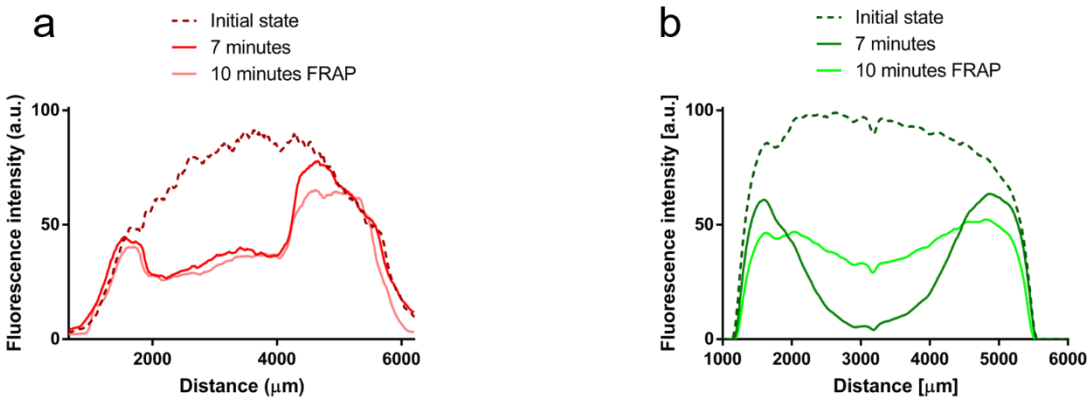

Figure 3.12: Quantification of bleaching and recovery dynamics for the analyzed ROIs. a) and b) Variations in the fluorescence intensity in the rectangular ROI defined in images a-c) and e-g), respectively, for the Ru-based oxygen-sensitive probe and soluble fluorescein. Plots show average fluorescence profiles for the analyzed droplets.

Furthermore, we found that the fluorescence of the probe was reduced to 50% after 2 minutes of continuous fluorescent light exposure and to 30% after 7 minutes (Figure 3.13a), which is comparable to what is observed with fluorescein (Figure 3.13b). Importantly, these experiments confirm that the oxygen-sensitive probe is covalently conjugated to the collagen matrix.

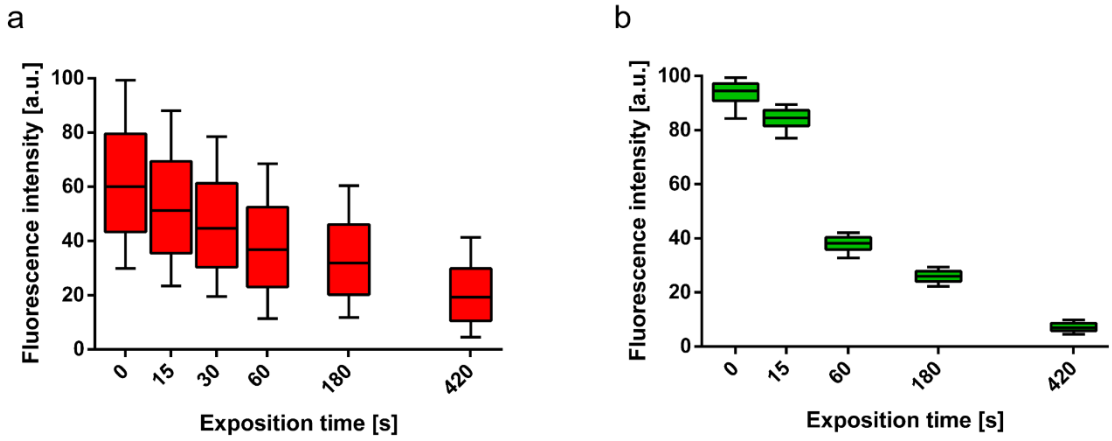

Figure 3.13: Variations in the fluorescence intensity (in the bleached circular ROI) as a function of the continuous irradiation time for the hydrogel conjugated oxygen-sensitive probe (a) and fluorescein free acid (b). Bleaching was carried out with a 488-fluorescent light (Intensilight C-HGFIE, Nikon, Tokyo, Japan) for the Ru-based oxygen-sensitive probe (e) and soluble fluorescein (k). Plots show average ± SEM.

3.3.4 Biocompatibility of the 3D oxygen-sensitive matrix.

As a next step, we tried to determine the highest probe concentration which could be safely used for cell culture. To this end, we examined cell viability after short-term and long-term culture in the oxygen-sensitive matrix for different Ru oxygen-sensitive probe concentrations.

HCT-116 cells were embedded in 1.2 mg/ml conjugated collagen hydrogels at a concentration of 10^6 cells/ml, and cultured in the gelated matrix for 24 h. Collagen with effective probe concentrations of 0, 2.4, 3.2, 3.8 and 8 µM were tested in this experiment.

Cell viability was quantified after 24 hours using NucBlue® and NucGreen® probes that respectively stain all cells and only dead cells. As shown in Figure 3.14, for concentrations lower than 3.8 µM, cell viability was unaffected by Ru-probe concentrations of 3.8 µM or lower (higher than 92%), but became significantly lower for collagen matrices with 8 µM oxygen-sensitive probes (82.85 ± 4.04, p=0.004). Based on these results, concentrations up to 3.8 µM in oxygen-sensitive probe can be used without posing a risk for cultured cells. Images for control and 3.8 µM of oxygen conjugated probe are shown in Figure 3.14b and c.

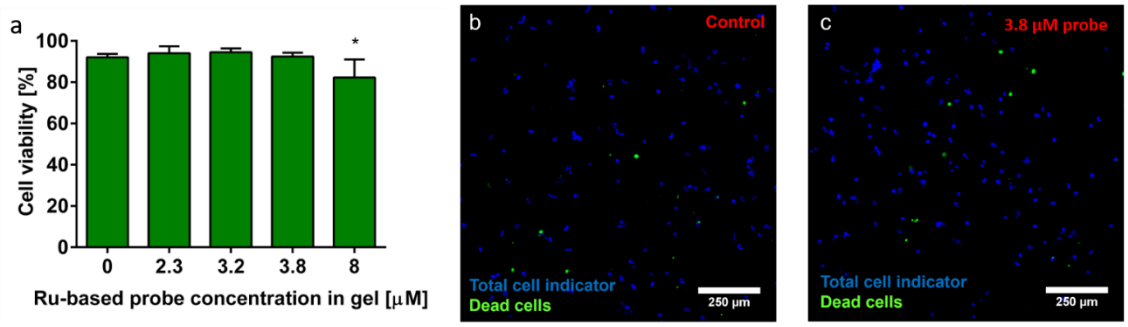

Figure 3.14: Biocompatibility of the oxygen-sensitive matrix. a) Biocompatibility was assessed after 24 hours with ReadyProbes® Nucblue® Live Cell Stain and Nucgreen® Dead (Dead cell probe) for HCT-116 colon cancer cells at a concentration of 10^6 cells/ml in the 3D oxygen-sensitive collagen matrices functionalized with different oxygen-probe concentrations (2.4, 3.2, 3.8 and 8 µM) as well as in control collagen matrices with no probe (p value < 0.008). b) Viability image for a control hydrogel after 24 hours. c) The image shows a hydrogel conjugated with 3.8 µM of the oxygen-sensitive probe. Graph shows average ± SEM.

To discard possible long-term effects on cell viability and proliferation, cell viability was also checked once a day for one week with the same fluorescent dyes as before, using a collagen matrix with a final oxygen-sensitive dye concentration of 3.8 µM and unconjugated collagen as a control. No significantly different results were observed between the 3.8 µM conjugated hydrogel and the unconjugated control hydrogel (Figure 3.15a). An image after 7 days can be found in Figure 3.15b.

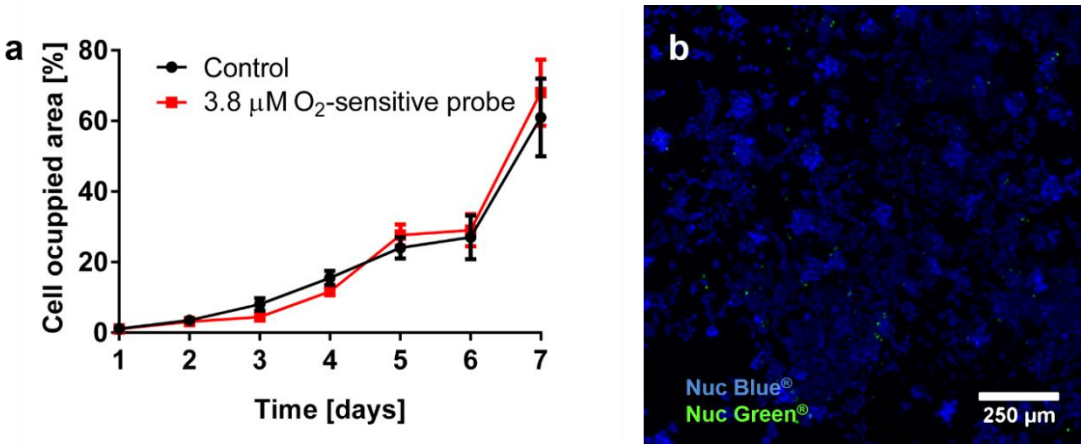

Figure 3.15: Cell viability assessed over a period of culture of 7 days after seeding 10^6 cell/ml in 3D (a). Cell viability was assessed with ReadyProbes® Nucblue™ Live Cell Stain and Nucgreen™ Dead (Dead cell probe). (b) Z-projection of cultured HCT-116 cells in 3D, stained with NucBlue® (total live cell indicator) and NucGreen® (dead cell indicator) after 7 days in a 3.8 µM oxygen-sensitive probe hydrogel. Graph shows average ± SEM.

Next to this, the cell-occupied area was quantified on each day by counting the number of blue pixels and normalizing this number to the total number of pixels in the image. The variations in the cell occupied area over a culture time of 7 days reveal a similar trend in cell proliferation for the control and the oxygen-sensitive collagen matrix containing, respectively, 0 and 3.8 µM oxygen-sensitive probe (Figure 3.16). Altogether, over a culture duration of 7 days, no statistically significant difference was found between both collagen matrices, without and with 3.8 µM oxygen-sensitive probe.

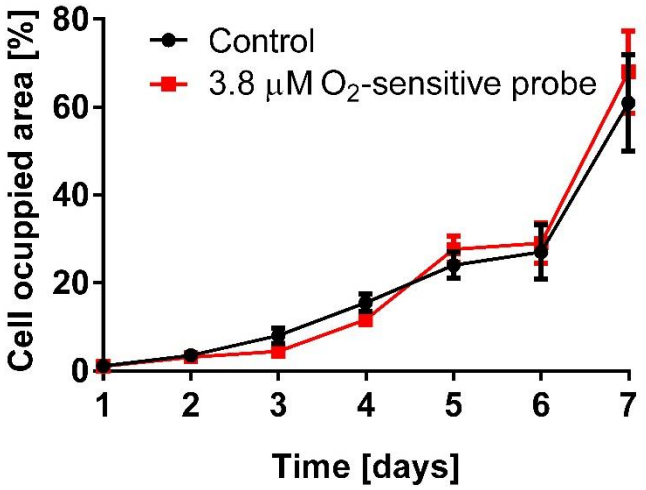

Figure 3.16: Cell proliferation assay in both control collagen and collagen conjugated with 3.8 µM oxygen-probe over a period of culture of 7 days; cell proliferation was quantified by measuring the NucBlue® positive surface area percentage in the image for the 3.8 µM probe-conjugated hydrogel.

Toxicity could however be caused not by the oxygen-sensitive probe itself but through the production of reactive oxygen species (ROS) upon excitation of the Ru-based complex by light. Therefore, in a second series of experiments, we examined the possible generation of ROS upon exposure to light as well as cell viability. The generation of ROS was studied using CellROX® Orange Reagent, which is a fluorescent real-time indicator of ROS concentration. As before, we compared control collagen matrices and collagen functionalized with 3.8 µM oxygen probe, with and without exposure to fluorescent light (488 nm), and in all four cases ROS production was quantified. In presence of oxygen-sensitive probe the ROS level was found significantly higher even without any exposure to light (2.7-fold increase), and increased even further when excited with 488-nm light (5.2-fold increase) (Figure 3.17).

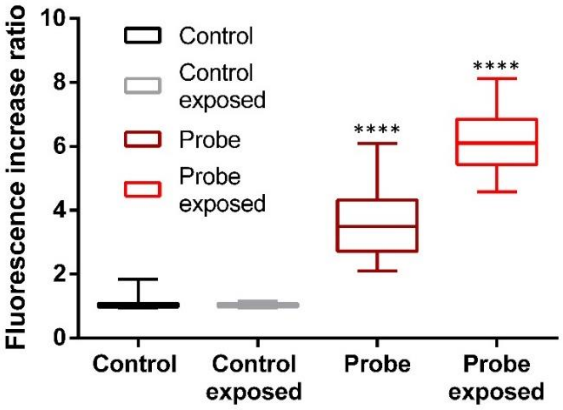

Figure 3.17: Quantification of the ROS levels in control and oxygen-probe-coupled collagen using CellROX® Orange Reagent before and after exposure to fluorescent light (λ = 488 nm; exposure for 1 s every 2.5 min for 1 h). Graph shows fluorescence increase ratio as average ± SEM.

Next, we checked if the increase in ROS in the cell environment would have an impact on cell viability. For all 4 series of samples (control collagen and collagen conjugated to 3.8 µM oxygen-sensitive probe, with and without exposure to light), cell viability was examined using NucGreen® and NucBlue®, both after 3 and 72 hours from exposure. In all cases, cell viability was 94-96%, showing no statistically significant differences between control hydrogels and oxygen-sensitive probe conjugated hydrogels (Figure 3.18). Thus, we found that despite the increased ROS concentration, no negative effect was found on cell viabilities at the examined time points.

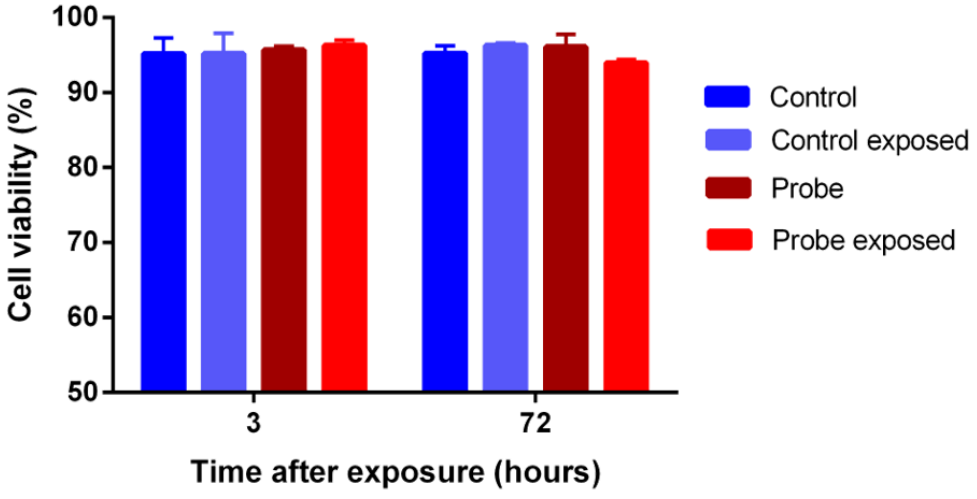

Figure 3.18: Cell viability (HCT-116) determined at 3 h and 72 h for control collagen and collagen conjugated with 3.8 µM oxygen-sensitive probe, after light exposure or without any exposure to light as described before. Graph shows average ± SEM.

3.3.5 Calibration of the 3D oxygen-sensitive matrix.

Finally, we performed a calibration for the 3D oxygen-sensitive matrix by correlating oxygen tension and fluorescence signal to be able in the future to derive a local oxygen concentration from the measured fluorescence signal during cell culture experiments. To that end, we pre-conditioned conjugated collagen hydrogels with 3.8 µM oxygen-sensitive probe under different oxygen tension conditions in a dedicated incubator with a tunable oxygen amount. Furthermore, we designed our measurement setup so that re-equilibration to atmospheric oxygen conditions (ca. 21%) after sample removal from the incubator would take a longer time compared to that required for the optical measurements. We ensured that equilibration would take at least 40 minutes (based on Fick's law, using diffusion coefficient of oxygen in water and calculated using Diffusion Time Calculator by Physiology Web) [260], whereas measurements would take a few minutes. Hence, we ensured that the concentration of oxygen in the hydrogel would remain the same as during the pre-conditioning step. Fluorescence values were extracted from confocal images for every oxygen concentration and line-fitted (Figure 3.19). The R^2 for the fitting was 0.9685. This calibration was used to convert fluorescence values to quantitative oxygen values in 3D hydrogels.

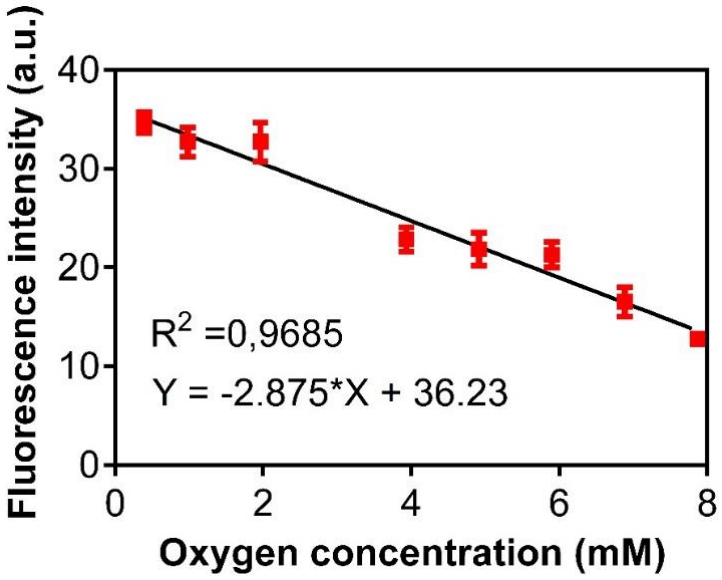

Figure 3.19: Calibration of the fluorescent response of the oxygen-sensitive matrix to hypoxia. Hydrogels were incubated for 24 hours at different oxygen concentrations (1, 2.5, 5, 10, 12.5, 15, 17.5 and 20%) and data were extracted from fluorescence images. Graph shows average ± SEM.

3.3.6 Application of the 3D oxygen-sensitive matrix for oxygen mapping of 3D cell culture.

After performing a fluorescent calibration on the oxygen-sensitive matrix, we used it as a tool for oxygen mapping in 3D cell culture. Firstly, we used it in to determine quantitative increases in 3D cell culture because of cell density and oxygen consumption by the cultured cells. To this end, we seeded three densities of HCT-116 colon cancer cells in hydrogels conjugated with 3.8 µM in oxygen-sensitive probe. After 24 hours, we imaged the hydrogel fluorescence and compared the resulting fluorescence intensity and found a significant fluorescence increase between the control (no seeded cells) and the lowest cell density ($0.25 \cdot 10^6$ cells/ml of 7.8% ($p = 0.0152$) (Figure 3.20). When comparing the fluorescence intensity of the $0.25 \cdot 10^6$ cells/ml to $5 \cdot 10^6$ cells/ml, the increase was of 27.5% arbitrary units, and was significantly higher ($p<0.0001$). Finally, when comparing $5 \cdot 10^6$ cells/ml to $40 \cdot 10^6$ cells/ml, the increase was found to be of 3.5-fold ($p<0.0001$). It can be observed that the higher the increase in fluorescence the higher the cell density difference. Furthermore, the oxygen-sensitive dye can sense both subtle and significant increases in cell concentration and, hence, of oxygen consumption in 3D.

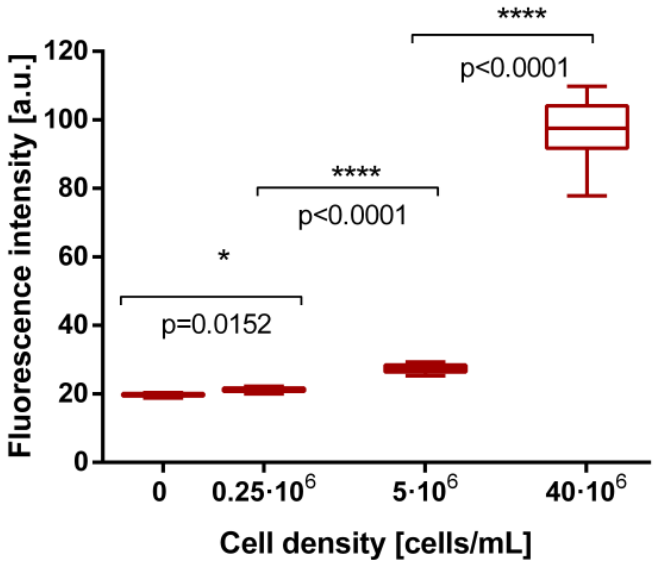

Figure 3.20: Response of the oxygen-sensitive matrix to oxygen consumption by different cell densities in a 3D cell culture. Cells were seeded at 0.25, 5 and 40 million cells/ml in oxygen-sensitive matrices conjugated with 3.8 µM of the oxygen-sensitive probe. Confocal images were taken after 24 hours and fluorescence values were extracted for each condition. Graph shows average ± SEM.

Following this, we chose the highest cell density from the previous experiment ($40{\cdot}10^6$ cells/ml) and observed its evolution overtime (1, 4 and 24 hours), to determine whether the hydrogel could be used to track oxygen changes produced by cell consumption overtime (Figure 3.21). Thereafter, we compared the fluorescence intensity observed after 1 hour and after 4 hours we observed a 10% increase in fluorescence in the system ($p < 0.0001$). Then, we compared the fluorescence increase from 4 to 24 hours and found a 29% increase in the oxygen-sensitive matrix fluorescence ($p < 0.0001$). All in all, these data confirm that the oxygen-sensitive matrix can detect subtle changes in oxygen concentration for a same system overtime.

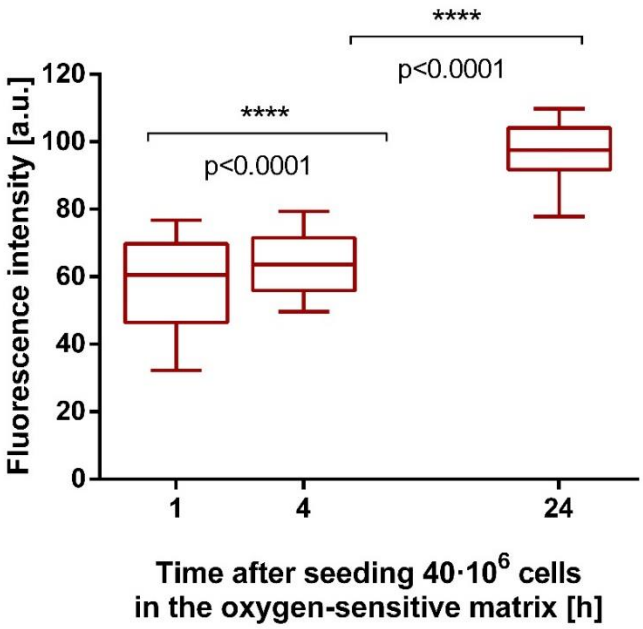

Figure 3.21: Response of the oxygen-sensitive matrix to oxygen consumption by a 3D cell culture at 1, 4 and 24 hours after seeding. $40{\cdot}10^6$ HCT-116 cells were seeded in a hydrogel conjugated with 3.8 µM oxygen-sensitive probe. Cell-induced oxygen depletion was assessed at the different time-points by means of confocal microscopy and the fluorescence values were extracted from the images. Graph shows average ± SEM.

Finally, we validated the use of the oxygen-sensitive matrix for oxygen mapping in a 3D microenvironment. To do so, we seeded $5{\cdot}10^6$ HCT-116 cells/ml in a 3.8 µM oxygen-sensitive matrix and performed confocal imaging as previously described. Confocal imaging raw data was transformed into oxygen values by means of the calibration described in previous sections. As can be seen in Figure 3.22, variations in oxygen are

more evident locally, around cultured cells and quickly decay with distance. Hence, they would not be detectable in a less distributed system.

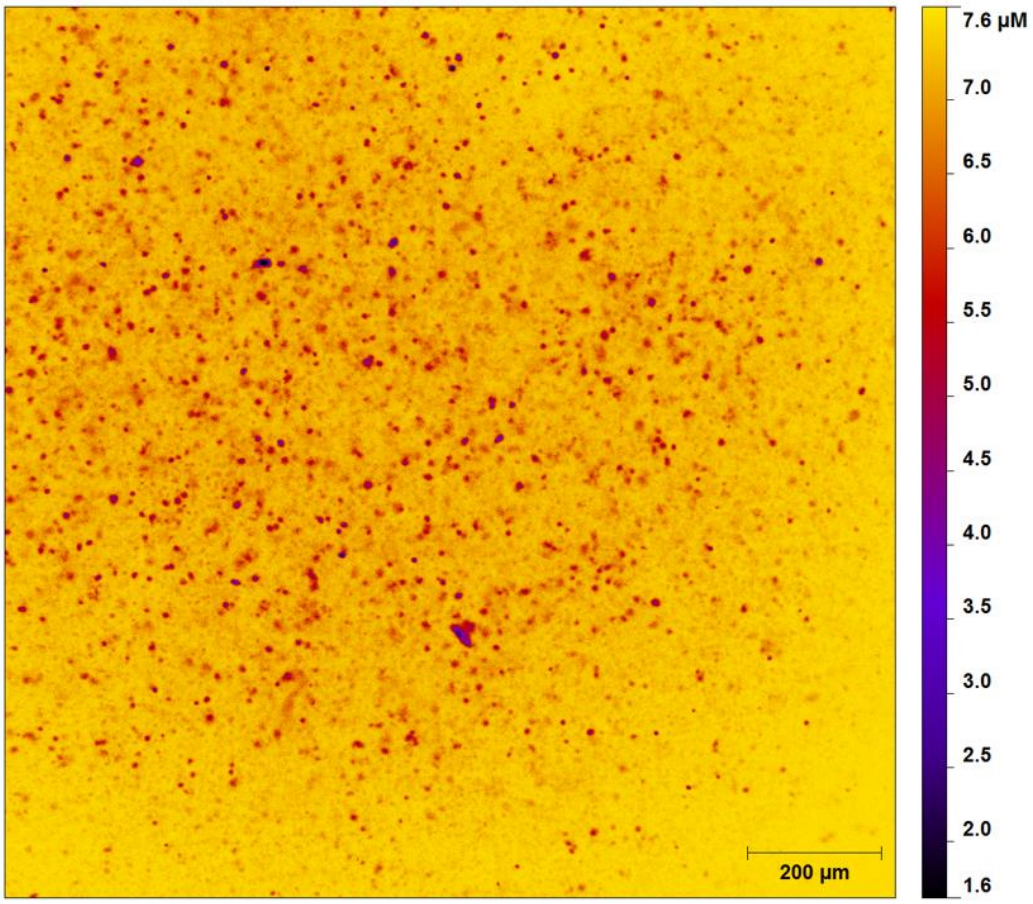

Figure 3.22: Oxygen map performed for a $5 \cdot 10^6$ HCT-116 cell/ml cell culture in a hydrogel conjugated with 3.8 µM of the oxygen-sensitive probe. Color scale can be observed on the slide for a more detailed view of oxygen variations.

3.4 Chapter summary.

Here, we have reported a novel oxygen-sensitive matrix based on collagen type I and including an oxygen-sensitive molecule ($Ru((bpp)_2(PHEN\text{-}PENT\text{-}COOH)^{2+}$) for local mapping of oxygen in 3D cell culture. To prepare the 3D oxygen-sensitive matrix, a ruthenium oxygen-sensing molecule with phenantroline-derived moieties was covalently attached to free amino groups of collagen before gelation, using EDC/NHS chemistry, with a typical coupling yield of 2-8 µM. The structure and mechanical properties of the collagen matrix remained unaffected after conjugation of the Ru-

based oxygen-sensitive probe, at least for final concentrations in the collagen of up to 8 µM. The conjugated collagen matrix supported growth and proliferation of HCT116 cells seeded in 3D in the material, with no significant difference compared to native collagen, demonstrating thereby its suitability for 3D cell culture experiments. As a next step, we calibrated the fluorescent signal of the conjugated collagen as a function of the oxygen concentration. Finally, we validated its use for locally mapping oxygen concentrations *in vitro*.

Altogether, the proposed approach and conjugated collagen matrix allows oxygen determination in a biocompatible way, at any point of the setup. The fact that the oxygen-sensitive probe is conjugated to a matrix of natural source has not been reported in the literature, to the author's knowledge, and presents many advantages over soluble probes. Firstly, collagen is a thoroughly characterized and widely used matrix for cell culture, which ensures cells are cultured in a biomimetic microenvironment. Secondly, the use of an ungelled matrix provides the user with the opportunity to choose a setup, rather than being constrained to a particular one. This fact permits coupling of different types of cellular assays with real-time on-the-spot oxygen monitorization *in vitro*.

Furthermore, probe loss and consequent variation on the signal are not an issue. Likewise, soluble probe diffusion inside cultured cells is prevented, thus avoiding unknown effects on oxygen consumption, cell metabolism and viability.

Finally, we believe such a material will be key to optimize culture conditions and perfusion protocols in 3D cell culture. Furthermore, the ability to correlate local variations in the oxygen tension and cell behavior renders this tool very powerful to assess cancer-related processes both *in vitro* and *ex vivo*, e.g., metastasis or drug resistance. These processes have been found to act as a prognosis marker, and therefore this newly developed tool becomes an asset for personalized medicine.

Chapter 4: Enabling cell recovery from 3D cell culture microfluidic devices for tumor microenvironment genetic signature evaluation.

4.1 Introduction.

The tumor microenvironment (TME) is currently recognized as a central player in tumor development and progression [261]. TME comprises the niche in which a tumor develops and comprises different cell types and distinctive cues of diverse sort [23]. Among the lasts, gradients of oxygen tension, nutrients and waste products are established in the malignant tissue, varying as a function of distance from the nearest supporting blood vessels [262]. This very specific TME is known to strongly influence tumor evolution, having also a deep impact on drug resistance and, as a consequence, on patient outcome [261,263].

Although TME is clearly organized in a 3D manner, most of the traditional *in vitro* cancer research is still performed using the classic 2D models based on the Petri dish. 2D models have historically provided researchers with invaluable insight on tumor biology, even though they reproduce many of the mentioned features of the TME with utter difficulty, which is critical in the context of targeted therapies. The development of molecular analysis techniques (e.g. genomics or proteomics) has allowed an unprecedented and highly precise molecular profiling of the tumors cells to find new molecular targets (e.g. VEGF or EGF); hence, they are the mainstream techniques in cancer research nowadays. Unfortunately, most of these molecular profiles obtained in 2D models can dramatically change when cancer cells grow in a more physiologic TME. Hence, many results obtained with traditional models do not match those observed *in vivo* [264].

As we have previously highlighted in the introduction, there is an urging need for new generation *in vitro* models, which progressively incorporate more features of the TME. By incorporating these enhanced models to traditional labs, more insight in tumor

development would be provided, hence improving and accelerating drug research and development [3,265,266].

In this context, microfluidics can reproduce complex biological three-dimensional microenvironments. Thanks to the small volumes manipulated through microfluidics and the fluid physical properties at the microscale, spatial control can be achieved, and gradients can be utilized to create a biomimimetic three-dimensional environment [267]. Thus, new complex problems inaccessible to traditional technologies can be investigated through microfluidics.

Keeping this in mind, we have reported the development and characterization of a microfluidic model of the tumor microenvironment, which overcomes many of the inspection drawbacks presented by three-dimensional multicellular spheroids and integrates the benefits of microfluidics and real-time monitoring in a user-friendly microfluidic device [268].

Despite the advantages of microfluidics, the adoption of these techniques in mainstream molecular biology and cancer research has not yet met the expectations surrounding the field [3,269]. Most of the microfluidic assays only offer a low number of read-outs, normally based on microscopy observations (e.g. migration of cells towards chemoattractants). Conversely, retrieving the cells in 3D culture within the microdevice for an in depth genomic or proteomic analysis constitutes an approach that remains challenging.

Therefore, the conjugation of microfluidics with genomics would result in an extremely powerful tool on the field of cancer research, combining the TME recreation by microfluidic devices with the massive screening of genomics/proteomics. Such an approach yet remains to be explored in the literature and it would provide a new robust set of comprehensive data for a new perspective on cancer research. Ideally, a protocol to retrieve these cells should be cost-effective, harmless to the cultured cells and rapid, if maintaining the effects of the TME on individual cell programming is intended. Arguably, the main obstacle to conjugating both these techniques is to maintain the benefits of the dimensionality achieved through microfluidics in

downstream techniques. Thus, coupling techniques should be aware of this fact and present alternatives to overcome this obstacle.

In this chapter, we summarize the development of a microfluidic tumor slice model inspired in spheroids performed previously in our group [268]. Moreover, we utilized it to further investigate some processes related with tumor development by means of RT-PCR. To achieve the latter objective, we have optimized a protocol to extract cells from three-dimensional protein ECM scaffolds confined within microfluidic devices by means of a quick enzymatic degradation process which does not affect cell viability. To demonstrate the capabilities of this methodology, we have cultured two different cell types in a harsh and starving environment and recovered them at different time points for RNA extraction. Subsequently, we used the extracted RNA to quantify the expression of genes related to processes taking place in both tumor microenvironments, such as hypoxia, cell death mechanisms and autophagy.

Finally, we have developed a method based on hydrogel patterning, intended to maintain the spatial organization encountered in the model. This patterning method, followed by cell sorting can be used to analyze different regions separately.

Overall, we have developed a method for coupling microfluidics with traditional molecular biology techniques without losing the cell organization achieved thanks to microfluidic devices.

4.2 Materials and methods.

4.2.1 Microdevice fabrication.

Cyclic olefin polymer-based microdevices were designed to allow user-friendly operation, avoiding the need for specialized clean-room processing equipment. The microdevice comprised a 2000 µm wide central chamber, flanked by two 700 µm wide, 250 µm deep lateral microchambers. The central microchamber was delimited from the lateral microchannels by parallelogram-shaped pillars that allowed liquid and cell confinement within hydrogels as described elsewhere [270]. Hence, lateral

microchannels remained hydrogel-free and were filled with media or collagenase solution when needed. Hydrogel injection was performed through dedicated inlets and outlets by manual pipetting. The configuration of the microdevice is shown in Figure 4.1.

Microdevices were fabricated by injection molding and attached to Petri dishes using biocompatible adhesive. Prior to their use in cell culture, microdevices were sterilized with 70% ethanol. After air-drying and 2 hours UV exposure, microdevices were ready for use.

A 3D cell culture system with injected hydrogel was confined to the central chamber. The lateral microchannels remained hydrogel-free and effectively served as 'surrogate blood vessels', as well as an entry point for cell staining and collagenase solutions.

4.2.2 Hydrogel preparation and setup handling.

1.2 mg/ml Type I rat tail collagen hydrogels were prepared as described in Chapter 2. Cells were trypsinized and resuspended to the desired cell concentration to incorporate in the pre-gelated collagen mixture. For assays performed in a hydrogel droplet format, a chilled tip was used to pipette one 3 µl droplet of cell suspension in collagen mixture described in the previous chapter per well in a 96 well plate. At least 4 droplets were prepared for each condition and assay.

Conversely, for 3D cell culture in the microdevices, the hydrogel mixture was injected into the microfluidic device by means of a micropipette. Additionally, a 10 µl hydrogel mixture droplet was placed on top of the inlet to prevent hydrogel evaporation. The filled microfluidic device was subsequently placed into an incubator for polymerization as described for droplets. 5 ml of culture medium were added to cover all the microdevices attached to the Petri dish. Culture medium was perfused through the lateral microchannels to allow oxygen and nutrient diffusion. In all experiments, the culture medium in the lateral microchannels was refreshed once a day by pipetting 10 µl through each lateral microchannel. When a different culture medium or solution (e.g. viability staining or collagenase solution) was desired, the culture medium was removed from the Petri dish by aspiration, 5 ml of the new medium was added and 10 µl were manually pipetted through the lateral microchannels.

4.2.3 Cell culture.

Human cell lines HCT-116 (colon carcinoma) were kindly donated by Dr. Luis Martinez Lostao. U-251 MG (glioblastoma) were purchased from the American Type Culture Collection (ATCC). Both cell types were routinely cultured in high glucose Dulbecco's Modified Eagle's Medium (DMEM) (Lonza, BE12-614F) supplemented with 10% Fetal bovine serum (FBS, Sigma-Aldrich F7524, non-USA origin), 2 mM L-glutamine (Lonza, 17-605C) and penicillin/streptomycin (Lonza, DE 17-602E) within a TEB-1000 humidified 5% CO_2 incubator (EBERS Medical Technology) at 37 ^{0}C.

4.2.4 Cell staining.

4.2.4.1 Cell viability.

To assess cell viability of the degradation procedure, individual cells needed to be distinguished. Thus, we used bisBenzimide H 33342 trihydrochloride (Hoechst33342, Sigma-Aldrich B2261) and propidium iodide (PI, Sigma-Aldrich P4170) for cell staining. Hoechst33342 stock solution was prepared by dissolving in DMSO to a concentration of 10 mg/ml, whereas PI was dissolved in distilled water to a final concentration of 2 mg/ml. Stock solutions were diluted 1:10000 and 1:1000 respectively in phosphate-buffered saline (PBS, Lonza BE17-516F) and gels were incubated with the solution for at least 15 minutes in the dark before imaging. Cells were visualized by confocal microscopy (Nikon Ti-E coupled to a C1 modular confocal microscope), being all cells stained blue (Hoechst33342) and dead cells (PI-positive) stained red.

For tumor development tracking, individual cell counting was not necessary. Hence, Hoescht33342 was substituted by Calcein AM solution. Stock solutions of 5mg/ml Calcein (CAM) (Life Technologies, C1430) and 2mg/ml propidium iodide (PI) (Sigma P4170) were dissolved in DMSO and distilled water respectively. To test cell viability within microfluidic devices and in Petri dishes, stock solutions of CAM and PI were diluted to 5 and 4 μg/ml, respectively, in phosphate-buffered saline (PBS) (Lonza BE17-516F). CAM/PI solution was perfused through the lateral microchannels. Cells were then visualized by confocal microscopy (Nikon Ti-E coupled to a C1 modular confocal microscope), with viable cells (CAM-positive) stained in green and dead cells (PI-

positive) stained in red. Cell viability profiles were evaluated by analyzing the fluorescence intensity of the viable/dead cells across the central microchamber. All confocal images were taken at different focal planes with subsequent image analysis performed using ImageJ software.

4.2.4.2 Proliferation assay with Premo Fucci.

Cell proliferation was observed in live cells using the Premo™ FUCCI Cell Cycle Sensor (ThermoFischer, P36237). Briefly, cells were transduced using a 50-virus particle/cell ratio for 48 hours. Transduced cells were trypsinized and cultured in 3D within the microdevice as described above. This cell cycle sensor was transduced into the cells using two different reporters coupled to TagRFP or emGFP that are expressed alternatively during the G1 phase or the S/G2/M phases respectively.

4.2.4.3 Hypoxia tracking.

For hypoxia tracking, Image-IT® stain was used as previously described in chapter 2. Stain was added to the gel at the concentration indicated in supplier's instructions.

4.2.4.4 Apoptosis labelling.

The CellEvent™ Caspase-3/7 Green Detection Reagent (ThermoFischer, R37111) was used to detect apoptosis. Reagent was diluted following supplier's instructions and added to the gel.

4.2.5 Validation of the model for drug testing.

Doxorubicin (DOX) (Selleckchem, S1208), was dissolved in DMSO at 50 mM and diluted to a final concentration of 30 µM in relevant media. The drug was perfused through the lateral microchannels as previously described and refreshed every 24 hours. DOX and PI naturally fluoresces red; thereby an alternative cell viability staining solution was used during DOX experiments: 50 µl of NucGreen® Dead 488 ReadyProbes® Reagent (Life technologies, R37109) and 50 µl of NucBlue® Live ReadyProbes® Reagent (Life technologies, R37605) were used as described in previous chapters. This solution

was perfused through the lateral channels, labelling all cells in blue and dead cells in green.

4.2.6 Hydrogel degradation procedure.

Collagenase P (Roche,11213857001, 2.3 IU/mg) was dissolved in PBS to a final concentration of 8 mg/ml (18 IU). Collagenase solutions were subsequently sterile-filtered and added to the hydrogels. For degradation of hydrogels in well plates, 100 µl were added per well. For degradation of hydrogels within microdevices, 50 µl of the collagenase solution were pipetted through each lateral channel of the microdevice as described in section 4.2.2. Collagenase incubation was performed at room temperature for 5-10 minutes. Afterward, the collagenase solution was aspirated through the inlet with a micropipette. This procedure was repeated once with PBS to maximize cell recovery. The recovered cell suspension was transferred to a fresh Eppendorf tube kept at 4^0C and washed with PBS before subsequent steps.

4.2.7 Hydrogel degradation tracking.

5 µl collagen hydrogels at 1.2 mg/ml were prepared in a glass-bottom Petri Dish (Ibidi, 81158) as described in section 3.2.5, and let stabilize overnight in an incubator.

Confocal reflection images were taken using a Nikon Eclipse Ti® microscope equipped with a C1 modular confocal microscope system. To visualize the collagen fibers, the barrier filter of a 450/35 nm filter cube was removed, and the sample was visualized using a 488-nm laser. In this configuration, hydrogel reflected laser light was captured by the photomultiplier tube, hence allowing the visualization of the collagen fibers. Collagenase P (Roche, 11213857001, 2.3 IU) was dissolved in PBS to final concentrations of 0.5, 2, and 8 mg/ml. Collagenase was added to the gels and incubated at room temperature for 5-25 minutes. The degradation process was tracked during this time, acquiring images as fast as possible in the system.

Image analysis was performed with Fiji® (http://fiji.sc/Fiji). Time lapse images were binarized and fibril occupied area was quantified overtime and plotted for each collagenase concentration.

4.2.8 Gene expression assays.

4.2.8.1 RNA extraction.

Embedded cells were extracted from collagen hydrogels confined in 2 microdevices, as described in section 4.2.6. Furthermore, RNA was extracted by using Total RNA Purification Plus Kit (Norgen Biotek Corp, 48400). When necessary, Lysis Step could be performed to harvested cells according to manufacturer's instructions and the resulting suspension could be stored at -80^0 C for posterior RNA extraction. Once extracted, RNA concentration and purity were assessed by means of absorbance measurements using a Biotek® Synergy™ HT multi reader (BioTek Instruments, Inc. VT, USA).

4.2.8.2 cDNA.

cDNA was synthesized by using PrimeScript™ RT-PCR Kit according to manufacturer's instructions. Briefly, 1 µg of RNA were taken from each sample and diluted to a final volume of 16 µl in an Eppendorf tube. 4 µl of 5x Master mix were added to a final volume of 20 µl. The mixture was incubated in a CFX96 Real-Time System (Bio-Rad, Spain) for 15 minutes at 37 ^{0}C, for 5 seconds at 85 ^{0}C and finally the mix was cooled down to 4 ^{0}C. The reaction was controlled with GAPDH as housekeeping gene.

4.2.8.3 qPCR.

PrimeTime® qPCR assay probes were purchased from IDT for the genes presented in table 4.1, where primers are also detailed:

Target genes	
Autophagy	
P62	5’-CCGATGTCATAGTTCTTGGTCTG-3’ 5’-CTGCCTTGTACCCACATCTC-3’
Bclin	5’-GAATCTGCGAGAGACACCATC-3’ 5’-ACAGCTCCATTACTTACCACAG-3’
LC3	5’- CTTCATCTGCAAAACTGAGACAG-3’ 5’- CAGGTGCAAGGAGAAAGGAT-3’
Proliferation	
Ki67	5’- GAAGCTGGATACGGATGTCA-3’ 5’- CGCCTGGTTACTATCAAAAGGA-3’
Cell Death	
Casp3	5’-GTTTGCTGCATCGACATCTG-3’ 5’-CTCTGGAATATCCCTGGACAAC-3’
Casp8	5’-GAGAGTCCGAGATTGTCATTACC-3’ 5’-CAAATCAACAAGAGCCTGCTG-3’
Casp9	5’-GTCCTCAACCTTCCTGGAAC-3’ 5’-GCCCAAGCTCTTTTCATCC-3’
TNF-α	5’- TCAGCTTGAGGGTTTGCTAC-3’ 5’-TGCACTTTGGAGTGATCGG-3’
RIP1	5’-GCACTGGTTCATGTTGATGG-3’ 5’-GACGGTTCTTCATCCTTTACGA-3’
Hypoxia	
HIF1A	5’- CAACCCAGACATATCCACCTC-3’ 5’- CTCTGATCATCTGACCAAAACTCA-3’

Table 4.1: RT-PCR primers for the chosen targets in gene profiling of the tumor microenvironment evolution. Sequences are detailed for both primers.

Probes were resuspended at a 20x concentration following manufacturer's instructions and stored at -20 ^{0}C until use. PrimeScript RT-PCR Kit was used to perform the RT-PCR reactions in a CFX96 Real-Time System. The conditions for the RT-PCR were the following:

$$95^0C\ 15\ s + \left\{\begin{matrix} 95^0C\ 15\ s \\ 60^0C\ 30\ s \end{matrix}\right\}_{40\ cycles} + 4^0C\ \infty$$

4.2.9 Patterning method.

In this chapter, the spatial heterogeneity is studied within the microdevices. To maintain this heterogeneity after extracting the cells, differential staining of the center of the microdevice compared to the edges is achieved through hydrogel patterning. To that end, two hydrogel mixtures of different viscosity were prepared. Hydrogel patterning within the microdevice central chamber was performed as described in previous literature [271]. To improve control and reproducibility over the width patterned regions, the outer hydrogel was supplemented with methylcellulose solution to increase the viscosity of the solution.

Methylcellulose solution was prepared as follows: 6gr of high viscosity (4000 cP, Sigma m-0512) methylcellulose were dissolved to any 500 ml of basal DMEM media by mixing with a magnetic stirrer for 2-3 hours. Once all the powder was dissolved, the volume was centrifuged at 5000g during 2 hours. Upper clear phase was carefully separated to avoid the presence of debris.

For the patterning procedure, the central microchamber was filled with a 50% methocel supplemented hydrogel, to which Fluospheres® were added (as detailed in previous chapters). Subsequently, a 3 µl droplet of non-supplemented hydrogel was placed on top of the inlet. Passive pumping produces an inner region of hydrogel with labelled cells, flanked with regions of non-labelled cells.

4.2.10 Image analysis.

Laser confocal and fluorescence images were acquired with a Nikon Eclipse Ti-E C1 confocal microscope. Images were analyzed using Fiji® software (http://fiji.sc/Fiji). Fluorescence intensity across the central microchamber of the microdevice was quantified in the different experiments by selecting a rectangular region across the central microchamber. The fluorescence intensity across that section was then determined using the Fiji® software in accordance with the software instructions. In cell viability experiments, viable and dead cells were manually counted, and cell viability was calculated as the percentage of viable cells relative to the total number of cells. For hydrogel degradation, tracking was performed by quantifying hydrogel fibril positive pixels relative to overall pixels in the picture overtime.

4.2.11 Statistical analysis.

All the experiments were repeated at least three times as independent biological repeats. All results are presented as the mean ± standard error. The normal distribution was tested by the Kolmogorov-Smirnov test. Statistical significance was set at $p < 0.05$. For nonparametric comparisons, a Kruskal-Wallis test was performed followed by the Mann-Whitney U-test.

4.3 Results and discussion.

4.3.1 Microdevice fabrication and setup.

In this chapter, a “tumor slice” microfluidic model of the tumor microenvironment described previously in our group was utilized. The first 8 figures presented in the chapter belong to previously published work from our group [268] and will be included and summarized to facilitate the understanding of the model and motivation for posterior experiments.

As a first approach, this model includes a high density of tumor cells, flanked by two surrogate blood vessels. The combination of these elements creates a spatially heterogeneous hypoxic and nutrient-depleted microenvironment (Figure 4.1a). To recreate this, cyclic olefin polymer-based microdevices were fabricated by injection

molding, and attached to Petri dishes using biocompatible adhesive (Figure 4.1 b, c) The final microdevice setup can be observed in the following figure (Figure 4.1d).

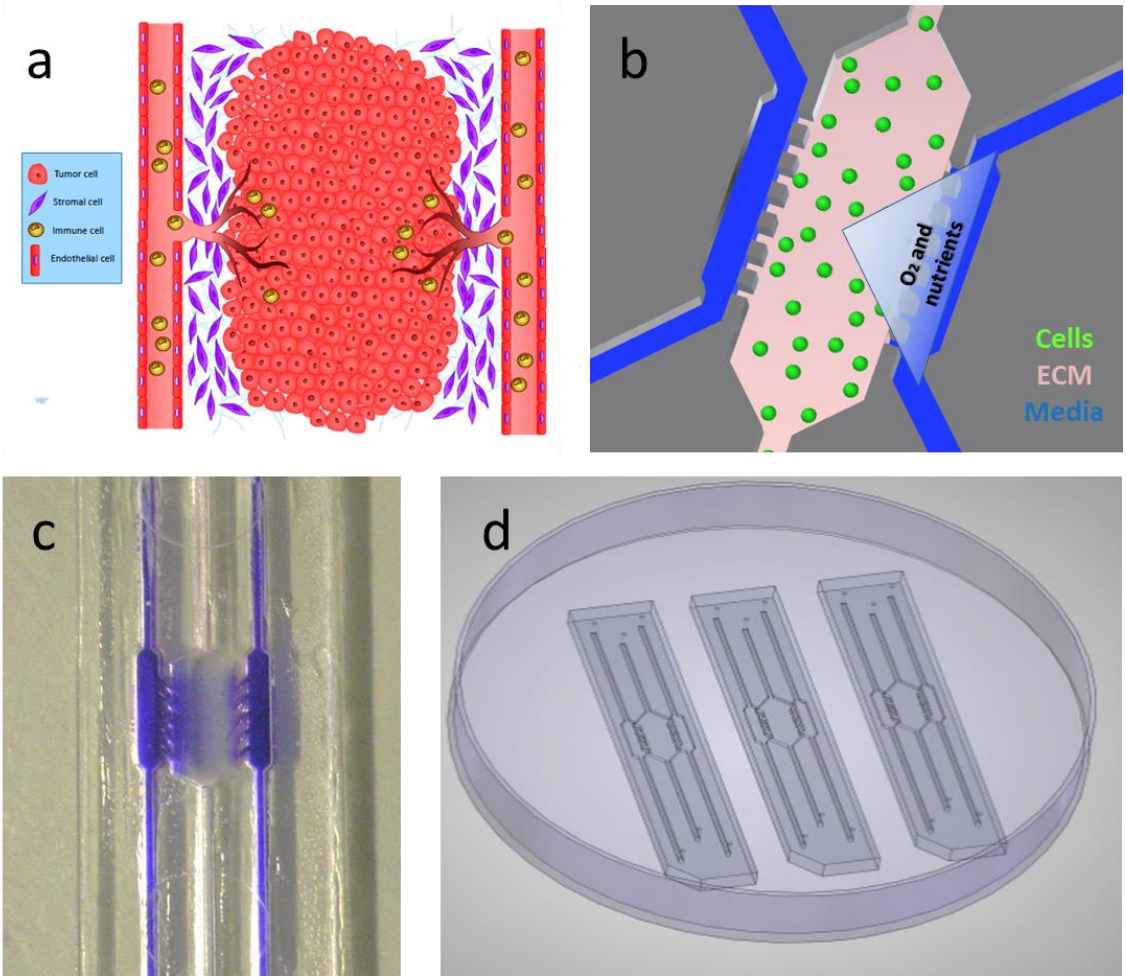

Figure 4.1: Schematic representation of the tumor microenvironment model reproduced in this chapter and microdevices utilized to that end. a) Schematic representation of the tumor microenvironment, including tumor cells, and stromal cells (fibroblasts, endothelium and immune cells). b) Schematic representation of the device and the configuration in which it was used. Cells (depicted here as green spheres) are embedded in a collagen matrix (pink in the figure) within the central microchamber of the microdevice. Media is subsequently perfused through both lateral microchannels. Nutrients and oxygen present in the media are consumed by cells located closer to the microchannels. Hence, gradients for oxygen and nutrients are created accordingly and their direction is represented by the blue triangle. c) Detailed image of a microdevice. In this case, a hydrogel was confined in the central microchamber, and water dyed with food coloring was perfused through both lateral microchannels, hence creating a color gradient along the central microchamber. d) Schematic representation of the setup utilized to handle the microdevices. Three microdevices were attached to a petri dish bottom by means of a biocompatible adhesive layer. Image adapted from Ayuso et al [268].

4.3.2 Necrotic core generation in the microdevice.

Firstly, we assessed the effects of different cell densities on cell viability within the microdevice. This was to demonstrate the generation of a necrotic core, which could develop due to oxygen and nutrient gradients within the microdevice. Hence, after assessing different cell densities of glioblastoma U-251 MG cells (4, 10 and 40 million cells) (Figure 4.2) we found that only at 40 million cells/ml did the necrotic core appear. Thereafter, we chose to work with this last concentration and further analyzed the evolution of this 3D culture system.

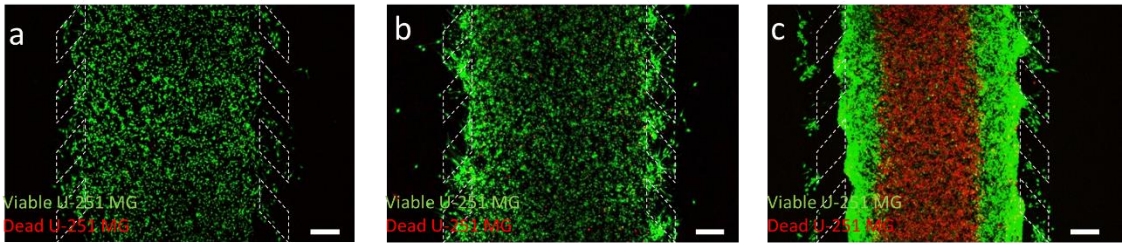

Figure 4.2: Necrotic core generation. U-251 MG cells embedded within the collagen hydrogel were cultured at different cell densities (4, 10 and 40 million cells/ml in A, B and C respectively) for 3 days. Cell viability was evaluated using the CAM/PI staining. Only at 40 million cells/ml a necrotic region appeared. Scale bar is 400µm. Image adapted from Ayuso et al [202].

In this previous work, we determined that both U-251 MG and HCT-116 cells generated a necrotic core in the microfluidic model. This necrotic core increased its width overtime, and presented different dynamics for the described cell types, probably relying in their different metabolism. In both cases, this 3D culture system can be used as a tumor-slice model, which we characterized and exploited in the rest of the chapter.

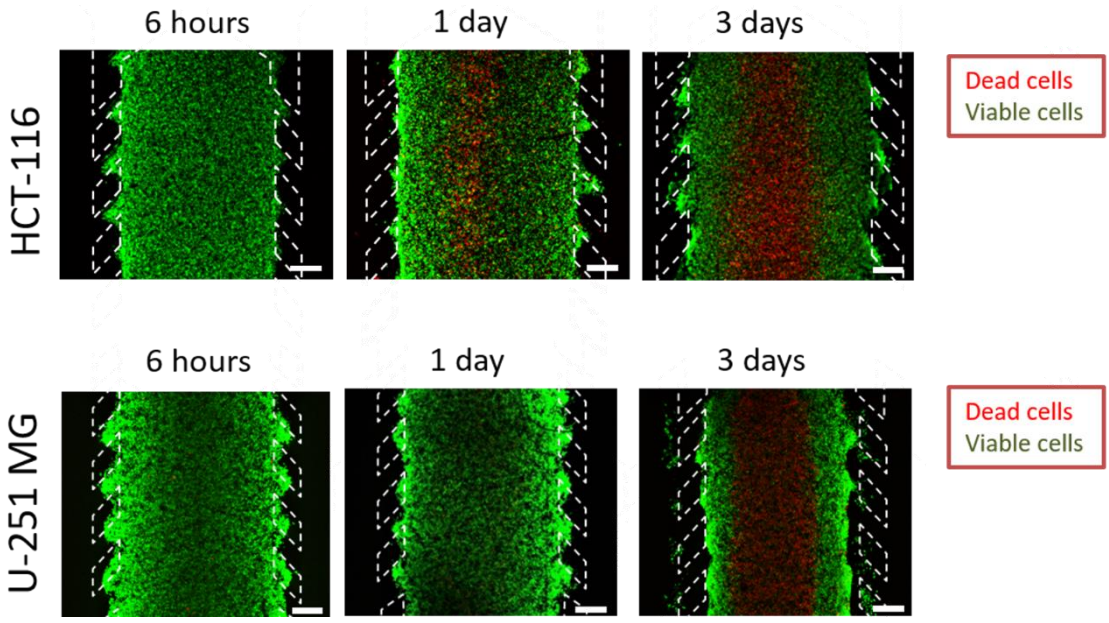

Figure 4.3: Necrotic core generation within the microdevice. U-251 MG and HCT-116 cells were embedded within the collagen hydrogel in the central microchamber. Above, 40 million HCT-116 cells/ml were confined in the central microchamber and cell viability was evaluated at different times using the PI/CAM staining, turning viable cells green, whereas dead ones appear in red. Below, the same experiment was repeated for U-251 MG cells. Scale bar is 400µm. Image adapted from Ayuso et al [202]

4.3.3 Cell proliferation in the model.

The previous results suggested the existence of gradients of nutrients and oxygen across the central microchamber. To check their effect on cell proliferation, we then used the Premo Fucci reporter system. In this system, cells are transfected with a dual reporter, which provides green fluorescence as cells are in proliferation, whereas it provides red fluorescence for cells arrested in the cell cycle. We then observed that, after 24 hours of seeding, green cells appeared to be more abundant in the edges, whereas red cells were homogenously distributed (Figure 4.4 A-D). To quantify these observations, we divided the central microchamber in 10 different regions (200 µm steps) parallel to the lateral microchannels, and quantified the number of red and green cells per region (Figure 4.4 E). All in all, these previous results indicate that proliferative cells were more abundant closest to the lateral microchannels (regions R1, R2, R9 and R10) (Figure 4.4 F).

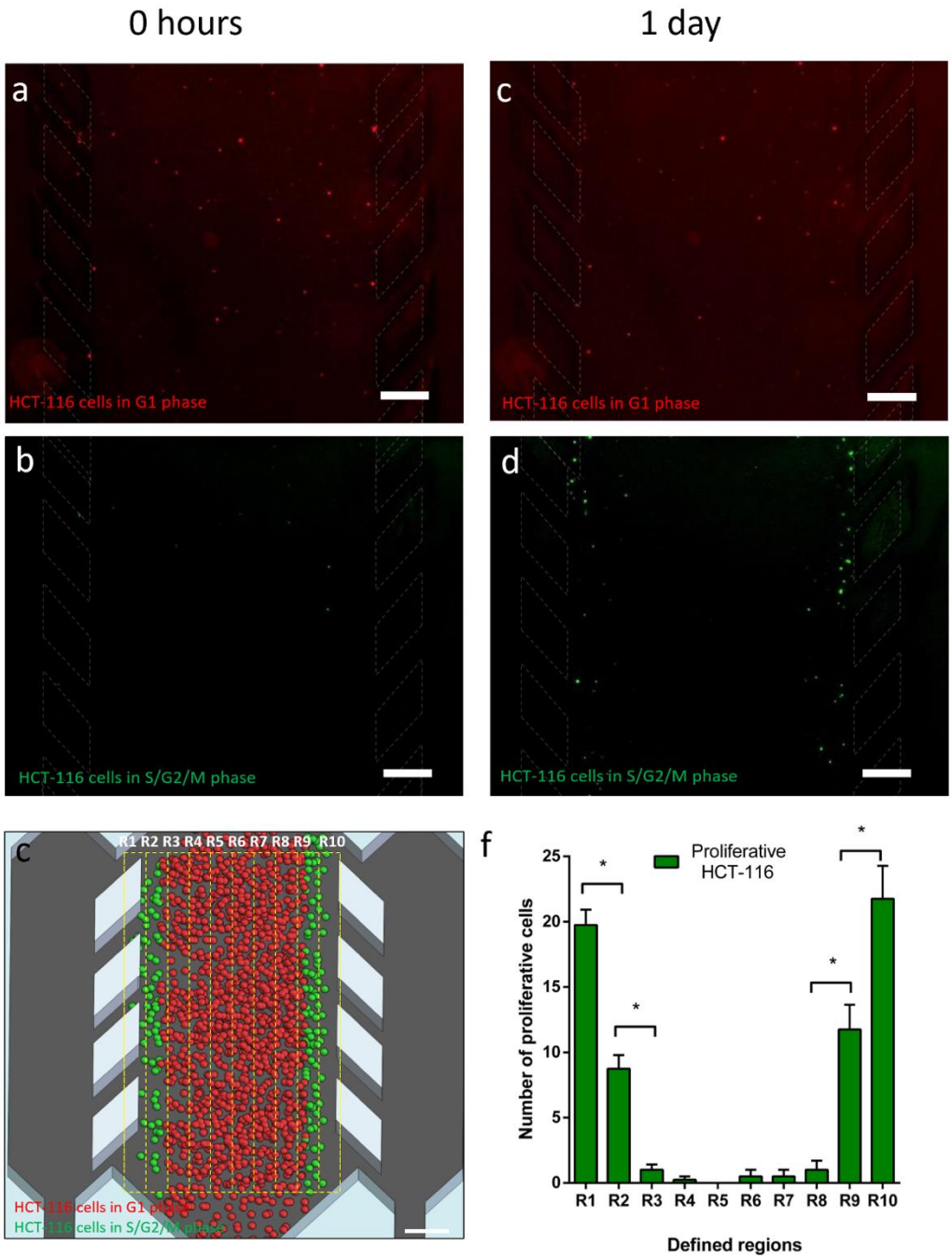

Figure 4.4: HCT-116 cell proliferation. 40 million HCT116 cells/ml were confined in the central microchamber; 5% of these cells were transduced with the cell cycle sensor Premo FUCCI®, showing non-proliferative cells in G1 phase in red, whereas actively dividing cells (S, G2 and M phases) appear green. a-b) After collagen polymerization, non-proliferative cells (in red) were randomly distributed along the central microchamber, whereas only a small fraction of the transduced cells were proliferating (in green). c-d) After 24 hours in cell culture, cell proliferation was clearly observed in those cells located nearby the lateral microchannels. e-f) Central microchamber was vertically divided in ten regions (200 µm steps) and proliferation was quantified as the number of green cells observed in each region. Scale bar is 400µm. Image adapted from Ayuso et al [268]

Interestingly, when this experiment was repeated for U-251 MG cells, proliferating cells appeared scarce and homogeneously distributed (Figure 4.5) [272]. This fact could be investigated more in-depth by means of genetic analysis.

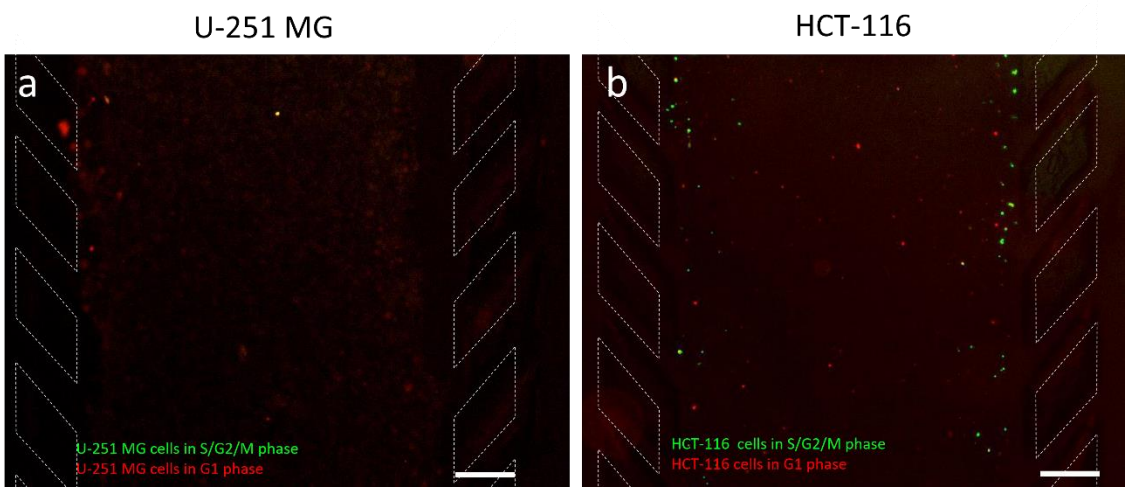

Figure 4.5: Cell proliferation for U-251 MG and HCT-116 cells. 40 million of U-251 MG (a) or HCT-116 (b) cells/ml were confined in the central microchamber; 5% of these cells were transduced with the cell cycle sensor Premo FUCCI®. After 24 hours, fluorescence images were taken, showing non-proliferative cells in G1 phase in red, whereas actively dividing cells (in S, G2 and M phases) appear green. Scale bar is 400 µm. Image reproduced from Ayuso et al [202].

4.3.4 Oxygen gradient in the microdevice.

The existence of an oxygen gradient was assessed using confocal microscopy and the hypoxia-sensitive dye Image-iT®. This dye increases its fluorescence as the oxygen tension sensed by the cell decreases (Figure 4.6 a-b). A steep gradient of hypoxia was observed in the first 200 µm through the "tumor slice" before reaching a plateau, where oxygen tensions were presumably minimal. Media refreshment through the lateral microchannels resulted in a sudden decrease in hypoxia levels after 1 minute. Hypoxia levels were restored after 4 h post-media refreshing. These results demonstrated that hypoxia was generated within the microdevice.

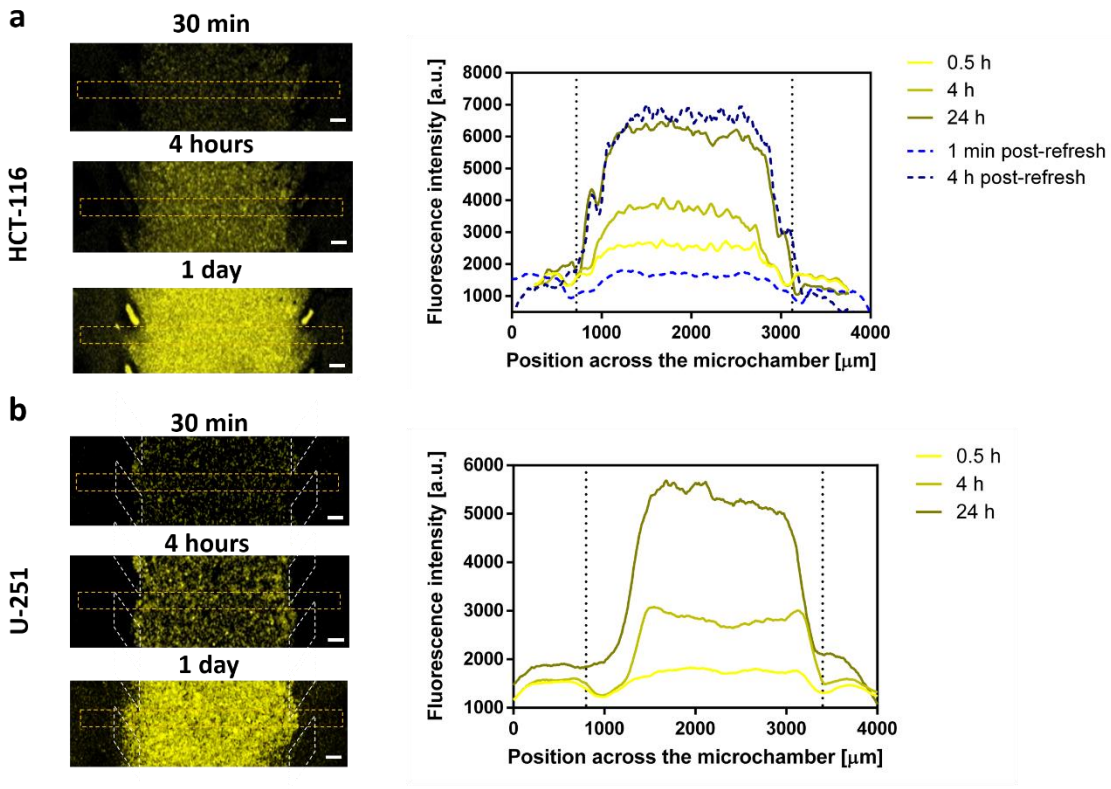

Figure 4.6: Oxygen profile analysis. HCT-116 and U-251 MG cells were embedded within the collagen hydrogel and cultured in the central microchamber. a) A hypoxia-sensing dye was added to the hydrogel/cell mixture prior to injection within the microdevice to characterize the hypoxia profile along the experiment. After collagen polymerization, culture medium containing the dye was added to the lateral channels to keep the dye concentration constant along the experiment. The left panels show that hypoxia-induced fluorescence intensity in the central microchamber increased during the experiment. The graph shows the hypoxia-induced fluorescence profile along the central microchamber. Hypoxia profile rapidly increased in the first 300 µm and reached a plateau in the center of the microchamber. 1ml of fresh media was injected through one lateral microchannel, reducing the hypoxia-induced fluorescence to initial values. 4 h post-refresh, the hypoxia-induced fluorescence reached again the values observed before refreshing. b) The same experiment was repeated for U-251 MG cells, showing a similar behavior. Scale bar is 200µm. Image adapted from Ayuso et al [202]

4.3.5 Apoptosis quantification.

Next, the mechanisms of cell death were investigated in the model. To this end, we used CellEvent® Apoptosis Reagent, which renders apoptotic cells fluorescent. Thereafter, apoptosis was found to occur in a moderate, yet constant manner throughout the central chamber of the microdevice. Hence, apoptosis was not confined to the necrotic area of the tumor slice model and did not account for the appearance of the necrotic core in the central area of the microdevice. This result suggesed that the PI-positive area in the center of the microdevice was due to necrosis, rather than to the progression of early stage apoptotic cells into late stage

apoptosis. This process could be explored further by means of genetic expression quantification.

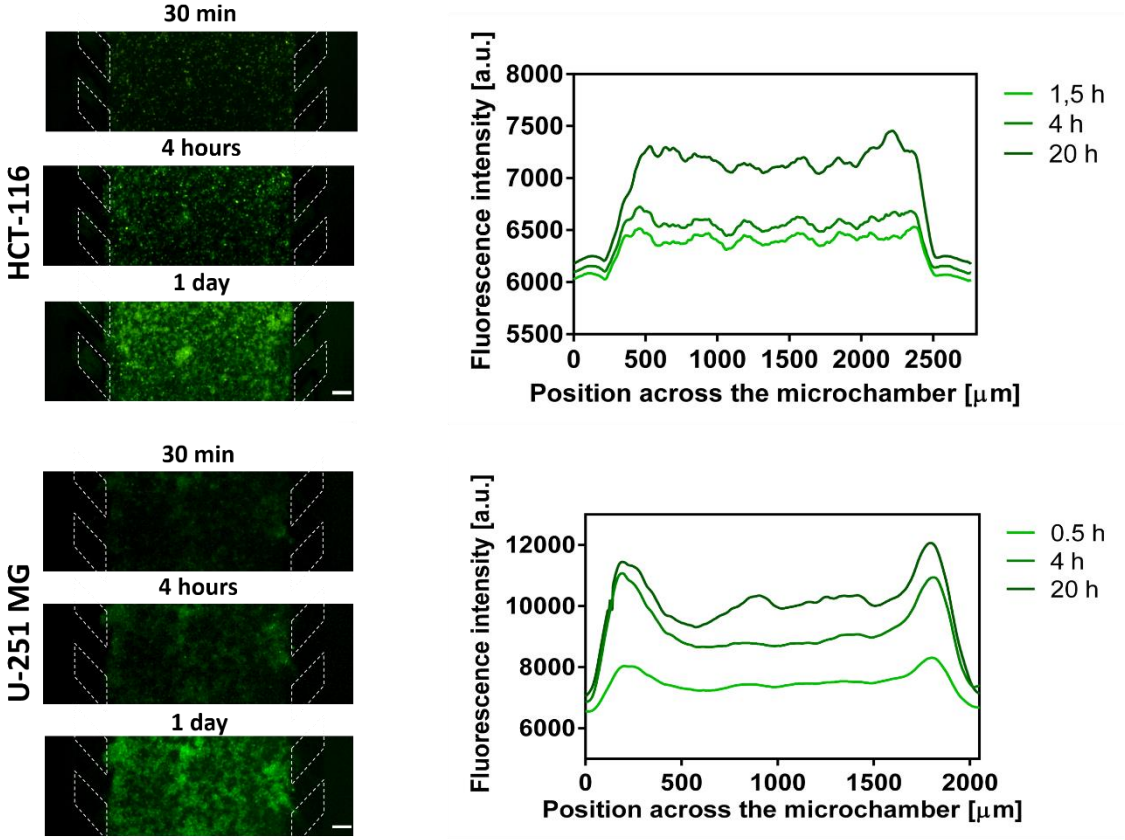

Figure 4.7: Apoptosis characterization for HCT-116 and U-251 MG cells. HCT-116 (a) and U-251 MG cells (b) were confined in the central microchamber. An apoptosis sensing dye was injected in the system, showing that apoptosis increased along the time in both cell lines. The graphs show the apoptosis profile across the delimited region. Image adapted from Ayuso et al [202].

4.3.6 Validation of the tumor slice model for drug testing.

Once the model was established, in previous work we validated it for drug testing applications. In this case, we chose doxorubicin (DOX), a standard of care drug with intrinsic fluorescence (Excitation/Emission peaks ca. 470/620 nm) [273]. First, the model was used to confirm drug penetration through the tumor slice model. To do so, we performed a diffusion assay, in which we tracked DOX fluorescence through the central microchamber of the microdevice in absence of cells. After 120 min, penetration had occurred through the entire central microchamber, obtaining comparable results to the assay in absence of cells (Figure 4.8 a). Next, we assessed the anti-tumor efficiency of DOX in the tumor slice model by injecting a 30 μM DOX

solution through the lateral microchannels. Cell viability comparison found an increase in cell mortality due to DOX treatment, which was limited to the outer rim of the tumor slice model (Figure 4.8 b).

Furthermore, we analyzed the fluorescence intensity profile for cell mortality after treatment with DOX, and found that, after the initial peak, the profile then decreased when we analyzed further into the central microchamber, to a point where no differences with control conditions were observed (Figure 4.8 c). This indicated that DOX efficiency was lower in necrotic areas, suggesting that this difference in cytotoxic response may have been due to a difference in the proliferative rate of the cells in these different regions as shown in Figure 4.3. This fact could be explored more in depth by means of gene expression quantification of the sensitive and resistant areas separately, to elucidate the genetic profile implied in the resistance mechanism.

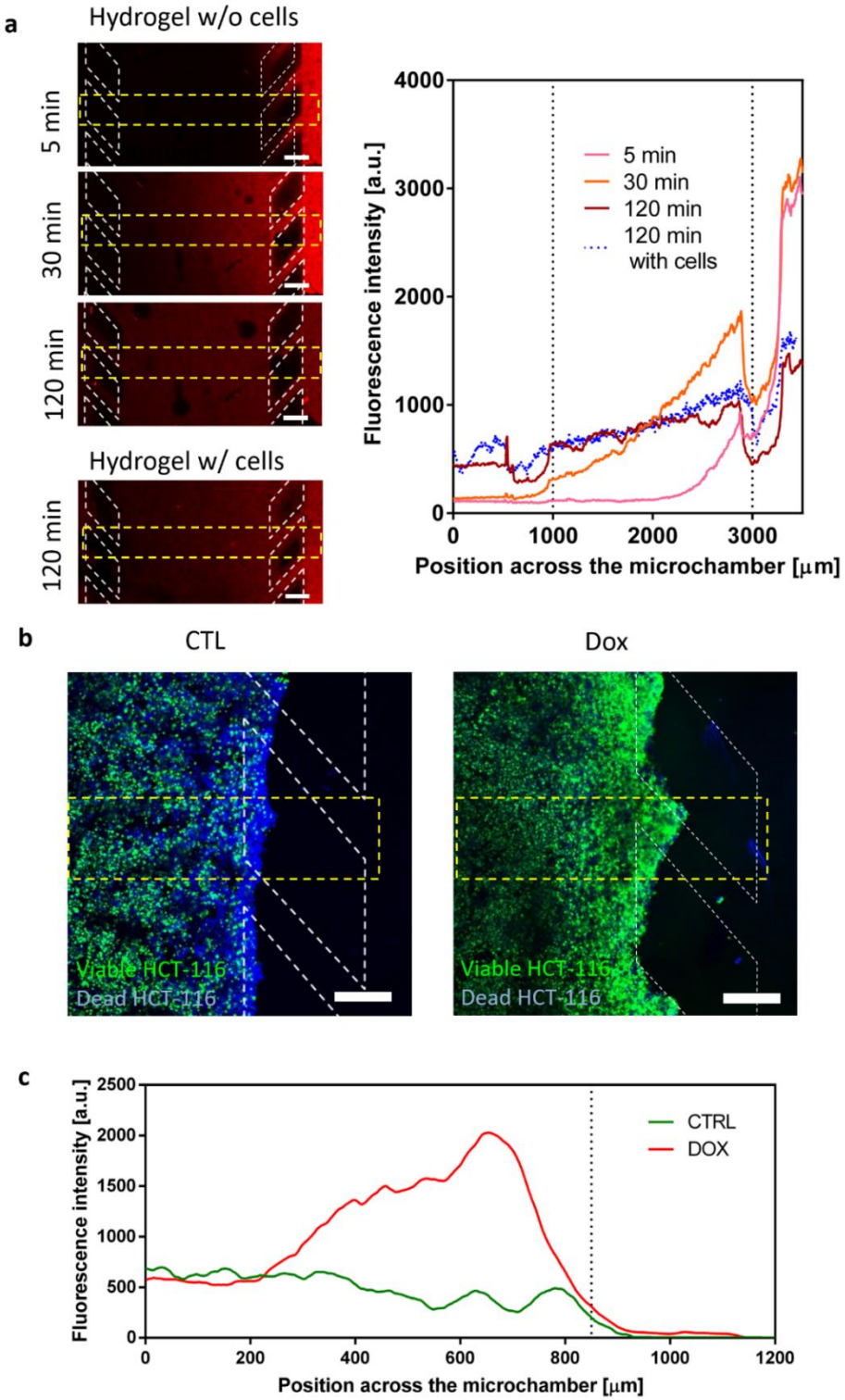

Figure 4.8: Doxorubicin effect on HCT-116 cells. The antiproliferative chemotherapy agent DOX was tested within the microdevice. a) 100 µM DOX was injected through one lateral microchannel to assess its penetration capacity through the hydrogel. The graph shows the doxorubicin diffusion profile along the time. b) 30 µM DOX was injected through both lateral microchannels to study the effect on cell viability. After 3 days in the presence of DOX, Nucblue and Nucgreen staining was injected through the lateral microchannel, showing all the cells in blue, whereas dead ones appear green. The graph shows the strong effect of doxorubicin on HCT-116 cell mortality. The green fluorescence intensity was analyzed along the delimited region. Image adapted from Ayuso et al [202].

4.3.7 Cell recovery from the microdevices.

All in all, previous results obtained in the group indicate that the model would greatly benefit from quantification of the genetic expression of the cells in the model.

. To this end, we adapted the tumor slice model to traditional molecular biology benchtop techniques by recovering the cultured cells in the central. Therefore, the tumor slice model, as well as 3D culture systems with a lower cell density, were extracted and their genetic profile was analyzed by RT-PCR (Figure 4.8). To enable cell recovery from the microdevices, an enzymatic degradation procedure was optimized to degrade the collagen hydrogel used as scaffold for the 3D cell culture.

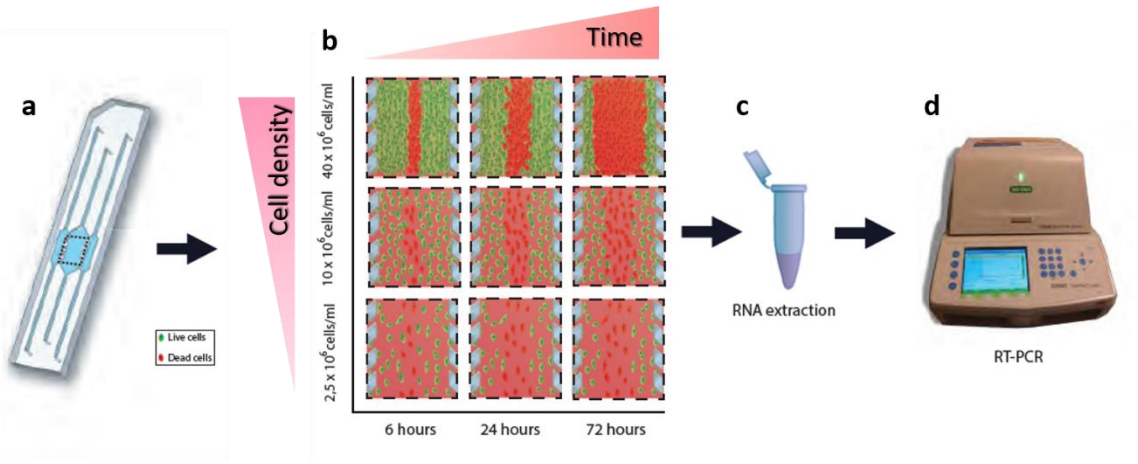

Figure 4.9: Scheme of the procedure for genomic analysis of the tumor microenvironment development. Cells are embedded in 3D in the central microchamber of the microfluidic device (a), generating different stages of tumor development according to cell concentration and time (b). Cells are extracted from the central microchamber via enzymatic degradation of the hydrogel and recollected in an Eppendorf tube for subsequent RNA extraction, cDNA synthesis (c) and RT-PCR to generate genetic profiles for different genes related to tumor metabolism.

To establish the cell recovery method, firstly we characterized the enzymatic degradation in terms of kinetics to optimize it for microfluidic applications.

First, we tracked the enzymatic degradation reaction kinetics by means of confocal reflection microscopy. The number of collagen fibrils diminished over time when the collagenase solution was added, progressively until no fibril is observed (Figure 4.10 a).

We also quantified in real time the area occupied by the collagen fibrils by means of Fiji, observing an exponential decay tendency in the curves (4.10 b). From this graph,

we can extract that the degradation dynamics is faster with higher concentrations of collagenase, as expected.

Furthermore, we fitted the linear fraction of the curve to a linear model and thus extracted the degradation velocities for each reaction. We found that the resulting graph was linear (y = 0.1457x + 0.0857). The constant term in this regression line is very small, which strongly suggests that the concentration of collagenase is the only factor contributing to the rate of the hydrogel degradation.

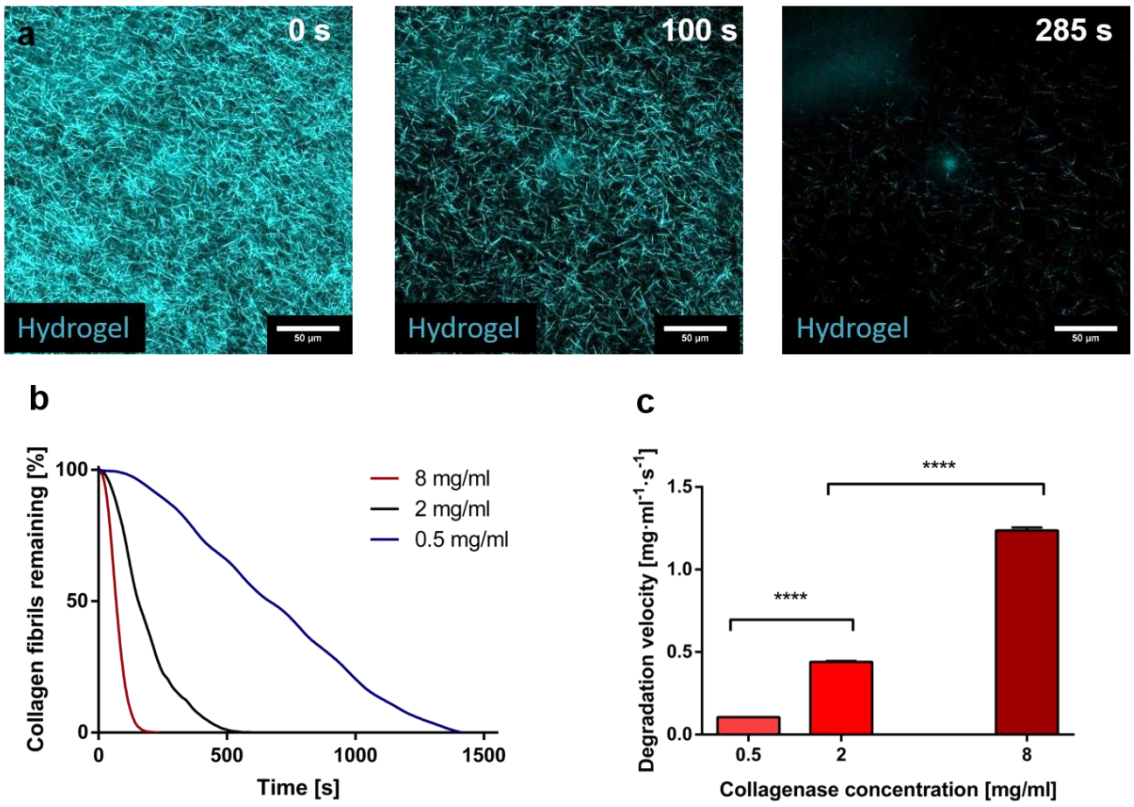

Figure 4.10: Optimization of the enzymatic degradation of collagen hydrogels. Confocal reflection microscopy of the degradation dynamics of a collagen hydrogel using an 8 mg/ml solution (18 IU/ml of collagenase P in PBS (a). The pictures show how the number of collagen fibrils constituting the hydrogel decreases overtime. (b) Quantification of the hydrogel degradation dynamics for different collagenase concentrations by means of area quantification for 0.5, 2 and 8 mg/ml. (c) Characterization of the degradation speed for the different collagenase concentrations. Linear fitting of the degradation speeds resulted in a linear equation (y = 0.1457x + 0.0857) R^2 = 0.9896. Graph shows average ± SEM (p-values < 0.001 in both cases).

On the other hand, we observed the degradation of a hydrogel confined within the central microchamber of the microdevice by Fluosphere® fluorescent tracking using time-lapse confocal microscopy. For quantification purposes, we divided the central chamber of the microdevice in 3 regions: the triangular regions, located further from the microchannels (sources of nutrients and oxygen); and a rectangular region, with more access to nutrients and oxygen (Figure 4.11a). At the beginning of the experiment, the hydrogel and the Fluospheres® were confined in the central microchamber of the microdevice. After pipetting collagenase solution (8 mg/ml) we observed how the Fluospheres® flowed out of the microdevice in a time scale consistent with the described kinetics (Figure 4.11b). Furthermore, after pipetting the degraded hydrogel out of the microdevice through the lateral microchannels, we observed that the majority of the Fluospheres® were extracted from the central microchamber. Only a fraction of those lying at the triangular ends of the central microchamber and in the central microchannels were not extracted, which constituted a statistically significant difference ($p<0.0001$).

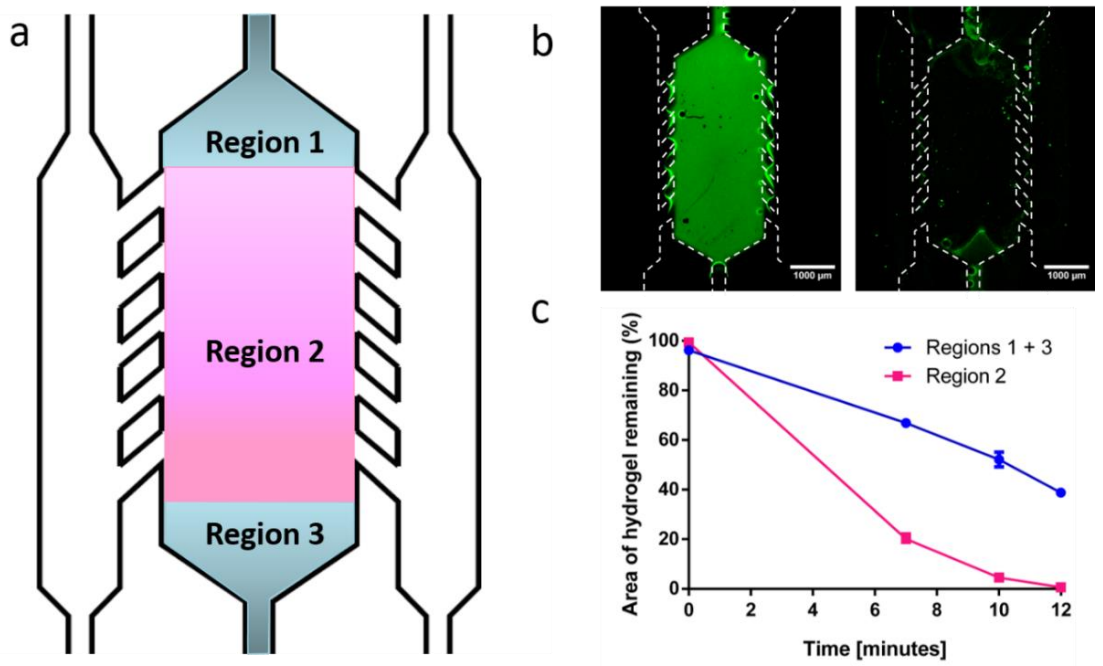

Figure 4.11: Recovery efficiency from the microdevices. a) The microdevice was divided into three different regions for the analysis: the triangular regions on both ends of the central microchamber and the rectangular region flanked by the pillars. b) Fluospheres® were embedded in a collagen hydrogel and confined in the central chamber of the microdevice. An 8 mg/ml collagenase P solution was pipetted through the lateral microchannels and incubated at room temperature for 7, 10 and 12 minutes. Images show the Fluospheres® before pipetting the collagenase solution and after 12 minutes. c) The area with remaining Fluospheres® was quantified for the defined regions and compared. Differences between regions 1+3 and region 2 were found statistically significant ($p<0.0001$).

4.3.8 Cell viability of the recovery procedure.

After establishing our degradation method, we proceeded to examine the possible effect of the collagenase on cell viability. To do so, we used both cell types used in this chapter (HCT-116 colon cancer cells and U-251 MG cells) and embedded them in a collagen hydrogel and cultured them for 24 hours. Next, we extracted and re-embedded cells using the highest collagenase concentration used in this work (8 mg/ml) (Figure 4.12 a). We evaluated cell viability by confocal microscopy with a viability staining after 72 hours compared to control conditions (Figure 4.12 b-c & e-f). No significant decrease in cell viability was found in any of the cell types used in this study (Figure 4.12d). Based on these results, we decided to use the highest collagenase

concentration for cell recovery from the microdevices, since it significantly accelerates the process and shows no damage to cell viability after 72 hours.

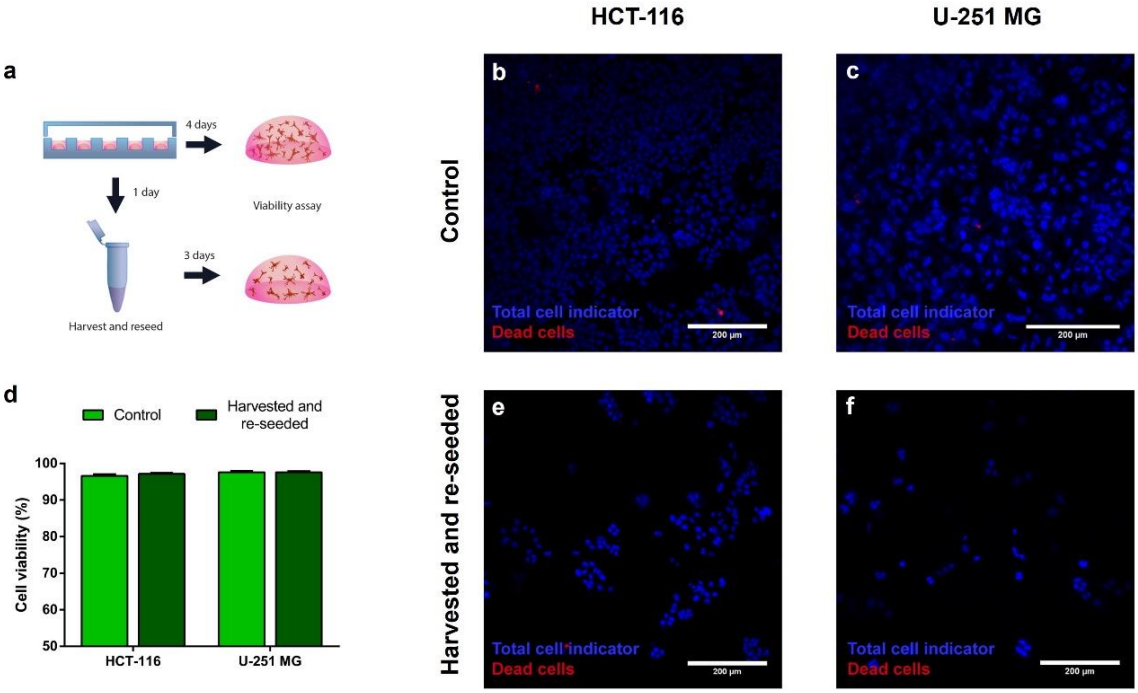

Figure 4.12: Biocompatibility of the cell extraction method. (a) Scheme of the experiment design. First, we embedded two distinctive cell types in collagen hydrogels. After 24 hours, cells were extracted from the hydrogels by enzymatic degradation with an 8 mg/ml (18 IU) solution of collagenase P in PBS. Recovered cells were thoroughly washed with PBS and re-embedded in collagen hydrogels. Cell viability was assessed after 72 hours by means of confocal imaging, the cell nuclei were stained (Hoechst 33342, blue) and a dead cell indicator was added to distinguish dead cells (propidium iodide, red). Results from extracted reseeded cells were compared with non-treated cells (control). Images of the control cells can be observed in (b) for HCT-116 cells and (c) for U-251 MG cells. Images of the recovered and re-embedded cells can be observed in (e) for HCT-116 cells and (f) for U-251 MG cells. (d) Quantification of cell viability for control and extracted and re-embedded cells, for both mentioned cell types used in this study.

4.3.9 Characterization of RNA extracted from recovered cells.

The next step to validate the cell recovery protocol is comparing the amount of RNA and its quality for control conditions (cells seeded in one well of a 6-well plate) and two microdevices. To do so, we used a commercial kit to extract RNA from both setups, and in case of the microdevices we first recovered the cells via incubation with collagenase solution, as described before. We first compared the concentration of RNA extracted and found that both setups produced approximately 170 ng/µl of RNA. Therefore, we found no statistically significant differences between the quantity of

RNA extracted from one well of a 6-well plate and from 2 microdevices (Figure 4.13, left panel).

Next, we assessed the quality of the extracted RNA, to discard a significant influence of the collagenase solution on RNA quality. Therefore, we assessed RNA quality by means of the 260/280 ratio. Interestingly, both setups produced 260/280 ratios of around 2, showing no significant differences between them (Figure 4.13, right panel). Overall, these data suggest that there is no negative influence of the extraction procedure on the quantity and quality of the RNA, as compared to one well of a 6-well plate.

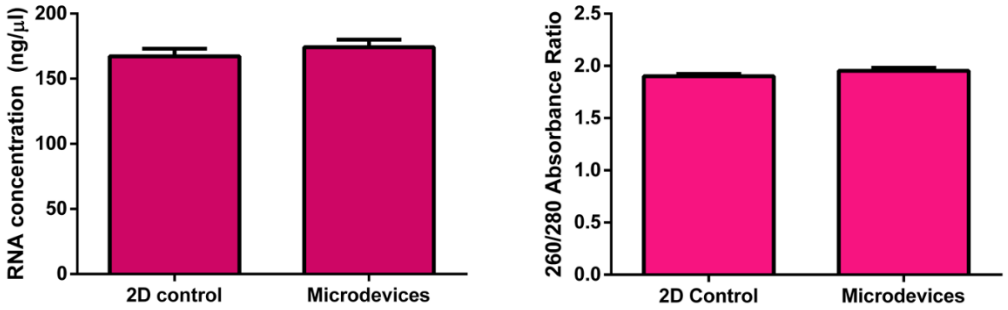

Figure 4.13: Assessment of the quantity and quality of RNA extracted from recovered cells. On the left, the graph shows the concentration of RNA extracted from 1 well of a 6-well plate and from 2 microdevices. On the right, the graph shows the quality of RNA extracted from the mentioned setups, expressed as 260/280 absorbance ratio. No statistically significant differences were found in either case.

4.3.10 RT-PCR demonstration of RNA from recovered cells.

Finally, for the purposes of this Thesis, we performed a proof of concept for real-time PCR analysis. First, we retrotranscribed the samples for a two-step RT-PCR procedure. Afterward, we chose various samples and performed a RT-PCR for the GAPDH gene, considered as an internal control. We also included negative controls in the quantification to discard cross-contamination. As shown in Figure 4.14, there was amplification in many samples, while others remained negative, as expected. Furthermore, the samples which showed no amplification matched the negative controls, thus disproving the presence of cross-contamination and validating the use of RNA from recovered cells for genetic profiling.

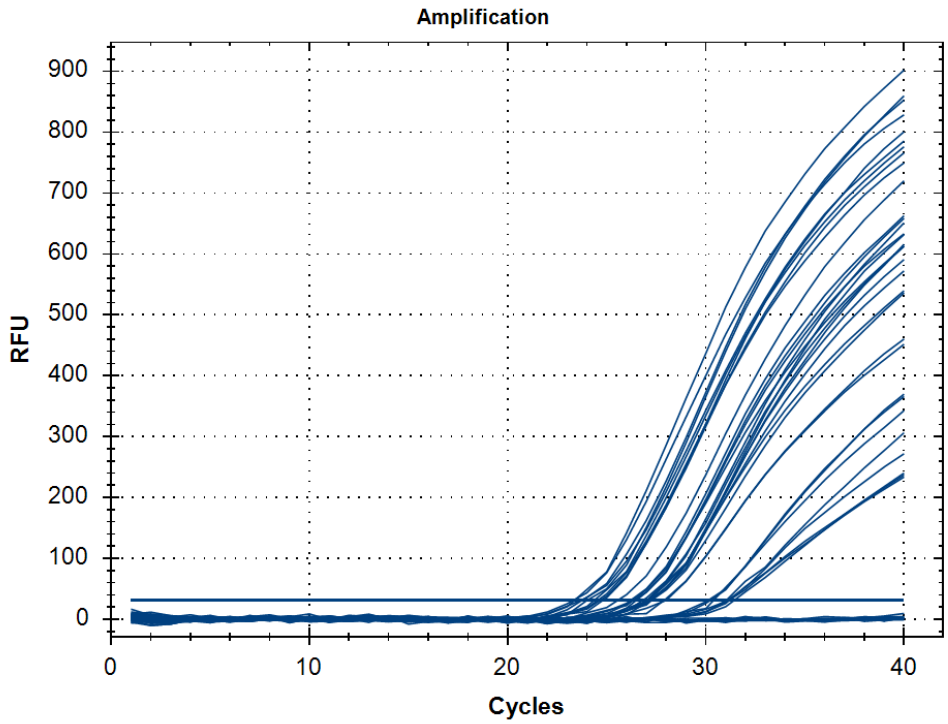

Figure 4.14: Proof of concept for the genetic profiling procedure. GAPDH was chosen as internal control to determine whether the RT-PCR method was viable on the RNA samples extracted from recovered cells. The image shows a capture from the RT-PCR program, indicating the amplification of many samples of the selected cohort.

4.3.11 Cell patterning in the microdevice.

As we discussed in previous sections, the spatial heterogeneity is a key aspect of the TME to be considered. Hence, we developed a method to pattern two different hydrogels in our microdevices, one inside the other. This fact is advantageous to discriminate different regions within the microdevice (for analysis purposes) or pattern different cell types to increase the complexity of the model.

The method is based on passive pumping mechanisms and requires generating hydrogels of different viscosity. Passive pumping is a mechanism occurring in fluids at the micro-scale and results in a driving force which can make liquids to flow through a microchannel. Based on this principle, the use of differently viscous hydrogels drives the width of the inner channel created by passive pumping. The higher the difference, the narrower the inner channel (Figure 4.15a).

To demonstrate this method in our microdevice, we first pipetted a highly viscous hydrogel by supplementation of 50% methylcellulose. Fluospheres® were added to this

hydrogel to observe the patterning. Next, a non-supplemented hydrogel droplet was placed on top of the inlet, and therefore passively pumped creating an inner non-labelled hydrogel (Figure 4.15 b). The patterning of both hydrogels can be observed in an orthogonal view (Figure 4.15 c). The fluorescence pattern strongly suggests the inner hydrogel created a "path" through the first hydrogel. Finally, we demonstrated the possibility of creating a HUVEC endothelium on the hydrogel interface by seeding the cells on a liquid-hydrogel interface. This can be achieved by substituting the second gel with PBS or culture media required for the cell seed (Figure 4.15 d). Overall, this method enables cell patterning in the central chamber of the microdevice, which can be used for combining different cell types, or for studying the normoxic and necrotic areas of the tumor slice model downstream separately.

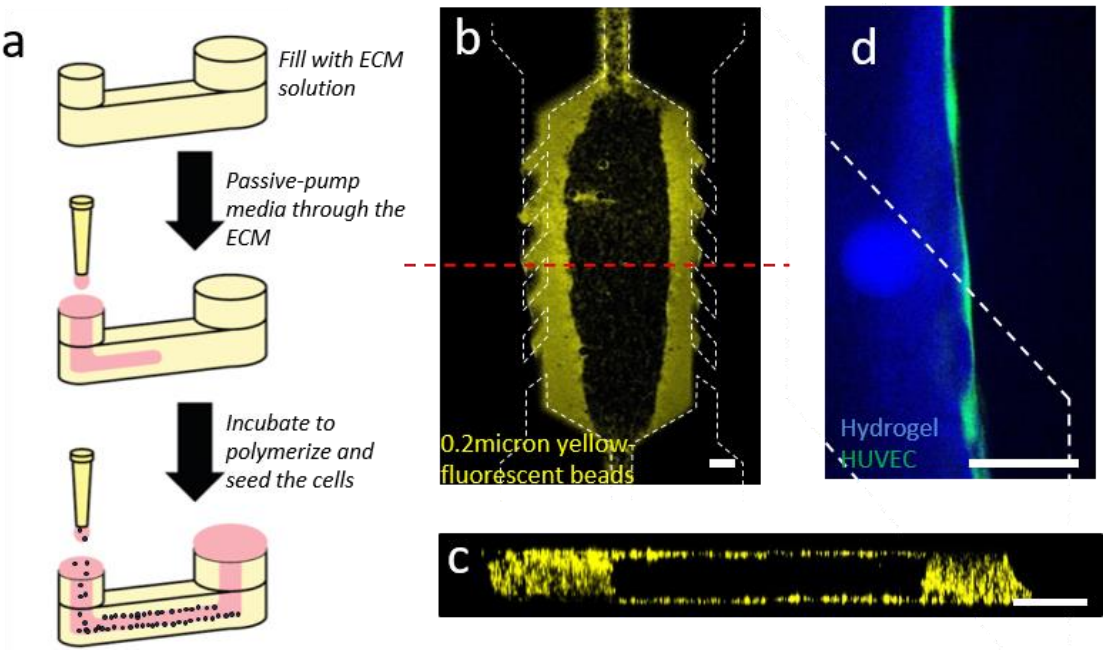

Figure 4.15: Patterning method in the microfluidic device. a) Protocol to generate blood vessel-like structures in microfluidic channels. After injecting a hydrogel, culture medium is injected through the channel to create a tunnel in the hydrogel. b) Example of tunnel through a hydrogel. For visualization purposes, 0.2µm diameter yellow-fluorescent spheres were embedded in the hydrogel. Scale bar is 400µm. c) Cross-section of the central microchamber. Scale bar is 400 µm. d) Image showing the HUVEC endothelium on the hydrogel interface. Hydrogel was visualized using confocal reflection microscopy and is shown in blue. HUVEC were stained with the CAM/PI solution, showing cells were alive. Scale bar is 150 µm.

4.4 Chapter summary.

In this chapter, we have established a "tumor slice model" by culturing cells in a microfluidic device at a sufficiently high density to generate necrotic cores. A necrotic core appeared after 1-3 days for the two different cell types. The appearance of a necrotic core is consistent with the existence of nutrient and hypoxia gradients. In the case of the latter, we have demonstrated their presence by using an oxygen-sensitive dye. Ultimately, both gradients have therefore a lower proliferation in the center of the central microchamber compared to the outer regions. All in all, this technique allows the reproduction of the spatial heterogeneity of a tumor *in vitro*, while enabling real-time monitoring of cellular and diffusion processes within the model.

Furthermore, we have developed a gel-in-gel patterning technique based on viscosity differences. This technique enables positioning of distinctive cells in the center of the microdevice chamber compared to the external regions. In particular, this facilitates the recreation of complex tissue structures *in vitro*, as well as permits labelling cells differently. Finally, by using proteolytic enzymes we have achieved the recovery of cells from a 3D cell culture in a hydrogel while maintaining their cell viability and within a short time-scale. Afterward, we have successfully extracted RNA from recovered cells, yielding a concentration and purity comparable to 2D controls in Petri dishes. Finally, we have successfully demonstrated RT-PCR for housekeeping genes using the extracted RNA from recovered cells. Moreover, the application of the patterning technique permits downstream discrimination of cells situated in the center (necrotic area) of the microdevice from cells situated in the edges (normoxic area). This fact enables the maintenance of spatial heterogeneity after cell recovery.

Overall, we have developed a microfluidic model of the TME, centered on the environment created by the tumor. The developed model includes the possibility of combining different cell types in the same microdevice and analyzing different regions of the model separately. We anticipate this model will provide valuable insight on the evolution of the tumor, which will potentially have a positive impact on *in vitro* and pre-clinical drug testing.

Chapter 5: Conclusions.

In this Thesis, we have used microfluidic approaches to reproduce and characterize accurately the tumor microenvironment. Hence, the main conclusions of the Thesis are summarized in a thematically organized manner below:

1. By means of capillarity, hydrophilic treatments and capillary valves, we have achieved a precise fluidic control to fill an open multiwell microfluidic device in only one pipetting step. Additionally, the generated liquid-air interface is flat and facilitates the generation of a 2D-3D co-culture microfluidic model of the tumor microenvironment.

2. Oxygen and proliferation gradients self-produced by the 3D embedded cells were achieved thanks to the oxygen-impermeable properties of SU-8.

3. The microfluidic 2D-3D model revealed the generation of gaps in the endothelium, which are consistent with the enhanced permeability and retention effect. In this context, the capacity of penetration and the anti-tumor efficiency have been probed for two TRAIL-based drug formulations, showing that LUV-TRAIL presents a higher bioactivity despite having a lower penetration rate through the endothelium.

4. We developed an oxygen-sensitive matrix which presents no significant differences from a native collagen matrix. This matrix allows detection of the oxygen tension at any location of a 3D assay without any modification of the culture system during the measurement thus avoiding the introduction of free elements which could interact with the system.

5. We have developed a mild enzymatic procedure to couple the tumor-slice model with gene profiling methods to characterize the tumor microenvironment for two different tumor types.

Capítulo 5: Conclusiones.

En esta tesis se han empleado aproximaciones microfluídicas para reproducir y caracterizar de manera precisa el microentorno tumoral. Así pues, las siguientes conclusiones de la presente tesis se detallan a continuación organizadas por temática:

1. Se ha logrado un control fluídico preciso para llenar un dispositivo microfluídico abierto al exterior mediante fuerzas capilares, tratamientos hidrofílicos y válvulas capilares, para generar un modelo microfluídico del microentorno tumoral mediante co-cultivo celular 2D3D.

2. Las propiedades físicas del SU-8, incluyendo la baja permeabilidad al oxígeno, han permitido la reproducción de gradientes de oxígeno y proliferación inducidos por las células.

3. La generación de poros en el endotelio del modelo microfluídico 2D3D son consistentes con el efecto de permeabilidad y retención mejorada. En dicho contexto, se ha determinado la capacidad de penetración y anti-tumoral de dos formulaciones de TRAIL, obteniendo el resultado de que LUV-TRAIL presenta una menor penetración, a la vez que una mayor bioactividad.

4. Se ha logrado una matriz sensible al oxígeno que no presenta modificaciones significativas con respecto a una matriz de colágeno convencional. Esta matriz permite la detección de la tensión de oxígeno en cualquier punto de un ensayo 3D sin menoscabo del sistema de cultivo celular durante la medida, y evitando la introducción de elementos libres que pudieran interaccionar con el sistema.

5. Hemos desarrollado un procedimiento enzimático para acoplar los modelos de “sección de tumor” con ensayos de perfilado genético para caracterizar el microentorno tumoral para dos tipos de tumor diferentes.

Chapter 6: Future work.

Although the obtained conclusions add further insight into the development and characterization of biomimetic systems of the tumor microenvironment, the obtained conclusions have opened other questions in that respect. Keeping this in mind, potentially interesting future research lines are mentioned within this section.

1. Increase the cellular complexity of our microfluidic tumor microenvironment models, adding more stromal components (such as immune cells and fibroblasts), assessing their interactions through exosome technology.

2. Characterize the validity of the enhanced tumor microenvironment model for drug testing applications.

3. Integrate the newly-developed oxygen-sensitive matrix in our model of the tumor microenvironment, to acquire real-time information on the oxygen profiles in the model.

4. Use the newly-developed oxygen-sensitive matrix to assess the possible drug-resistance of primary tumor cells, and to provide insight for the development of personalized medicine approaches for cancer patients.

5. Explore the effect of different microenvironments on the gene expression profile for different cancer models.

6. Utilize the information extracted from genetic profiles to characterize drug resistance evolution in tumor development.

7. Utilize the enhanced tumor-microenvironment model for high-throughput *in vitro* drug testing and contrast the results with those obtained in traditional petri dish models.

Output.

Journal publications.

1. "Nanoindentation-based imaging of alginate microcapsules for biocompatibility assessment" Maria Virumbrales-Muñoz, Edorta Santos, Laura Paz, Ignacio Ochoa, Jose Luis Pedraz, Manuel Doblaré, Luis Fernández. Manuscript in preparation for Nature Methods.

2. "Cell recovery from 3D cell culture microfluidic devices: bridging the gap between microfluidics and cancer genomics." María Virumbrales-Muñoz, Jose M. Ayuso, Alodia Lacueva, Inés Marmol, M. Jesús Rodriguez-Yoldi, Manuel Doblare, Luis Fernández, Ignacio Ochoa. Manuscript in preparation for Scientific Reports.

3. "Oxygen-sensitive three-dimensional matrix for in situ hypoxia detection in cell culture" María Virumbrales-Muñoz, José M. Ayuso, Ignacio Ochoa, Manuel Doblare, Luis J. Fernandez, Séverine Le Gac. Manuscript in preparation for Advanced Functional Materials.

4. "Multiwell capillary force-based microfluidic device for optical inspection of the endothelium integrity in co-culture models" María Virumbrales-Muñoz, José M. Ayuso, Marta Olave, Rosa Monge, Diego de Miguel, Luis Martínez-Lostao, Séverine Le Gac, Manuel Doblare Ignacio Ochoa, Luis J. Fernandez. Manuscript sent to Scientific Reports (March 2017)

5. "Glioblastoma on a microfluidic chip: Generating pseudopalisades and enhancing aggressiveness through blood vessel obstruction events" Jose M. Ayuso; Rosa Monge; Alicia Martinez-Gonzalez; Maria Virumbrales-Munoz; Guillermo A. Llamazares; Javier Berganzo; Aurelio Hernandez-Lain; Jorge Santolaria; Manuel Doblare; Christopher Hubert; Jeremy N. Rich; Pilar Sanchez-Gomez; Victor M. Perez-Garcia; Ignacio Ochoa; Luis J. Fernandez. Neuro-Oncology 2017; doi: 10.1093/neuonc/now230

6. "Development and characterization of a microfluidic model of the tumor microenvironment" Jose M. Ayuso, María Virumbrales-Muñoz, Alodia Lacueva, Pilar M. Lanuza, Elisa Checa-Chavarria, Pablo Botella, Eduardo Fernández, Manuel Doblare, Simon J. Allison, Roger M. Phillips, Julián Pardo, Luis J. Fernandez, Ignacio Ochoa. Scientific Reports. 2016 Oct 31;6:36086. doi: 10.1038/srep36086.

7. “Graphene oxide increases the viability of C2C12 myoblasts microencapsulated in alginate.” J. Ciriza; L. Saenz del Burgo; M. Virumbrales-Muñoz; I. Ochoa; L. J. Fernandez; G. Orive; M. R. Hernandez; J. L. Pedraz. International Journal of Pharmaceutics. 2015 Sep 30;493(1-2):260-70. doi: 10.1016/j.ijpharm.2015.07.062. Epub 2015 Jul 26.

Conference proceedings.

1. “Enabling gene profiling in microfluidic models for precision medicine.” María Virumbrales-Muñoz, Jose M. Ayuso, Alodia Lacueva, Manuel Doblaré, Ignacio Ochoa, Luis Fernández. Making it Personal: Cancer Precision Medicine. Amsterdam, (Netherlands). 13-16/3/2017. Poster

2. “Glioblastoma on a microfluidic chip: Mathematical and experimental validation of the pseudopalisades formation hypothesis” Alicia Martínez-González, Jose M. Ayuso, Rosa Monge, María Virumbrales-Muñoz, Guillermo A. Llamazares, Aurelio Hernández-Laín, Manuel Doblaré, Pilar Sánchez-Gómez, Ignacio Ochoa, and Luis J. Fernández, Víctor M. Pérez-García. World Federation of Neurooncology Societies Zurich (Switzerland). 4/5/2017. Poster

3. “Oxygen sensitive hydrogel matrix for cell culture and 3D oxygen concentration mapping” María Virumbrales-Muñoz; Adithya Sridhar; Rosa Monge; José M. Ayuso; Guillermo Llamazares; Ignacio Ochoa; Albert Ruggi; Luis Fernandez; Séverine Le Gac. Micro-TAS 2016. Dublin (Ireland) 9/10/2016. Poster.

4. “Oxygen sensitive hydrogel matrix for 3D cell culture and 3D oxygen concentration mapping”. María Virumbrales-Muñoz; Adithya Sridhar; Rosa Monge; José M. Ayuso; Guillermo Llamazares; Ignacio Ochoa; Albert Ruggi; Luis Fernandez; Séverine Le Gac. Nanobiotech Montreaux 2016. Montreux (Switzerland). 7/11/2016.

5. “Biomimetic microfluidic platform for 2D3D co-culture cancer models” María Virumbrales-Muñoz, Jose María Ayuso, Rosa Monge, Guillermo A. Llamazares, Marta Olave, Manuel Doblaré, Luis J. Fernández, Ignacio Ochoa. EACR24: From basic research to precision medicine. Manchester (United Kingdom) 9/7/2016. Poster.

6. “Engineering glioblastoma microenvironment in a chip to study cell response”. José María Ayuso, Rosa Monge, Guillermo A. Llamazares, María Virumbrales-Muñoz, Alodia Lacueva, Marta Olave, Manuel Doblaré, Luis J. Fernández,

Ignacio Ochoa. EACR24: From basic research to precision medicine. Manchester (United Kingdom) 9/7/2016. Poster.

7. “Microdevices as models to study the tumor behavior in high density cell cultures”. Jose M. Ayuso, María Virumbrales-Muñoz, Alodia Lacueva, Clara Alcaine, Rosa Monge, Guillermo A. Llamazares, Rebeca Guerrero, Alan Vigueras, Marta Olave, Manuel Doblaré, Luis J. Fernández, Ignacio Ochoa. EACR conference series 2016: A matter of life or death, Amsterdam, (The Netherlands). 28/01/2016. Poster.

8. “Oxygen-sensitive hydrogel for 3D cell culture and monitoring of biological samples” María Virumbrales-Muñoz, Adithya Sridhar, Rosa Monge, Jose María Ayuso, Guillermo A. Llamazares, Ignacio Ochoa, Albert Ruggi, Luis Fernández, Séverine Le Gac. NanoBioTech Montreaux (Switzerland). 18/10/2015. Poster.

9. "Engineering glioblastoma microenvironment in a chip to study cell response". Jose M. Ayuso, Maria Virumbrales-Muñoz, Guillermo A. Llamazares, Rosa Monge, Alan Vigueras, Pablo Sánchez, Marta Olave, Manuel Doblaré, Luis J. Fernández, Ignacio Ochoa II International Symposium on Clinical and Basic Investigation in Glioblastoma, Toledo (Spain), 9/09/2015. Poster.

10. "Biomimetic tumor microenvironment based on non-gas permeable polymeric microfluidic microdevices". Ignacio Ochoa, Rosa Monge, Guillermo A. Llamazares, Jose M. Ayuso, María Virumbrales-Muñoz, Alan Vigueras, Jorge Santolaria, Kamyar Afarinkia, Victoria Vinader, Haneen A. Basheer, Luis J. Fernandez. EACR Conference series 2014: Goodbye flat biology, Berlín (Germany). 2/11/2014. Poster.

Talks.

1. “Tubeless microfluidic device to study tumor-endothelium interactions” María Virumbrales-Muñoz. I Congreso Nacional de Jóvenes Investigadores en Biomedicina (ConBioPreVal 2016). Valencia (Spain). 28/11/2016. Oral Presentation.

2. “Biomimetic microfluidic devices: Advanced tumor models for apoptosis monitoring.” A. Vigueras; Virumbrales-Muñoz; M. Olave; R. Monge; J.M. Ayuso; G.

Llamazares; I. Ochoa-Garrido; L.J. Fernández. XII National congress on cell death. Aporeunión. Zaragoza (Spain). 20/05/2015. Oral Presentation.

Patents.

1. “Dispositivo conector para circuitos microfluídicos”. [P201631295]. July 2016.
2. “Dispositivo y sistema microfluídico para el estudio de cultivos celulares.” [P201531607]. June 2015.

Prizes.

1. “Best oral communication Prize” María Virumbrales-Muñoz. I Congreso Nacional de Jóvenes Investigadores en Biomedicina (ConBioPreVal 2016). Valencia (Spain). 28/11/2016.

2. Finalist at the Three Minute Thesis Contest. “Medicina Personalizada”. Zaragoza (Spain) 28/11/2016.

3. “EACR Poster Award”. "Engineering glioblastoma microenvironment in a chip to study cell response". José M. Ayuso, Maria Virumbrales-Muñoz, Guillermo A. Llamazares, Rosa Monge, Alan Vigueras, Pablo Sánchez, Marta Olave, Manuel Doblaré, Luis J. Fernández, Ignacio Ochoa. II International Symposium on Clinical and Basic Investigation in Glioblastoma, Toledo (Spain), 9/09/2015. Poster.

Appendix 1: Graphene oxide increases the viability of C2C12 myoblasts microencapsulated in alginate.

A1 Introduction to Atomic force microscopy.

Atomic force microscopy (AFM) is a generic term grouping a sort of techniques of surface measurements based on the interaction of a sharp nanometer-sized tip with the sample surface. They were first utilized by Binnig and Quate in 1986 [274], although they are adapted from scanning tunneling microscope in 1985, a similar technique intended to image structures at an atomic level [275].

AFM allows superficial characterization of a sample with nanometric and even atomic resolution. Furthermore, the variation of the tip properties enables different kinds of surface characterization. (e.g.) topographic, mechanical, magnetic, molecular recognition or affinity and even the identification of different compounds in a complex sample [276-281]. These variety of techniques are represented in Figure A1.

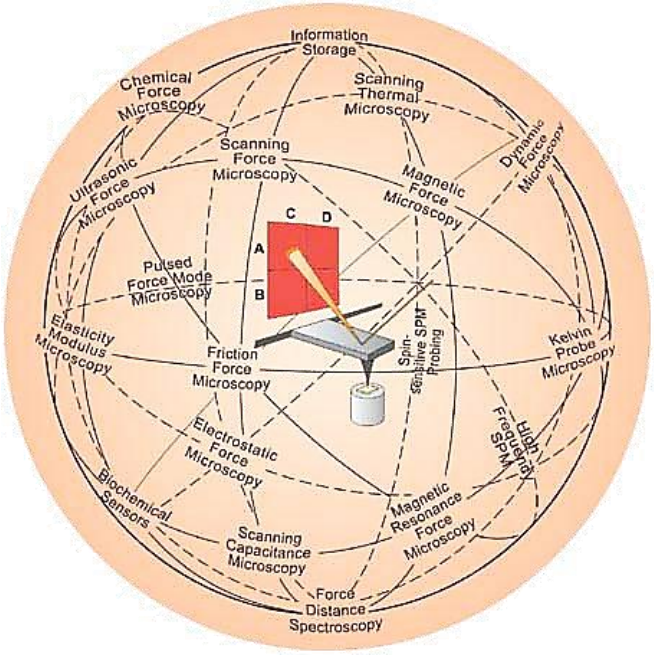

Figure A1: The AFM (center) has inspired a variety of other scanning probe techniques. Originally the AFM was used to image the topography of surfaces, but by modifying the tip it is possible to measure other quantities (for example, electric and magnetic properties, chemical potentials, friction and so on), and to perform various types of spectroscopy and analysis. Image reproduced with permission [282].

AFM is based on the interaction of a microscopic probe (usually known as cantilever) with the sample surface. The effect of such interaction on the sample translates into a cantilever deflection, which is most commonly detected by means of a laser-based optical system. More specifically, a laser reflects on the cantilever and is directed onto a photodiode, which interprets the luminous signal into an electric and measurable one in Volts (Figure A2) [283,284].

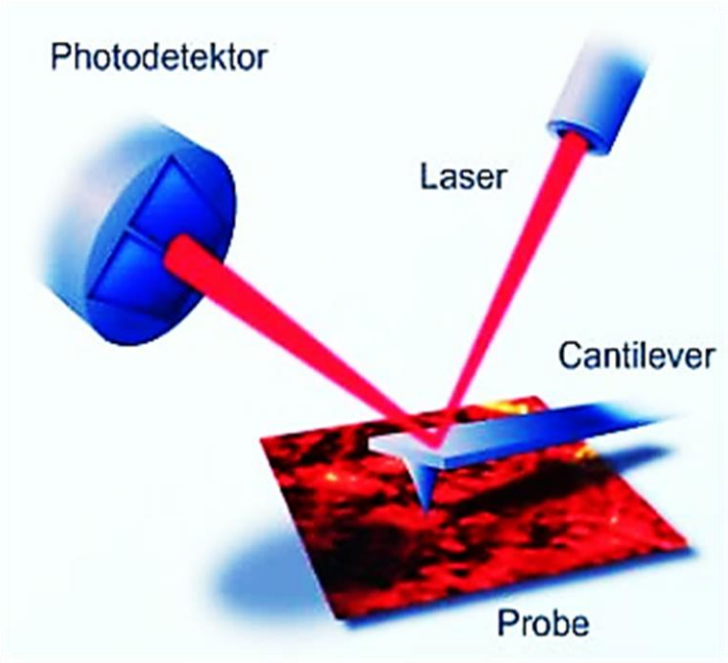

Figure A2: Scheme of the operation of an AFM. A laser beam impacts on the back of the cantilever and reflects onto the photodetector. The deflections of the cantilever while interacting with the sample are detected through the movement of the laser beam upon the photodiode. Images reproduced from Handbook Nanowizard® AFM Version 4.3-07/2015 JKP Instruments.

To convert these electric measurements in force measurements, the cantilever is calibrated previously based on Hooke's law. This calibration can be performed via diverse methods, all eventually determining the elastic constant of the cantilever [285].

AFM presents many advantages over traditional methods of microscopy. The main advantage is that its resolution does not rely on lenses, and therefore it is not limited by diffraction. Conversely, AFM resolution is limited by the interaction of the probe with the surface, which may go down to a few picometers. Furthermore, AFM provides much information about the nature of the surfaces, even during the same scanning

motion. Moreover, AFM can also be used to modify a surface, through the technique known as dip-pen [286]. Finally, an important advantage of AFM is that sample preparation is easy, and modification of the sample for processing is unnecessary [287,288]. This is possible, since measurements in air and liquid are compatible even with sub-nanometric resolution.

However, AFM also presents a few limitations. Firstly, acquisition times are usually long, which incurs in sample displacement due to thermal effects. Finally, these techniques require a continuous medium for measuring. In other words, they are not very useful to examine solid-solid or liquid-liquid interfaces [289].

As it was mentioned in this section, AFM comprises many techniques and measurement modes. For the purposes of this Thesis, we will only explain one measurements mode: force-spectroscopy-based imaging. In this mode, the cantilever is brought into contact with the sample surface with a defined force. Very close to the surface, the cantilever jumps into contact with the surface, thanks to weak forces between both elements. The indentation of the cantilever in the sample provides stiffness data. Furthermore, while the cantilever is in contact with the sample, repulsive contacts between sample and cantilever appear. Afterward, the cantilever is retracted from the sample, although the contact persists, thus informing of adhesive forces between cantilever and sample. At some point, retraction force will overcome adhesion forces. Hence, the cantilever finally retracts from the sample (Figure A3).

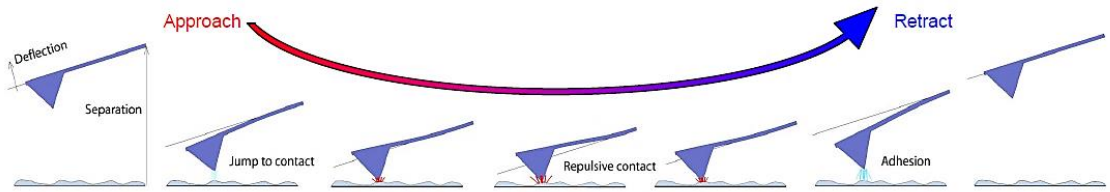

Figure A3: Scheme of the forces present in tip-sample interactions during approach and retraction cycles.

In this Thesis, we have used force mapping and QI® (Quantitative Imaging). Both these work modes are based on consecutive force spectroscopy sets organized in grids. While the first one focuses on extracting information about stiffness and adhesive forces, the second one also provides topography data, simultaneously to stiffness and adhesive forces.

A feature of the AFM equipment utilized in this Thesis is that it is ideally suited to handle liquid samples. It includes a thermostated setup compatible with 30 mm Petri Dishes, which makes it possible to work comfortably in liquids (including other than distilled water) in relatively big setups pre-conditioned to a physiological temperature, such as the one described in the following work.

In the following section, an application of AFM through force-spectroscopy-based imaging in physiological conditions is described.

A2 Application of AFM to microcapsule characterization.

A2.1 Introduction.

Cell microencapsulation is widely used in research as a delivery system for therapeutic drugs. The structure of the capsule enables the flow of nutrients and gases (O_2 and CO_2) between its outer and inner side, as well as the waste outlet and release of therapeutic molecules produced de novo by encapsulated cells. The aim is to create a suitable microenvironment that promotes and controls cell viability and proliferation. Furthermore, microcapsules protect the cells from the immunological rejection they would suffer from if cells were directly implanted in an immunocompetent host. In fact, microcapsules do not allow the entrance of immunoglobulins or the recognition of the cells by the immune system [290]. Different biomaterials such as agarose, chitosan or hyaluronic acid have been used for cell microencapsulation [99,291,292]. However, alginate remains the most common choice for the development of such systems due to its excellent biocompatibility and suitable mechanical properties [102]. Pancreatic islets encapsulation in alginate matrices is the field in which cell microencapsulation has made more progress, with promising results starting in the early 90s. Encouragingly, one patient got to be independent of insulin injections for 9 months thanks to the intraperitoneal administration of pancreatic islets encapsulated in alginate [293-295]. Currently, clinical trials are assessing the use of encapsulated xenogeneic islet transplants and they are showing an adequate biosafety profile

together with high effectiveness in patients with type I diabetes mellitus [296,297]. Our research group has previously studied the microencapsulation of genetically modified C2C12 myoblasts to secrete erythropoietin (EPO), and showed that the encapsulation of these cells allows the release of EPO for at least 210 days in an allogeneic transplant and for 98 days in a xenogeneic transplant [298,299].

Despite the great promise of cell encapsulation technology, there have been continuous challenges in cell therapy using microencapsulated cells. The major one has been to decrease the number of dying cells inside the microcapsules. In fact, these cells release factors that are detrimental to the health of neighboring cells. Moreover, they can be released to the host environment eliciting an antigenic response [300]. Thus, the search of new materials that can enhance microencapsulated cells viability is one the most important current trends on cell microencapsulation field.

Research on graphene, a two-dimensional sheet with exceptional electrical, mechanical and thermal properties, has grown exponentially since its discovery. Its application in electronic and optoelectronic systems, in medicine, as photoconductive materials and delivery systems of therapeutic drugs, or even in tissue engineering has been explored [301]. Similarly, the application of nanomaterials from graphene derivatives, such as graphene oxide, has been studied. Graphene oxide (GO) is a chemically modified highly oxidized form of graphene, consisting of single atom thick layer of graphene sheets with carboxylic acid, epoxide and hydroxyl groups [301]. Thus, for example, surfaces of graphene and GO have shown to support proliferation and differentiation of induced pluripotent stem cells, promoting differentiation toward endoderm lines such as the insulin producing cells [302]. Moreover, graphene and GO increase the adhesion, proliferation and differentiation of mesenchymal stem cells toward osteogenic and adipogenic lines respectively [303,304]. GO has also shown a higher rate of maturation from murine myoblasts into myotubes compared with other materials [305]. Although most of the studies reported are performed on two-dimensional (2D) graphene materials, three-dimensional (3D) scaffolds have also been studied. For instance, graphene foams support neural stem cell (NSC) proliferation and differentiation toward neuronal lineages [306]. 3D composite scaffolds have also been fabricated with gelatin methacrylate and GO, enhancing gelatin methacrylate

mechanical and electrical properties, while not affecting the viability of encapsulated fibroblast cells [307]. Overall, graphene materials, either on 2D or 3D, seem to promote the proliferation of different cell types although more detailed in vitro characterization of scaffolds needs to be done. Because of the unique properties of GO, we propounded to combine cell microencapsulation technology with this material. In fact, the selection of suitable polymer-matrices is essential to achieve long-term treatments with encapsulated cells. For example, alginate and pectin microcapsules have shown more resistance and maintenance of an adequate microenvironment for enclosed GDNF secreting Fischer rat 3T3 fibroblasts than the combination of alginate with other materials, such as cellulose sulfate or agarose [308]. Currently, there is only one study that has combined alginate capsules with GO. In this study, the size of alginate beads containing GO was 50 millimeters of diameter, suggesting the application of these spheres as efficient copper adsorption material [309]. The aim was to incorporate different concentrations of GO into 160 mm-diameter alginate microcapsules, characterize their physical properties and test its biocompatibility with EPO producing C2C12 myoblasts within the microcapsules for future clinical applications.

A2.2 Material and methods.

A2.2.1 Biomaterials.

Graphene oxide (GO) 5 wt.% was obtained from Graphenea Company (Spain). The product was suspended in water and sonicated for 1 h to obtain a higher percentage of monolayer flakes. Ultra-pure low-viscosity and high glucuronic acid alginate (LVG) was purchased from FMC Biopolymer (Norway). Poly-L-lysine hydrobromide (PLL, 15–30 kDa) was purchased from Sigma–Aldrich (St. Louis, MO).

A2.2.2 Atomic force microscopy (AFM).

Mechanical characterization of capsules was measured by AFM on a JPK Nanowizard 3 (JPK instrument, Berlin, Germany) coupled with an inverted microscope (NIKON Ti, Nikon Instruments). The samples were maintained at constant temperature by a PetriDish Heater® included in the system. QI® and Force Mapping modes were used for topography and apparent Young's moduli respectively, since they have been reported as successful methods for these applications [90,310]. PNP-TR cantilevers (NanoAndMore, GMBH) with tip A were chosen due to the adequacy of its nominal spring constant, (0.32 N/m). Each tip was precisely characterized by thermal noise method before each measurement.

For the experimental setup, the capsule was immobilized first to place the cantilever centered on top. Briefly, a 100-nm nylon mesh (Merck Millipore) was fixed to a Petri dish using a standard cyanoacrylate adhesive. Then, the dish was filled with Dulbecco's Modified Eagle's Medium (Sigma–Aldrich) and 20 mM in HEPES buffer (Sigma–Aldrich). Ten microliters of the capsule suspension were subsequently pipetted on the center of the dish and left alone for 5 min to let them reach 37 ^{0}C. Finally, a capsule centered within the nylon holes was identified by means of the optical microscope, and the AFM measurements were carried out.

At least 5 capsules for each sample were studied. Image and data were processed with JPK Data Processing (JPK Instrument, Berlin, Germany) software. QI image data were flattened and low frequency enhancement was subsequently performed on each image. Young's moduli were calculated by applying the Hertz model to each curve in the Force Map. Mode values were extracted from data histograms for every microcapsule.

A2.2.3 Statistical analysis.

Statistical analysis was performed using SPSS software, version 21.00.1, or GraphPad Prism 5.01 (GraphPad Inc., San Diego, CA). Data are expressed as mean ± standard error of the mean. Values from $p < 0.05$ to $p < 0.001$ were considered significant for comparison of groups using ANOVA, Tukey's post hoc test.

A2.3 Results.

Firstly, we attempted to produce alginate microcapsules smaller than 200 mm of diameter containing different concentrations of graphene oxide (GO) from the highest concentration of 1 mg GO/ml to the lowest of 50 µg GO/ml, based on previous descriptions of GO encapsulation into 0.5 cm of diameter alginate gel beads [309]. GO concentrations of 1 mg/ml plugged up the pneumatic atomization generator (Bioencapsulation portable platform Cellena), being 500 µg/ml the highest suitable GO concentration to incorporate into the matrix of alginate microcapsules with this system. After recovering the microcapsules from the CaCl2 where they gellified, it was already evident the presence of GO inside the microcapsules by simply observing the increase on brown color intensity as the GO concentration was raised (Figure A4).

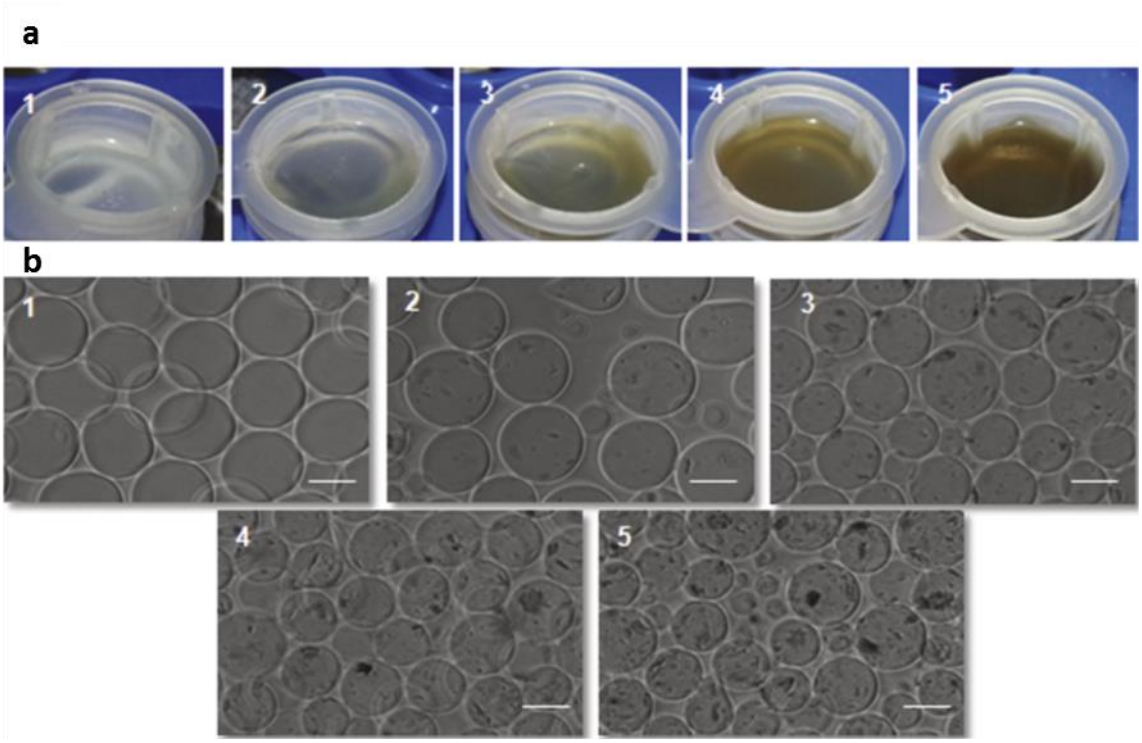

Figure A4: Fabrication and final aspect of the fabricated alginate microcapsules. (A) Macroscopic images of alginate and alginate–GO microcapsules collected over 100 mm strainers. (B) Microscopy images from alginate and alginate–GO microcapsules. Scale bar 100 mm. Note: final concentration of GO in the core of microcapsules: (1) alginate microcapsules without GO, (2) 50 mg/ml, (3) 125 mg/ml, (4) 250 mg/ ml and (5) 500 mg/ml.

Another key property on alginate microcapsules is their external surface. Thus, we analyzed our alginate–GO microcapsules under atomic force microscopy (AFM) [311]. Firstly, we performed Force Mapping experiments on each capsule, to extract Young's moduli, since measurements tended to be most precise through this method. Force Mapping was followed by QI imaging for each capsule. We found this method was most appropriate for our samples, given that they are loosely immobilized and the applied force can be easily controlled through this method [312].

Our results showed very homogeneous topographical images for capsules lacking coatings and GO, with more smoothed surfaces after PLL and alginate coating addition. In fact, the PLL and alginate coating seemed to cover the grooves present in non-coated microcapsules (Fig. A5 A, B). However, the addition of GO nanoparticles seemed to create inhomogeneous surface structures, which arose more frequently when GO concentrations were increased (Fig. A5 C–F). When PLL was added to alginate–GO microcapsules, a certain evenness of the surfaces was observed, particularly for intermediate GO concentrations, as the images produced were flatter than those ones corresponding to non-coated microcapsules (Fig. A5 D, F). Therefore, we could confirm that the coating of alginate microcapsules containing GO with PLL and alginate improves their surface biocompatibility by providing a smoother surface.

As for apparent Young's moduli, capsules lacking coatings and GO showed the highest values. When coatings were added, apparent Young's moduli of microcapsules dropped, probably due to the low rigidity of the PLL compared to the core (Fig. A6). When alginate–GO, microcapsules were compared, apparent rigidity on the coated ones increased above non-coated stiffness values, while higher concentrations of GO tend to increase apparent rigidity in microcapsules. This suggests an interaction between alginate and GO nanoparticles, which could be creating a lower density structure and a lower apparent Young's Moduli. The interaction between alginate and GO nanoparticles could be established through edge-to-edge or face-to-face interactions between Ca^{2+} and GO, since Ca^{2+} has shown to be effective in aggregating GO nanosheets [313,314].

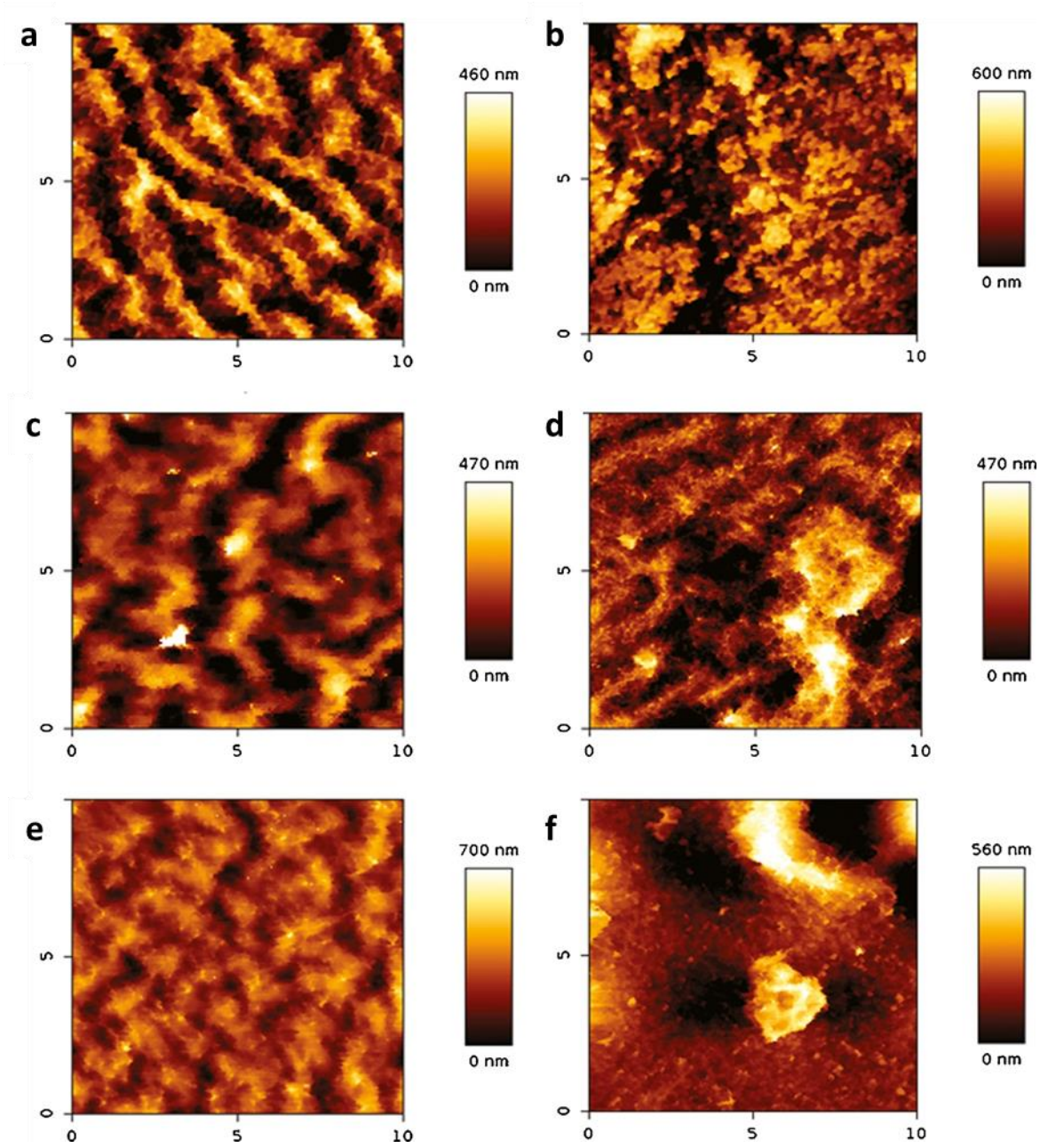

Figure A5. Atomic force microscopy (AFM) images from microcapsules containing graphene oxide (A) without GO non-coated microcapsules. (B) Without GO coated microcapsules. (C) With 125 mg/ml GO non-coated microcapsules. (D) With 500 mg/ml GO coated microcapsules. (E) With 125 mg/ml GO non-coated microcapsules. (F) With 500 mg/ml GO coated microcapsules. Scale bar in mm.

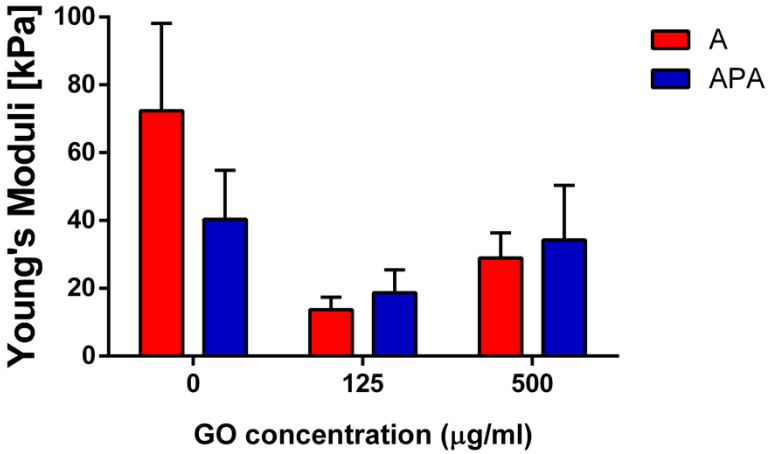

Figure A6: Apparent Young's Moduli for the alginate microcapsules as measured through Force Spectroscopy. Microcapsules of 0, 125 and 500 μg/ml of graphene oxide, both with and without poly-lysine-alginate coating were examined. No statistically significant differences were found.

A2.4 Conclusions.

Altogether, our results show that GO concentrations between 25 and 50 mg/ml increase the viability, metabolic activity and membrane integrity of encapsulated C2C12–EPO myoblasts. The better viability obtained by the presence of GO inside the capsules could be beneficial for the therapy, since it provides a healthier microenvironment for the encapsulated cells. Moreover, the fact that GO contains a range of functional groups facilitates its application in Biomedicine. Importantly, GO shows good properties in this sense since it is cheap to produce, has a large surface area and has shown low toxicity. In conclusion, this kind of biocompatibility studies in alginate–GO cell microencapsulation (3D cultures) should be performed for each cell type and therapeutic protein since the GO concentrations might affect the viability of each cell type while the adsorption capacity of the GO nanoparticles might also be different depending on the secreted protein. Moreover, the size of GO particles should be controlled because different sizes seem to induce different responses from cells [315,316].

References.

1. Bernstein (February 2011) Bernstein Research Pipeline Report.

2. Scannell JW, Blanckley A, Boldon H, Warrington B (2012) Diagnosing the decline in pharmaceutical R&D efficiency. Nat Rev Drug Discov 11: 191-200.

3. Sackmann EK, Fulton AL, Beebe DJ (2014) The present and future role of microfluidics in biomedical research. Nature 507: 181-189.

4. Marshall JC (2014) Why have clinical trials in sepsis failed? Trends Mol Med 20: 195-203.

5. Andrade EL, Bento AF, Cavalli J, Oliveira SK, Freitas CS, et al. (2016) Non-clinical studies required for new drug development - Part I: early in silico and in vitro studies, new target discovery and validation, proof of principles and robustness of animal studies. Brazilian Journal of Medical and Biological Research 49.

6. Bunnage ME (2011) Getting pharmaceutical R&D back on target. Nat Chem Biol 7: 335-339.

7. Kostewicz ES, Abrahamsson B, Brewster M, Brouwers J, Butler J, et al. (2014) In vitro models for the prediction of in vivo performance of oral dosage forms. European Journal of Pharmaceutical Sciences 57: 342-366.

8. Seo BR, Delnero P, Fischbach C (2014) In vitro models of tumor vessels and matrix: engineering approaches to investigate transport limitations and drug delivery in cancer. Adv Drug Deliv Rev 69-70: 205-216.

9. Banerjee J, Shi Y, Azevedo HS (2016) In vitro blood–brain barrier models for drug research: state-of-the-art and new perspectives on reconstituting these models on artificial basement membrane platforms. Drug Discov Today 21: 1367-1386.

10. Edwards AM, Arrowsmith CH, Bountra C, Bunnage ME, Feldmann M, et al. (2015) Preclinical target validation using patient-derived cells. Nat Rev Drug Discov 14: 149-150.

11. Paul SM, Mytelka DS, Dunwiddie CT, Persinger CC, Munos BH, et al. (2010) How to improve R&D productivity: the pharmaceutical industry's grand challenge. Nat Rev Drug Discov 9: 203-214.

12. Moreno L, Pearson AD (2013) How can attrition rates be reduced in cancer drug discovery? Expert Opin Drug Discov 8: 363-368.

13. Siegel RL, Miller KD, Jemal A (2016) Cancer statistics, 2016. CA Cancer J Clin 66: 7-30.

14. Ferlay J, Soerjomataram I, Dikshit R, Eser S, Mathers C, et al. (2015) Cancer incidence and mortality worldwide: Sources, methods and major patterns in GLOBOCAN 2012. Int J Cancer 136: E359-E386.

15. Bray F, Ren J-S, Masuyer E, Ferlay J (2013) Global estimates of cancer prevalence for 27 sites in the adult population in 2008. Int J Cancer 132: 1133-1145.

16. M. Ervik FL, J. Ferlay, L. Mery, I. Soerjomataram, F. Bray (2016) Cancer Today. Lyon, France: International Agency for Research on Cancer. . Cancer Today.

17. Harrington KJ (2011) Biology of cancer. Medicine 39: 689-692.

18. Bertram JS (2000) The molecular biology of cancer. Molecular Aspects of Medicine 21: 167-223.

19. Hanahan D, Weinberg RA (2000) The Hallmarks of Cancer. Cell 100: 57-70.

20. Espina V, Liotta LA (2011) What is the malignant nature of human ductal carcinoma in situ? Nat Rev Cancer 11: 68-75.

21. Hanahan D, Weinberg RA (2011) Hallmarks of cancer: the next generation. Cell 144: 646-674.

22. Joyce JA (2005) Therapeutic targeting of the tumor microenvironment. Cancer Cell 7: 513-520.

23. Balkwill FR, Capasso M, Hagemann T (2012) The tumor microenvironment at a glance. J Cell Sci 125: 5591-5596.

24. Quail DF, Joyce JA (2013) Microenvironmental regulation of tumor progression and metastasis. Nat Med 19: 1423-1437.

25. Hanahan D, Coussens Lisa M (2012) Accessories to the Crime: Functions of Cells Recruited to the Tumor Microenvironment. Cancer Cell 21: 309-322.

26. Mehlen P, Puisieux A (2006) Metastasis: a question of life or death. Nat Rev Cancer 6: 449-458.

27. Tomasek JJ, Gabbiani G, Hinz B, Chaponnier C, Brown RA (2002) Myofibroblasts and mechano-regulation of connective tissue remodelling. Nat Rev Mol Cell Biol 3: 349-363.

28. Bergers G, Song S (2005) The role of pericytes in blood-vessel formation and maintenance. Neuro-Oncology 7: 452-464.

29. Ribeiro AL, Okamoto OK (2015) Combined Effects of Pericytes in the Tumor Microenvironment. Stem Cells International 2015: 868475.

30. Fang J, Nakamura H, Maeda H (2011) The EPR effect: Unique features of tumor blood vessels for drug delivery, factors involved, and limitations and augmentation of the effect. Adv Drug Deliv Rev 63: 136-151.

31. Khawar IA, Kim JH, Kuh HJ (2015) Improving drug delivery to solid tumors: priming the tumor microenvironment. J Control Release 201: 78-89.

32. Gajewski TF, Schreiber H, Fu Y-X (2013) Innate and adaptive immune cells in the tumor microenvironment. Nat Immunol 14: 1014-1022.

33. Frantz C, Stewart KM, Weaver VM (2010) The extracellular matrix at a glance. J Cell Sci 123: 4195-4200.

34. Lu P, Takai K, Weaver VM, Werb Z (2011) Extracellular Matrix Degradation and Remodeling in Development and Disease. Cold Spring Harbor perspectives in biology 3: 10.1101/cshperspect.a005058 a005058.

35. Bergamaschi A, Tagliabue E, Sørlie T, Naume B, Triulzi T, et al. (2008) Extracellular matrix signature identifies breast cancer subgroups with different clinical outcome. J Pathol 214: 357-367.

36. Kessenbrock K, Plaks V, Werb Z (2010) Matrix Metalloproteinases: Regulators of the Tumor Microenvironment. Cell 141: 52-67.

37. Discher DE, Janmey P, Wang YL (2005) Tissue cells feel and respond to the stiffness of their substrate. Science 310: 1139-1143.

38. Handorf AM, Zhou Y, Halanski MA, Li W-J (2015) Tissue Stiffness Dictates Development, Homeostasis, and Disease Progression. Organogenesis 11: 1-15.

39. Wang JH, Thampatty BP (2006) An introductory review of cell mechanobiology. Biomech Model Mechanobiol 5: 1-16.

40. Frey MT, Tsai IY, Russell TP, Hanks SK, Wang Y-l (2006) Cellular Responses to Substrate Topography: Role of Myosin II and Focal Adhesion Kinase. Biophys J 90: 3774-3782.

41. Chen CS, Mrksich M, Huang S, Whitesides GM, Ingber DE (1997) Geometric control of cell life and death. Science 276: 1425-1428.

42. Beebe DJ, Mensing GA, Walker GM (2002) Physics and applications of microfluidics in biology. Annu Rev Biomed Eng 4: 261-286.

43. Images D (2017) https://fr.dreamstime.com.

44. Keenan TM, Folch A (2008) Biomolecular gradients in cell culture systems. Lab Chip 8: 10.1039/b711887b.

45. Eccles SA (2005) Targeting key steps in metastatic tumour progression. Curr Opin Genet Dev 15: 77-86.

46. Brahimi-Horn MC, Pouyssegur J (2009) HIF at a glance. J Cell Sci 122: 1055-1057.

47. Semenza GL (2010) Defining the role of hypoxia-inducible factor 1 in cancer biology and therapeutics. Oncogene 29: 625-634.

48. Semenza GL (2003) Targeting HIF-1 for cancer therapy. Nat Rev Cancer 3: 721-732.

49. Rapisarda A, Uranchimeg B, Scudiero DA, Selby M, Sausville EA, et al. (2002) Identification of small molecule inhibitors of hypoxia-inducible factor 1 transcriptional activation pathway. Cancer Res 62: 4316-4324.

50. Subarsky P, Hill RP (2003) The hypoxic tumour microenvironment and metastatic progression. Clin Exp Metastasis 20: 237-250.

51. Tredan O, Galmarini CM, Patel K, Tannock IF (2007) Drug resistance and the solid tumor microenvironment. J Natl Cancer Inst 99: 1441-1454.

52. Knoll G, Bittner S, Kurz M, Jantsch J, Ehrenschwender M (2016) Hypoxia regulates TRAIL sensitivity of colorectal cancer cells through mitochondrial autophagy. Oncotarget.

53. Lee Y-J, Lee J-H, Moon J-H, Park S-Y (2014) Overcoming Hypoxic-Resistance of Tumor Cells to TRAIL-Induced Apoptosis through Melatonin. International Journal of Molecular Sciences 15: 11941-11956.

54. Minchinton AI, Tannock IF (2006) Drug penetration in solid tumours. Nat Rev Cancer 6: 583-592.

55. Baker BM, Chen CS (2012) Deconstructing the third dimension: how 3D culture microenvironments alter cellular cues. J Cell Sci 125: 3015-3024.

56. Ivanov DP, Coyle B, Walker DA, Grabowska AM (2016) In vitro models of medulloblastoma: Choosing the right tool for the job. J Biotechnol 236: 10-25.

57. Von Der Mark K, Gauss V, Von Der Mark H, Muller P (1977) Relationship between cell shape and type of collagen synthesised as chondrocytes lose their cartilage phenotype in culture. Nature 267: 531-532.

58. Huang H, Ding Y, Sun XS, Nguyen TA (2013) Peptide hydrogelation and cell encapsulation for 3D culture of MCF-7 breast cancer cells. PLoS One 8: e59482.

59. Kim JB (2005) Three-dimensional tissue culture models in cancer biology. Semin Cancer Biol 15: 365-377.

60. Cukierman E, Pankov R, Yamada KM (2002) Cell interactions with three-dimensional matrices. Curr Opin Cell Biol 14: 633-639.

61. Cukierman E, Pankov R, Stevens DR, Yamada KM (2001) Taking cell-matrix adhesions to the third dimension. Science 294: 1708-1712.

62. Håkanson M, Cukierman E, Charnley M (2014) Miniaturized pre-clinical cancer models as research and diagnostic tools. Adv Drug Deliv Rev 69–70: 52-66.

63. Yip D, Cho CH (2013) A multicellular 3D heterospheroid model of liver tumor and stromal cells in collagen gel for anti-cancer drug testing. Biochem Biophys Res Commun 433: 327-332.

64. Price KJ, Tsykin A, Giles KM, Sladic RT, Epis MR, et al. (2012) Matrigel basement membrane matrix influences expression of microRNAs in cancer cell lines. Biochem Biophys Res Commun 427: 343-348.

65. Tibbitt MW, Anseth KS (2009) Hydrogels as extracellular matrix mimics for 3D cell culture. Biotechnol Bioeng 103: 655-663.

66. Edmondson R, Broglie JJ, Adcock AF, Yang L (2014) Three-Dimensional Cell Culture Systems and Their Applications in Drug Discovery and Cell-Based Biosensors. Assay and Drug Development Technologies 12: 207-218.

67. Xu X, Gurski LA, Zhang C, Harrington DA, Farach-Carson MC, et al. (2012) Recreating the tumor microenvironment in a bilayer, hyaluronic acid hydrogel construct for the growth of prostate cancer spheroids. Biomaterials 33: 9049-9060.

68. Doyle AD, Carvajal N, Jin A, Matsumoto K, Yamada KM (2015) Local 3D matrix microenvironment regulates cell migration through spatiotemporal dynamics of contractility-dependent adhesions. Nat Commun 6: 8720.

69. Fraley SI, Feng Y, Krishnamurthy R, Kim DH, Celedon A, et al. (2010) A distinctive role for focal adhesion proteins in three-dimensional cell motility. Nat Cell Biol 12: 598-604.

70. Pek YS, Wan AC, Ying JY (2010) The effect of matrix stiffness on mesenchymal stem cell differentiation in a 3D thixotropic gel. Biomaterials 31: 385-391.

71. Bokhari M, Carnachan RJ, Cameron NR, Przyborski SA (2007) Culture of HepG2 liver cells on three dimensional polystyrene scaffolds enhances cell structure and function during toxicological challenge. J Anat 211: 567-576.

72. Boxberger HJ, Meyer TF (1994) A new method for the 3-D in vitro growth of human RT112 bladder carcinoma cells using the alginate culture technique. Biol Cell 82: 109-119.

73. Hosseinkhani H, Azzam T, Kobayashi H, Hiraoka Y, Shimokawa H, et al. (2006) Combination of 3D tissue engineered scaffold and non-viral gene carrier enhance in vitro DNA expression of mesenchymal stem cells. Biomaterials 27: 4269-4278.

74. Ma T, Li Y, Yang ST, Kniss DA (1999) Tissue engineering human placenta trophoblast cells in 3-D fibrous matrix: spatial effects on cell proliferation and function. Biotechnol Prog 15: 715-724.

75. Mehta BC, Holman DW, Grzybowski DM, Chalmers JJ (2007) Characterization of arachnoidal cells cultured on three-dimensional nonwoven PET matrix. Tissue Eng 13: 1269-1279.

76. Huebsch N, Arany PR, Mao AS, Shvartsman D, Ali OA, et al. (2010) Harnessing Traction-Mediated Manipulation of the Cell-Matrix Interface to Control Stem Cell Fate. Nature materials 9: 518-526.

77. Martino MM, Mochizuki M, Rothenfluh DA, Rempel SA, Hubbell JA, et al. (2009) Controlling integrin specificity and stem cell differentiation in 2-D and 3-D environments through regulation of fibronectin domain stability. Biomaterials 30: 1089-1097.

78. Nath S, Devi GR (2016) Three-dimensional culture systems in cancer research: Focus on tumor spheroid model. Pharmacol Ther 163: 94-108.

79. Wang C, Tang Z, Zhao Y, Yao R, Li L, et al. (2014) Three-dimensional in vitro cancer models: a short review. Biofabrication 6: 022001.

80. Mehta G, Hsiao AY, Ingram M, Luker GD, Takayama S (2012) Opportunities and challenges for use of tumor spheroids as models to test drug delivery and efficacy. J Control Release 164: 192-204.

81. Elliott NT, Yuan F (2011) A review of three-dimensional in vitro tissue models for drug discovery and transport studies. J Pharm Sci 100: 59-74.

82. Tung YC, Hsiao AY, Allen SG, Torisawa YS, Ho M, et al. (2011) High-throughput 3D spheroid culture and drug testing using a 384 hanging drop array. Analyst 136: 473-478.

83. Ota H, Miki N (2013) Microtechnology-based three-dimensional spheroid formation. Frontiers in bioscience (Elite edition). pp. 37-48.

84. Ivanov DP, Grabowska AM (2017) Spheroid arrays for high-throughput single-cell analysis of spatial patterns and biomarker expression in 3D. Sci Rep 7: 41160.

85. Ritter CA, Perez-Torres M, Rinehart C, Guix M, Dugger T, et al. (2007) Human breast cancer cells selected for resistance to trastuzumab in vivo overexpress epidermal growth factor receptor and ErbB ligands and remain dependent on the ErbB receptor network. Clin Cancer Res 13: 4909-4919.

86. Bazou D, Maimon N, Gruionu G, Munn LL (2016) Self-assembly of vascularized tissue to support tumor explants in vitro. Integr Biol (Camb) 8: 1301-1311.

87. Caliari SR, Burdick JA (2016) A practical guide to hydrogels for cell culture. Nat Methods 13: 405-414.

88. Cosgrove BD, Mui KL, Driscoll TP, Caliari SR, Mehta KD, et al. (2016) N-cadherin adhesive interactions modulate matrix mechanosensing and fate commitment of mesenchymal stem cells. Nat Mater 15: 1297-1306.

89. Yoon SH, Mofrad MR (2011) Cell adhesion and detachment on gold surfaces modified with a thiol-functionalized RGD peptide. Biomaterials 32: 7286-7296.

90. Markert CD, Guo X, Skardal A, Wang Z, Bharadwaj S, et al. (2013) Characterizing the micro-scale elastic modulus of hydrogels for use in regenerative medicine. J Mech Behav Biomed Mater 27: 115-127.

91. Annabi N, Tamayol A, Uquillas JA, Akbari M, Bertassoni LE, et al. (2014) 25th Anniversary Article: Rational Design and Applications of Hydrogels in Regenerative Medicine. Advanced Materials 26: 85-124.

92. Birkedal-Hansen H, Moore WG, Bodden MK, Windsor LJ, Birkedal-Hansen B, et al. (1993) Matrix metalloproteinases: a review. Crit Rev Oral Biol Med 4: 197-250.

93. Choi NW, Cabodi M, Held B, Gleghorn JP, Bonassar LJ, et al. (2007) Microfluidic scaffolds for tissue engineering. Nat Mater 6: 908-915.

94. Paguirigan A, Beebe DJ (2006) Gelatin based microfluidic devices for cell culture. Lab Chip 6: 407-413.

95. Chan JM, Zervantonakis IK, Rimchala T, Polacheck WJ, Whisler J, et al. (2012) Engineering of in vitro 3D capillary beds by self-directed angiogenic sprouting. PLoS One 7: e50582.

96. Leung BM, Moraes C, Cavnar SP, Luker KE, Luker GD, et al. (2015) Microscale 3D collagen cell culture assays in conventional flat-bottom 384-well plates. J Lab Autom 20: 138-145.

97. Jeon JS, Bersini S, Whisler JA, Chen MB, Dubini G, et al. (2014) Generation of 3D functional microvascular networks with human mesenchymal stem cells in microfluidic systems. Integr Biol (Camb) 6: 555-563.

98. Moreno-Arotzena O, Meier JG, Del Amo C, Garcia-Aznar JM (2015) Characterization of Fibrin and Collagen Gels for Engineering Wound Healing Models. Materials (Basel) 8: 1636-1651.

99. Gerecht S, Burdick JA, Ferreira LS, Townsend SA, Langer R, et al. (2007) Hyaluronic acid hydrogel for controlled self-renewal and differentiation of human embryonic stem cells. Proceedings of the National Academy of Sciences 104: 11298-11303.

100. Kim IL, Khetan S, Baker BM, Chen CS, Burdick JA (2013) Fibrous hyaluronic acid hydrogels that direct MSC chondrogenesis through mechanical and adhesive cues. Biomaterials 34: 5571-5580.

101. Kievit FM, Florczyk SJ, Leung MC, Veiseh O, Park JO, et al. (2010) Chitosan-alginate 3D scaffolds as a mimic of the glioma tumor microenvironment. Biomaterials 31: 5903-5910.

102. Siti-Ismail N, Bishop AE, Polak JM, Mantalaris A (2008) The benefit of human embryonic stem cell encapsulation for prolonged feeder-free maintenance. Biomaterials 29: 3946-3952.

103. Kleinman HK, Martin GR (2005) Matrigel: basement membrane matrix with biological activity. Semin Cancer Biol 15: 378-386.

104. Huang CP, Lu J, Seon H, Lee AP, Flanagan LA, et al. (2009) Engineering microscale cellular niches for three-dimensional multicellular co-cultures. Lab Chip 9: 1740-1748.

105. Biondi M, Guarnieri D, Yu H, Belli V, Netti PA (2013) Sub-100 nm biodegradable nanoparticles: in vitro release features and toxicity testing in 2D and 3D cell cultures. Nanotechnology 24: 045101.

106. Mei L, Fu L, Shi K, Zhang Q, Liu Y, et al. (2014) Increased tumor targeted delivery using a multistage liposome system functionalized with RGD, TAT and cleavable PEG. Int J Pharm 468: 26-38.

107. Lodish H BA, Zipursky SL, et al. (2000) Section 22.3, Collagen: The Fibrous Proteins of the Matrix. In: Freeman NYWH, editor. Molecular Cell biology. Accessed on 20/02/2017 https://www.ncbi.nlm.nih.gov/books/NBK21582/.

108. De Wever O, Hendrix A, De Boeck A, Westbroek W, Braems G, et al. (2010) Modeling and quantification of cancer cell invasion through collagen type I matrices. Int J Dev Biol 54: 887-896.

109. Baker EL, Srivastava J, Yu D, Bonnecaze RT, Zaman MH (2011) Cancer cell migration: integrated roles of matrix mechanics and transforming potential. PLoS One 6: e20355.

110. Fang M, Goldstein EL, Turner AS, Les CM, Orr BG, et al. (2012) Type I Collagen D-spacing in Fibril Bundles of Dermis, Tendon and Bone: Bridging Between Nano- and Micro-Level Tissue Hierarchy. ACS Nano 6: 9503-9514.

111. Lutolf M, Hubbell J (2005) Synthetic biomaterials as instructive extracellular microenvironments for morphogenesis in tissue engineering. Nat Biotechnol 23: 47-55.

112. Lutolf M, Hubbell J (2003) Synthesis and physicochemical characterization of end-linked poly (ethylene glycol)-co-peptide hydrogels formed by Michael-type addition. Biomacromolecules 4: 713-722.

113. Lutolf M, Lauer-Fields J, Schmoekel H, Metters A, Weber F, et al. (2003) Synthetic matrix metalloproteinase-sensitive hydrogels for the conduction of tissue regeneration: engineering cell-invasion characteristics. Proceedings of the National Academy of Sciences 100: 5413-5418.

114. Chen L, Xiao Z, Meng Y, Zhao Y, Han J, et al. (2012) The enhancement of cancer stem cell properties of MCF-7 cells in 3D collagen scaffolds for modeling of cancer and anti-cancer drugs. Biomaterials 33: 1437-1444.

115. Choe MM, Tomei AA, Swartz MA (2006) Physiological 3D tissue model of the airway wall and mucosa. Nat Protoc 1: 357-362.

116. Jones CAR, Liang L, Lin D, Jiao Y, Sun B (2014) The spatial-temporal characteristics of type I collagen-based extracellular matrix. Soft Matter 10: 8855-8863.

117. Lin S, Gu L (2015) Influence of Crosslink Density and Stiffness on Mechanical Properties of Type I Collagen Gel. Materials (Basel) 8: 551.

118. Gohler C, Karl A, Korber N, Koch C, Reichenbach A, et al. (2014) Characterization of extracellular matrix remodelling enzymes in the sclera after collagen cross linking (SXL). Acta Ophthalmologica 92: 0-0.

119. Hobeika L, Barati MT, Caster DJ, McLeish KR, Merchant ML Characterization of glomerular extracellular matrix by proteomic analysis of laser-captured microdissected glomeruli. Kidney International 91: 501-511.

120. Gay S, Fietzek PP, Remberger K, Eder M, Kühn K (1975) Liver cirrhosis: Immunofluorescence and biochemical studies demonstrate two types of collagen. Klin Wochenschr 53: 205-208.

121. Zipfel WR, Williams RM, Christie R, Nikitin AY, Hyman BT, et al. (2003) Live tissue intrinsic emission microscopy using multiphoton-excited native fluorescence and second harmonic generation. Proceedings of the National Academy of Sciences 100: 7075-7080.

122. Whitesides GM, Ostuni E, Takayama S, Jiang X, Ingber DE (2001) Soft lithography in biology and biochemistry. Annu Rev Biomed Eng 3: 335-373.

123. Thery M (2010) Micropatterning as a tool to decipher cell morphogenesis and functions. J Cell Sci 123: 4201-4213.

124. Wu D, Yotnda P (2011) Induction and testing of hypoxia in cell culture. J Vis Exp.

125. Guo M, Song LP, Jiang Y, Liu W, Yu Y, et al. (2006) Hypoxia-mimetic agents desferrioxamine and cobalt chloride induce leukemic cell apoptosis through different hypoxia-inducible factor-1alpha independent mechanisms. Apoptosis 11: 67-77.

126. Bartolome S, Dhillon NK, Buch S, Casillan AJ, Wood JG, et al. (2009) Deferoxamine mimics the pattern of hypoxia-related injury at the microvasculature. Shock 31: 481-485.

127. Ahmad Y, Mishra S, Arya A, Paul S, Sharma M, et al. (2016) Revisiting cobalt chloride preconditioning to prevent hypobaric hypoxia-induced damage: identification of global proteomic alteration and key networks. Funct Integr Genomics 16: 281-295.

128. Lee J-W, Bae S-H, Jeong J-W, Kim S-H, Kim K-W (2004) Hypoxia-inducible factor (HIF-1)[alpha]: its protein stability and biological functions. Experimental & molecular medicine 36: 1.

129. Heit B, Tavener S, Raharjo E, Kubes P (2002) An intracellular signaling hierarchy determines direction of migration in opposing chemotactic gradients. J Cell Biol 159: 91-102.

130. Chen H, He Z, Bagri A, Tessier-Lavigne M (1998) Semaphorin–neuropilin interactions underlying sympathetic axon responses to class III semaphorins. Neuron 21: 1283-1290.

131. Foxman EF, Kunkel EJ, Butcher EC (1999) Integrating conflicting chemotactic signals. J Cell Biol 147: 577-588.

132. Boyden S (1962) The chemotactic effect of mixtures of antibody and antigen on polymorphonuclear leucocytes. Journal of Experimental Medicine 115: 453-466.

133. Zigmond SH (1977) Ability of polymorphonuclear leukocytes to orient in gradients of chemotactic factors. J cell Biol 75: 606-616.

134. Zicha D, Dunn G, Jones G (1997) Analyzing chemotaxis using the Dunn direct-viewing chamber. Basic Cell Culture Protocols: 449-457.

135. Fick A (1855) V. On liquid diffusion. The London, Edinburgh, and Dublin Philosophical Magazine and Journal of Science 10: 30-39.

136. Edward JT (1970) Molecular volumes and the Stokes-Einstein equation. J chem Educ 47: 261.

137. Ogston A, Sherman T (1961) Effects of hyaluronic acid upon diffusion of solutes and flow of solvent. J Physiol 156: 67.

138. Speizer L, Haugland R, Kutchai H (1985) Asymmetric transport of a fluorescent glucose analogue by human erythrocytes. Biochimica et Biophysica Acta (BBA) - Biomembranes 815: 75-84.

139. Zou C, Wang Y, Shen Z (2005) 2-NBDG as a fluorescent indicator for direct glucose uptake measurement. Journal of Biochemical and Biophysical Methods 64: 207-215.

140. Rajakumar N, Elisevich K, Flumerfelt BA (1993) Biotinylated dextran: a versatile anterograde and retrograde neuronal tracer. Brain Res 607: 47-53.

141. (2010) The Molecular Probes® Handbook. In: Scientific TF, editor. 11 ed. https://www.thermofisher.com/es/es/home/references/molecular-probes-the-handbook/mp-handbook-download.html?email=mvirumbralesmunoz@gmail.com&status=500&form-submit-token=baab19f2b2b33e33e1759beeca1881: Thermo Fisher Scientific. pp. 965.

142. Ramanujan S, Pluen A, McKee TD, Brown EB, Boucher Y, et al. (2002) Diffusion and Convection in Collagen Gels: Implications for Transport in the Tumor Interstitium. Biophys J 83: 1650-1660.

143. Aref AR, Huang RY, Yu W, Chua KN, Sun W, et al. (2013) Screening therapeutic EMT blocking agents in a three-dimensional microenvironment. Integr Biol (Camb) 5: 381-389.

144. Chatzinikolaidou M (2016) Cell spheroids: the new frontiers in in vitro models for cancer drug validation. Drug Discov Today 21: 1553-1560.

145. Katt ME, Placone AL, Wong AD, Xu ZS, Searson PC (2016) In Vitro Tumor Models: Advantages, Disadvantages, Variables, and Selecting the Right Platform. Front Bioeng Biotechnol 4.

146. Weiswald LB, Bellet D, Dangles-Marie V (2015) Spherical cancer models in tumor biology. Neoplasia 17: 1-15.

147. Hickman JA, Graeser R, de Hoogt R, Vidic S, Brito C, et al. (2014) Three-dimensional models of cancer for pharmacology and cancer cell biology: capturing tumor complexity in vitro/ex vivo. Biotechnol J 9: 1115-1128.

148. Regier MC, Alarid ET, Beebe DJ (2016) Progress towards understanding heterotypic interactions in multi-culture models of breast cancer. Integrative Biology 8: 684-692.

149. Arrigoni C, Bersini S, Gilardi M, Moretti M (2016) In Vitro Co-Culture Models of Breast Cancer Metastatic Progression towards Bone. Int J Mol Sci 17.

150. Katt ME, Placone AL, Wong AD, Xu ZS, Searson PC (2016) In Vitro Tumor Models: Advantages, Disadvantages, Variables, and Selecting the Right Platform. Front Bioeng Biotechnol 4: 12.

151. Koffi D, Touré AO, Varela M-L, Vigan-Womas I, Béourou S, et al. (2015) Analysis of antibody profiles in symptomatic malaria in three sentinel sites of Ivory Coast by using multiplex, fluorescent, magnetic, bead-based serological assay (MAGPIX™). Malaria journal 14: 509.

152. Nam J-M, Thaxton CS, Mirkin CA (2003) Nanoparticle-based bio-bar codes for the ultrasensitive detection of proteins. Science 301: 1884-1886.

153. Buss H, Chan TP, Sluis KB, Domigan NM, Winterbourn CC (1997) Protein carbonyl measurement by a sensitive ELISA method. Free Radical Biology and Medicine 23: 361-366.

154. Perez-Hernandez J, Cortes R (2015) Extracellular Vesicles as Biomarkers of Systemic Lupus Erythematosus. Disease Markers 2015: 7.

155. (2017) Products for exosome investigation and analysis. In: FisherScientific, editor.

156. Bhatia SN, Ingber DE (2014) Microfluidic organs-on-chips. Nat Biotechnol 32: 760-772.

157. Casavant BP, Berthier E, Theberge AB, Berthier J, Montanez-Sauri SI, et al. (2013) Suspended microfluidics. Proc Natl Acad Sci U S A 110: 10111-10116.

158. Du G, Fang Q, den Toonder JMJ (2016) Microfluidics for cell-based high throughput screening platforms—A review. Analytica Chimica Acta 903: 36-50.

159. Huh D, Hamilton GA, Ingber DE (2011) From 3D cell culture to organs-on-chips. Trends Cell Biol 21: 745-754.

160. Portillo-Lara R, Annabi N (2016) Microengineered cancer-on-a-chip platforms to study the metastatic microenvironment. Lab Chip 16: 4063-4081.

161. Young EW, Beebe DJ (2010) Fundamentals of microfluidic cell culture in controlled microenvironments. Chem Soc Rev 39: 1036-1048.

162. Bischel LL, Lee S-H, Beebe DJ (2012) A Practical Method for Patterning Lumens through ECM Hydrogels via Viscous Finger Patterning. J Lab Autom 17: 96-103.

163. Jiménez-Torres JA, Peery SL, Sung KE, Beebe DJ (2016) LumeNEXT: A Practical Method to Pattern Luminal Structures in ECM Gels. Advanced healthcare materials 5: 198-204.

164. Bersini S, Jeon JS, Dubini G, Arrigoni C, Chung S, et al. (2014) A microfluidic 3D in vitro model for specificity of breast cancer metastasis to bone. Biomaterials 35: 2454-2461.

165. Jeon JS, Bersini S, Gilardi M, Dubini G, Charest JL, et al. (2015) Human 3D vascularized organotypic microfluidic assays to study breast cancer cell extravasation. Proc Natl Acad Sci U S A 112: 214-219.

166. Polacheck WJ, Zervantonakis IK, Kamm RD (2013) Tumor cell migration in complex microenvironments. Cell Mol Life Sci 70: 1335-1356.

167. Zervantonakis IK, Hughes-Alford SK, Charest JL, Condeelis JS, Gertler FB, et al. (2012) Three-dimensional microfluidic model for tumor cell intravasation and endothelial barrier function. Proc Natl Acad Sci U S A 109: 13515-13520.

168. Sobrino A, Phan DTT, Datta R, Wang X, Hachey SJ, et al. (2016) 3D microtumors in vitro supported by perfused vascular networks. Sci Rep 6: 31589.

169. Phan DTT, Wang X, Craver BM, Sobrino A, Zhao D, et al. (2017) A vascularized and perfused organ-on-a-chip platform for large-scale drug screening applications. Lab Chip 17: 511-520.

170. Adler M, Polinkovsky M, Gutierrez E, Groisman A (2010) Generation of oxygen gradients with arbitrary shapes in a microfluidic device. Lab Chip 10: 388-391.

171. Su X, Young EW, Underkofler HA, Kamp TJ, January CT, et al. (2011) Microfluidic cell culture and its application in high-throughput drug screening: cardiotoxicity assay for hERG channels. J Biomol Screen 16: 101-111.

172. Nowell PC (1976) The clonal evolution of tumor cell populations. Science 194: 23-28.

173. Cooke SL, Temple J, MacArthur S, Zahra MA, Tan LT, et al. (2011) Intra-tumour genetic heterogeneity and poor chemoradiotherapy response in cervical cancer. Br J Cancer 104: 361-368.

174. Floor SL, Dumont JE, Maenhaut C, Raspe E (2012) Hallmarks of cancer: of all cancer cells, all the time? Trends Mol Med 18: 509-515.

175. Kotzar G, Freas M, Abel P, Fleischman A, Roy S, et al. (2002) Evaluation of MEMS materials of construction for implantable medical devices. Biomaterials 23: 2737-2750.

176. Mao Y, Keller ET, Garfield DH, Shen K, Wang J (2013) Stromal cells in tumor microenvironment and breast cancer. Cancer Metastasis Rev 32: 303-315.

177. Maeda H, Matsumura Y (2011) EPR effect based drug design and clinical outlook for enhanced cancer chemotherapy. Adv Drug Deliv Rev 63: 129-130.

178. Harink B, Le Gac S, Truckenmuller R, van Blitterswijk C, Habibovic P (2013) Regeneration-on-a-chip? The perspectives on use of microfluidics in regenerative medicine. Lab Chip 13: 3512-3528.

179. Picollet-D'hahan N, Dolega ME, Liguori L, Marquette C, Le Gac S, et al. A 3D Toolbox to Enhance Physiological Relevance of Human Tissue Models. Trends in Biotechnology 34: 757-769.

180. Young EWK (2013) Cells, tissues, and organs on chips: challenges and opportunities for the cancer tumor microenvironment. Integrative Biology 5: 1096-1109.

181. Song JW, Cavnar SP, Walker AC, Luker KE, Gupta M, et al. (2009) Microfluidic endothelium for studying the intravascular adhesion of metastatic breast cancer cells. PLoS One 4: e5756.

182. Funamoto K, Zervantonakis IK, Liu Y, Ochs CJ, Kim C, et al. (2012) A novel microfluidic platform for high-resolution imaging of a three-dimensional cell culture under a controlled hypoxic environment. Lab Chip 12: 4855-4863.

183. MacFarlane M, Ahmad M, Srinivasula SM, Fernandes-Alnemri T, Cohen GM, et al. (1997) Identification and molecular cloning of two novel receptors for the cytotoxic ligand TRAIL. J Biol Chem 272: 25417-25420.

184. Zervantonakis IK, Hughes-Alford SK, Charest JL, Condeelis JS, Gertler FB, et al. (2012) Three-dimensional microfluidic model for tumor cell intravasation and endothelial barrier function. Proceedings of the National Academy of Sciences of the United States of America 109: 13515-13520.

185. Zervantonakis IK, Kothapalli CR, Chung S, Sudo R, Kamm RD (2011) Microfluidic devices for studying heterotypic cell-cell interactions and tissue specimen cultures under controlled microenvironments. Biomicrofluidics 5.

186. Bersini S, Jeon JS, Dubini G, Arrigoni C, Chung S, et al. (2014) A microfluidic 3D in vitro model for specificity of breast cancer metastasis to bone. Biomaterials 35: 2454-2461.

187. Bersini S, Jeon JS, Kamm RD, Moretti M (2015) Human 3D Vascularized Organotypic Microfluidic Models for the Study of Breast Cancer Cell Extravasation. Tissue Engineering Part A 21: S207-S207.

188. Bersini S, Jeon JS, Moretti M, Kamm RD (2014) In vitro models of the metastatic cascade: from local invasion to extravasation. Drug Discovery Today 19: 735-742.

189. Chen MB, Lamar JM, Li R, Hynes RO, Kamm RD (2016) Elucidation of the Roles of Tumor Integrin beta 1 in the Extravasation Stage of the Metastasis Cascade. Cancer Res 76: 2513-2524.

190. Bischel LL, Young EW, Mader BR, Beebe DJ (2013) Tubeless microfluidic angiogenesis assay with three-dimensional endothelial-lined microvessels. Biomaterials 34: 1471-1477.

191. Sung KE, Beebe DJ (2014) Microfluidic 3D models of cancer. Adv Drug Deliv Rev 79-80: 68-78.

192. Puccinelli JP, Su X, Beebe DJ (2010) Automated high-throughput microchannel assays for cell biology: Operational optimization and characterization. JALA Charlottesv Va 15: 25-32.

193. Srinivasan B, Kolli AR, Esch MB, Abaci HE, Shuler ML, et al. (2015) TEER measurement techniques for in vitro barrier model systems. J Lab Autom 20: 107-126.

194. Chen S, Einspanier R, Schoen J (2015) Transepithelial electrical resistance (TEER): a functional parameter to monitor the quality of oviduct epithelial cells cultured on filter supports. Histochem Cell Biol 144: 509-515.

195. Yeste J, Illa X, Gutiérrez C, Solé M, Guimerà A, et al. (2016) Geometric correction factor for transepithelial electrical resistance measurements in transwell and microfluidic cell cultures. Journal of Physics D: Applied Physics 49: 375401.

196. Montanez-Sauri SI, Sung KE, Puccinelli JP, Pehlke C, Beebe DJ (2011) Automation of three-dimensional cell culture in arrayed microfluidic devices. J Lab Autom 16: 171-185.

197. de Miguel D, Lemke J, Anel A, Walczak H, Martinez-Lostao L (2016) Onto better TRAILs for cancer treatment. Cell Death Differ 23: 733-747.

198. De Miguel D, Gallego-Lleyda A, Ayuso JM, Pejenaute-Ochoa D, Jarauta V, et al. (2016) High-order TRAIL oligomer formation in TRAIL-coated lipid nanoparticles enhances DR5 cross-linking and increases antitumour effect against colon cancer. Cancer Lett 383: 250-260.

199. Jokinen V, Suvanto P, Franssila S (2012) Oxygen and nitrogen plasma hydrophilization and hydrophobic recovery of polymers. Biomicrofluidics 6: 16501-1650110.

200. Crampton SP, Davis J, Hughes CC (2007) Isolation of human umbilical vein endothelial cells (HUVEC). J Vis Exp: 183.

201. DeCicco-Skinner KL, Henry GH, Cataisson C, Tabib T, Gwilliam JC, et al. (2014) Endothelial cell tube formation assay for the in vitro study of angiogenesis. J Vis Exp: e51312.

202. Ayuso JM, Virumbrales-Muñoz M, Lacueva A, Lanuza PM, Checa-Chavarria E, et al. (2016) Development and characterization of a microfluidic model of the tumour microenvironment. Sci Rep 6: 36086.

203. De Miguel D, Basanez G, Sanchez D, Malo PG, Marzo I, et al. (2013) Liposomes decorated with Apo2L/TRAIL overcome chemoresistance of human hematologic tumor cells. Mol Pharm 10: 893-904.

204. De Miguel D, Gallego-Lleyda A, Galan-Malo P, Rodriguez-Vigil C, Marzo I, et al. (2015) Immunotherapy with liposome-bound TRAIL overcomes partial protection to soluble TRAIL-induced apoptosis offered by down-regulation of Bim in leukemic cells. Clin Transl Oncol 17: 657-667.

205. Martinez-Lostao L, Garcia-Alvarez F, Basanez G, Alegre-Aguaron E, Desportes P, et al. (2010) Liposome-bound APO2L/TRAIL is an effective treatment in a rheumatoid arthritis model. Arthritis Rheum 62: 2272-2282.

206. Nemani KV, Moodie KL, Brennick JB, Su A, Gimi B (2013) In vitro and in vivo evaluation of SU-8 biocompatibility. Materials Science & Engineering C-Materials for Biological Applications 33: 4453-4459.

207. Ni M, Tong WH, Choudhury D, Rahim NAA, Iliescu C, et al. (2009) Cell Culture on MEMS Platforms: A Review. International Journal of Molecular Sciences 10: 5411-5441.

208. Lorenz H, Despont M, Fahrni N, LaBianca N, Renaud P, et al. (1997) SU-8: a low-cost negative resist for MEMS. Journal of Micromechanics and Microengineering 7: 121-124.

209. Gerhardt H, Betsholtz C (2005) How do endothelial cells orientate? In: Clauss M, Breier G, editors. Mechanisms of Angiogenesis. Basel: Birkhäuser Basel. pp. 3-15.

210. Laviola L, Orlando MR, Incalza MA, Caccioppoli C, Melchiorre M, et al. (2013) TNFalpha signals via p66(Shc) to induce E-Selectin, promote leukocyte transmigration and enhance permeability in human endothelial cells. PLoS One 8: e81930.

211. Lee E, Pandey NB, Popel AS (2015) Crosstalk between cancer cells and blood endothelial and lymphatic endothelial cells in tumour and organ microenvironment. Expert Rev Mol Med 17: e3.

212. De Miguel D, Gallego-Lleyda A, Ayuso JM, Pawlak A, Conde B, et al. (2016) Improved Anti-Tumor Activity of Novel Highly Bioactive Liposome-Bound TRAIL in Breast Cancer Cells. Recent Pat Anticancer Drug Discov 11: 197-214.

213. Cantarella G, Di Benedetto G, Ribatti D, Saccani-Jotti G, Bernardini R (2014) Involvement of caspase 8 and c-FLIPL in the proangiogenic effects of the tumour necrosis factor-related apoptosis-inducing ligand (TRAIL). FEBS J 281: 1505-1513.

214. Niles WD, Coassin PJ (2008) Cyclic olefin polymers: innovative materials for high-density multiwell plates. Assay Drug Dev Technol 6: 577-590.

215. Gurramkonda C, Zahid M, Nemani SK, Adnan A, Gudi SK, et al. (2013) Purification of hepatitis B surface antigen virus-like particles from recombinant Pichia pastoris and in

vivo analysis of their immunogenic properties. Journal of Chromatography B-Analytical Technologies in the Biomedical and Life Sciences 940: 104-111.

216. Cirstea D, Hideshima T, Santo L, Eda H, Mishima Y, et al. (2013) Small-molecule multi-targeted kinase inhibitor RGB-286638 triggers P53-dependent and -independent anti-multiple myeloma activity through inhibition of transcriptional CDKs. Leukemia 27: 2366-2375.

217. Nemani N, Santo L, Eda H, Cirstea D, Mishima Y, et al. (2013) Role Of Decorin In Multiple Myeloma (MM) Bone Marrow Microenvironment. Blood 122.

218. Aaij R, Adeva B, Adinolfi M, Adrover C, Affolder A, et al. (2013) Measurement of D0-D0 mixing parameters and search for CP violation using D0 --> K+ pi- decays. Phys Rev Lett 111: 251801.

219. Eda H, Santo L, Cirstea DD, Yee AJ, Scullen TA, et al. (2013) A Novel Bruton's Tyrosine Kinase Inhibitor CC-292 In Combination With The Proteasome Inhibitor Carfilzomib Iimpacts Multiple Myeloma Bone Microenviroment With Resultant Anti-Myeloma Activity. Blood 122.

220. Carreau A, El Hafny-Rahbi B, Matejuk A, Grillon C, Kieda C (2011) Why is the partial oxygen pressure of human tissues a crucial parameter? Small molecules and hypoxia. J Cell Mol Med 15: 1239-1253.

221. Clark LC, Jr., Wolf R, Granger D, Taylor Z (1953) Continuous recording of blood oxygen tensions by polarography. J Appl Physiol 6: 189-193.

222. Ramamoorthy R, Dutta PK, Akbar SA (2003) Oxygen sensors: Materials, methods, designs and applications. Journal of Materials Science 38: 4271-4282.

223. Van Rossem FB, J; De Boer, H; Abbas, Y; De Weerd, E; Van den Berg, A; Le Gac, S. (2016) Sensing oxygen at the millisecond time-scale using an ultra-microelectrode array (UMEA). Sens Act A.

224. Licha K, Olbrich C (2005) Optical imaging in drug discovery and diagnostic applications. Adv Drug Deliv Rev 57: 1087-1108.

225. Ruggi A, Reinhoudt DN, Velders AH (2011) Biomedical Applications of Metal-Containing Luminophores. Bioinorganic Medicinal Chemistry: Wiley-VCH Verlag GmbH & Co. KGaA. pp. 383-406.

226. Wise RR, Naylor AW (1985) Calibration and use of a Clark-type oxygen electrode from 5 to 45°C. Anal Biochem 146: 260-264.

227. Marin C, Fernández E (2010) Biocompatibility of Intracortical Microelectrodes: Current Status and Future Prospects. Frontiers in Neuroengineering 3: 8.

228. Wang X-d, Chen H-x, Zhao Y, Chen X, Wang X-r (2010) Optical oxygen sensors move towards colorimetric determination. TrAC Trends in Analytical Chemistry 29: 319-338.

229. Bahadar H, Maqbool F, Niaz K, Abdollahi M (2016) Toxicity of Nanoparticles and an Overview of Current Experimental Models. Iranian Biomedical Journal 20: 1-11.

230. Ruggi A, van Leeuwen FWB, Velders AH (2011) Interaction of dioxygen with the electronic excited state of Ir(III) and Ru(II) complexes: Principles and biomedical applications. Coordination Chemistry Reviews 255: 2542-2554.

231. Papkovsky DB, Dmitriev RI (2013) Biological detection by optical oxygen sensing. Chem Soc Rev 42: 8700-8732.

232. Mehta G, Mehta K, Sud D, Song JW, Bersano-Begey T, et al. (2007) Quantitative measurement and control of oxygen levels in microfluidic poly(dimethylsiloxane) bioreactors during cell culture. Biomed Microdevices 9: 123-134.

233. Chen J, Kim HD, Kim KC (2013) Measurement of dissolved oxygen diffusion coefficient in a microchannel using UV-LED induced fluorescence method. Microfluidics and Nanofluidics 14: 541-550.

234. Adler M, Polinkovsky M, Gutierrez E, Groisman A (2010) Generation of oxygen gradients with arbitrary shapes in a microfluidic device. Lab on a Chip 10: 388-391.

235. O'Donovan C, Twomey E, Alderman J, Moore T, Papkovsky D (2006) Development of a respirometric biochip for embryo assessment. Lab Chip 6: 1438-1444.

236. Carraway ER, Demas JN, Degraff BA, Bacon JR (1991) Photophysics and Photochemistry of Oxygen Sensors Based on Luminescent Transition-Metal Complexes. Anal Chem 63: 337-342.

237. Funamoto K, Zervantonakis IK, Liu YC, Ochs CJ, Kim C, et al. (2012) A novel microfluidic platform for high-resolution imaging of a three-dimensional cell culture under a controlled hypoxic environment. Lab on a Chip 12: 4855-4863.

238. Lam RH, Kim MC, Thorsen T (2009) Culturing aerobic and anaerobic bacteria and mammalian cells with a microfluidic differential oxygenator. Anal Chem 81: 5918-5924.

239. Lo JF, Sinkala E, Eddington DT (2010) Oxygen gradients for open well cellular cultures via microfluidic substrates. Lab on a Chip 10: 2394-2401.

240. Grist SM, Oyunerdene N, Flueckiger J, Kim J, Wong PC, et al. (2014) Fabrication and laser patterning of polystyrene optical oxygen sensor films for lab-on-a-chip applications. Analyst 139: 5718-5727.

241. Thomas PC, Raghavan SR, Forry SP (2011) Regulating oxygen levels in a microfluidic device. Anal Chem 83: 8821-8824.

242. Oppegard SC, Nam KH, Carr JR, Skaalure SC, Eddington DT (2009) Modulating Temporal and Spatial Oxygenation over Adherent Cellular Cultures. PLoS One 4.

243. Toncelli C, Arzhakova OV, Dolgova A, Volynskii AL, Bakeev NF, et al. (2014) Oxygen-sensitive phosphorescent nanomaterials produced from high-density polyethylene films by local solvent-crazing. Anal Chem 86: 1917-1923.

244. Wang L, Acosta MA, Leach JB, Carrier RL (2013) Spatially monitoring oxygen level in 3D microfabricated cell culture systems using optical oxygen sensing beads. Lab on a Chip 13: 1586-1592.

245. Chen W, Lisowski M, Khalil G, Sweet IR, Shen AQ (2012) Microencapsulated 3-dimensional sensor for the measurement of oxygen in single isolated pancreatic islets. PLoS One 7: e33070.

246. Lambrechts D, Roeffaers M, Kerckhofs G, Roberts SJ, Hofkens J, et al. (2013) Fluorescent oxygen sensitive microbead incorporation for measuring oxygen tension in cell aggregates. Biomaterials 34: 922-929.

247. Acosta MA, Jiang X, Huang P-K, Cutler KB, Grant CS, et al. (2014) A microfluidic device to study cancer metastasis under chronic and intermittent hypoxia. Biomicrofluidics 8: 054117.

248. Dmitriev RI, Kondrashina AV, Koren K, Klimant I, Zhdanov AV, et al. (2014) Small molecule phosphorescent probes for O-2 imaging in 3D tissue models. Biomaterials Science 2: 853-866.

249. Cao J, Nagl S, Kothe E, Köhler JM (2014) Oxygen sensor nanoparticles for monitoring bacterial growth and characterization of dose–response functions in microfluidic screenings. Microchimica Acta 182: 385-394.

250. Jenkins J, Dmitriev RI, Morten K, McDermott KW, Papkovsky DB (2015) Oxygen-sensing scaffolds for 3-dimensional cell and tissue culture. Acta Biomater 16: 126-135.

251. Quaranta M, Borisov SM, Klimant I (2012) Indicators for optical oxygen sensors. Bioanal Rev 4: 115-157.

252. Grist SM, Chrostowski L, Cheung KC (2010) Optical oxygen sensors for applications in microfluidic cell culture. Sensors (Basel) 10: 9286-9316.

253. Ashley N (2013) Regulation of intestinal cancer stem cells. Cancer Lett 338: 120-126.

254. Mathonnet M, Perraud A, Christou N, Akil H, Melin C, et al. (2014) Hallmarks in colorectal cancer: angiogenesis and cancer stem-like cells. World J Gastroenterol 20: 4189-4196.

255. Boudaoud A, Burian A, Borowska-Wykret D, Uyttewaal M, Wrzalik R, et al. (2014) FibrilTool, an ImageJ plug-in to quantify fibrillar structures in raw microscopy images. Nature Protocols 9: 457-463.

256. Jaiswal AK, Dhumal RV, Ghosh S, Chaudhari P, Nemani H, et al. (2013) Bone Healing Evaluation of Nanofibrous Composite Scaffolds in Rat Calvarial Defects: A Comparative Study. Journal of Biomedical Nanotechnology 9: 2073-2085.

257. Moreno-Arotzena O, Meier JG, del Amo C, Garcia-Aznar JM (2015) Characterization of Fibrin and Collagen Gels for Engineering Wound Healing Models. Materials 8: 1636-1651.

258. Ciriza J, del Burgo LS, Virumbrales-Munoz M, Ochoa I, Fernandez LJ, et al. (2015) Graphene oxide increases the viability of C2C12 myoblasts microencapsulated in alginate. International Journal of Pharmaceutics 493: 260-270.

259. Song LL, Hennink EJ, Young IT, Tanke HJ (1995) Photobleaching Kinetics of Fluorescein in Quantitative Fluorescence Microscopy. Biophysical Journal 68: 2588-2600.

260. PhysiologyWeb (2016) Diffusion Time Calculator. www.physiologyweb.com.

261. Chen F, Zhuang X, Lin L, Yu P, Wang Y, et al. (2015) New horizons in tumor microenvironment biology: challenges and opportunities. BMC Med 13: 45.

262. Whiteside TL (2008) The tumor microenvironment and its role in promoting tumor growth. Oncogene 27: 5904-5912.

263. Junttila MR, de Sauvage FJ (2013) Influence of tumour micro-environment heterogeneity on therapeutic response. Nature 501: 346-354.

264. Kimlin LC, Casagrande G, Virador VM (2013) In vitro three-dimensional (3D) models in cancer research: an update. Mol Carcinog 52: 167-182.

265. van der Meer AD, van den Berg A (2012) Organs-on-chips: breaking the in vitro impasse. Integr Biol (Camb) 4: 461-470.

266. Bersini S, Moretti M (2015) 3D functional and perfusable microvascular networks for organotypic microfluidic models. J Mater Sci Mater Med 26: 180.

267. van Duinen V, Trietsch SJ, Joore J, Vulto P, Hankemeier T (2015) Microfluidic 3D cell culture: from tools to tissue models. Curr Opin Biotechnol 35: 118-126.

268. Ayuso JM, Virumbrales-Munoz M, Lacueva A, Lanuza PM, Checa-Chavarria E, et al. (2016) Development and characterization of a microfluidic model of the tumour microenvironment. Sci Rep 6: 36086.

269. Berthier EY, E.W.K.; Beebe, D. (2012) Engineers are from PDMS-land, Biologists are from Polystyrenia. Lab On A Chip 12: 1193–1396.

270. Ayuso JM, Monge R, Llamazares G, Moreno M, Agirregabiria M, et al. (2015) SU-8 based microdevices to study self-induced chemotaxis in 3D microenvironments. Frontiers in Materials 2.

271. Bischel LL, Lee SH, Beebe DJ (2012) A practical method for patterning lumens through ECM hydrogels via viscous finger patterning. J Lab Autom 17: 96-103.

272. Ayuso JM, Monge R, Martínez-González A, Virumbrales-Muñoz M, Llamazares GA, et al. (2017) Glioblastoma on a microfluidic chip: Generating pseudopalisades and enhancing aggressiveness through blood vessel obstruction events. Neuro-Oncology: now230.

273. Dai X, Yue Z, Eccleston ME, Swartling J, Slater NKH, et al. Fluorescence intensity and lifetime imaging of free and micellar-encapsulated doxorubicin in living cells. Nanomedicine: Nanotechnology, Biology and Medicine 4: 49-56.

274. Binnig G, Quate CF, Gerber C (1986) Atomic force microscope. Physical review letters 56: 930.

275. Binnig G, Rohrer H, Gerber C, Weibel E (1982) Surface studies by scanning tunneling microscopy. Phys Rev Lett 49: 57.

276. Jalili N, Laxminarayana K (2004) A review of atomic force microscopy imaging systems: application to molecular metrology and biological sciences. Mechatronics 14: 907-945.

277. Neuman KC, Nagy A (2008) Single-molecule force spectroscopy: optical tweezers, magnetic tweezers and atomic force microscopy. Nat Methods 5: 491.

278. Rief M, Oesterhelt F, Heymann B, Gaub HE (1997) Single molecule force spectroscopy on polysaccharides by atomic force microscopy. Science 275: 1295-1297.

279. Muller DJ, Dufrene YF (2011) Atomic force microscopy: a nanoscopic window on the cell surface. Trends Cell Biol 21: 461-469.

280. Müller DJ, Dufrene YF (2008) Atomic force microscopy as a multifunctional molecular toolbox in nanobiotechnology. Nature nanotechnology 3: 261-269.

281. Muller DJ, Krieg M, Alsteens D, Dufrene YF (2009) New frontiers in atomic force microscopy: analyzing interactions from single-molecules to cells. Curr Opin Biotechnol 20: 4-13.

282. Gerber C, Lang HP (2006) How the doors to the nanoworld were opened. Nat Nano 1: 3-5.

283. Vahabi S, Salman BN, Javanmard A (2013) Atomic force microscopy application in biological research: a review study. Iranian journal of medical sciences 38: 76.

284. Eaton P, West P (2010) Atomic force microscopy: Oxford University Press.

285. Gates RS, Osborn WA, Pratt JR (2013) Experimental determination of mode correction factors for thermal method spring constant calibration of AFM cantilevers using laser Doppler vibrometry. Nanotechnology 24: 255706.

286. Piner RD, Zhu J, Xu F, Hong S, Mirkin CA (1999) " Dip-pen" nanolithography. Science 283: 661-663.

287. Balnois E, Wilkinson KJ (2002) Sample preparation techniques for the observation of environmental biopolymers by atomic force microscopy. Colloids and Surfaces A: Physicochemical and Engineering Aspects 207: 229-242.

288. Tanem BS, Kamfjord T, Augestad M, Løvgren TB, Lundquist M (2003) Sample preparation and AFM analysis of heterophase polypropylene systems. Polymer 44: 4283-4291.

289. Marcuello C (2014) Mecanismos catalíticos en sistemas proteicos estudiados a nivel de molécula única.: University of Zaragoza. 322 p.

290. Orive G, Santos E, Pedraz JL, Hernandez RM (2014) Application of cell encapsulation for controlled delivery of biological therapeutics. Adv Drug Deliv Rev 67-68: 3-14.

291. Dang SM, Gerecht-Nir S, Chen J, Itskovitz-Eldor J, Zandstra PW (2004) Controlled, scalable embryonic stem cell differentiation culture. Stem Cells 22: 275-282.

292. Li Z, Leung M, Hopper R, Ellenbogen R, Zhang M (2010) Feeder-free self-renewal of human embryonic stem cells in 3D porous natural polymer scaffolds. Biomaterials 31: 404-412.

293. de Vos P, Faas MM, Strand B, Calafiore R (2006) Alginate-based microcapsules for immunoisolation of pancreatic islets. Biomaterials 27: 5603-5617.

294. Lim F, Sun AM (1980) Microencapsulated islets as bioartifical endocrine pancreas. Science 210: 908-910.

295. Soon-Shiong P, Heintz RE, Merideth N, Yao QX, Yao Z, et al. (1994) Insulin independence in a type 1 diabetic patient after encapsulated islet transplantation. The Lancet 343: 950-951.

296. Calafiore R, Basta G, Luca G, Lemmi A, Montanucci MP, et al. (2006) Microencapsulated Pancreatic Islet Allografts Into Nonimmunosuppressed Patients With Type 1 Diabetes. First two cases 29: 137-138.

297. Basta G, Montanucci P, Luca G, Boselli C, Noya G, et al. (2011) Long-Term Metabolic and Immunological Follow-Up of Nonimmunosuppressed Patients With Type 1 Diabetes Treated With Microencapsulated Islet Allografts. Four cases 34: 2406-2409.

298. Murua A, Orive G, Hernández RM, Pedraz JL (2009) Xenogeneic transplantation of erythropoietin-secreting cells immobilized in microcapsules using transient immunosuppression. Journal of Controlled Release 137: 174-178.

299. Orive G, De Castro M, Ponce S, Hernández RM, Gascón AR, et al. (2005) Long-Term Expression of Erythropoietin from Myoblasts Immobilized in Biocompatible and Neovascularized Microcapsules. Molecular Therapy 12: 283-289.

300. Lim GJ, Zare S, Van Dyke M, Atala A (2010) Cell Microencapsulation. In: Pedraz JL, Orive G, editors. Therapeutic Applications of Cell Microencapsulation. New York, NY: Springer New York. pp. 126-136.

301. Goenka S, Sant V, Sant S (2014) Graphene-based nanomaterials for drug delivery and tissue engineering. Journal of Controlled Release 173: 75-88.

302. Chen GY, Pang DWP, Hwang SM, Tuan HY, Hu YC (2012) A graphene-based platform for induced pluripotent stem cells culture and differentiation. Biomaterials 33: 418-427.

303. Lee WC, Lim CHYX, Shi H, Tang LAL, Wang Y, et al. (2011) Origin of Enhanced Stem Cell Growth and Differentiation on Graphene and Graphene Oxide. ACS Nano 5: 7334-7341.

304. Nayak TR, Andersen H, Makam VS, Khaw C, Bae S, et al. (2011) Graphene for Controlled and Accelerated Osteogenic Differentiation of Human Mesenchymal Stem Cells. ACS Nano 5: 4670-4678.

305. Ku SH, Park CB (2013) Myoblast differentiation on graphene oxide. Biomaterials 34: 2017-2023.

306. Li N, Zhang Q, Gao S, Song Q, Huang R, et al. (2013) Three-dimensional graphene foam as a biocompatible and conductive scaffold for neural stem cells. Sci Rep 3: 1604.

307. Shin SR, Aghaei-Ghareh-Bolagh B, Dang TT, Topkaya SN, Gao X, et al. (2013) Cell-laden Microengineered and Mechanically Tunable Hybrid Hydrogels of Gelatin and Graphene Oxide. Advanced Materials 25: 6385-6391.

308. Ponce S, Orive G, Gascón AR, Hernández RM, Pedraz JL (2005) Microcapsules prepared with different biomaterials to immobilize GDNF secreting 3T3 fibroblasts. Int J Pharm 293: 1-10.

309. Algothmi WM, Bandaru NM, Yu Y, Shapter JG, Ellis AV (2013) Alginate–graphene oxide hybrid gel beads: An efficient copper adsorbent material. J Colloid Interface Sci 397: 32-38.

310. Nikolaev NI, Muller T, Williams DJ, Liu Y (2014) Changes in the stiffness of human mesenchymal stem cells with the progress of cell death as measured by atomic force microscopy. J Biomech 47: 625-630.

311. Bünger CM, Gerlach C, Freier T, Schmitz KP, Pilz M, et al. (2003) Biocompatibility and surface structure of chemically modified immunoisolating alginate-PLL capsules. Journal of Biomedical Materials Research Part A 67A: 1219-1227.

312. Dhahri S, Ramonda M, Marliere C (2013) In-situ determination of the mechanical properties of gliding or non-motile bacteria by atomic force microscopy under physiological conditions without immobilization. PLoS One 8: e61663.

313. Park S, Lee K-S, Bozoklu G, Cai W, Nguyen ST, et al. (2008) Graphene Oxide Papers Modified by Divalent Ions—Enhancing Mechanical Properties via Chemical Cross-Linking. ACS Nano 2: 572-578.

314. Wu L, Liu L, Gao B, Muñoz-Carpena R, Zhang M, et al. (2013) Aggregation Kinetics of Graphene Oxides in Aqueous Solutions: Experiments, Mechanisms, and Modeling. Langmuir 29: 15174-15181.

315. Mu Q, Su G, Li L, Gilbertson BO, Yu LH, et al. (2012) Size-Dependent Cell Uptake of Protein-Coated Graphene Oxide Nanosheets. ACS Appl Mater Interfaces 4: 2259-2266.

316. Russier J, Treossi E, Scarsi A, Perrozzi F, Dumortier H, et al. (2013) Evidencing the mask effect of graphene oxide: a comparative study on primary human and murine phagocytic cells. Nanoscale 5: 11234-11247.

Author acknowledges Kjpargeter / Freepik for the illustrations utilized in the cover and bookmarker of this Thesis.